AIX-MARSEILLE UNIVERSITE
FACULTE DES SCIENCES

THESE DE DOCTORAT

Ecole Doctorale Physique et Sciences de la matière

Mention : *Matière condensée et Nanosciences*

Présentée par

Liang CHEN

en vue d'obtenir le grade de docteur de l'Université d'Aix-Marseille

Dynamical microstructure formation in 3D directional solidification of transparent model alloys : in situ characterization in DECLIC-DSI under diffusion transport in microgravity

Soutenue le 29 novembre 2013 devant le jury composé de

Dr.	N. BERGEON	(Co-directrice de thèse)
Dr.	B. BILLIA	(Directeur de thèse)
Prof.	M. GEORGELIN	(Examinateur)
Prof.	K. KASSNER	(Rapporteur)
Prof.	A. LUDWIG	(Rapporteur)
Prof.	B. ZAPPOLI	(Examinateur)

CONTENTS

General introduction

Phenomena resulting from solidification widely exist in nature. Solidification is a phase transition from liquid state to solid state that, for a pure substance, occurs when the temperature is reduced below a critical value at constant pressure. The physical properties and atomic arrangement of the phases before and after the transition are drastically changed. One of the most common solidification examples for a pure substance in nature is the transition from water to ice, familiar to human beings. For multicomponent systems, the liquid and solid phases generally have different chemical compositions given by thermodynamic equilibrium as long as the transformation is not too fast.

a)

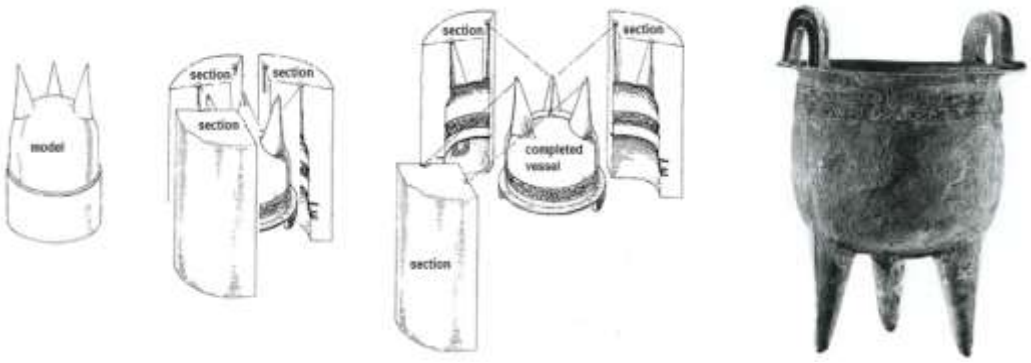

b)

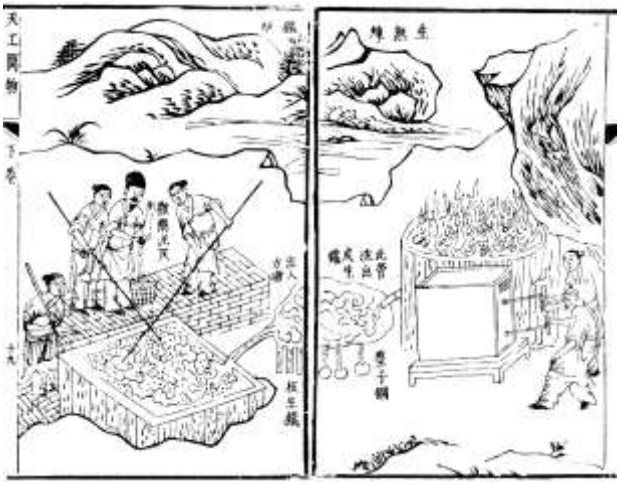

Figure 1. –a) Diagram showing basic components for a piece mold casting of a bronze tripod ding [L. Ledderose, Ten Thousand Things: Module and Mass Production in Chinese Art, Princeton University Press, 2000] and (right) a bronze cast ding from 1400-1300 BC (H: 54 cm, D: 40.7 cm, W: 9.6 kg). –b) Chinese iron workers smelting iron ore to make pig iron and wrought iron, with the puddling process displayed on the left and men operating a blast furnace on the right (from Tiangong Kaiwu encyclopedia printed in 1637, Ming Dynasty).

Casting of metallic materials is ancient (Figure 1), and era of mankind evolution (Bronze Age, Iron Age) are named after metallurgy stages. Nowadays, casting, welding, growth of

semiconductors from the melt etc. are all solidification processes in modern industry. For example, turbine blades for energy production in land-based power-plants and for jet engines, low-emission energy-effective engines for cars (Figure 2), lightweight metallic foams of interest for absorbing crashes, so called supermetals as thin sheets for electronic components with ultimate strength, high performance magnets, medical implants such as hip replacements, fine metallic powders to catalyze chemical reactions …

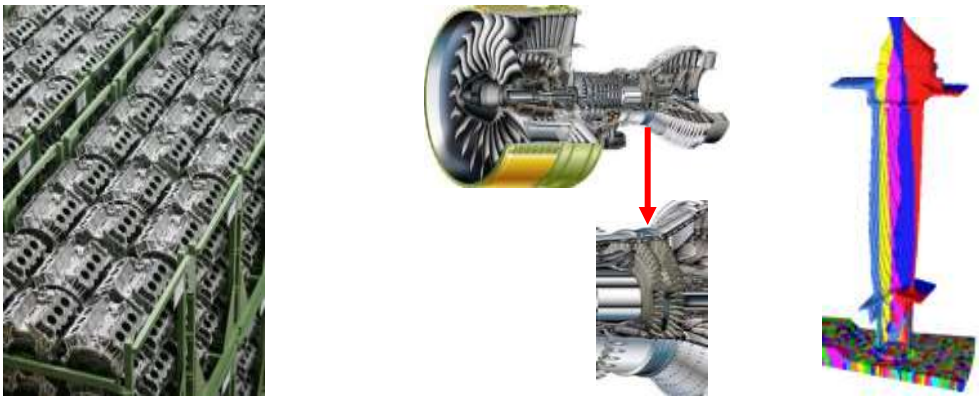

a b c

Figure 2. a) V6-Diesel engine blocks cast for Mercedes cars by Hydro Aluminium b) Cutaway view of the Engine Alliance GP7200 engine for Airbus A380 with a close-up on the turbine blades. c) THERCAST® simulated 3D grain-structure in a turbine blade geometry produced by investment casting, with the selection with time of a few columnar grains visible on the outer surface.

The solidification microstructure formed during the casting and solidification processing from the melt is a critical issue. For example, columnar dendrites are required for aero-engine turbine blades capable of operation at ever higher temperature with excellent creep properties and life in service. Instead, a dendrite equiaxed grain structure is required for homogeneous macroscopic behavior under mechanical stress, such as for car engine blocks. Besides the grain structure, the dendrites, which control the mechanical properties through their branch spacing and concomitant micro segregation of the chemical species, have thus to be designed in accordance to new materials specifications.

To produce materials reaching performance under ever-higher specific requirements, it is now recognized that this is most efficiently achieved by means of theoretical modeling and predictive quantitative numerical simulations of grain-structure formation in processes using sophisticated integrated software. In practice, the improvement of the design and processing of advanced materials follows the progress of the sophisticated numerical simulations developed following the explosion in available computation resources. Close comparison with precisely controlled benchmark experiments is mandatory for guidance and validation.

Directional solidification is a powerful technique to study pattern formation since the process parameters can be accurately controlled and the response of the interface can be quantitatively examined through the imaging of the spatio-temporal evolution of the interface patterns. Under terrestrial conditions convection effects dominate in bulk samples, which prevent precise characterization of microstructure selection. In this case, many experiments are done in thin samples to avoid the effects of convection. But diffusion-controlled experiments in thin samples give microstructures that are neither 2D nor 3D. Phase-field simulation and experiments in 3D have shown that the fundamental physics of pattern selection in 2D and 3D is significantly different [1]. Thus, a benchmark experimental study in bulk samples is required under low gravity conditions. Accordingly, in the frame of the joint work of DSIP (Dynamical Selection of 3D Interface Patterns) and MISOL3D (Microstructures de Solidification 3D) projects, respectively selected by NASA and CNES, microgravity experiments in a model transparent system have been planned on ISS using the directional solidification insert (DSI) in the DECLIC facility designed and built by CNES [2]. In this thesis, we carried out several runs in the frame of the MISOL3D/DSIP project, each run consisting of a series of solidification experiments with different control parameters. These experiments were monitored in quasi real-time by telescience and commands sent from the ground to DSI through the CADMOS Center (CNES) in Toulouse and NASA. In situ observation allowed identifying the critical dynamical phenomena and then extracting the benchmark data through image processing and analysis. Those data are the first and uppermost outcomes from the MISOL3D/DSIP project. Meanwhile, the phase field simulation counterpart was done by DSIP partners in USA, in cooperation with scientists from the Theory and Simulation team of IM2NP. Our experimental benchmark results in the limit of diffusion transport obtained in space conditions have been used for quantitative comparison with the simulation predictions.

This thesis contains 5 chapters. In the first chapter, the basic principles of Bridgman-type directional solidification are introduced. Also, the mechanisms and conditions of the morphological instability of the planar solid-liquid interface are presented, and the interface pattern formation is described in both diffusive conditions and in the presence of gravity-driven convection in the melt. Then, the influence of the anisotropy on growth patterns is noticed. Finally, the use of transparent alloys in directional solidification experiments is briefly summarized.

In the second chapter, the DECLIC facility, the dedicated DSI equipment and the MISOL3D/DSIP project are detailed, as well as the processing of experiments, the image treatment technique and the various methods used to extract the long-desired benchmark data.

In the third chapter, we focus on the first morphological instability of the smooth solid-liquid interface that gives way to the cellular and dendritic microstructures. Relevant

characteristic parameters are measured: - cell/dendrite primary spacing, which includes the average value and spacing distribution, - the order/disorder level of the extended cell/dendrite array by means of both the Minimal Spanning Tree method and the counting of the number of nearest neighbors. Beyond those measurements, we also characterize the dynamics of interface pattern formation, which comprises two phases - evolution of the interface pattern from its very birth at the smooth solidification front and - steady state growth morphology. The mechanisms of 3D-shape and array adjustment are analyzed.

In the fourth chapter, we address the secondary instabilities evidenced in our 3D-experiments on transparent bulk samples: - cellular array oscillation and - multiplet microstructures. Their characteristic parameters are measured. Results on cellular array oscillation are also compared with the phase field simulations and a good agreement is obtained.

In the fifth and last chapter, comparing the μg experiments with similar experiments done on ground under 1g in the Engineering Model of DSI enables to clarify the influence of buoyancy convection on the morphological instability of the smooth interface and on cellular/dendritic patterns.

The thesis closes with a general conclusion, and statement of pending questions and perspectives stemming from the current investigation.

Chapter 1. Basic phenomena in alloy solidification

1.1. Pattern formation in alloy solidification from the melt

Pattern formation is crucial in many crystal growth processes, such as solution growth, vapor growth, electrochemical deposition of metals on surfaces, growth of thin films by vapor deposition, solid-state transformations and chemical reactions. In this thesis, we are interested in the dynamics of morphological instability of the solid-liquid interface leading to pattern formation (cellular and dendritic growth in practice) in solidification processing of a transparent model alloy, succinonitrile – 0.24 wt% camphor, that freezes like metals.

Depending on the experimental procedure that is used, the growth can be free, directional or both like in the case of ingot casting. Here, we focus on the Bridgman-type directional solidification, at low pulling rate, as all our experiments are done in such conditions. In directional growth, a positive temperature gradient is imposed in the solid and liquid so that the heat is extracted through the solid in ideal case (laterally infinite sample or adiabatic conditions at the crucible wall). It is fair to say that, for transparent organic alloys, this is far from reality due to alloy thermal conductivity much lower than that of the glass crucible so that heat extraction through the crucible wall rather than the solid may be a critical issue; this will be discussed in the following chapter.

Directional solidification of alloys produces two types of substructures: striations formed by a particular arrangement of rod crystals separated by sub-boundaries [3], which do not result from morphological instability and thus will not be further discussed, and cellular or dendritic microstructures emerging from the breaking of the smooth solidification front when the system is driven above a critical threshold related to the applied control parameters of the process, where solute accumulation/rejection in the liquid would be too strong and no longer sustainable ahead of a flat interface [4,5].

1.2. Directional solidification in a Bridgman-type furnace

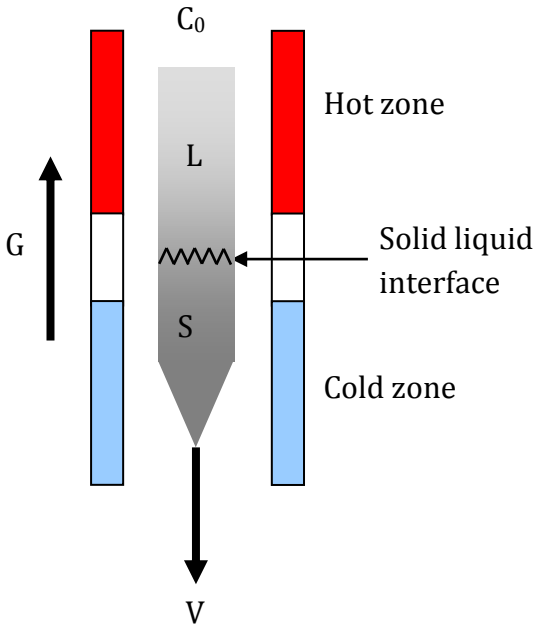

Figure 1.1. Schematic representation of Bridgman-type solidification

Bridgman-type solidification is sketched in Figure 1.1. The sample is placed in a temperature gradient achieved by imposing fixed temperatures to the hot and cold zones in Figure 1.1. The liquid material is solidified either by translating the sample into cold zone, which corresponds to our experimental case, or by moving the thermal assembly in opposite direction. For a binary alloy, the axial temperature gradient G, the pulling velocity V and the solute concentration C_0 are the three control parameters. Inception of directional solidification can be either triggered on a solid seed made of a single crystal of purposely selected orientation or left free to follow nucleation of several nuclei of random orientations. Most generally, two of the control parameters are kept fixed during Bridgman solidification, and one is systematically varied. Let's take the pulling velocity V as an example. The flat solid-liquid interface will undergo morphological instability and then develop several spatial microstructures as V is increased, in particular the cellular and dendritic microstructures shown in Figure 1.2.

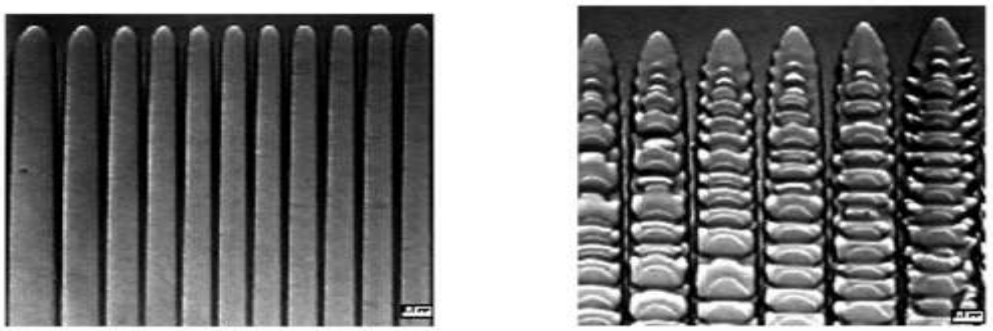

a b

Figure 1.2. The two most common microstructures resulting from the morphological instability of the solid-liquid interface in alloy directional solidification: -a) deep cells, V ≤ 8 μm/s, -b) dendrites, V ≥ 20 μm/s. Thin samples of succinonitrile - 0.7 wt % salol directionally solidified at G = 3.8 K/cm [6].

1.3. Basic equations of directional solidification of a binary alloy

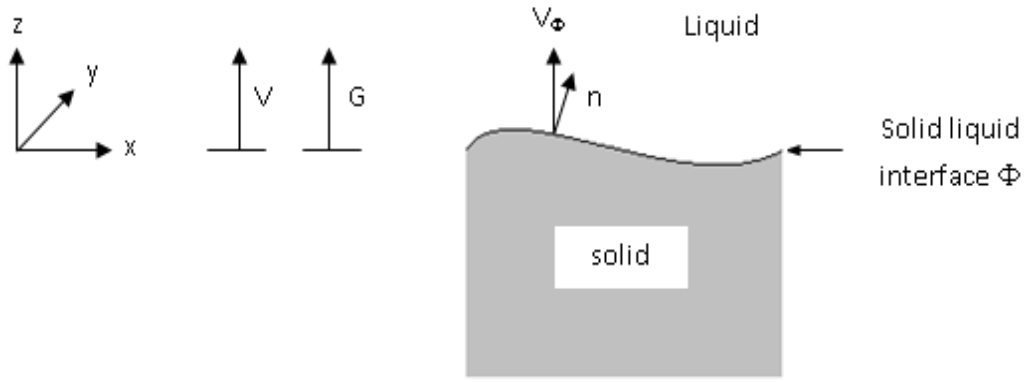

Figure 1.3. Ideal directional solidification from the melt of a binary alloy of initial solute concentration C_0 at imposed pulling velocity V in a constant temperature gradient G.

The basic equations which govern the solidification process are introduced here. To simplify the model, we consider an ideal situation with several assumptions:

1: The solid and liquid have the same density.

2: Solute diffusion in solid is ignored as it is several orders of magnitude slower than that in liquid.

3: The temperature is continuous at the solid-liquid interface.

4: Local thermodynamic equilibrium at the solid-liquid interface.

5: All the physico-chemical coefficients are constant.

6: The elastic or plastic effects in the solid are ignored.

7: No convection is present in the liquid.

Then, the equations for heat balance in the liquid (L) and solid (S) phases read:

$$\frac{\partial T_i}{\partial t} = D_{th}^{i} \nabla^2 T_i + V \frac{\partial T_i}{\partial z} \quad 1.1$$

where the index i can be S or L. T_i and $D_{th.i}$ are the temperature and the thermal diffusivity in phase i respectively.

Solute balance in the liquid:

$$\frac{\partial C}{\partial t} = D_L \nabla^2 C + V \frac{\partial C}{\partial z} \quad 1.2$$

with C and D_L the solute concentration and diffusion coefficient in the melt, respectively.

For a solidifying system, the bulk equations should be complemented with the balances of heat and solute at the solid – liquid interface. The thermal balance at the interface is given by:

$$\left[K_S \vec{\nabla} T_s - K_L \vec{\nabla} T_L\right]_{\Phi} \cdot \vec{n} = L \vec{V}_{\phi} \cdot \vec{n} \quad 1.3$$

where L is the latent heat of fusion per unit volume. $\vec{V}_{\Phi}$ and $\vec{n}$ are the growth velocity and the normal at the phase boundary, directed towards the liquid, and K_S and K_L the thermal conductivities of solid and liquid. ϕ means that the concerned quantities have to be evaluated at the solidification front.

Solute flux balance at interface:

$$D_L [\nabla C]_{\Phi} \cdot \vec{n} = [C_S - C]_{\Phi} V_{\Phi} \cdot \vec{n} \quad 1.4$$

where C_S is the solute concentration in solid.

The continuity of temperature at the interface implies:

$$T_{L\Phi} = T_{S\Phi} = T_{\Phi} \quad 1.5$$

and it follows from the assumption of local thermodynamic equilibrium at the solidification front, which is widely established for solids growing with a rough solid-liquid interface, that

$$C_{S,\phi} = k C_{\phi} \quad 1.6$$

which defines the solute partition coefficient k (Figure 1.4), and the Gibbs-Thomson condition

$$T_\Phi = T_M + mC_\Phi + \Gamma\kappa_\Phi \qquad 1.7$$

with T_M the melting temperature of the pure material, m the liquidus slope, $\Gamma(= T_M\gamma/\mathrm{L})$ the Gibbs-Thomson coefficient function of the solid-liquid surface tension γ, and κ_Φ the local interface curvature. Here we assume the alloy has a dilute concentration so that k and m can be considered as constants.

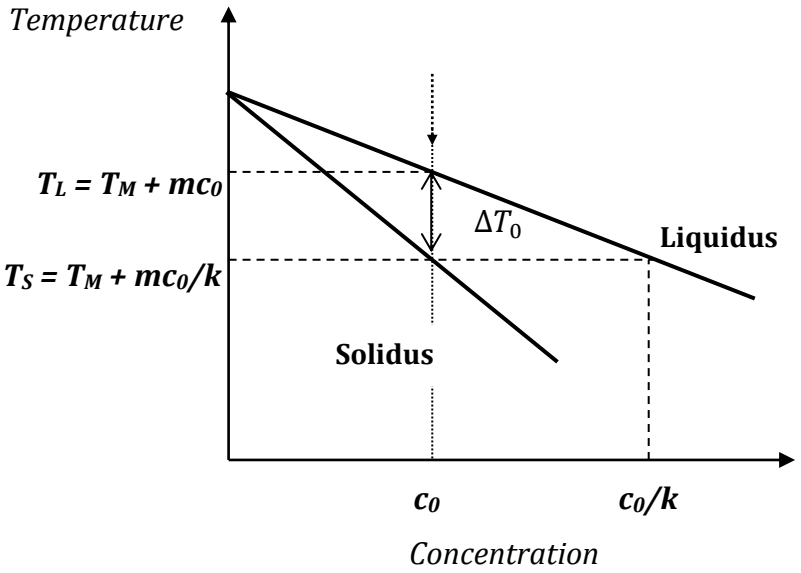

Figure 1.4. Schematic representation of the low solute concentration side of the phase diagram of a dilute binary alloy (k < 1). The liquidus and solidus are considered linear in first approximation.

It is long recognized that it is convenient to introduce length scales in the theoretical analysis and modeling of alloy solidification. The three length scales that are most commonly used are introduced here. Two can be defined by considering steady-state solidification with a planar front:

- The solute diffusion length l_s

$$l_s = \frac{D_L}{V} \qquad 1.8$$

where V is the growth velocity equal to the pulling rate.

- The thermal diffusion length l_T

$$l_T = \frac{\Delta T_0}{G} \qquad 1.9$$

with $\Delta T_0 = mC_0(k-1)/k$ the equilibrium freezing range of the alloy for linear solidus and liquidus lines.

Thermal diffusivity varies from 10^{-3} cm^2/s for organics to 10^{-1} cm^2/s for metals, which is several orders of magnitude larger than the solute diffusivity (about 10^{-5} cm^2/s), heat diffusion is much faster than solute diffusion. Thus, slow solute diffusion is often the limiting physical process, and the solute diffusion length l_s the most important length scale. Accordingly, the time scale is defined by D_L/V^2 from the equation of solute diffusion.

Curvature appears with non-planar microstructures forming at the solid-liquid interface. In addition to the solute and thermal diffusion lengths, l_s and l_T, this interface curvature introduces a third length scale, the capillary length l_c.

$$l_c = \frac{\Gamma}{\Delta T_0} = \frac{\Gamma}{m(C_s - C)_\phi} = \frac{\Gamma}{mC_\phi(k-1)} \qquad 1.10$$

In non-dimensional form, the microstructure characteristics are determined by the relative magnitudes of the three length scales as for instance noticed by Langer [7] and Trivedi [8]. Several choices are possible, for example $\nu = l_T/l_s$ and $A = kl_c/l_s$ when adopting the solutal length as the reference. Then, the shape parameters of a microstructure (primary spacing λ, tip radius R and the microstructure amplitude $\Delta\phi$ …) are scaled by the solutal length to obtain the dimensionless parameters. Those parameters are called Peclet numbers *Pe:* $Pe_\lambda = \lambda/l_s$, $Pe_R = R/l_s$, $Pe_{\Delta\phi} = \Delta\phi/l_s$. When the interface microstructure is dendritic, new characteristic shape parameters have to be introduced, in particular the secondary arm spacing, distance of the first secondary branch from the dendrite tip, dendrite trunk diameter, tertiary arm spacing etc., and corresponding Peclet numbers.

1.4. Morphological instability of the solid liquid interface

Planar interface instability is the first step in the formation of a microstructure at the solidification front, such as the cellular and dendritic patterns illustrated in Figure 1.2. For a pure material, the thermodynamic driving force at the origin of the interface instability is just the thermal undercooling of the liquid below the melting point. Thus, the interface will be stable if the temperature gradient in front of the interface is positive, and unstable if it is negative [9].

For a binary alloy material solidified directionally in a stabilizing positive temperature gradient G, the solutal driving force at the origin of interface morphological instability was first postulated by Rutter and Chalmers [5] and modeled by Tiller et al. [10] in 1953, who named it "constitutional supercooling" to explicitly refer to its solutal origin.

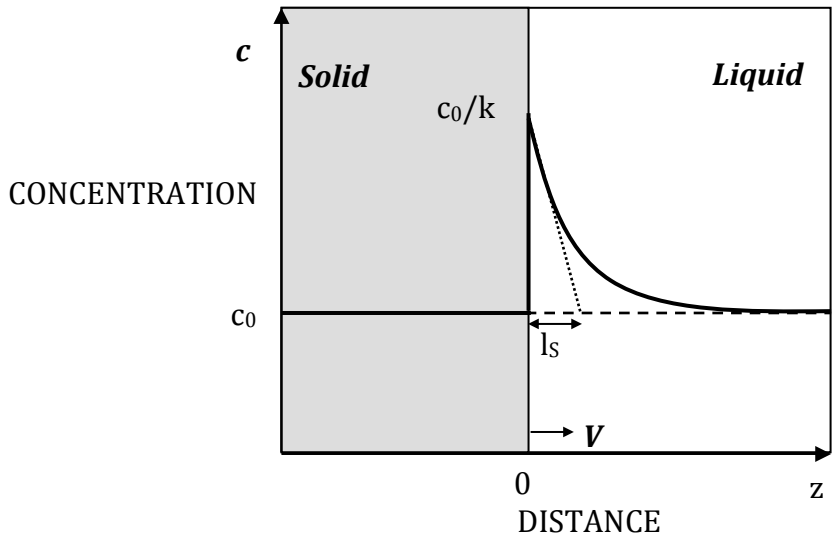

Figure 1.5. Solute concentration profile for steady state solidification of a binary alloy with a planar solid-liquid interface.

A binary alloy of initial solute concentration C_0, and a segregation coefficient k, is solidified at a constant velocity V. If $k < 1$, solute is rejected from the solid upon solidification and accumulated in the melt in front of the interface. Consequently, a solute boundary layer will progressively build up and reach steady state. The solute concentration profile in the liquid at steady state is given by:

$$c(z) = c_0\left[1 + \left(\frac{1-k}{k}\right) exp\left(-\frac{V}{D_L}z\right)\right] \qquad 1.11$$

where z is the distance in the liquid from the interface. (Figure 1.5).

The local equilibrium temperature T_{eq} at the interface in the liquid is obtained from the relation 1.6:

$$T_{eq}(z) = T_M + mC_L(z) \qquad 1.12$$

The actual temperature of liquid $T_L(z)$ is given by:

$$T_L(\mathrm{z}) = T_M + m\frac{C_0}{k} + Gz \qquad 1.13$$

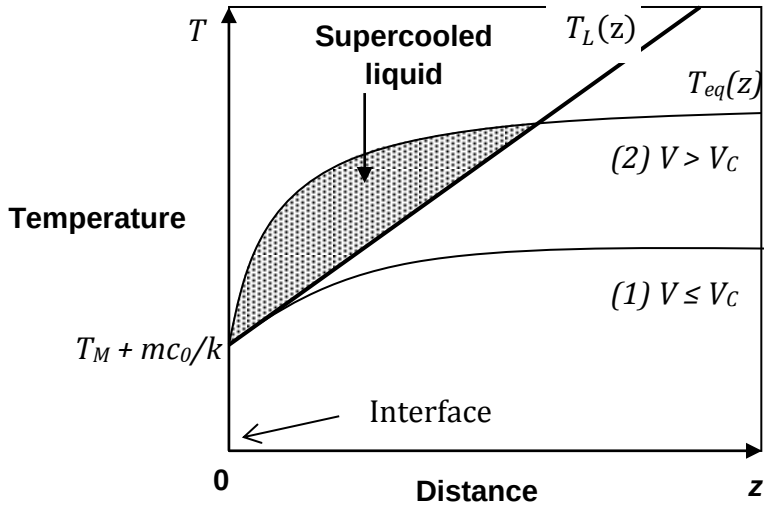

Figure 1.6. Temperature profile in the liquid ($T_L(z)$) compared to the equilibrium temperature $T_{eq}(z)$ for respectively (1) the stable interface case, (2) the unstable interface case.

If we plot the actual temperature profile $T_L(z)$ and the equilibrium temperature profile $T_{eq}(z)$ together as shown in Figure 1.6, two different cases are distinguished that depends on the pulling rate V (the pulling rate V_c corresponds to the transition between the two cases:

(1) $V \leq V_c$: The equilibrium solidification temperature is always cooler than the actual temperature. In this case, small protrusions at the interface will be melted back by the hot liquid. Therefore, they will not amplify and the solid-liquid interface is always stable.

(2) $V > V_c$: There exists in the liquid a zone in front of the solid-liquid interface, indicated in Figure 1.6 , where the equilibrium solidification temperature exceeds the actual temperature. This supercooling caused by the variation of solute concentration is named constitutional supercooling. Now, any small protrusion at the flat interface will be able to grow up in this area, which will result in morphological instability of the phase boundary.

The critical velocity V_c that corresponds to the transition from stable region to unstable region is given by:

$$G = \left.\frac{\partial T_{eq}}{\partial z}\right|_{z=0} = mC_0 \frac{(k-1)}{k} \frac{V}{D_L} = mG_c \qquad 1.14$$

Figure 1.6 indicates that the solid-liquid interface is unstable if the gradient of equilibrium solidification temperature at the interface, mG_C, is greater than the actual temperature gradient G. Making use of equation 1.14, the condition for instability of the planar solid-liquid interface is obtained

$$V > V_c = \frac{kGD_L}{(k-1)mC_0} \tag{1.15}$$

This constitutional supercooling criterion can be used to examine whether the flat solid-liquid interface is unstable or not, but it also has limitations. First, it is based on thermodynamic equilibrium considerations, whereas solidification and interface evolution are intrinsically non-equilibrium processes. Second, the local curvature of the perturbed interface is not considered although it will increase the free energy of the system. Third, the evolution tendency of the interface morphology cannot be described. Furthermore, this theory is no longer valid in rapid solidification where non-equilibrium effects (e.g. solute trapping) may become prevalent.

1.4.1. Linear stability analysis

The detailed linear stability analysis of the planar interface instability during directional solidification was first carried out by Mullins and Sekerka [11] who calculated the evolution with time of a sinusoidal perturbation $\phi(x,t) = \delta(t)\sin(\omega x)$ of the flat interface of infinitesimal amplitude *δ(t)*. The growth velocity of the perturbed solidification front is then equal to

$$V + \frac{\partial \phi(x,t)}{\partial t} = V + \frac{\partial \delta(t)}{\partial t} sin(\omega x) = V + \delta_t \, sin(\omega x) \tag{1.16}$$

The planar solid-liquid interface is unstable if any sinusoidal Fourier component of wavenumber ω grows, i.e. if $\partial\delta(t)/\partial t > 0$, and stable if none grows. The initial evolution of a perturbation is given by

$$\frac{\delta_t}{\delta} = \omega V \frac{mG_C\left(\omega^* - \frac{V}{D_L}\right) - \left(\frac{K_S G_S + K_L G_L}{K_S + K_L} + \Gamma\omega^2\right)\left(\omega^* - V\frac{(1-k)}{D_L}\right)}{\frac{L}{K_S + K_L}\left(\omega^* - V\frac{(1-k)}{D_L}\right) + 2\omega m G_C} \tag{1.17}$$

where $\omega^* = (V/2D_L) + [(V/2D_L)^2 + \omega^2]^{1/2}$.

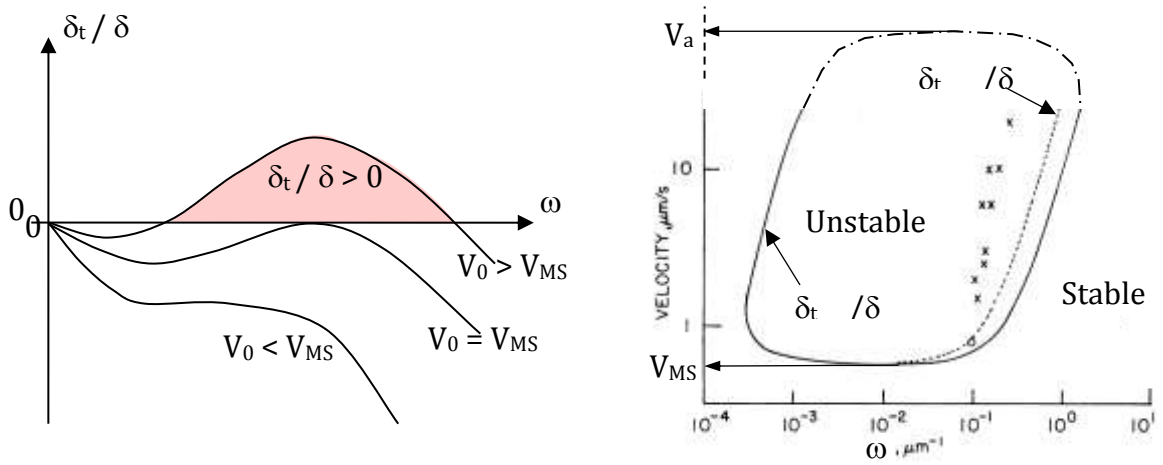

a b

Figure 1.7. –a) Variation of perturbation amplification rate δ_t/δ with the wave number ω predicted by the linear analysis of morphological instability of the planar solid-liquid interface in directional solidification of a binary alloy (V_{MS}: critical velocity of transition Mullins-Sekerka from stable to unstable front). –b) Morphological stability diagram (V, ω) showing the stable and unstable domains for succinonitrile – 0.35 wt% acetone, G = 42.8 K/cm [12]**, and the variation of the wavenumber of the Fourier mode with maximum amplification (- - - - -). The - · - · - · - curve is a schematic extension of the limit of morphological stability to show that the flat interface is planar for velocities above V_a.**

The evolution of δ_t/δ with wavenumber ω is shown in Figure 1.7. As the denominator of the RHS of Equation 1.17 is always positive, the sign of δ_t/δ, and thus morphological stability ($\delta_t/\delta < 0$) or instability ($\delta_t/\delta > 0$), depends only on the numerator. As in the constitutional supercooling criterion, the driving force of morphological instability is the solute concentration gradient G_C, the stabilizing effect of temperature gradient is now weighted, $G_w = (K_S G_S + K_L G_L)/(K_S + K_L)$, and further stabilization is introduced by the capillary term $\Gamma\omega^2$. The threshold of morphological instability corresponds to $\delta_t/\delta = 0$ and $\partial(\delta_t/\delta)/\partial\omega = 0$, i.e. the curve $V = V_{MS}$ in Figure 1.7-a. The Mullins-Sekerka criterion of morphological stability is classically written

$$\frac{G_w}{mG_C} \geq S \qquad 1.18$$

where S is a function that expresses the stabilizing effect of capillarity ($S \leq 1$), which was calculated by Mullins and Sekerka as a function of parameter $A = k^2\,\Gamma\,V/[mC_0(k-1)D_L]$ for a series of values of the solute segregation coefficient k [13]. At relatively low pulling rates, as in our microgravity experiments, the stabilizing effect of capillary is sufficiently weak to be neglected (S is close to unity) so that and the Mullins-Sekerka criterion reduces to the so-called Modified Constitutional Supercooling Criterion

$$\frac{G_w}{mG_C} \geq 1 \qquad 1.19$$

which is not significantly different for transparent organic alloys for which $K_S \approx K_L$.

The Mullins-Sekerka theory considers steady-state as the basic state with established steady-state solute diffusion field while in reality, morphological instability always occurs during the initial solidification transient, which follows the application of the pulling rate when the experiment is started from rest, and thus before the steady-state concentration field is realized. Several analyses of initial solidification transient are available, and the model elaborated by Warren and Langer [14], which describes the building of the non-steady state solute distribution, has become the standard approach. It is assumed that the temperature field is frozen and the time-dependent solute profile in the liquid is approximated by

$$C(z,t) = C_0 + \left(C_\phi(t) - C_0\right) exp\left[-\frac{\left(z - z_\phi(t)\right)}{l_s(t)}\right] \qquad 1.20$$

Initially, the interface is at the alloy liquidus temperature (Figure 1.8-a), at $z_0 = mC_0/kG$ in the frame attached to the isotherms with z = 0 for the melting temperature of pure material.

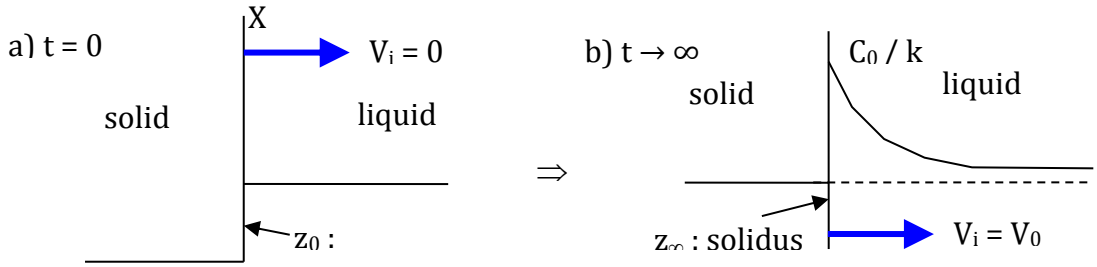

Figure 1.8. Sketch of the initial state (a) and final state (b) for planar front solidification during the recoil of the solid-liquid interface from liquidus to solidus in the initial transient.

The Warren - Langer approach leads to two coupled equations

$$V_\phi(t) = V + \dot{z}_\phi(t) = \frac{D_L\left(z_\phi(t) - z_\infty\right)}{\left(l_s(t)(1-k)z_\phi(t)\right)} \qquad 1.21$$

and

$$\dot{l}_s(t) = \left[\frac{D_L\left(z_\infty - kz_\phi(t)\right)}{l_s(1-k)z_\phi(t)}\right] - \frac{l_s\dot{z}_\phi(t)}{(z_0 - z_\infty)} \qquad 1.22$$

With $z_\phi(t)$ the interface position in the thermal field. z_0 the initial position of the interface (at the liquids temperature). z_∞ the asymptotic position of the interface for t $\rightarrow\infty$ (at the solidus temperature).

Numerical resolution is easy by making use of the analytical expressions valid at short times, $l_S(t) = (8Dt/3)^{1/2}$ and $z_\phi(t) = z_\infty - Vt + V\sqrt{\frac{2D}{3}}t^{\frac{3}{2}}/\left(|z_\infty|(1-k)\right)$, and gives the evolution of $C_\phi(t), V_\phi(t), l_s(t)$ and $z_\phi(t)$. Losert et al. [15] have shown that agreement between experiment and theory is very satisfactory for solidification of a transparent organic alloy in thin sample configuration, where the frozen-temperature assumption is good (Figure 1.9).

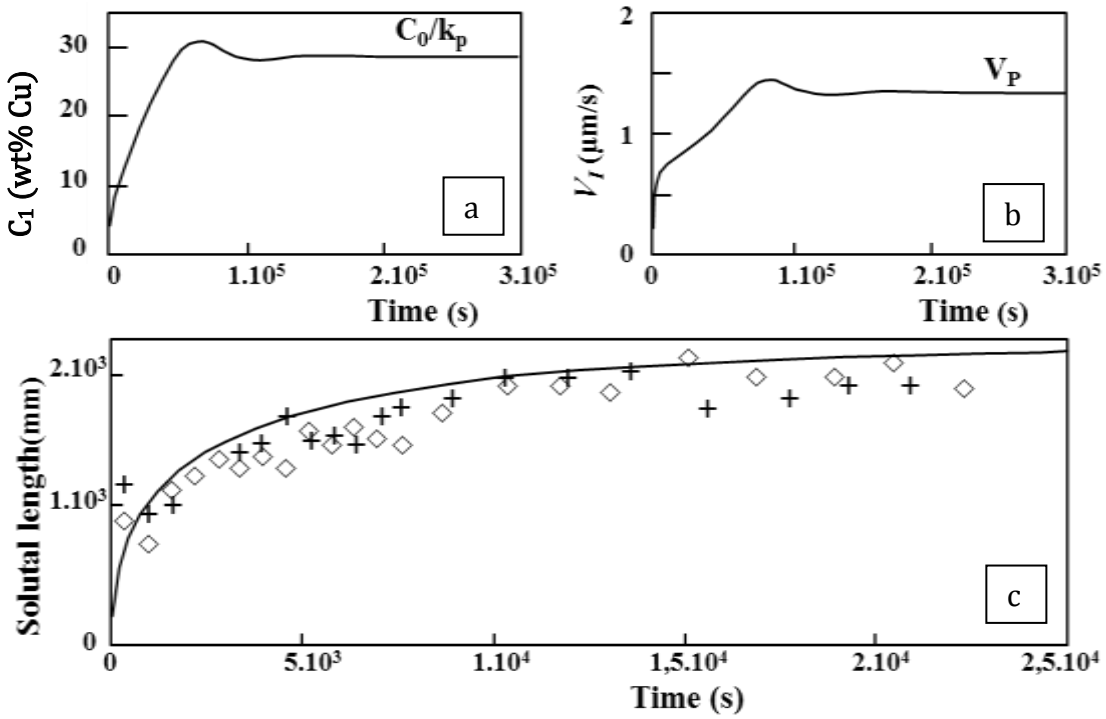

Figure 1.9. Diagrams showing the evolution, in the initial solidification transient of –a) the solute concentration C_Φ at the interface in the liquid and -b) the solidification front velocity V_Φ (Al – 4 wt% Cu, V = 1.35 µm/s, G = 37 K/cm, k = 0.14). –c) Comparison of experimental evolution of the solutal length l_s with the theoretical prediction of Warren – Langer model[15].

The Warren-Langer model is of great practical interest as it has been repeatedly found that the threshold of morphological instability in initial solidification transient verifies

the Mullins-Sekerka criterion (Equation 1.18), when the instantaneous values of solutal length and solute concentration at the interface in the liquid are used [16].

1.5. Non-planar interface microstructures: cells and dendrites

As the control parameter of directional solidification, V/V_C in practice for our experiments increases, the non-planar interface morphology becomes deeper and deeper and adopts a series of shapes, the two basic ones being cells preceding dendrites with sidebranches.

1.5.1. Cellular growth

The finger like microstructure that first develops following the inception of morphological instability of the smooth solidification front is the cellular microstructure. It is one of the most common microstructures of basic fundamental interest, although dendrites with sidebranches prevail in casting. Over the years, several models have been developed to describe the cellular microstructure characteristics. A few of the most representative ones are introduced here:

- 1) Bower-Brody-Flemings (BBF) model: These authors considered the array growth of deep cells assuming flat isotherms isotherm, no solute diffusion in the solid, negligible curvature effect in the tip region and small constitutional supercooling in the intercellular groove. Then, the average solute concentration in the plane perpendicular to the growth direction that passes at the tip is taken as the tip concentration C_t and the solute balance equation is written as:

$$V(C_t - C_0) = -D\left.\frac{\partial C}{\partial z}\right|_{z=z_t} \tag{1.23}$$

From local thermodynamic equilibrium at the solid-liquid interface, the gradient of solute concentration is expressed as G/m so that the tip concentration of a deep cell takes the simple form

$$C_t = C_0 - \frac{DG}{mV} \tag{1.24}$$

The BBF model was found to agree well with experimental data in the several succinonitrile-based systems for the whole cell domain [17,18].

-2) Hunt model: In this model, the average composition at a distance from the tip is like in the BBF model, and a radial contribution is added by using Zener's approximation [19]. The final relationship derived by Hunt obtained for the tip undercooling ΔT^* is the following

$$C_t = C_0 - \frac{DG}{mV}\left[1 + Pe_R\left(\frac{C_t(k-1)V}{D} - \frac{G}{m}\right)\right] \quad 1.25$$

The selection of the cell primary spacing has motivated numerous theoretical modeling in literature. These models of steady-state cellular solidification allow a continuous band of primary spacing. Therefore, consideration of steady-state only is not sufficient to determine the final selection, and over the years a series of more or less ad-hoc principles have been invoked such as minimum undercooling, minimum entropy production, marginal stability …

Among the phenomenological models developed for the description of the cellular growth, Hunt [20] and Kurz and Fisher [21] models are worth noting, but the agreement was rather poor when compared to the cellular experimental data. A basically similar model proposed by Trivedi [22], in which the marginal stability criterion is used, shows a better fit with the experimental data for the average primary spacing observed in experiments. Now the major effort has shifted to the analysis of the stability of stationary patterns and the dynamical process of cellular microstructure formation. Only a few experiments are carried out to study the dynamical process. A comprehensive insight into the formation of cellular array was gained in the studies of Trivedi et al. on thin samples of transparent organic alloys [12,23,24]. The initial morphological instability is found to be localized at grain (sub) boundaries, from which it then propagates laterally and amplifies till a stable pattern is formed. The instability/cell wavelength increases with time so that the final spacing is different from the initial one. Furthermore, the study of Seetharaman [25] has shown that the cell amplitude gets saturated before the steady-state cell spacing is established by cell-elimination and tip-splitting processes.

1.5.2. Cell-dendrite transition

When the level of morphological instability V/V_C becomes substantial, the smooth cellular body undergoes a side branching instability and converts to a dendritic structure. Afirst expression for the critical velocity of this transition was proposed by Kurz and Fisher [26]:

$$V_{cd} = \frac{1}{k}V_c \quad 1.26$$

that does not depend on any cell shape parameter (spacing, tip radius …).

Nevertheless, experimental studies of the transition from cellular to dendritic structures [27–29] have shown that cells and dendrites coexist over a range of velocities under fixed values of G and C. This coexistence is the mere consequence of the pretty wide

distribution of primary spacing in usual experiments started from rest where the cell array is not prepared with a uniform stable spacing imposed by some trick, such as laser spots. Actually, the transition occurs when the local cell spacing reaches some critical value for side branching, at a velocity close to V_{cd}. The onset of side branching has been studied and it was found that there are many possible mechanisms. Therefore, different criteria have been proposed [6, 26, 27]

Accordingly, coexistence of both cellular and dendritic structures in the transition region reflects the fact that part of the spacing distribution is on the dendrite side (larger spacings) while the smaller spacings are still lying on the cell side. In other words, the two stable branches of solutions exist together, the branch of cellular microstructures together with that of dendritic microstructures. Besides, according to experiments on thin rectangular samples the cell-dendrite transition is subcritical so that the general characteristics of the planar-cellular-dendritic transitions as pulling velocity is increased can be represented by the bifurcation diagram below (Figure 1.10).

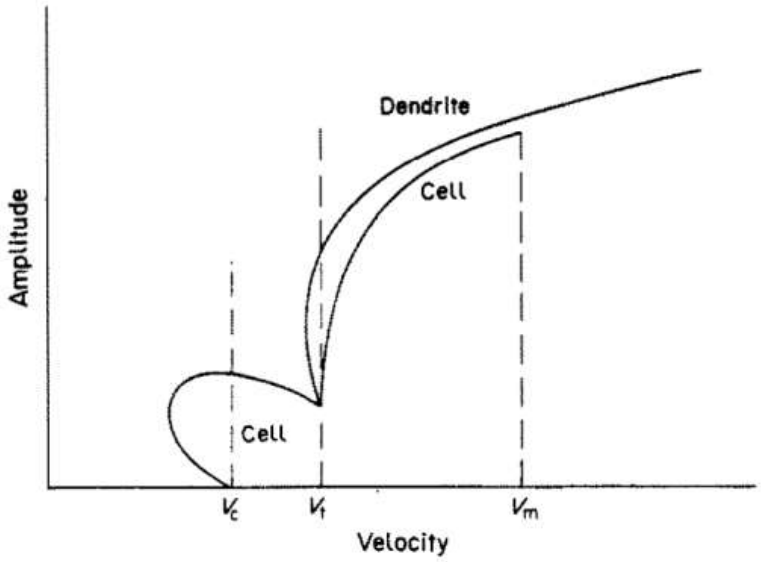

Figure 1.10. Schematic diagram showing the subcritical bifurcations for the planar-cellular transition and cellular to dendritic transition. [29]

1.5.3. Dendritic growth

The dendrite is the most common pattern forming in alloy solidification. It is primarily characterized by the tip radius and first, second, tertiary and even higher-order branches (Figure 1.11). In order to solve the complicated dendrite problem, several models have been developed based on the solutions of the thermal and solute diffusion problems. For directional solidification, the thermal contribution becomes rapidly negligible so that the formation of the dendritic structure is generally determined by considering the solute diffusion transport only. Then, the problem is to find the dendritic shape that satisfies one steady-state diffusion equation with the constraint that the growth rate should equal the pulling rate in directional solidification.

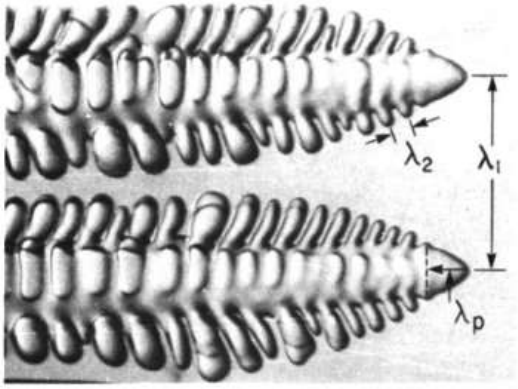

Figure 1.11. Dendritic microstructure in succinonitrile-0.4 wt% acetone alloy (thin sample). [23]

The starting point is the Ivantsov approach of the growth of a free dendrite of a pure substance in thermally undercooled melt [24]. The mathematical solution is a parabolic branchless steady state shape dendrite when the surface tension is ignored as found by Ivantsov in 1947. This can be transposed to isothermal solidification of a binary alloy, which gives the relation between the Péclet number Pe_R and the dimensionless supersaturation Ω which is defined as:

$$\Omega = \frac{C_t - C_0}{C_t(1-k)} \qquad 1.27$$

The Ivantsov relationship is written:

$$\Omega = Iv(Pe) \qquad 1.28$$

Where the Ivantsov function *Iv(Pe)* is defined as:

$$Iv(Pe) = \frac{1}{2}Peexp(\frac{1}{2}Pe)E_1(\frac{1}{2}Pe) \qquad 1.29$$

with

$$E_1\left(\frac{1}{2}Pe\right) = \int_{\frac{1}{2}Pe}^{\infty} \frac{exp(-z)}{z}\,dz \qquad 1.30$$

the first exponential integral.

For steady-state directional solidification at a constant velocity, this model shows how the tip undercooling of a dendrite varies as a function of its tip radius. A thicker dendrite will growth at larger undercooling, and thus lag behind. Calculations by Horvay et al [30] shows a linear relationship between the undercooling and the Péclet number at small Ω. The limitation in free dendrite growth is that in this model only the product *RV* is fixed for a given undercooling Ω. In a directional solidification experiment in which the pulling rate is fixed, the Ivantsov model predicts multiple solutions which relate dendrite tip undercooling with the dendrite tip radius. Yet, the experiments show that for a given velocity, the tip radius is uniquely selected for dendrites growing with negligible interaction with neighbors. Furthermore, dendrites prefer to grow along a specific direction which is also not accounted for in the Ivantsov model. All this indicates that a new effect must be introduced to stabilize the dendritic interface and lead to the unique selection of the tip radius.

The solution was to incorporate the contribution of interfacial energy into the dendrite growth problem through the Gibbs-Thomson boundary condition, and postulate that the dendrite shape (needle like) was only slightly modified by the presence of the capillary effect. The solution was obtained by Temkin [31] and Trivedi [32]. However, those solutions still not give a self-consistent solution of the steady-state dendrite growth problem.

Langer and Muller-Krumbhaar [33] have then carried out a linear stability analysis of an Ivantsov parabola, and found that a range of tip radii at which a dendrite could grow in a stable way. Therefore, these authors argued that radii may become unstable because of the presence of the secondary branches tending to increase the tip radius to its maximum value. They referred to this dendrite tip selection process as the *marginal stability criterion*. The important relationship obtained from this marginal stability criterion is:

$$VR^2 = \frac{\Gamma D}{\sigma^* k \Delta T_0} \qquad 1.31$$

where σ^* is the stability constant whose value of σ^* is found around 0.025 [11,28,34,35]. This relationship can be transformed to make apparent the solute gradient in liquid at the tip:

$$mG_c = \frac{\Gamma}{\sigma^* R^2} \qquad 1.32$$

The marginal stability condition is thus realized when the solute effect (the left-hand-side of the equation) is balanced by the capillary effect (right-hand-side of the equation). The results predicted by using the marginal stability assumption are generally in satisfactory agreement with the experimental findings [34,36,37].

More recently, the mathematically self-consistent and rigorous microsolvability theory has emerged [38]. The final result can be set in the same form as the marginal stability condition, the only but major difference being in the expression of σ^*, which now contains the relevant and sound physics. This similarity has resulted in continuing the use of Equation 1.32 for practical application, mostly because σ^* is often estimated with limited precision only.

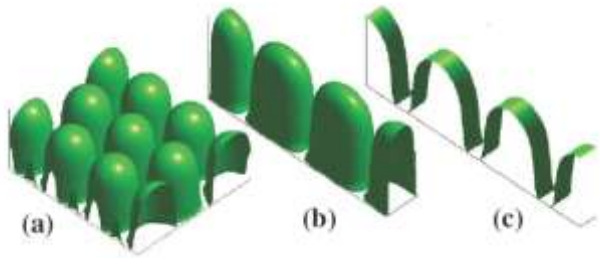

Figure 1.12. Examples of steady-state cell shapes calculated by the phase-field method For G = 38K/cm, SCN 0.7 wt% salol and V = 5µm/s [1]. **-a) 3D-hexagonal array, -b) and c) cell array in thin sample geometries for a sample thickness of 33µm and 22µm respectively.**

Today, the phase-field modeling method has rapidly advanced and become the method of choice as it is now able to address quantitatively most of the phenomena occurring during solidification [39]. Even, precise massively parallel 3D-numerical simulations, accessing length and time scales of several millimeters and several hours comparable to the scales in experiments, have become feasible in a reasonable computation time [40,41]. This approach has been used in particular to provide a detailed description of the morphological instability and selection of the solid-liquid interface microstructure [1][42]. Solidification of dendrites of pure substances was simulated for both strong and weak undercooling [42,43]. More recently, the solidification of alloys has been discussed in the case of free growth and in directional growth [44,45]. Models taking into account the fluid motion [46][47] or with coupled heat and solute diffusion [48] have also been developed.

In spite of all the theoretical progress achieved in last two decades, older phenomenological models that have provided analytical relationships for the shape characteristic parameters, which show the right physical trends, are still in use in semi-quantitative approach. Although the dendrite tip radius is the key length scale for solute micro segregation that controls the final properties of the solid material, it will turn out that the primary spacing is the most visible shape parameter in our experiments. Several

analytical models are available for the primary dendrite spacing, among which Hunt's model:

$$\lambda = [32/\sigma^*]^{1/4}[\Gamma D k]^{1/4} V^{-1/4} G^{-1/2} \Delta T_0{}^{1/4} \quad 1.33$$

and Kurz and Fisher's model:

$$\lambda = [342]^{1/4}[\Gamma D/k]^{1/4} V^{-1/4} G^{-1/2} \Delta T_0{}^{1/4} \quad 1.34$$

The two models have the same power-law exponents for the three control parameters. They predict a unique value of primary spacing that can be ascribed to the average value of primary spacing for given solidification conditions. It is worth noting that both the advanced theoretical analyses and experiments show a range of stable spacing in reality. This led Hunt and Lu to elaborate a model [49], and derive from the computational results showing the band of stable spacing analytical relationships for the minimum stable spacing [50].

Kurz and Trivedi [51] attempted to synthetize the power-law relationships for various characteristic length scales l_i of the microstructure. They found that this can be easily expressed by means of the three characteristic lengths through:

$$l_i = A(l_T)^a (l_S)^b (l_C)^c \quad 1.35$$

where A is a constant (= $(2/\sigma^*)^{1/2}$ for growth controlled by heat diffusion and $(k\sigma^*)^{-1/2}$ for growth controlled by solute diffusion) and $a + b + c = 1$. The exponents obtained by Trivedi and Kurz are summarized in Table 1.1.

Table 1.1. Exponents of the Trivedi and Kurz power law [51] **for different characteristic lengths of the interface structure: equation 1.36.**

l_i	a	b	c
Dendrite tip radius	1/2	0	1/2
Primary spacing	1/4	1/2	1/4
Secondary spacing	1/3	1/3	1/3
Wavelength at V_c	1/3	1/3	1/3

1.6. Secondary instabilities of cell array

Breathing modes are generic secondary oscillatory instabilities of spatially modulated interface patterns [52]. They have been experimentally and theoretically studied in 2D for both cellular [53–55] and two-phase eutectic interfaces [56–58]. They have also been theoretically predicted for 3D cellular growth [59,60].

In directional solidification of a binary alloy, the primary morphological instability is that of the planar solid-liquid interface, which gives way to the formation of cellular and dendritic patterns. These microstructures form patterns that lose stability in domains of control parameters where other branches of non-planar microstructures are more stable, and thus form preferentially. The transition from regular cell/dendrite branch to such branches of solutions is called secondary instability. Actually, a diversity of secondary instabilities is generic of spatially modulated interface patterns [61]. Theoretical study of Kassner et al. [62] in rapid solidification regime shows that several modes of the secondary instabilities can be found, in particular the parity-breaking (PB) mode and the vacillating-breathing (VB) mode are most interesting as both multiplet microstructures [63] and cell oscillation [54] were observed in 2D-directional solidification experiments. The PB mode is characterized by the formation of asymmetric cells. Collet et al. [64] suggested that the PB mode results from the loss of stability of the symmetric cells against parity-breaking fluctuations. Experimental study by Jamgotchian et al [63] in directional solidification of thin samples showed that the asymmetric cells (doublet, higher order multiplets) are stable solutions for the cellular pattern. Then, the numerical study by Kopczynski et al. [65] of cellular directional solidification using the symmetric model explained how the regular cell solution becomes unstable when multiplet branches bifurcate from the main singlet branch, causing the transition to patterns similar to those observed in experiments. The second common example of secondary instability is the VB mode. Cell oscillation is characterized by a periodic variation of both the cell width and tip position without variation of the primary spacing. The most comprehensive experimental study of this collective array oscillation is that carried out by Georgelin et al. on thin samples of a dilute succinonitrile alloy [54]. In the one-dimensional array of cells, each cell oscillates in phase opposition with its two neighbors. The oscillatory bifurcation corresponds to a spatial period doubling. New observations from our 3D-experiments in microgravity in DECLIC-DSI will be presented and discussed in chapter 4.

1.7. Influence of convection

Under normal solidification conditions on Earth, natural convection (not caused by an external field or applied stimulus) is almost unavoidable and often significant for bulk samples, possibly dominating the diffusion transport of heat and/or mass. Natural convection may have several origins:

1) Different densities between two liquid phases.
2) Non-uniform surface tension at a fluid-fluid surface (Marangoni convection).
3) Temperature or concentration gradient in the melt causing unstable density profile with respect to gravity vector.

In alloy directional solidification, the first two cases can be ignored [66,67] and the analysis restricted to convection associated to the temperature/concentration gradient(s) in the melt only. From a physical point of view, it is clear that the presence of the convective flow near the growth interface to some extent changes the local balances of solute and temperature. This explains the influence of the convection on morphological instability and the formation of cellular/dendritic microstructures [68–70]. Conversely, the interface microstructures may alter the convection pattern and fluid flow velocity, which is especially important for the dendrites growth in casting.

1.7.1. The hydrodynamic equations in the melt

In the presence of natural convection in the liquid phase, we must add the equations associated to hydrodynamics, the momentum conservation (Navier – Stokes) and the mass conservation (continuity equation) to the directional solidification equations. The complexity of the problem increases, mostly due to the coupling of the heat and solute balances in liquid with the Navier-Stokes equation that is highly nonlinear.

- Momentum conservation: In the Boussinesq approximation (i.e. variation of the density in the liquid < density itself except in the term related to gravity), the Navier – Stokes equation reads:

$$\frac{\partial \vec{u}}{\partial t} + \vec{u}\nabla\vec{u} = -\frac{1}{\rho}\nabla p + v\nabla^2\vec{u} + \frac{\rho}{\rho_0}g \qquad 1.36$$

where $\vec{u}$ is the fluid velocity vector, p is the dynamic pressure, v is the kinematic viscosity, ρ is the density and g the gravitational acceleration. The index 0 indicates the state of reference.

Continuity equation in the case of an incompressible fluid:

$$\nabla\vec{u} = 0 \qquad 1.37$$

- Equation of state for melt density: The Navier-Stokes and incompressibility equations have to be complemented by the state equation for the melt density. In the presence of concentration and temperature variations, this equation is written in a linear approximation

$$\rho = \rho_0[1 - \beta_T(T - T_0) + \beta_C(C - C_0)] \qquad 1.38$$

Where β_T is the thermal expansion coefficient and β_C the opposite of the solutal expansion coefficient:

$$\beta_T = -\frac{1}{\rho_0}\left(\frac{\partial \rho}{\partial T}\right)_C \quad 1.39$$

$$\beta_C = \frac{1}{\rho_0}\left(\frac{\partial \rho}{\partial C}\right)_T \quad 1.40$$

1.7.2. Nature convection in directional solidification

In ideal directional solidification (no transverse gradient), the main cause of the convection is the change in density of the liquid with temperature (thermal convection) and/or solute concentration (solutal convection). The origin of convection is then varying buoyancy: the liquid tends to rise locally where its density is lower than the average density, and sinks down where its density is higher. The configuration of the liquid can be stable or unstable. (Figure 1.13)

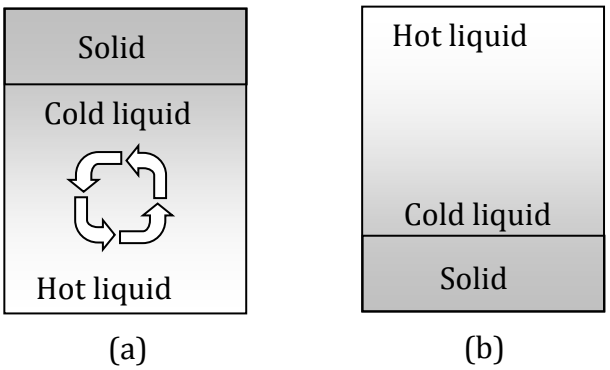

Figure 1.13. Thermal convection in ideal directional solidification (no transverse gradient). –a) Unstable case (downward solidification), -b) Stable case (upward solidification).

It is worth noting that the ideal situation is very rarely achieved in practice. Indeed, the different thermal conductivities of the solid phase, liquid phase and the crucible wall cause curvature of the solid liquid interface, which induces the existence of a radial gradient of temperature and associated gradient of solute concentration for alloy, orthogonal to gravity, which are at the origin of radial-gradient induced convection (radial convection in brief), unavoidable as there is no threshold for fluid flow in this case.

In directional growth of a binary alloy, the solute concentration and temperature profiles given by equations 1.7 and 1.11 are shown in Figure 1.14 for *k<1*.

In upward solidification configuration, the vertical thermal gradient is always a stabilizing force (hot liquid above the cold one) acting against both the morphological instability of the solid-liquid interface and hydrodynamic instability of the melt. In contrast, the vertical solute concentration gradient can be either stabilizing or providing

the destabilizing driving force depending on the value of the solute partition coefficient k and the radio of the solute and solvent density: if $k<1$ and the solute is lighter than the solvent (heavier solute for $k>1$), the basic quiescent configuration is unstable and convective motion appears in the melt: thermal solutal convection. The question that arises is thus to know the hydrodynamic stability of the liquid layer adjacent to the interface when the two longitudinal gradients (thermal and solutal) are antagonist. If one considers that the Lewis number, defined as the ratio of the heat diffusion coefficient to the solute diffusion coefficient, $Le = \frac{D_{th}}{D_L}$, is >> 1 for metallic and transparent systems (of the order 10^2-10^3 for SCN-based alloys), the destabilizing effect associated with the solute concentration gradient will take over the stabilizing contribution linked to the temperature gradient that vanishes on short time scale.

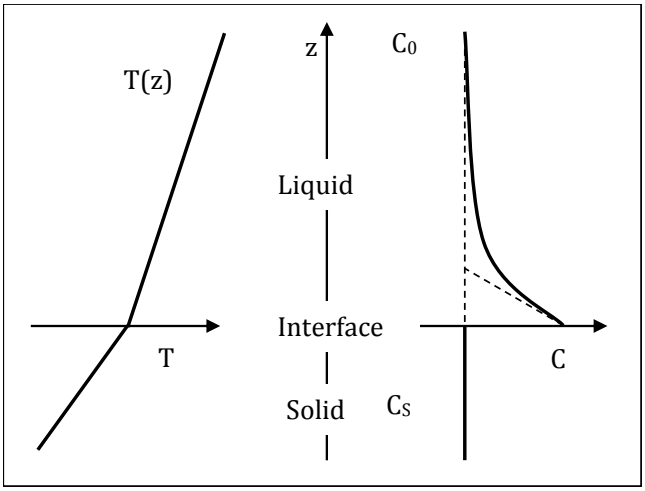

Figure 1.14. The temperature and concentration profiles at the solid liquid interface in alloy directional solidification.

It is worth noting that in bulk samples, the most common type of natural convection dominating is the radial gradient induced one. In directional solidification, it is due to heat flow entering the sample to maintain the melt on especially in transparent alloys, that present low thermal conductivities compared to the crucible one, to the difficulty to evacuate latent heat [71].

1.7.3. Interaction of natural convection with Mullins-Sekerka instability

Morphological instability under fluid flow in the bulk of liquid phase

On earth, gravity is the main source of hydrodynamic instability of the melt leading to fluid flow that may interact in a complex way with the solidification process and affect the Mullins–Sekerka instability.

The first effects of this liquid stirring are the reduction of the solute boundary layer adjacent to the solidification front to a thickness δ, written $\Delta = \delta V/D_L$ in nondimensional form, and solute enrichment of the bulk liquid ($C_\infty > C_0$) for $k < 1$, which influence the conditions of morphological instability of the planar front [72,73]. These authors take bulk convection into account by using the boundary layer approach introduced by Burton et al. [74] to model solute transport during the growth of semiconductors by the Czochralski method with forced convection (crystal rotation and/or crucible rotation). The bulk liquid is assumed homogenous at concentration C_∞ ahead of the boundary layer δ in which solute transport is by diffusion only. In contradistinction with Coriell et al.[72], Favier and Rouzaud [73] consider a deformable solute boundary layer to get rid of reflexing artifacts when δ becomes too small (strong convection) with respect to the wavelength of the interface perturbation.

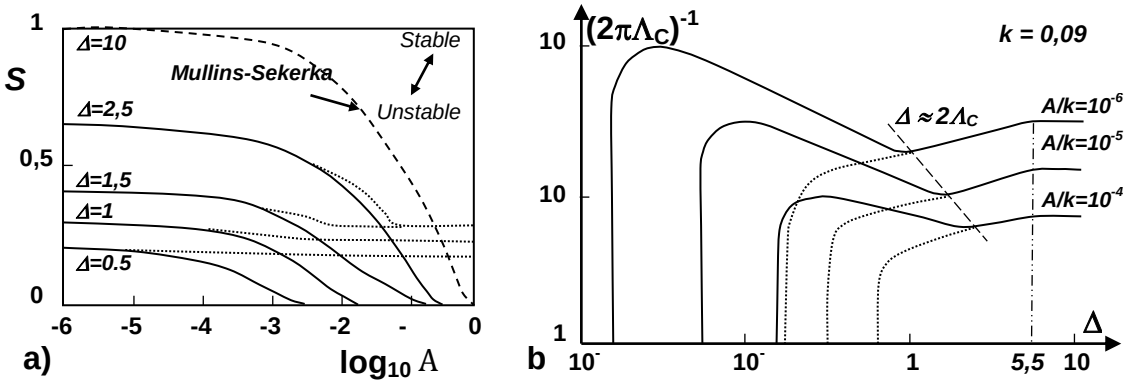

Figure 1.15. Influence of bulk convection in liquid phase (full lines), characterized by the nondimensional thickness of the solute boundary layer, on the morphological instability of the planar solidification front [73]**: -a) Evolution of the threshold of instability for dilute Al – Cu system (k = 0.14), -b) Evolution of nondimensional critical wavelength Λ_C. Dashed curves show the artifacts when a rigid solute boundary layer is used** [72]**.**

Under bulk convection, planar front grows with solute macrosegregation characterized by the effective solute partition coefficient $k_{eff} = C_{S,\phi}(t)/C_\infty(t)$, which approaches unity as the magnitude of fluid flow is decreasing. When time dependence is weak, $k_{eff} = C_{S,\phi}/C_\infty$, the basic state can be considered as quasi-stationary so that it follows from the interface balance of solute, Figure 1.15, that the driving force of morphological instability, $m\,\partial C/\partial z|_\phi$, reads $k_{eff} m G_c$. For most of the alloys ($k < k_{eff} < 1$), there is thus a reduction of the instability driving force and a broadening of the stability domain in the Mullins – Sekerka diagram (Figure 1.15-a). Accordingly, the stability function S in criterion (Equation 1.18) tends towards $k_{eff} = k/[k + (1-k)\exp(-\Delta)]$. Regarding the dimensionless critical wavelength at onset of morphological instability $\Lambda_C = \lambda_C V/D_L$ (Figure 1.15-b), the deformable boundary layer δ allows to predict the decrease observed experimentally when fluid flow starts to be significant ($\Delta \approx 10^{-1} - 1$). In general, convection causes a decrease in the characteristic instability wavelength at the interface

[75,76]. Conversely, when convection is comparatively weak, i.e. $\Delta \approx 2\Lambda_C$ (or $\delta \approx 2\lambda_C$), the behavior in the limit of diffusion transport is recovered.

Fluid-flow localization of Mullins-Sekerka instability

Fluid flow interaction with solidification may result in complex patterns. Beyond shifting the onset, the Mullins–Sekerka instability is often localized (Figure 1.16) by following the solute macrosegregation associated to the convection rolls [77,78] .

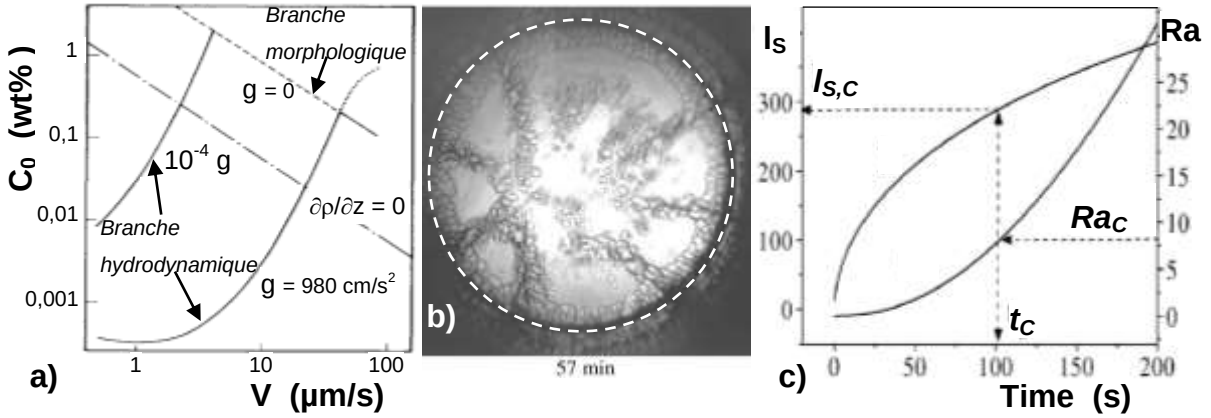

Figure 1.16. –a) Diagram giving the critical tin concentration above which morphological/ hydrodynamic instability occurs in the Pb-Sn system for G = 200 °C/cm [79]**. –b,c) Morphological instability localized at the walls of the hexagonal convection cells formed by "outward-hexagonal" liquid flow** [78][71] **resulting from the thermosolutal instability induced by the rejection of lighter solute. Succinonitrile–0.2 wt% acetone alloy, V = 1.5 mm/s, crucible ID = 10 mm (- - - -).**

The linear stability analysis of coupled morphological and hydrodynamic instabilities in upward solidification (//-g) of a binary alloy is due to Coriell et al. [79] and to Hurle et al [80]. Typically, the stability limit presents a convective branch neatly distinct from the morphological branch, with a transition from hydrodynamic instability to morphological instability when the pulling velocity is increased (Figure 1.16-a). The critical wavelength of hydrodynamic instability (~ 20 l_S ~ cm) being several orders of magnitude larger than that of morphological instability (~ 10-100 µm), the coupling between the two modes of instability is generally very weak. However, there may exist some rare cases where the hydrodynamic morphology coupling is strong, especially when $k \to 0$ [81]. This explains that in practice morphological instability, which initiates in places where solute concentration is higher, is localized by the convection (macro) structures (Figure 1.16-b,c). For the pulling velocity in the experiment of Figure 1.16-b, $20D/V$ = 1.6 cm (> crucible diameter φ) but the two instabilities occur in the initial solidification transient, which necessitates recourse to the Warren-Langer model. Indeed, in this approach l_S increases from 0 to D/V, V_Φ from 0 to V and C_Φ from C_0 to C_0/k. It follows that the classical dimensionless number for hydrodynamic instability, the Rayleigh number

$$Ra = \frac{\alpha_C g V_\varphi C_\Phi (k-1) {l_S}^4}{\nu {D_L}^2} \quad 1.41$$

also increases from zero so that the onset Ra_C of hydrodynamic instability hydrodynamique is crossed at t_C during initial solidification transient at a solutal length $l_{S,C}$ small enough for a few hexagonal convection cells to fit in the crucible diameter, and localize morphological instability (Figure 1.16-c).

The linear analysis of coupled morphological and hydrodynamic instabilities was extended to the situation were in the basic state there is already fluid flow in the bulk liquid [82].

Effect of natural convection on cell/dendrite patterns

The effect of natural convection on cell/dendrite patterns will be further addressed latter in the course of this thesis. Overall, in the presence of convection in the melt the cell spacing is altered and the cellular array presents irregularities in cell size and more topological defects [83]. When convection is avoided, for example in the microgravity environment of space, the cellular array is more regular and homogeneous [84]. The growth direction and kinetics of columnar dendrites are changed by fluid flow. The growth direction of the dendrite tip is tilted towards the incoming flow as evidenced by Okamoto et al. on a transparent alloy [85]. The growth kinetics of the dendrite tip also depends on the liquid flow direction. At fixed undercooling, the tip radius is smaller and the growth rate higher for dendrites growing against the flow than for those growing in the flow direction [86,87]. The same effect is observed for the dendrite side arms [85].

Macroscopic modulation of the front at the crucible scale and axial solute macrosegregation is observed for cells and dendrites, which result from either thermal/solutal convection in the bulk liquid or solute-driven convection generated inside the solute boundary layer [75,88]. The porous semi-solid dendrite mush may also undergo thermosolutal instability resulting in plumes of light fluid penetrating into the bulk liquid like jets [89–91]. This phenomenon, nicely imaged recently using X-ray radiography (Figure 1.17) [92], is causing one of the most detrimental defects in casting, namely freckles [93].

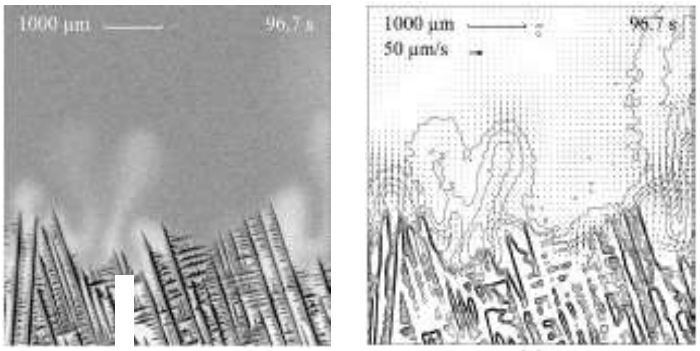

Figure 1.17. Dendritic growth in directional solidification of Ga-30 wt % In [92]**: -a) Snapshot of growing dendritic mush with solutal plumes in the melt showing solute segregation obtained by in situ X-ray radioscopic visualization, and –b) corresponding flow field (vector plot) calculated by optical flow approach at the given time offset relative to the first image (contour lines correspond to lines of constant brightness/solute concentration in image (a).**

Finally, thermosolutal convection creates a hydrodynamic motion across the sample, which leads to a significant change in the radial distribution of concentration. [75,94] [71].

1.8. Influence of anisotropy

1.8.1. Anisotropy of surface tension

The surface tension γ depends on the local crystallographic orientation of the solid-liquid interface. For a 3D crystal, the surface tension can be expressed by a function $\gamma(\vec{n})$, where n is the normal to the interface, with n_i the components of n in the <*100*> axes of a cubic crystal. For a rough cellular interface where the anisotropy is weak, γ is given by:

$$\gamma(\vec{n}) = \gamma_0\{1 + \delta_{str}[4(n_1^4 + n_2^4 + n_3^4) - 3]\} \qquad 1.42$$

where γ_0 is a constant and δ_{str} is the strength of crystal anisotropy.

For a anisotropic surface tension, surface tension γ is replaced in the capillary constant Γ by the surface stiffness $\sigma(\theta)$ which is written as:

$$\sigma(\theta) = \gamma(\theta) + \frac{\partial^2\gamma(\theta)}{\partial\theta^2} = \gamma_0(1 - 15\delta_{str}\cos 4\theta) \qquad 1.43$$

where θ is the angle between the interface normal and the reference axis.

In 3D, the stiffness is tensor:

$$\sigma_{ij} = \gamma\delta_{ij} + \frac{\partial^2\gamma}{\partial\varphi_i\partial\varphi_j} \qquad 1.44$$

1.8.2. Anisotropy in directional solidification

Many physicochemical parameters can to some extent be anisotropic, which under particular conditions may turn out to be critical as for instance shown by Coriell et al. for solid thermal conductivity [95]. In directional solidification, the focus has been on surface tension anisotropy and interface kinetics anisotropy that both have a key role in the Gibbs-Thomson equation, and may combine or compete. Surface tension anisotropy, which will only be considered in the phase-field simulations to be compared with the results of our experiments, is recognized to be essential for the mere existence of solutions in free dendrite growth [96,97]. It also tends to inhibit dendrite tip splitting rendering primary spacing selection more difficult at significant anisotropy.

In free dendritic growth, many theoretical studies have focused on the crucial role played by crystalline anisotropy in the selection process of the microstructure [98]. It is now well established that it is the anisotropy of surface tension which selects the tip radius and the growth velocity of the dendrite. This selection by the anisotropy has been experimentally demonstrated by Ben-Jacob et al. in the case of viscous fingering [99].

Another well-known evidence is the variation of the orientation of the steady state growth microstructures as a function of the solidification velocity for the non-faceted materials with low surface tension anisotropy [100,101]. At low pulling velocity, the cells are oriented along the direction of heat flow, which is the withdrawing direction. For higher pulling velocity, when the microstructure has become dendritic, the preferred growth is that of highest surface energy, <*100*> in cubic systems.

An experimental and numerical study on this topic was carried out by Akamastu et al. [102–104] in thin film directional solidification of a CBr_4-8 mol% C_2Cl_6 alloy, see for example Figure 1.18. The results showed that the tilt angle α, defined as $\tan\alpha = V_d/V$, where V is the pulling velocity and V_d is the drift velocity, is related to the spacing Péclet number $Pe_\lambda = \lambda V/D$. In the limit of large Pe_λ values (Pe_λ>7), α tends to a constant value, determined by the crystal orientation relative to the pulling direction. This result was also found numerically by Okada and Saito [105].

Furthermore, the tilt of the dendrites for anisotropic materials results in two remarkable effects on the microstructures: -1) the dendrites are always asymmetric because the concentration field around is asymmetric, -2) a phenomenon of lateral drift of the microstructures at constant velocity is observed [103]. This drift due to the anisotropy

(surface tension or kinetic attachment) of the material cannot be interpreted by linear models [106].

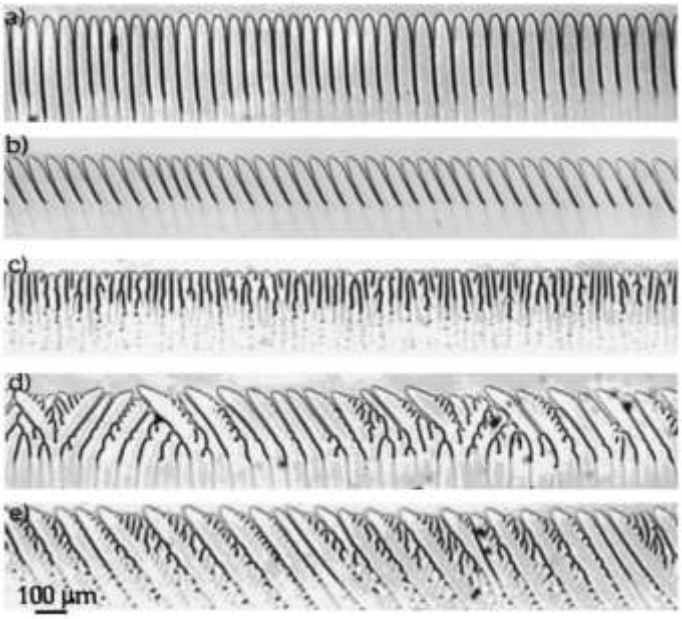

Figure 1.18. Microstructure observed on the same crystal of CBr_4-C_2Cl_6 for different pulling velocities: –a) symmetrical cellular structures (V = 3.1 µm/s), -b) tilted dendritic structures (V = 23.9 µm/s), -c) seaweed structures (V = 31.1 µm/s), -d) coexistence of rightward- and leftward-tilted dendrites (V = 31 µm/s), -e) titled low anisotropy dendrites (V = 31.1 µm/s). [104]

1.9. History of using transparent model alloy in the study of solidification microstructures

Researchers seeking for fundamental mechanisms and engineers engaged in the tailoring of new or improved materials are both looking for simpler model experiments capturing the essence of the phenomena and timely providing the benchmark data on the formation of the solidification microstructures that are necessary to the clarification of critical pending issues and the sound advancement and validation of the numerical predictions in process modeling.

The characterization of the dynamical formation, and selection, of the solidification microstructure in experiments on metallic alloys is usually difficult and limited because of the opacity of metallic materials. Thus, the endeavor was to identify transparent model systems that behave like metals. This quest was based on the criterion suggested in 1958 by Jackson [107,108] that the solidification process depends on the roughness of the solid-liquid interface at atomic scale. The interface roughness is characterized by the parameter α:

$$\alpha = \frac{L\xi}{RT_E} = (\Delta S_f/R) \cdot \xi \qquad 1.45$$

where L is the latent heat of fusion, R the gas constant, TE the equilibrium temperature of the phases, ξ a factor depending on the crystallography of the interface and ΔS_f the entropy of fusion.

The solidification kinetics, which is dictated by the easiness of the attachment of atoms/molecules at the growth interface, is also linked to α. A small α corresponds to an atomically rough solid-liquid interface and thus fast attachment of atoms, whereas the interface is atomically flat for high α, and growth faceted. The critical value of α is about 2, which in practice corresponds for instance to semiconductors. For most metals, α is less than 2. Then the endeavor was to identify transparent model systems with α smaller than 2. Jackson and Hunt [109] found 11 organic systems with α less than 2 that do solidify as metals, and obtained typical cellular and dendritic microstructures from these organic materials. As the solid and liquid phases are transparent, the in-situ and real time observation of the solidifying interface is enabled. Actually, a systematic study of this special class of organic crystal was done previously by Timmermans [110]. He found in particular that the first solid phase, just below the melting point, is cubic and highly plastic. He thus named those materials "plastic crystals" [111]. Many "plastic crystals" have been found but only few of them can be used in the solidification studies. One major problem is the melting point, either too high or too low. The preferred material has become succinonitrile which has a melting temperature near the normal ambient temperature, and many transparent alloys based on succinonitrile are used in the solidification experiments. The most common solutes are water, acetone, salol and camphor. In our experiments, the model transparent alloy succinonitrile-camphor is chosen since its phase diagram and physico-chemical properties are well determined, and also because the risk of gas bubbles are reduced.

In situ and real time observation of alloy solidification being available with transparent organic model systems, experimental studies of interface dynamics have been restricted primarily to thin samples where fluid flow is eliminated [23,28,54,102,112,113]. It was then tempting to simplify processing by investigating in microgravity [114–116]. Indeed, the reduced-gravity environment of space is highly beneficial as it renders negligible one of the most critical parameters, gravity, which can interact in multiple ways in experiments on ground. The basic understanding learned from previous studies relieved from churning of the alloy melt by gravity-driven fluid flow has been fostering the development of physically better and more accurate models for the growth of the solidification microstructure, the prediction of materials properties and, eventually, helped improving manufacturing on Earth. Since pioneer and precursor experiments (Figure 1.19) that have paved the way [117–121], [122], solidification processing in space has thus installed as a key area of microgravity research. Figure I.* shows two striking examples. Dendritic directional solidification of Al-Cu alloys was performed in microgravity in the GHF (Gradient Heating Facility) instrument of the French space agency CNES during the D1 Spacelab mission in 1985. Among other, the drastic

reduction in primary spacing on earth due to gravity-driven fluid flow was unambiguously demonstrated [76,123]. IDGE (Isothermal Dendritic Growth Experiment) provided separate and quantitative test of the Ivantsov steady-state shape and selection theory of free dendrite growth under diffusion transport, which was not possible before [124–126]. Hundreds of IDGE experiments were carried out aboard the space–shuttle Columbia, as part of NASA's USMP–2 to –4 shuttle missions in 1994, 1996 and 1997. Dendrites were monitored in situ in pure succinonitrile and pivalic acid, which exhibit significantly different tip shapes and overall morphologies. Both steady-state tip speed and tip radii were measured as functions of the initial supercooling from the global dendrite images provided by the IDGE flight instruments (35–mm films and then full gray-scale videos).

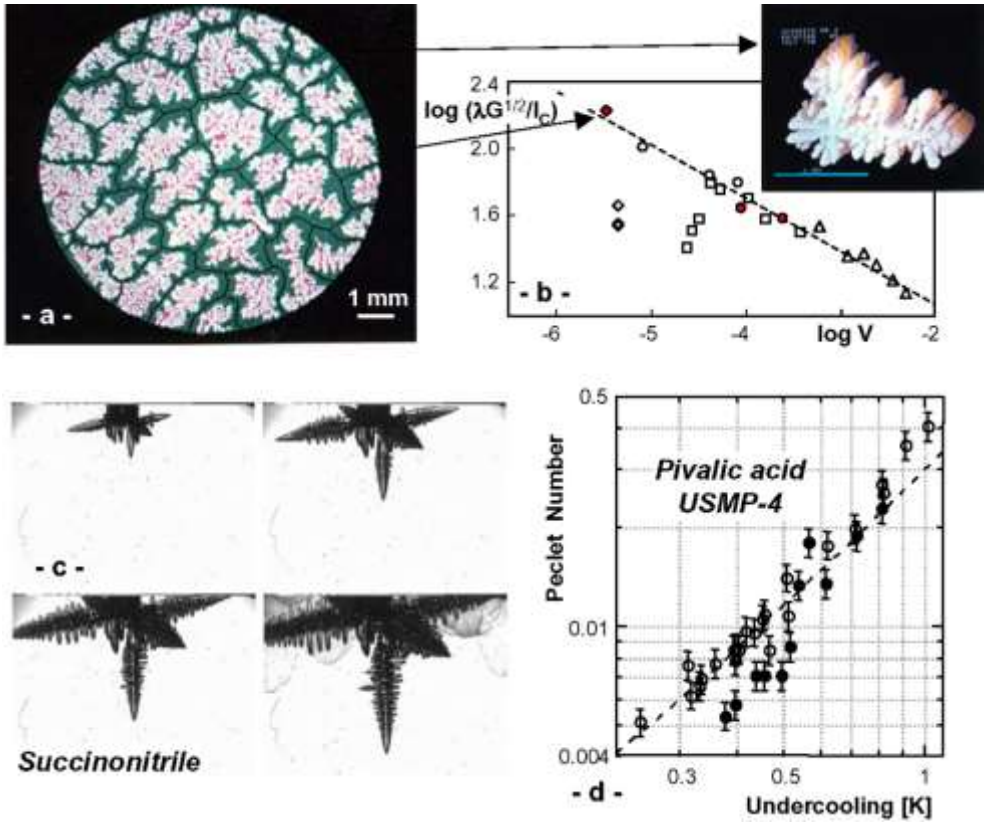

Figure 1.19. –a) Post mortem observation on transverse cross section of a columnar dendritic array formed in microgravty at V= 4.2 µm/s and G = 30 °C/cm in Al – 26 wt% Cu (D1-Spacelab mission, 1985), with huge dendrite spacing (1.5 mm) compared to that on earth (450 µm), and –b) outputs: microgravity data (Filled symbols) following the diffusion theory (Dashed line) in the non-dimensional (spacing, velocity)-diagram and three-dimensional reconstruction of the morphology of an individual dendrites from a series of closely-spaced cross-sections showing the coarsening of side-arms [76,123]**. –c,d) In situ characterization of dendrite free growth in undercooled melt of transparent organic surrogates for metals** [124–126]**. images of the formation of a succinonitrile dendrite (c) and (d) diagram showing a slowing down of dendrite growth velocity (Pe ~ $V^{1/2}$) in the absence of fluid flow (Filled circles: microgravity data, IDGE-USMP4, 1997; Open circles: 1g data).**

Studies of the basics of materials processing on transparent organic model systems, i.e. grain structure, dendrite morphology, mushy zone characteristics, Columnar-to-Equiaxed Transition conditions [127], equiaxed growth [128,129], micro-macro-segregation of chemical species …, have been extended to rapid solidification [130,131], eutectic [132][133][134], peritectic [135], monotectic[136], intermetallic alloy growth and more generally multiphase multicomponent alloy solidification [137].

Until recently, and still now for studies on bulk samples of thickness more than about 1 mm, in situ observation was conditioned by transparency to visible light (Figure 1.19-c, Figure 1.20-a to c). This has changed with the enhancement of the brilliance of synchrotron radiation. Indeed, synchrotron X-ray imaging techniques (radiography, tomography, topography) have extended in situ, real-time monitoring of the formation of the solidification microstructure to representative metallic systems (e.g. Al–Si alloys widely used for the production of aluminum cast parts), with pioneering work at synchrotrons such as the European Synchrotron Radiation Facility – ESRF (Figure 1.20-d and e), has made accessible the in situ monitoring of the solidification of "real" materials of direct interest to industry, which are opaque to visible light [138–143], [144].

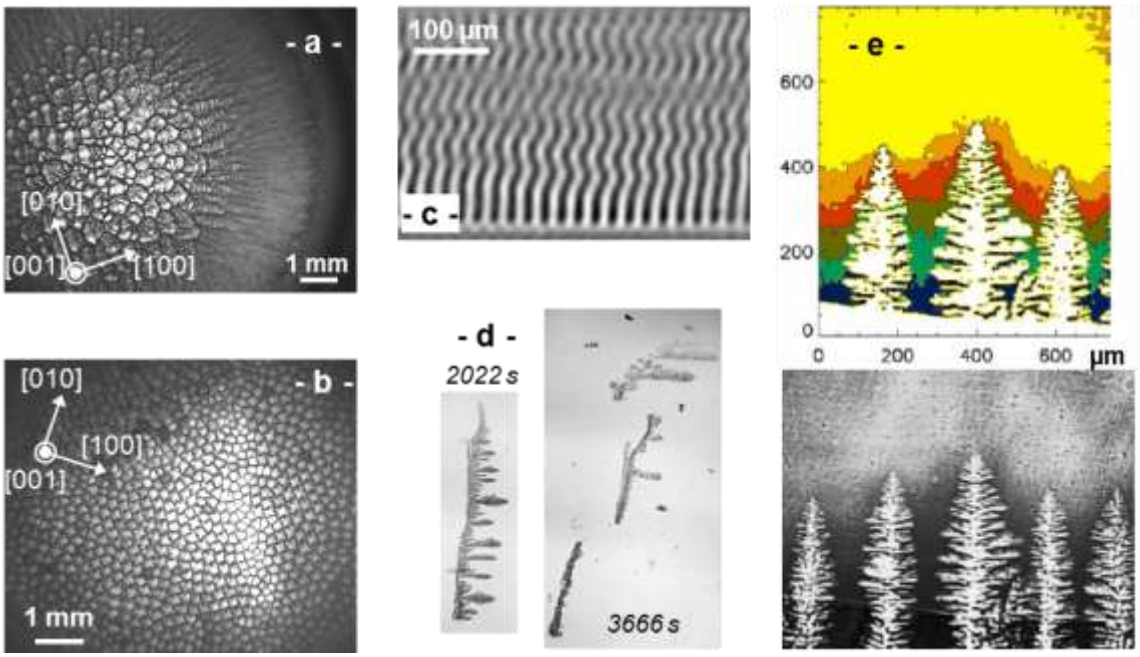

Figure 1.20. In situ and real-time observation of the solidification microstructure in three-dimensional samples. Optical methods on transparent model systems: – a,b) [001]-dendrites viewed from above during directional solidification of dilute succinonitrile – camphor alloys in DECLIC-Directional Solidification Insert of CNES [145,146] **showing that the localization of vertical dendrites at the center in ground experiment (a) is effectively cured in microgravity experiments under diffusion transport (b) as recently observed in the first microgravity experiments carried out on ISS where laterally extended arrays of dendrites formed (IM2NP, Aix-Marseille University). –c) Zig-zag instability of lamellae in directional solidification of CBr_4-C_2Cl_6 eutectic** [147]**. - Synchrotron X-ray imaging on metallic systems: -c) disorientation of the dendrite stem (evidenced by the splitting of the dendrite image into pieces on topography) during directional cooling down of Al - 7wt% Si (IM2NP, Aix-Marseille University). –d) Solute field in the interdendritic liquid, varying from 33 wt% Cu (black) to 30 wt% Cu (yellow) in the melt ahead (dendrites are white), determined from the grey levels in the radiograph below** [92,141]**.**

Chapter 2. Experiments and Methods of pattern characterization

During this thesis, we carried out and analyzed experiments of directional solidification on a transparent model alloy, in a cylindrical crucible to get experimental benchmark data for extended patterns in the limit of diffusion transport. Experiments were conducted in the DECLIC-DSI facility of CNES while it was onboard the International Space Station for about one year and after its return on earth to analyze convection influence. Benchmark data correspond to reliable quantitative measurements of relevant pattern characteristics, as the primary spacing, the order/disorder level, the type of pattern, etc... This chapter is dedicated to the detailed description of all experimental methods. In the first two parts are presented the DECLIC device, the concept of inserts and the design of the Directional Solidification Insert (DSI) as well as the experimental sequences. Experiments lead to a huge amount of data, mainly as images. Therefore, a majority of results are obtained through image analyses so that specific procedures had to be developed to process all these images. This will be described in the third part of the chapter.

2.1. The DECLIC-DSI device

2.1.1. The DECLIC project

DECLIC is a multiuser facility that has been developed by the French space agency CNES (Centre National d'Etudes Spatiales) [148]. In 1991, in the microgravity prospective seminar, the CNES recommended the development of a device dedicated to study in situ and in real time the directional solidification of bulk transparent alloys (3D growth) in microgravity. In 1993, CNES began the project CHEOPS (Caractérisation par Holographie pour l'Etude et l'Observation des Phénomènes de Solidification) corresponding to a multi-user facility for in situ and real time observation of solidification and other phenomena in transparent media.

In 1996, the project became DECLIC [149]. The resulting DECLIC facility is a compact, multi-user facility for conducting experiments in the fields of fluid physics and materials science, and more generally on transparent media, within the microgravity environment of the International Space Station (ISS). The main part of the facility is common to all experiments and mainly contains electronics (for regulation, data acquisition and management, communication . . .) and some optical resources (laser, optics, cameras). Three different inserts that contain elements specific to each topic (and especially specimen cartridges) complete the facility: 2 of them are dedicated to the study of critical fluids; the third one, called DSI (Directional Solidification Insert) is for solidification. The DECLIC facility of CNES was launched with 17-A shuttle flight (August 2009) and installed on board the International Space Station as part of a joint NASA/CNES research program. The main instrument monitoring is made from the

CADMOS center (Figure 2.1), the French User Support and Operation Centre (USOC) in Toulouse. Taking advantage of provided tele-science capabilities, scientists have the possibility to follow in near real-time conditions and to remotely control experiments.

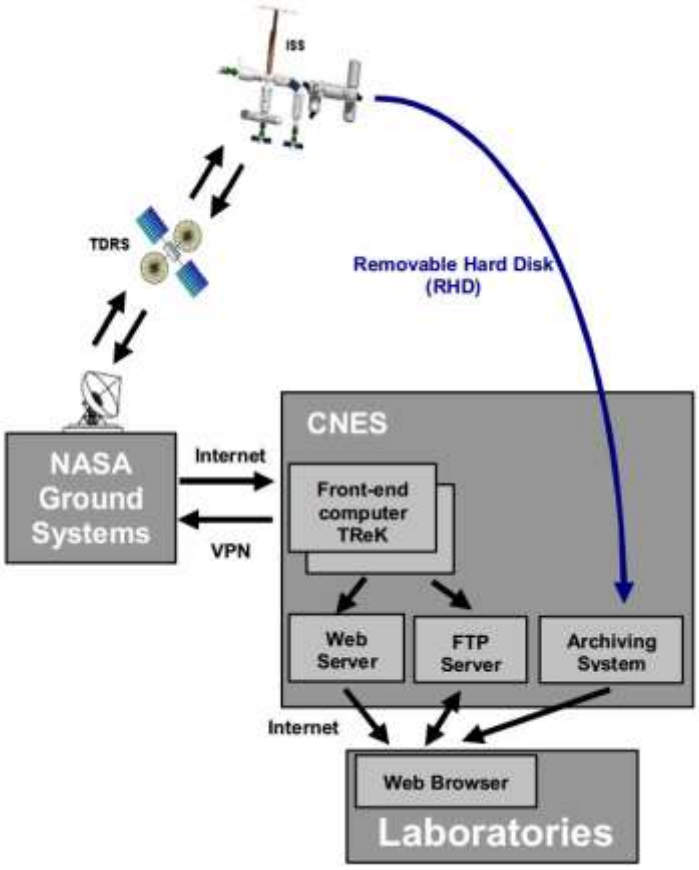

Figure 2.1. This figure shows the transfer of the data and commands in the whole system, between ISS and ground, from laboratories to CNES to NASA and NASA to ISS. Experiments have been performed onboard ISS from December 2009 to February 2011 and a series duplicate on ground from September 2011 to January 2012.

2.1.2. DECLIC-DSI device

The DSI insert (Figure 2.2) mainly contains 2 elements: the Bridgman furnace and the experimental cartridge. Some specific optical elements are also included in the insert, even if the main optical parts belong to the common part of DECLIC (LEDs, cameras, laser. . .) [2,148].

2.1.3. Experimental cartridge

The experimental cartridge (Figure 2.3) includes the quartz crucible and a system of volume compensation made of stainless steel that is useful to accommodate the specimen volume variations associated to phase changes. The cylindrical crucible has an inner diameter of ten millimeters and a length that enables about ten centimeters of solidification, thus allowing the study of the whole development of extended 3D patterns from their initial stages to the steady state. The crucible is equipped with a flat glass window at the bottom and a lens immersed in the melt at the top.

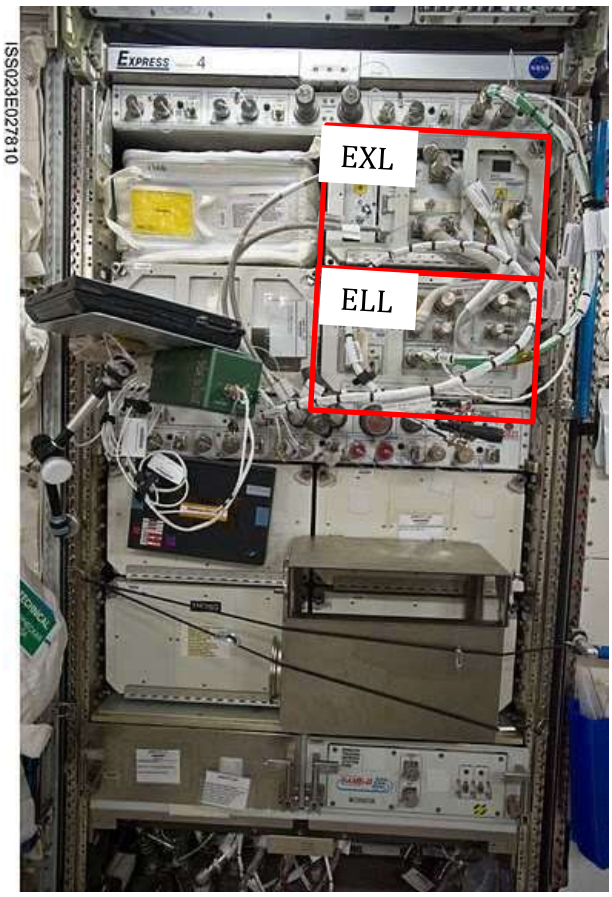

Figure 2.2. DECLIC payload fitted in the EXPRESS RACK 4 of the ISS in the Japanese module KiBo. The two DECLIC lockers (EXL: EXperiment LockerEXL and ELL: ELectronic Locker) are located in the top right quarter of the rack.) The ELL is at the bottom while the EXL is at the top. The ELL houses all the power, data handling and high accuracy thermal regulation electronics, and manages the whole system and the scientific experiment execution. The EXL host the optical bench, and also receives the experiment insert (like DSI).

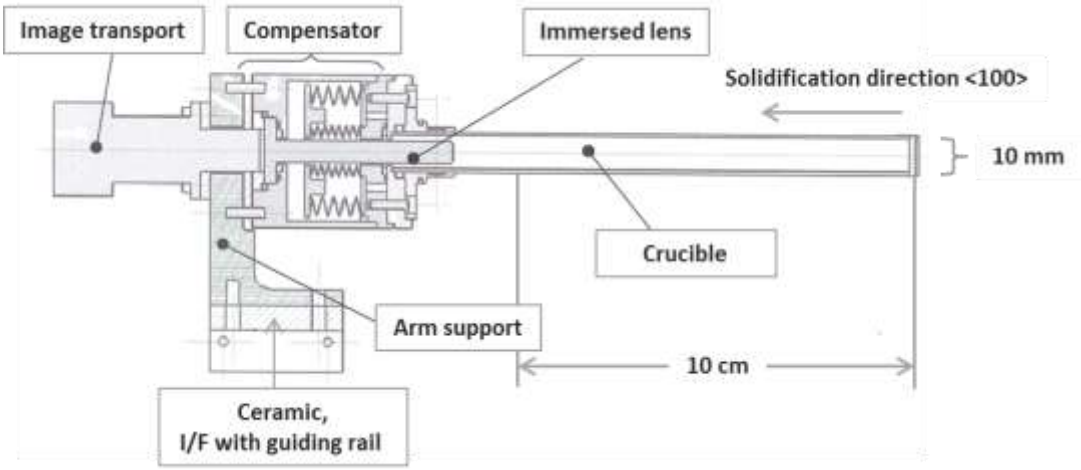

Figure 2.3. Experimental cartridge

The Bridgman-type furnace

A furnace heating system (the hot zone) associated to a cooling system (the cold zone) create and maintain a temperature gradient. The thermal gradient is controlled by

regulating the hot and cold zones, respectively located above and below the adiabatic area where the interface is positioned. Upward solidification is achieved by pulling the crucible down into the cold zone of the furnace at a rate ranging from 0.1 to 30 µm/s. The adiabatic zone also includes a "booster heater", thin annular heating ring, which locally injects power (from 0 to 7 W) into the crucible to flatten the solidification front during cartridge translation.

Optical system

The main observation mode is the Direct Axial Observation. It takes advantage of the complete axial transparency of the cartridge provided by the immersed lens and the bottom glass window but the interface can also be observed from the side. A scheme of optical diagnostics is given in Figure 2.4

- Direct observation in axial direction (growth direction): the light coming from a LED crosses the whole sample from the bottom to the top. An image of the solid-liquid interface is formed outside the furnace and projected on a CCD camera. This observation mode is used to visualize the microstructure appearing on the liquid-solid interface (grain boundaries, cells, dendrites. . .) during the transient stage as well as the stationary one. This observation mode is also equipped with a zoom permitting the detailed study of the pattern dynamics.

- Direct observation in transverse direction: the light coming from two LEDs crosses the sample from one side to the other. This observation mode provides a rapid control of interface position and curvature as well as an absolute measurement of its position. Before application of pulling velocity, the interface shape, located at the liquidus isotherm, is usually flat. For some cases, function of the temperatures of hot and cold areas, it may be convex (or concave) if it is located in an area of entering fluxes (outing fluxes). Its curvature increases and its position is modified during solidification.

- Interferometric observation in axial direction: the interferometer is a Mach-Zehnder one, using a polarised He-Ne laser (wavelength λ = 632.8nm). Interference fringes appear at the recombination of the laser beam passing through the whole length of the crucible with the reference one passing outside the crucible and result from the difference of optical paths between these two beams. Those fringes can be understood as level curves of the solid liquid interface and the height between two successive fringes is related to the difference of refractive index between the solid and the liquid phases. The analysis of interferograms provides the 3D shape of either the interface or the cell/dendrite caps; this process will be detailed in §2.3.5.

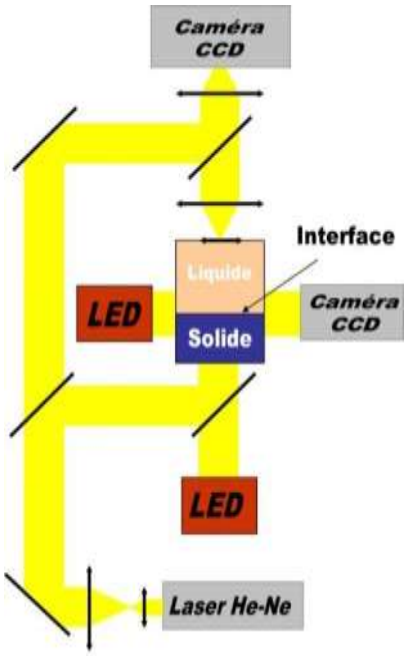

Figure 2.4. Optical diagnostics in DECLIC-DSI, the yellow lines correspond to the optical paths. The CCD cameras provide grey level images with a resolution of 1024 pixels x 1024 pixels. Since the direct axial observation and the interferometric observation share the same CCD camera, the two kinds of images cannot be taken at the same time.

Interface curvature and fluid flow effects on ground

The crucible used to carry out our experiments is a cylindrical quartz tube with an inner diameter of ten millimeters, a wall thickness of 1 mm and with a length that enables a solidification of about ten centimeters. In such a bulk sample, the interface is no longer flat after a pulling velocity is applied. This macroscopic curvature is mainly due to the significant difference of heat conductivities between the quartz and the succinonitrile alloy. Indeed, as quartz conducts heat much faster than the alloy, the evacuation of the latent heat generated during solidification is more efficiently done through the crucible. Therefore, the sample is cooler near the wall than in the middle, and a radial temperature gradient appears. As a consequence the flat interface becomes concave (Figure 2.5). On earth, the radial thermal gradient drives fluid flow, ascending in the center of the crucible and descending near the glass wall. The solute boundary layer that is formed during the solidification of alloys is then swept by fluid flow and a radial concentration gradient between the border and the center of the crucible forms. The solute concentration increases [71] in the center, inducing local recoil of the interface position to accommodate the local decrease of the equilibrium interface temperature. The curvature of the macroscopic solid-liquid interface is therefore locally increased in the center as observed on Figure 2.5, with the formation of a pit. Thermal and concentration radial gradients are associated to a variation of the level of morphological instability along the interface leading to a radial gradient of microstructure from the border to the center.

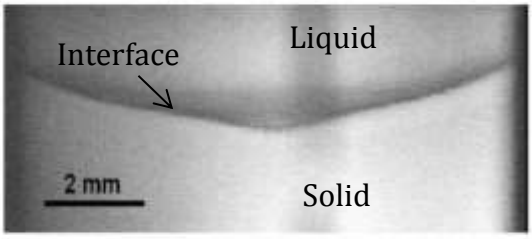

Figure 2.5. Side view of a concave interface deformed by convection influence during ground experiments. The central pit results from solute accumulation due to fluid flow. (Lab model of DECLIC – DSI; SCN 0.3 wt% water; V = 10 µm/s, G = 30 K/cm) [150].

Another effect of the interface curvature on the microstructure dynamics is also observed. Indeed, when the interface is concave, an angle exists between the pulling direction, parallel to the observation axis, and the normal to the interface. As long as the growth direction is not constrained to <100> by anisotropy, the cells grow perpendicular to the solid-liquid interface. Thus, the cell growth velocity has a radial component which in top view makes the cell array gliding from their birthplace on the periphery to the center of the crucible, where they get eliminated by newcomers. This advection phenomenon has been observed on thin samples (2D) [151] where a controlled interface curvature was purposely imposed. More recently, Weiss et al. [146] observed in 3D samples (on the laboratory model of the DECLIC-DSI) cell birth, drift and overgrowth on a naturally concave front. They report on acceleration of sliding due to fluid flow compared to the simple geometric sliding due to the angle between the thermal gradient and the pulling velocity.

Such phenomena lead to heterogeneous patterns. In order to study the cellular array evolution in homogeneous patterns, it is mandatory to control the interface curvature. This is realized by means of a booster heater located at the level of the solidification front [152]. It is a thin heating O- ring placed around the crucible and located at the bottom of the adiabatic zone, more or less close to the solid-liquid interface. The temperature of the booster heater is adjusted by applying a current of appropriate intensity. The role of this local heating is to compensate the latent-heat extraction through the crucible wall by heat injection, which is not always fully possible.

2.1.4. Experimental procedure

Experimental conditions.

Six runs of 2 or 3 weeks each of microgravity experiments have been performed from April 2010 to April 2011. During these runs, a large range of experimental conditions have been studied. Since the solute concentration is fixed on ground at the time of cartridge filling, remaining control parameters are the thermal gradient and the applied pulling rate. Usually, the thermal gradient is set at the beginning of a run and cycles of

melting-homogenization-solidification sequences are performed with just varying the pulling rates.

The whole range of explored experimental conditions is summarized in a matrix as in Figure 2.7. Long solidifications at constant pulling rate are represented on the diagonal of the matrix whereas the other crosses indicate solidification with 2 successive different pulling rates (solidification of 30 mm at V_1 followed by 30 mm at V_2, with an abrupt jump between the 2 steps).

Control of experiments

A web browser system (VisuWeb) developed by Cadmos Center (French User Support and Operation Centre) in Toulouse is used to control and observe the experiment in real-time from the laboratory. It presents as a web site with different pages. The main page (Figure 2.8) is splitted into 2 parts: on the right side, axial or transverse real-time images can be observed; on the left side, the value of some selected experimental data (temperatures of thermal areas, motor positions...) are given. Images acquired at "high" frequencies are recorded on a removable hard disk onboard ISS whereas only one image per minutes exists between the image acquisition onboard ISS and its transmission on ground. This nearly real-time observation is used by scientists to modify and adjust experimental parameters. In our case, we mainly adjust the image quality parameters (brightness, gain...). The transmission of telecommands from scientists to CADMOS is done using a communication tool called Ivods, developed by NASA, which enables a permanent audio and vocal link between the IM2NP Lab in Marseille and the CADMOS in Toulouse.

Based on ground preliminary studies, the temperatures of the different thermal areas, including the temperature of the booster heater, have been set to impose a thermal gradient of the order of 20 K/cm and adjusted at the beginning of experiment to locate the interface roughly in the middle of the adiabatic area. Partial melting is then performed (A solid seed of 20 mm is always kept to preserve the single crystal of selected orientation). Stabilization is then realized during 24h before triggering solidification.

Thermal gradient measurement

An experimental determination of the thermal gradient G at the interface has been performed using the following procedure. The method is to measure the displacement of the interface Δz associated to a small shift ΔT of the control temperatures of hot and top of cold zones (Figure 2.6):

Then the gradient can be written as

$$G = \Delta T/\Delta z \qquad 2.1$$

Measurements are performed at rest and all changes are supposed to be small enough so that the interface stands in the same area of thermal field. In our case, considering the location of the interface (see Figure 2.6-b), the control area are the hot zone and the booster heater so that the thermal shift was applied to these areas. For example, for temperatures of hot zone and booster heater respectively of 85°C and 45°C (358 K and 318 K), a ΔT = (2.1 ± 0.1) K was applied and we measured Δz =(0.76 ± 0.03) mm (compare Figure 2.6-b and Figure 2.6-c). The experimental gradient G_1 is then 28 ± 3 K/cm. We also used another set of temperatures that led to a gradient at rest, measured with the same method, of G_2 =12 ± 2 K/cm.

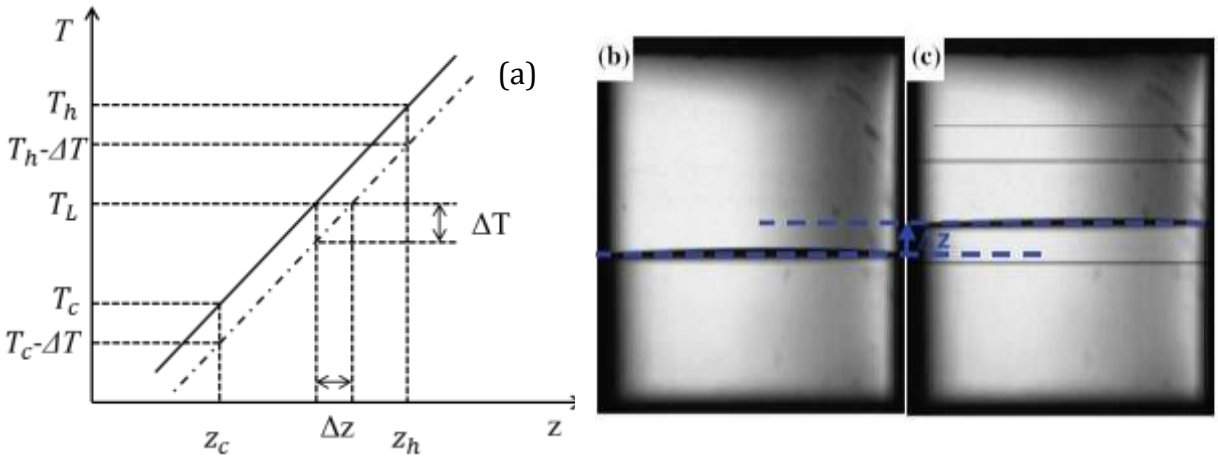

Figure 2.6. a : Temperature gradient measurement by shifting the hot zone and cold zone temperatures. With T_h temperature in hot zone and T_C temperature in cold zone, T_L interface temperature, ΔT the imposed shift of temperatures and Δz the displacement of interface. b: Side image of the interface at rest before changing the temperatures of both the booster heater and the hot zone. c: Side image of the interface at rest after decrease of 2 K of both temperatures of the booster heater and the hot zone. (G = 28 K/cm, V = 0).

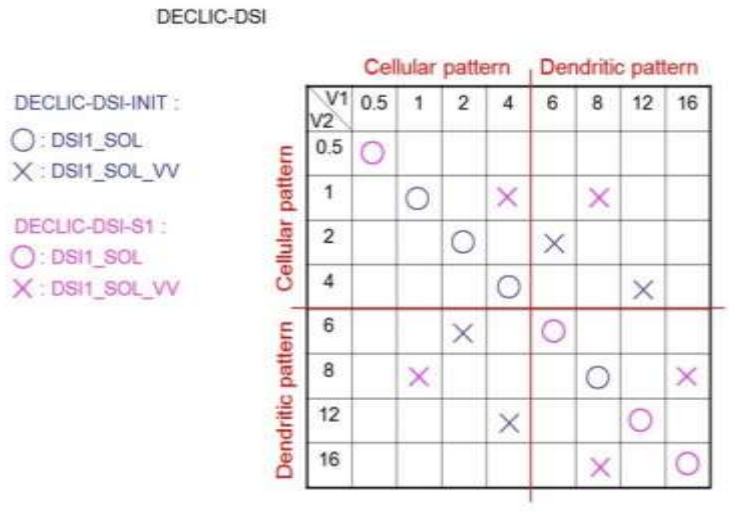

Figure 2.7. Experimental matrix summarizing the experiments conducted during the two first runs of space experiments (G = 28 K/cm). O: long solidification at constant pulling rate (V_1 = V_2 = pulling rate; 60 mm of growth). X: solidification with jump of pulling rates (30 mm at V_1, 30 mm at V_2).

Figure 2.8. Snapshot of VisuWeb.

2.2. Succinonitrile – 0.24 wt% camphor sample

2.2.1. Transparent alloy system

The material used is an organic transparent alloy based on succinonitrile ($C_2H_4(CN)_2$). Succinonitrile is an organic substance that solidifies like metals. Such material presents a rough interface [109], and micro structures similar to those observed in metallic systems (like cells and dendrites for example) can then develop at the solid liquid interface. The structure of the first solid phase is a face centered cubic (fcc) one, with one succinonitrle molecule on lattice sites [153]. Solid liquid transparency allows us to study the interface in situ and in real time. The advantage of this material is that it has a melting point close to the room temperature (331.24K), (Table 2.1) which is much lower than a real metallic alloy, and it has a gap large enough between melting point and boiling point. Table 2.1 gives some properties of pure succinonitrile.

Table 2.1. Some properties of pure succinonitrile.

Melting point (T_M)	331.24 K
Enthalpy of fusion (L)	3.713 kJ/mol
Molar entropy of fusion (ΔH_f)	11.12 J/mol K
Molar mass (M)	80.09 g/mol
Density of liquid (ρ_L)	0.975 x 10^3 kg/m^3
Density of solid (ρ_S)	1.016 x 10^3 kg/m^3
Thermal conductivity of solid (K_S)	0.224 J/ms K
Thermal conductivity of liquid (K_L)	0.223 J/ms K
Interface energy (γ)	8.95 x 10^{-3} J/m^2
Gibbs-Thomson coefficient (Γ)	0.64 x 10^{-7} mK

The alloy we used is a succinonitrile-camphor (Figure 2.9) of a very low concentration. This alloy has been recently studied by Teng and Liu [154]. For a concentration lower than 2%, k = 0.2; the diffusion coefficient of camphor in the liquid is $D_L = 0.23*10^{-9}$ m^2/s. The slope of the liquidus is a function of concentration: m = -1.3825 + 0.0726C – 1.83 * 10^3 C^2 K/pds%. The phase diagram from Ten and Liu is in overall agreement with that determined by Witusiwitz et al [155]. Excepting on the solidus curve and limit at solubility. This point is not fully clarified, which introduces some uncertain by the value of k and maybe D_L. These differences are important for us as they affect the value of k. Very recently, the same authors [156] have processed to a redetermination of the phase diagram that confirms the questioning about the k value and strongly pushes for a lower limit of solubility compared to the one given by Teng and Liu. These questions may sometimes be discussed in the following parts.

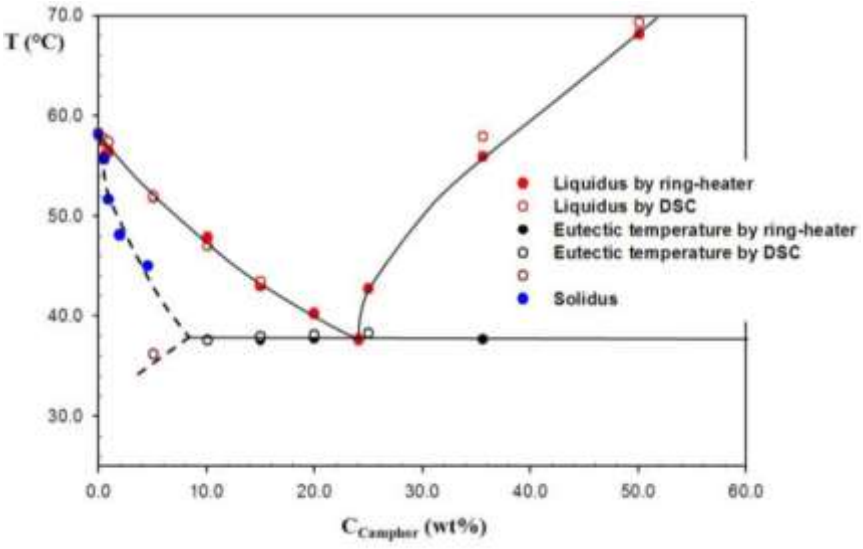

Figure 2.9. Phase diagram for succinonitrile – camphor [154].

2.2.2. Sample preparation

A Succinonitrile (SCN) - 0.24 wt % Camphor alloy is used in this study. For filling the crucible, SCN purified by NASA by both distillation and zone melting was used. The alloy is prepared at the IM2NP by adding the solute and a glass cartridge sealed under vacuum is obtained at this step. This alloy is transferred to the experimental cartridge during the filling process. All these procedures for sample preparation are carefully realized under vacuum to avoid humidity contamination. The detail of these procedures can be found in [5]. Once sealed, an oriented solid seed is grown (see §2.2.3) before the delivery of the experimental cartridge to CNES to be installed in the DSI.

2.2.3. Grain selection for <100> dendrites

In the case of dendrites, the growth direction is strongly influenced by the crystal orientation [103,157]. Without taking care of that fact, the starting fully melted sample solidifies into a polycrystal which exhibits a diversity of grains. Since each grain is a single crystal with random orientation and dendrites grow along <100> directions in the cubic system, this leads to a diversity of dendrite morphologies at the solid liquid interface (Figure 2.10). It is clear that to get unambiguous benchmark data on the dendritic array, it is mandatory to avoid this kind of interface morphology. It is thus necessary to grow a single crystal to obtain only one dendrite orientation but this is not sufficient. This single crystal has to be well orientated, meaning with a <100> direction parallel (or the closest to parallel) to the crucible axis, i.e. parallel to the observation axis. In that case, the dendrites, which behave like optical fibers, are neatly seen from the top by illumination through the sample axis.

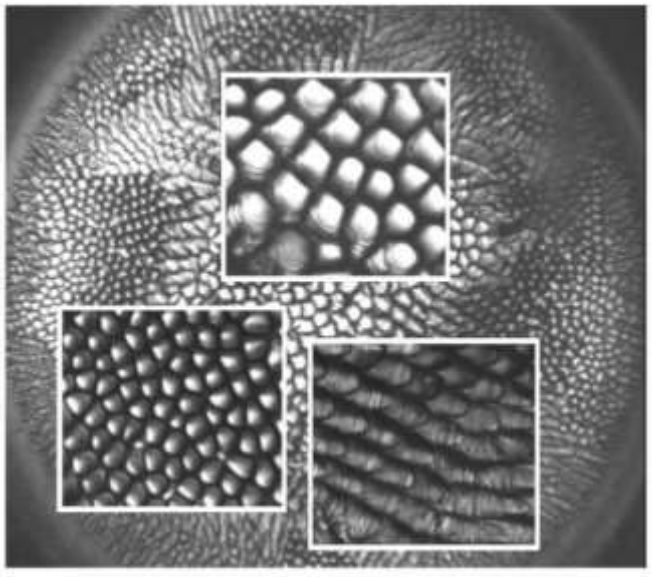

Figure 2.10. Top-view image of the interface during columnar growth showing a large number of grains with different dendrite orientations. (SCN - 0.1 wt% acetone, V=10µm/s and G=30 K/cm; lab model of DECLIC-DSI). Diameter: 10mm.

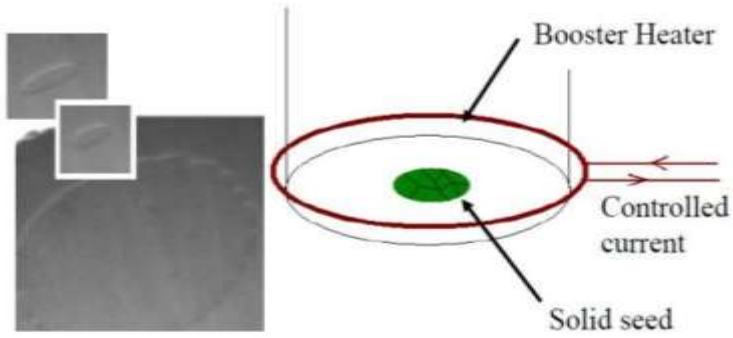

Figure 2.11. Left: Selection and expansion of the last grain. Right: the booster heater around the bottom of the crucible.

Obtaining a well-oriented crystal can be achieved in two steps by using the booster heater. Starting from the melt, a very thin solid seed is first realized by pulling. Then, increasing the booster heater temperature, all the small grains formed at the bottom window of the crucible are melted but one (Figure 2.11). By decreasing the booster heater temperature, this last grain is then expanded laterally until it fills the whole section of the sample. The whole process is controlled by real time observation. At this point, the obtained solid seed is a single crystal but, obviously, the random crystalline orientation depends on the last grain present in the crucible and cannot be chosen. In order to check the orientation of the single crystal, a high pulling velocity corresponding to dendritic growth is applied. If the orientation is not correct, i.e. dendrite growth direction not parallel enough to the observation axis, the whole solid seed is re-melted and the procedure is repeated until success. For the flight cartridge, the process of grain – selection has been performed in the lab before integration of the cartridge in the DSI.

2.3. Statistical Analyses of the interface microstructure

Several parameters are extracted from the observed images to characterize the pattern: the primary spacing, parameters for order-disorder (Minimal Spanning Tree), the number of neighbors of cells/dendrites ... During one solidification step, thousands of images are obtained and each original image contains hundreds of cells. Systematic analyses are to be performed so that semi-automatic procedures have been developed to handle this task. In the next part, I will introduce all the technical details of image treatments and statistical analysis methods.

2.3.1. Image post-processing

A good quality of binary image is a prerequisite to carry on the statistical analyses, to obtain an accurate result performed on the largest possible area of the image. Several

image treatments are applied to obtain a clean binary image using the following software:

- ImageJ or Fiji: to equilibrate brightness;
- Visilog: to separate stuck cells and to thin boundaries between cells (skiz function);
- Photoshop: to correct residual mistakes.

This is illustrated in Figure 2.12 that shows 3 images corresponding to the 3 fore mentioned steps of image treatment. Figure 2.12-a is an original top view image obtained from DECLIC-DSI experiment. Figure 2.12-b is the corresponding binary image and Figure 2.12-c is the image obtained after the "skiz" treatment. The original image is a BMP type grey level image with a resolution of 1024 pixels x 1024 pixels. The center of the original image is much brighter than the border; this brightness heterogeneity makes the definition of threshold value for binarization difficult. A pretreatment using the function named enhance local contract in the Fiji software reduces this brightness problem. For binarization (Visilog software), all pixels with grey level higher than the threshold are turned to 1 and the other ones are turn to 0 (in a binary image, 1 means black color and 0 means white color). The grey scale threshold value cannot be too large, otherwise the microstructure sticks all together, nor too small to avoid the loss of structure details. But even if the grey level is correctly selected, there are still cells that stick together. Therefore the function "open" in Visilog can be used to separate them. (The function “open” will detect the thinnest part of one single object and where it will cut the object into two independent parts. As the whole structure is like a dumbbell shape, this function is very useful in the cell structure analysis since the “sticking” part of two cells is exactly the thinnest part;. For dendritic structure, this function would cut off the secondary arms of the dendrites; therefore, it is not suitable for dendritic structure.) After the skiz treatment, the boundary between two adjacent cells is just a single line. Finally, the image resulting from skiz treatment is superimposed to the original image using Photoshop to compare and to correct manually if necessary. The binary image obtained at the end of this image post - processing is used as the input of several macro procedures that I have developed with Visilog to extract characteristics of the pattern. Characteristics parameters measurements are detailed in the following parts.

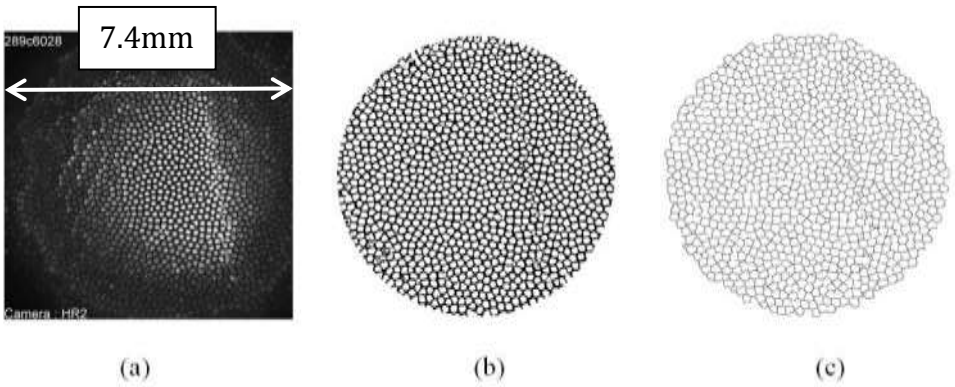

Figure 2.12. Image processing from original image to the image "skiz", with a: original image. b: Binary image with a chosen grey level and. c: Image "Skiz" obtained from Visilog analysis.

2.3.2. Primary spacing

The primary spacing is defined as the distance between the tips of two neighboring cells or dendrites. It is the first characteristic parameter of the solidification microstructure easier measure in our investigation. In top view images, cell tips are assimilated to cell centers. Since each cell has more than 2 neighbors, the spacing is more difficult to measure than in 2D experiments. Several methods described below have been evaluated.

Method of "round shaped cells"

A first approach is to consider each cell as a disk [158] and to define the primary spacing as the diameter. From this definition, we have:

$$\lambda = 2 * \sqrt{S/\pi} \qquad 2.2$$

The surface area of each cell S is measured by Visilog.

Method of "polygon shaped cells"

For a more accurate approximation, we can add the influence of the number of neighbors [159]. For example, if a cell has six neighbors, it can be simply considered as a perfect hexagonal array instead of a disk. Considering the Figure 2.13, the surface S of a regular polygon with N sides is:

$$S = Na\frac{\lambda}{2} \qquad 2.3$$

with $a = (\lambda/2)\tan\theta$ and $\theta = \pi/N$.

So that:

$$\lambda = \sqrt{4S/(N\ tan(\frac{\pi}{N}))} \qquad 2.4$$

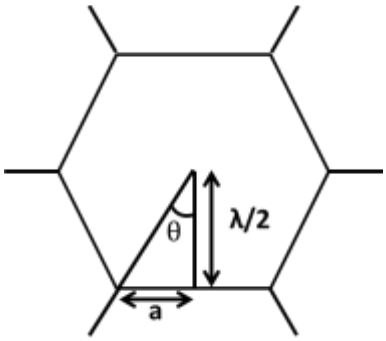

Figure 2.13. Illustration of the "polygon shaped cells" method for a hexagonal cell.

Center to center distances:

From the fundamental definition, the primary spacing can be measured directly from the center to center distance, which is of course more accurate as no shape hypothesis is required (Figure 2.14-a, the primary spacings are indicated with the red segments). Starting from a "skiz image", each cell and its nearest neighbors can be identified using a procedure developed with Visilog. Segments linking adjacent cells are measured so that a histogram of center to center distances for the whole pattern can be drawn.

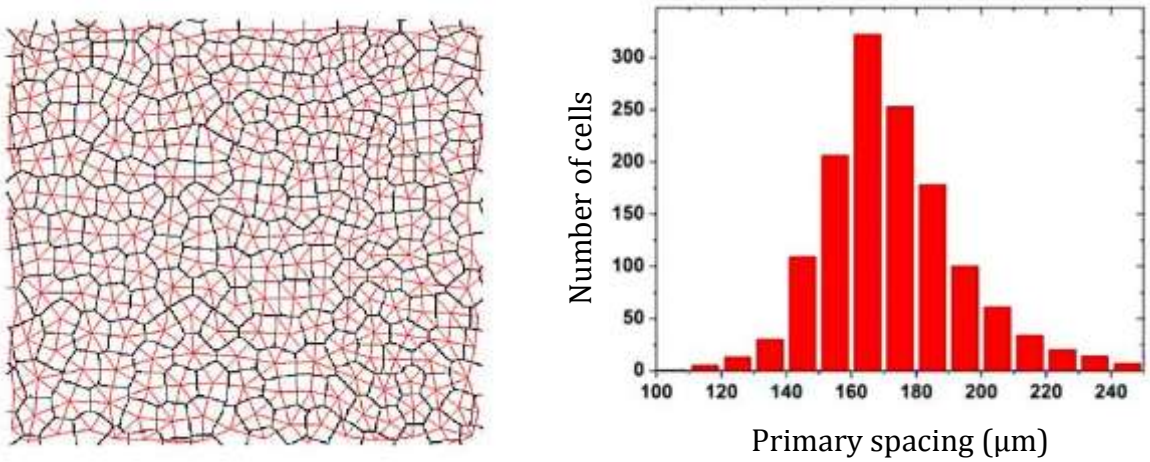

a b

Figure 2.14. a) Measurement of the primary spacing directly from center to center distances. The red segments are the primary spacing superimposed on the cell array (black one). b) The histogram of primary spacing from center to center distance measurements.

Comparison of the different methods of primary spacing measurement

Logically, the statistical analysis of the center to center distances is the best method to characterize the pattern as it directly reflects the distribution of primary spacing.

Measurement is direct so that no geometric factor needs to be introduced in extracting of primary spacing.

Table 2.2 compares the results of measurements with the 3 different methods, for 3 solidification lengths. The corresponding histograms for solidification length of 6.9mm were given in Figure 2.15. The average values are close for the three methods, but the distribution is sharper for the round and polygon methods: for all solidification length, the standard deviation is significantly larger with the center to center method. Moreover, the evolution of the standard deviation, that describe the selection of spacing during pattern evolution, are masked with the geometric methods. Considering these results, the center to center method will be used for all primary spacing measurements.

Table 2.2, comparison of the three methods of primary spacing measurement, with λ: average primary spacing and σ: standard deviation. (V = 4 µm/s, G = 28 K/cm).

Solidification length	Center to center distance method		Round shape method		Polygon method	
L (mm)	λ (pixel)	σ	λ (pixel)	σ	λ (pixel)	σ
6.9	197.28	30.24	193.68	15.84	182.88	16.56
9.5	192.96	27.36	189.36	13.68	179.28	14.4
12.2	182.88	24.48	179.28	17.28	169.2	16.56

FFT method in determination of the primary spacing

Some images cannot be treated by the previous methods, especially those obtained during the transient step of microstructure formation. An example of such images is given in Figure 2.16-a: cells are not yet defined and closed. Dendritic structures may also be difficult to analyze by previous methods due to secondary arms (Figure 2.16-b). Because of the periodic structure underlying the images, the Fast Fourier transform method can be used to calculate the distribution and average value of primary spacing. A Fourier transformation image turns an image from

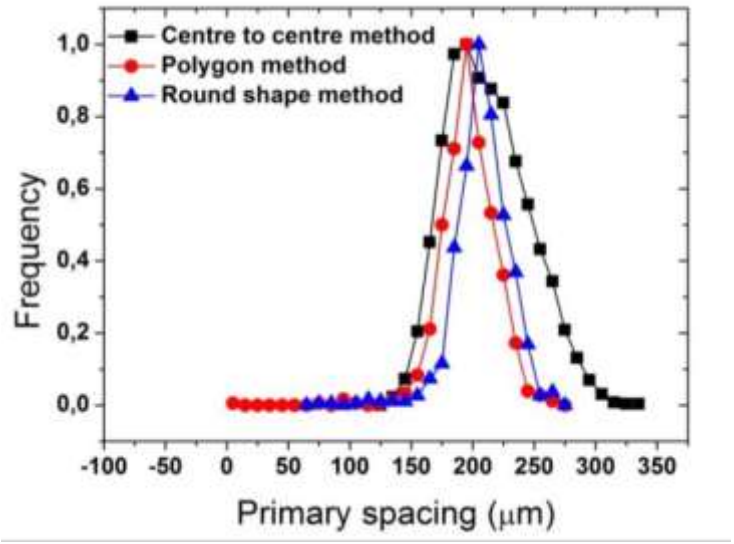

Figure 2.15. Primary spacing distribution for the 3 different measurement methods. (V = 4 µm/s, G = 28 K/cm, solidification length of 6.9 mm).

the spatial domain to the frequency domain. Each point in the Fourier transformed image corresponds to a spatial frequency in the original image.

For an N x N pixels digital image, the Discrete Fourier Transformation is given by:

$$F(k,l) = \sum_{m=0}^{N-1} \sum_{n=0}^{N-1} f(m,n) exp^{-i2\pi\left(\frac{km}{N}+\frac{ln}{N}\right)} \qquad 2.5$$

with $f(m,n)$, the grey value of the pixel localized by its coordinates (m,n) in the original image (spatial domain) and $F(k,l)$, the grey value of the pixel localized by its coordinates (k,l)in the transformed image (frequency domain).

The FFT of the image (for example Figure 2.16-c) is obtained using a function of Visilog: then it was circularly averaged leading to a 1D power spectrum (Figure 2.16-d). The frequency axis of the main peak is associated to the primary spacing by λ = N/f, with N the spacing of the original image and f the frequency which is also the x axis of the spectrum figure. Figure 2.16-e gives an example of analyze of the same microstructure obtained with the FFT and center to center distance method. The distributions obtained from the 2 different methods are highly overlapped thus validating the use of FFT method as a complement.

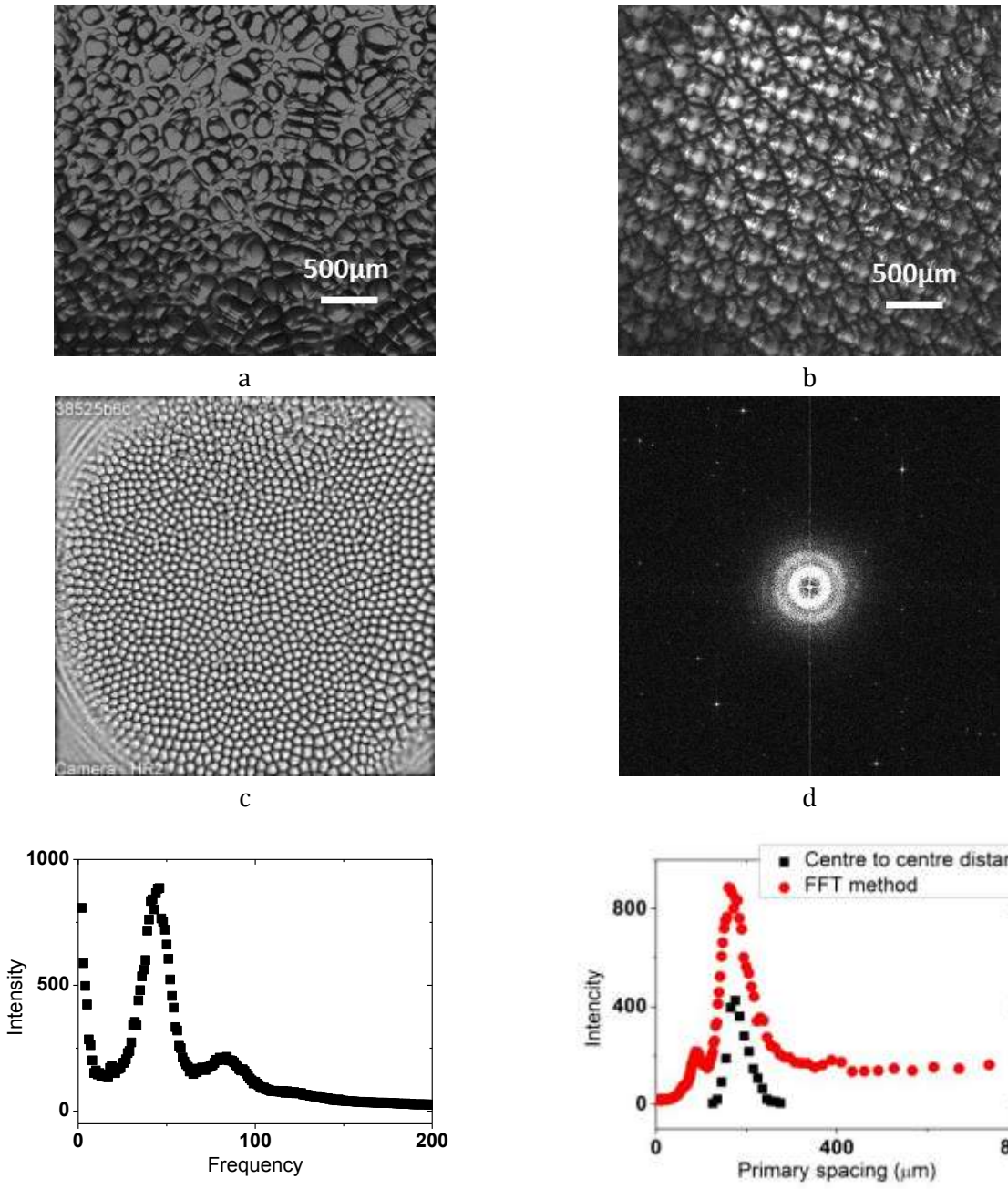

Figure 2.16. Primary spacing measurement with FFT method. a) Example of microstructure in early stages of solidification. b) Example of highly branched dendritic structure (V = 12µm/s, G = 12K/cm, 1g). c - e) Analysis of a cellular pattern by FFT method (V = 4 µm/s, G = 28 K/cm) with c) pattern image. d) FFT image of c). e) Corresponding circular average distribution of frequency. f) Comparisons of the distribution of primary spacing extracted from FFT and center to center distance methods.

2.3.3. Minimal Spanning Tree analysis of array disorder

C. Dussert has developed a statistical method called Minimal Spanning Tree (MST) [160], based on graph theory, that can be used to study the order-disorder of a set of points. In this graph theory, points are called nodes and pairs of nodes are called edges; each edge is characterized by a number called "edge weight". The space area that contains nodes is called "sample volume". A tree is defined as a connected graph between nodes without closed loops, and a Minimal Spanning Tree is a tree that contains all the nodes and for which the sum of the edges weights is minimal. In our experiments, nodes are defined as the center of the cells or dendrites and the weights are defined as the lengths between two centers (nodes). One graph can have more than one possible minimal spanning tree if there exists some equal weighted edges, but the sum of the weights is unique.

Two parameters, the normalized average length m and the standard deviation σ characterize the MST distribution of lengths.

The normalization of m and σ is defined as [160]:

$$m = \frac{m^*(N-1)}{N\sqrt{S}} \qquad 2.6$$

$$\sigma = \frac{\sigma^*(N-1)}{N\sqrt{S}} \qquad 2.7$$

with N the number of nodes and S the area occupied by the nodes. Equations 2.6 and 2.7 are functions of N. A test was then done to find out the minimum number of cells required for a representative statistical result (Figure 2.17-c and d). Both m and σ became stable if N passed a value of 150. This number can be easily satisfied in our images.

A given perfectly regular array is associated to a specific normalized value of m, depending on the shape of the unit cell, with σ = 0. For example, for a hexagonal array, m=1.075, and for a square array, m = 1. Those highly organized arrays are located on the m-axis of the m-σ diagram. Then if disorder is added to each cell center position gradually, a path will be created from the highly ordered point of each array (with σ = 0) to a point corresponding to a random distribution (random point in Figure 2.17-b). In the figure, the two paths respectively represent hexagonal (the one started from (1.075, 0)) and square arrays (the one started from (1,0)) with different levels of disorder. The array type is determined by both m and σ values whereas the order level is determined only by σ. All other distribution can be plotted in the (m, σ) plan and compared with those well characterized structure paths.

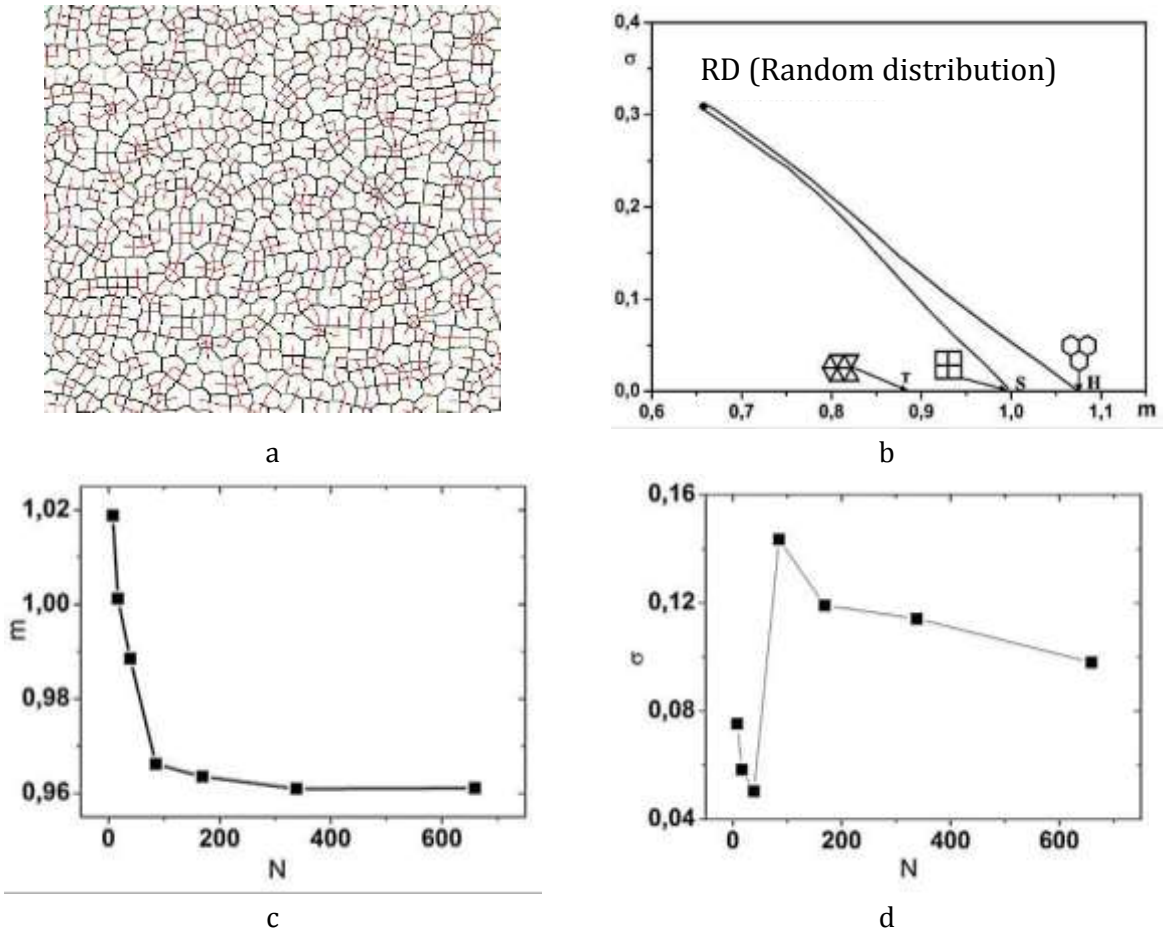

Figure 2.17. a) Example of MST (red tree) superposed onto the microstructure (black array). b) m-σ diagram where two solid lines are plotted which correspond to increasing level of disorder for two types of pattern (square and hexagonal structures). c and d) Evolution of the average value of m and σ as a function of the number of cells N. (V = 4µm/s, G = 28K/cm, SCN-0.24%pds camphor)

2.3.4. Nearest neighbor analysis

The number of neighbors gives information about the quantity of topological defects in the pattern. This measurement is performed by a procedure that we developed in the Visilog software. Starting from a skiz image, all triple and quadruple intersections (that correspond to the crossover point of 3 or more cells) are detected and removed so that only a figure of segments remains. Each segment corresponds to a boundary between two cells so that counting the number of segments attached to one cell gives the number of neighbors. An example of such an analysis is given in Figure 2.18: each cell of the image is labeled with the number of neighbors. The histogram of the number of neighbors can also be extracted from measurement and used to compare different patterns.

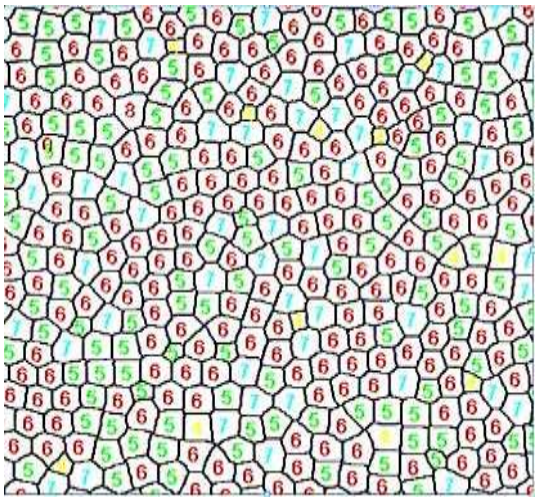

Figure 2.18. Example of nearest neighbor counting. The number of the nearest neighbor is marked in the skiz image with different colors. (V = 4µm/s, G = 28K/cm, SCN-0.24%pds camphor)

2.3.5. Interferometric analysis

The DECLIC-DSI is equipped with an interferometer settled on the axial direction of the crucible, using a polarized He-Ne laser (wavelength λ = 632.8nm). The analysis of interferometric images is used to determine the interface shape and its motion. Interference fringes appear at the recombination of the laser beam passing through the crucible with a reference beam passing outside. The fringes result from the difference of optical paths between those two beams. Passing from one fringe to the following one corresponds to a variation of the object optical path which equals λ. This observation mode provides patterns of fringes that can be considered as interface level curves. During the experiment, the main variations of optical paths are attributed to variations of the lengths of different phases (solid/liquid). Space variation is obtained by comparing the optical paths of parallel rays crossing the interface at different places but at the same time t; corresponding interferometric fringes are related to the interface shape. Time variation is obtained by comparing the optical paths of one ray at different times; the observed sliding of fringes is due to the motion of the interface. It is worth noting that, in the following developments, the effects of concentration variations on refractive indices are neglected considering the fact that alloys of very low solute concentrations are used; refractive indices are thus considered solely temperature-dependent.

Space variation

As illustrated in Figure 2.19-a, the optical paths (OP) of the two rays at a time t differ only close to the interface, on the thickness L, which is solid for ray 1 and liquid for ray 2. The temperature field surrounding the interface is considered homogeneous along the interface. If 1 and 2 correspond to two side by side fringes, then:

$$OP_1 - OP_2 = L(n_{\phi S} - n_{\phi L}) = L\Delta n_\phi = \lambda \quad 2.8$$

with:

L: difference in solid length between fringe 1 and fringe 2.

λ: laser wavelength.

$n_{\phi S}$: refractive index of solid at the interface temperature.

$n_{\phi L}$: refractive index of liquid at the interface temperature.

Δn_ϕ: difference of refractive indices between solid and liquid at the interface.

Time variation

In case of stationary growth, the interface position is fixed in the furnace frame (the interface rate is equal to the pulling rate V). As represented in Figure 2.19-b, during a time Δt, the length of solid increases of VΔt and the length of liquid respectively decreases of the same quantity. The optical path of a ray taken at times t and t + Δt is consequently modified:

$$OP(t + \Delta t) - OP(t) = V\Delta t(n_S(T_{CZ}) - n_L(T_{HZ})) \quad 2.9$$

with:

$n_S(T_{CZ})$: refractive index of solid at the temperature of the cold zone T_{CZ}.

$n_L(T_{HZ})$: refractive index of liquid at the temperature of the hot zone T_{HZ}

If Δt corresponds to the crossing of one fringe, then:

$$\lambda = \Delta t V \Delta n_{SL} \quad 2.10$$

with:

$\Delta n_{SL} = n_S(T_{CZ}) - n_L(T_{HZ})$: difference of refractive indices between cold solid and hot liquid.

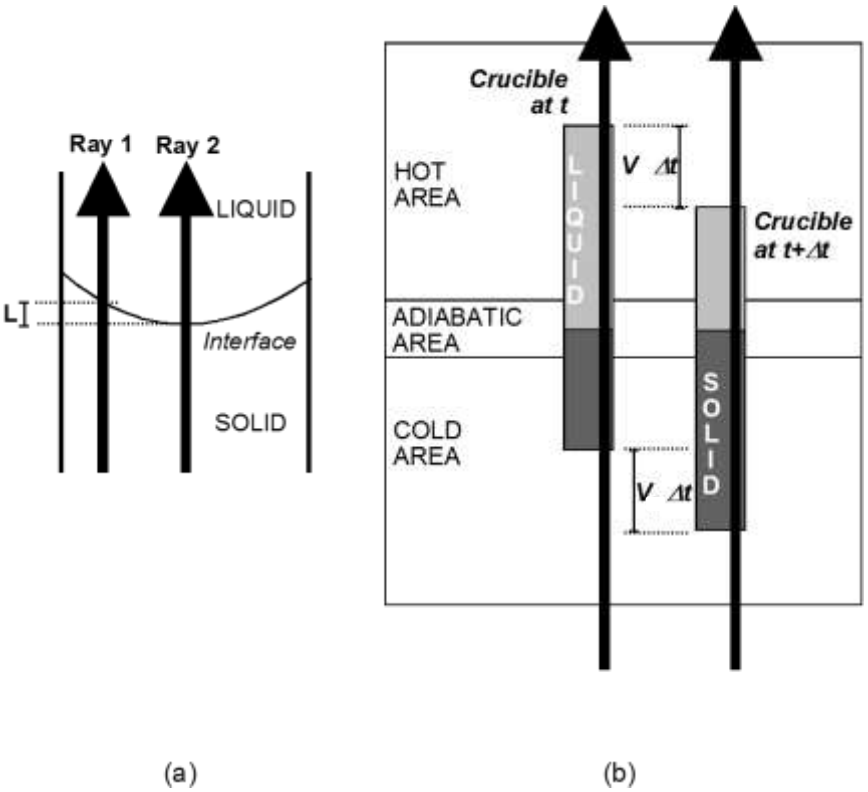

Figure 2.19. Interferometry analysis of stationary growth. A) Spatial analysis: comparison of optical paths of two rays at the same time. b) Time analysis: evolution of the optical path of one ray between t and Δt.

Refractive index

It clearly appears from expressions 2.9 and 2.10 that the knowledge of refractive indices in both solid and liquid phases, and of their variations with temperature, is critical to extract quantitative data from interferometric images. Several measurements have been performed to determine the variation of the refractive index of pure SCN in liquid phase as a function of temperature, but they are usually not completed by similar data in solid state ([159], unpublished data from Liu and Trivedi or other unpublished data from Zeiss). The differences of refractive indices required for our analyses can be calculated on the basis of the only complete characterization of the SCN refractive indices as a function of T, for both phases, that has been done by MacFarlane et al. [161]. Using their data:

$$\Delta n_{\phi} = 0.019$$

$$\Delta n_{SL} = 0.034$$

To get more accurate data, measurements of the indices have been performed in situ. Δn_{ϕ} is determined using Equation 2.8. Two interferometric images taken while the interface is still smooth are used. The first image (for example Figure 2.20-a)

corresponding transvers view is used to visualize the interface shape. During pulling, the interface moves downwards and its shape changes (Figure 2.20-b). The transverse view enables the determination of the height differences (noted L) between the highest point of the interface (noted H.P on Figure 2.20) and two other side points (L.P and R.P). The variation of height differences between the two transverse images is related to variation of the number of fringes on corresponding interferometric images. For example, on Figure 2.20-a, the height L varies from 5 pixels to 12 pixels and this is associated to two additional fringes. So that $\Delta n_\phi = (2 \text{ fringes } \times \lambda/\Delta L) = 0.013$. Such measurements have been performed on several couples of images, leading to the value of $\Delta n_\phi = 0.013 \pm 0.001$ that we well use in our interferometric analyses.

Δn_{SL} is determined during steady-state growth using Equation 2.10. The time ΔT required for N fringes to pass at the same interface point is measured and $\Delta n_{SL} = N\lambda/V\Delta t$. The value of $\Delta n_{SL} = 0.035 \pm 0.002$ was than obtained and it will be used for analyses.

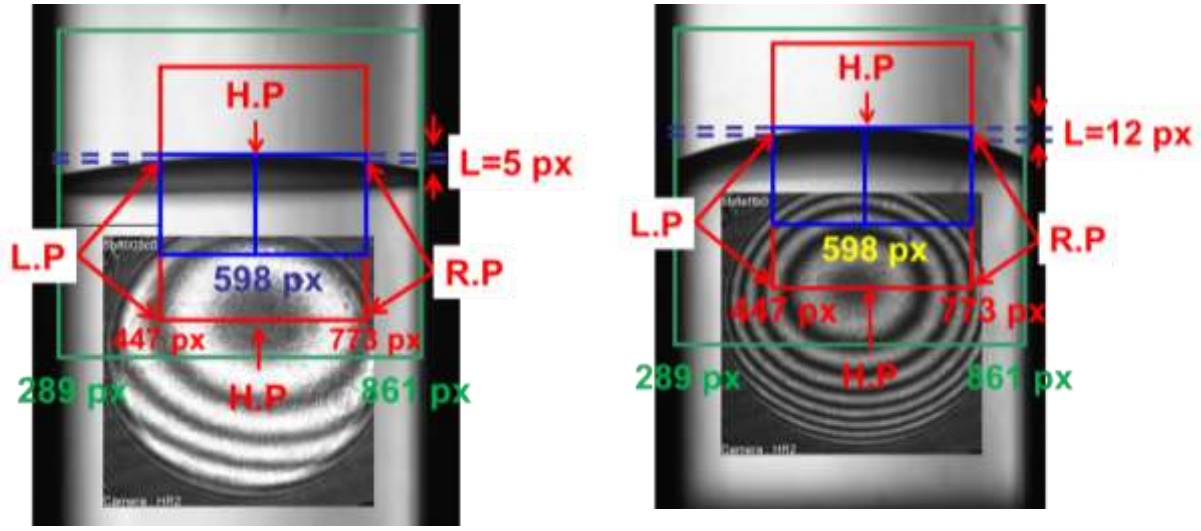

a b

Figure 2.20. Measurement of Δn_ϕ. Side view and corresponding interferometric image of the interface. a) At rest. b) during pulling at V = 0.25 µm/s, G = 12 K/cm. "H.P" makes the highest point of the interface while "L.P" and "R.P" refer to two measurement points, respectively located on the left and right sides of "H.P".

Application of interferometric analysis to the cell/dendrite shape reconstruction

Let us reconstruct for example the cell marked on Figure 2.21-a Equation 2.8 is applied to attribute a height to each fringe, setting the point z = 0 at the tip. Two neighboring fringes correspond to a height difference of 48.7 µm . The cell/dendrite profile is therefore described by 2 points corresponding to the 2 fringes observed on Figure 2.21-a. This is not sufficient to precisely rebuild the tip shape. This is the reason why this spatial analysis is combined with temporal analysis by using several successive images of the same cell/dendrite.

The principle is described in Figure 2.22. The top view corresponds to a schematic representation of 2 fringes f1 and f2 located on a cell/dendrite tip, at 2 different times. At t, these 2 fringes give 2 points on the cell/dendrite profile as described previously. Let us consider for example the motion of the fringe noted f1 between t and t+dt. A fringe corresponds to a precise value of the optical path so that the optical paths of f1 at t and t+dt are equal. The side view of figure 1c points out the evolution associated of f1 during dt, hence:

$$OP_{f1}(t+dt) - OP_{f1}(t) = 0$$

$$\Rightarrow V_p dt\left(n_S(T_{CZ}) - n_L(T_{HZ})\right) + dz\left(n_{L\phi} - n_{S\phi}\right) = 0 \qquad 2.11$$

$$\Rightarrow dz = dtV_p\Delta n_{SL}/\Delta n_{\phi} \qquad 2.12$$

This relation allows placing the point corresponding to the fringe f1 at t + dt, at the distance dz of the point corresponding to f1 at t. This adds an intermediate point to the profile given by f1(t) and f2(t). Simultaneously, the same analysis is performed for f2(t + dt) and fringes of superior orders. An average of 8 to 10 intermediate images is used on a time interval that roughly corresponds to the sliding of 1 fringe.

An example of such reconstruction applied to the cell pointed in Figure 2.21-a is given in Figure 2.21-b. It gives the profile in the marked longitudinal cross-section.

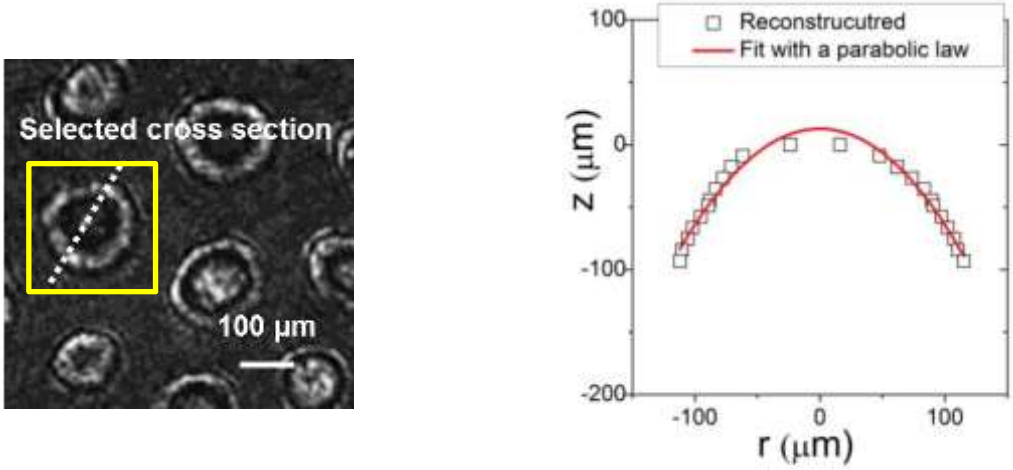

a b

Figure 2.21. Cell shape reconstruction. a) Interferometric image with the selected cell. b) Tip profile in a selected cross section.

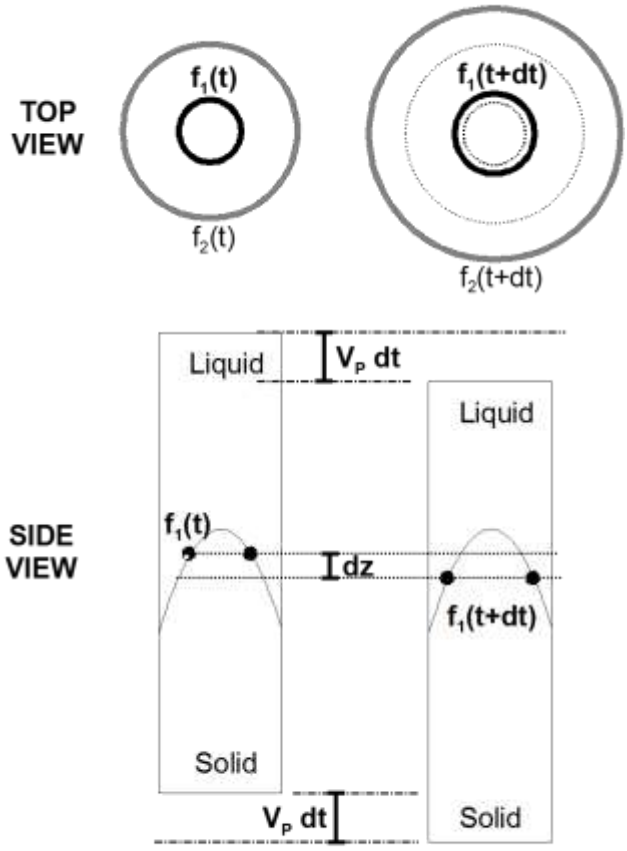

Figure 2.22. Principle of cellular/dendrite profile analysis. The top view is a schematic representation of real interferometric images. Side view enables to visualize the variation of composition of the optical path of fringe 1 between t and t+dt.

Chapter 3. Pattern formation and evolution

3.1. Introduction

Characterizing the solidification pattern during steady state growth as well as understanding its formation from the morphological instability of the smooth interface and evolution with the control parameters is important since the final mechanical properties are mainly determined by its characteristic length scales. As exposed in chapter 1, many theoretical models have been proposed in the literature to describe the primary spacing λ as a function of the three control parameters [20][162][22], namely the thermal gradient G, the solute concentration C and the solidification rate V. Those models result in a power law variation of λ, $\lambda = A \cdot C^{0.25} G^{-0.5} V^{-0.25}$, with A a constant that depends on the physical parameters of the alloy. Several investigations have been performed to check these models [22][163][164]. Most of them have been conducted on thin samples to avoid convection influence. But in that case, pattern organization is modified by dimensionality as cells or dendrites are necessarily aligned and may not be representative of a real extended 2D pattern; recent numerical studies using a quantitative phase–field model have also pointed out a strong influence of dimensionality on the branch structure [1]. Recently, some experiments on metallic alloys have been performed in microgravity on bulk samples [165][114][166] but only post-mortem analyses could be conducted so that the development of microstructure was still unreachable. Moreover, only a limited number of experiments can be conducted in such a configuration as one sample can be used only once. The combination of in situ observation and microgravity is mandatory to overcome these difficulties and being able to extract benchmark data for a large range of experimental parameters. Being able to get such benchmark data was one of the key motivations of the DECLIC-DSI project [167]. The instrument is designed to perform in situ observation on 3D transparent sample; its installation on the International Space Station for sure provides the microgravity environment but it also allows the long duration use required to perform numerous experiments. Furthermore, telescience is a perfect tool for monitoring each of these experiments. As previously mentioned, we have then been able to study the whole microstructure formation for a two order of magnitude variation for pulling rate and two different values of the applied thermal gradient [168].

In this chapter, we will first describe the microstructure formation, before focusing on the mechanisms of primary spacing evolution. Analyses during the steady state growth will then be presented and compared to classical theoretical models.

3.2. Pattern formation

A solidification with V = 4 µm/s and G = 28 K/cm is described here so that one can have a general idea of the process of the pattern formation during solidification.

Figure 3.1 shows some critical images during this solidification that correspond to the typical pattern at different stages of solidification. At V = 4 µm/s, morphological instability develops quite fast as depicted by linear ridges along sub-boundaries that finally underline a quite complex array. Between these defects, in areas that are still smooth, some poxes appear (at t = 7.4 min): that can be described as a pit depression dimple decorated by a circular undulation of the interface. Ridges underlining sub-boundaries progressively split in the transverse directions and simultaneously, a quite uniform corrugation that corresponds to the initial visible wavelength of morphological instability invades the interface (t = 8.2 min). The amplitude of all those interface modulations starts to increase, channels are forming but it is still difficult to identify cells (t = 12.5 min,). At this stage, the dynamic of the interface is extremely fast and the disorder high. There is then a progressive decrease of disorder and a clear pattern of deep cells is eventually reached (t = 35.5 min). The dynamics then clearly slows down and gets limited to progressive size adjustment and ordering. These phenomena will be quantitatively described later.

Qualitatively, all experiments follow the same process. A difference with pulling rate is observed for the triggering of instability. At very low pulling rates, instability triggers almost exclusively with poxes uniformly distributed on the interface whereas for larger pulling rates, the triggering involves more and more ridges.

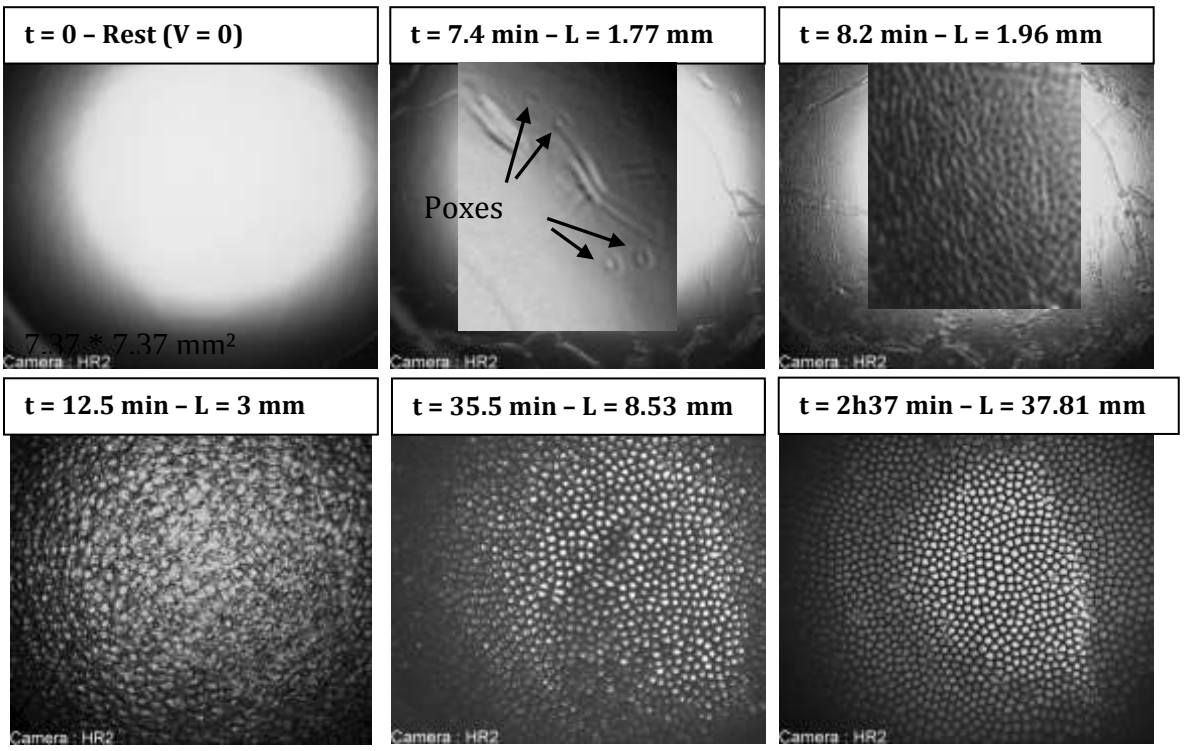

Figure 3.1. Typical sequence of formation of the interface microstructure (V = 4 µm/s, G = 28 K/cm). The solidification time t and solidification length L for each image are indicated.

3.3. Front recoil during initial transient

Initial transient corresponds to the first stage of the evolution from an interface at rest (V = 0) to the steady-state situation characterized by a growth velocity equal to the pulling rate. This evolution has been for example described by Warren and Langer [14]. The smooth interface, initially located on the isotherm of the liquidus temperature, first starts moving towards the solidus temperature so that the solidification front moves backward relative to the temperature gradient. Simultaneously, according to the phase diagram, solute is rejected in the liquid and the solute boundary layer progressively builds up. As the interface velocity increases, the front undergoes the Mullins-Sekerka instability. The microstructure then progressively develops. These authors built an analytical model that describes the variation of the interface velocity and of the solute boundary layer with time during the transient of a planar front. This process is never completed as instability develops before the achievement of the steady-state planar front. The growth of microstructure is associated to a cell tip growth inside the liquid so that the tip temperature is higher than the steady-state interface temperature of the planar front (see for example the Bower-Brody-Flemings model [169]).

The interface recoil is investigated by measuring the motion of the interface in the adiabatic area using transverse observation. As long as the interface is smooth, measurements are quite simple as its shape is well defined. Measurements are performed both on the side and in the center of the crucible so that the curvature and its evolution are also obtained. In most cases, when microstructure develops, the interface position is much more difficult to determine due to the macroscopic concavity and the integration of the whole thickness of the sample on the image; tips at different depth and different heights are superposed. The Figure 3.2 gives some examples of such measurement points for different interface shapes. Results for 3 pulling rates (G=28 K/cm) are given in Figure 3.3. The three recoil profiles display a similar evolution characterized by a fast variation of the position at the beginning, a quite abrupt slow down most of the times associated to a small inverse interface motion and finally very slow and regular recoil. The observation of the corresponding top-view images reveals that the abrupt slow-down is associated to the development of the microstructure, as illustrated on the small images of Figure 3.3. It therefore marks the end of the validity of planar front analysis.

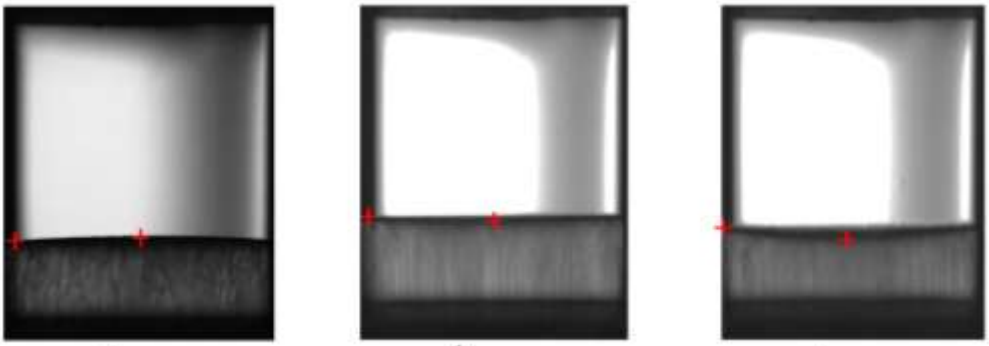

a b c

Figure 3.2. Interface position and curvature measurements. The three images correspond to 3 different interface shapes, with a) convex interface (V = 0.5 µm/S, G = 28 K/cm). b) Quasi-flat interface (V = 2 µm/S, G = 28 K/cm). c) Concave interface (V = 4 µm/S, G = 28 K/cm). The two red points correspond to the two measurements (the center and side one).

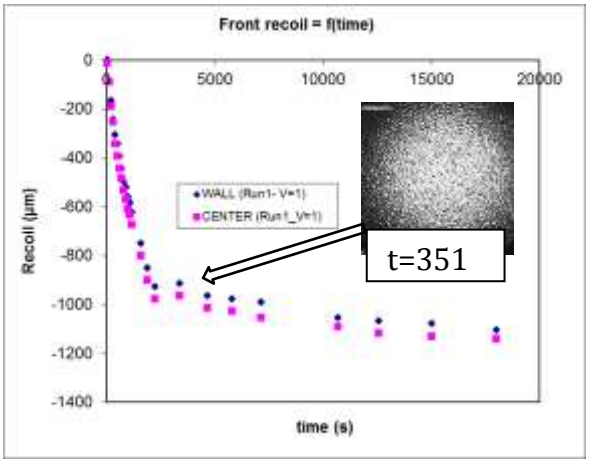

a

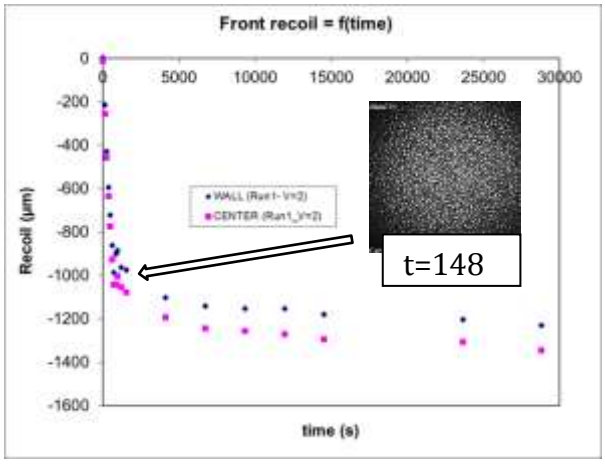

b

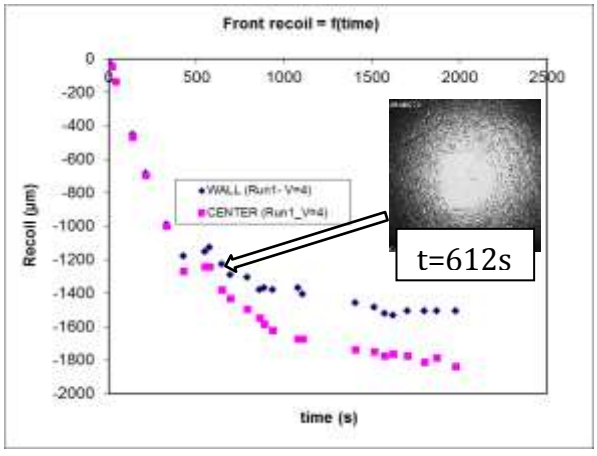

c

Figure 3.3 . Measurements of the interface recoil as a function of time. With a, b, c correspond to a pulling rate V of 1, 2 and 4µm/s respectively, (G = 28K/cm). Top – view images taken when recoils abruptly slow down reveal a spatially developed microstructure but at its early stage of formation.

Considering theories of solidification with a planar front, the amplitude of the recoil corresponds to the transition of the interface from the liquidus to the solidus isotherms: $\Delta z = (m_L C_0/G)(k-1)/k$ according to the phase diagram. For the gradient of temperature G = 28 K/cm, this displacement Δ_Z is evaluated at 466 µm, it is not function of pulling rate. In the case of microstructure development, the tip undercooling T_L-T_{tip} (T_l:

liquidus temperature, T_{tip}: tip temperature) decreases with pulling rate [169] so that the maximum recoil should correspond to the planar front recoil, and a decrease of this recoil should be observed with increasing pulling rate. It first clearly appears that this value is largely overcome for all considered pulling rates. Differences between this theoretical case and experimental measurements are then striking: all experimental recoils (between 1000µm and 1600µm at center for G = 28 K/cm) are larger than the planar front one (Δ_Z) and the recoils increase with pulling rate.

To explain the differences, one may consider first some thermal effects [170][171]. The first one is the transport of heat through the crucible wall during crucible movement that shifts the isotherms down. This effect tends to be more important for materials of low thermal conductivity compared to that of the ampoule and for sure increases with pulling rate. The second one is the latent heat release, which is also dependent on pulling rate. Latent heat generation tends to curve the interface but also to modify the thermal gradient and isotherm shape. All these effects are difficult to evaluate but they both indicate that the thermal field is affected by crucible motion so that the frozen thermal condition which is considered in fore-mentioned models is not valid. The effect of latent heat on curvature is at least very clear considering the evolution with time of the difference between border and center positions of the interface for the 3 cases presented in Figure 3.3. The curvature increases with time, concomitantly with the increase of interface rate, to stabilize in the slow variation part of the recoil curves.

However, it seems difficult to explain with these arguments so large differences between the theoretical and experimental values at the very low pulling rates considered: at 1 µm/s, the front recoil is already more than twice the theoretical one. A more serious issue lies in the correct knowledge of the physical parameters of the alloy. Recently, Witusiewicz et al. [156] redetermined of the phase diagram of the SCN-Camphor system to check the discrepancy between their previous characterization in 2004 [155] and the one performed by Teng et al. in 2006 [154], especially regarding the solubility limit. The new data are currently under study in the team as they affect the partition coefficient k. The experimental determination of the thermal gradient G at rest maybe also under question.

3.4. Dynamical studies

In this part, we will characterize the pattern evolution and especially analyze the mechanisms of spacing selection.

The primary spacing evolution with time during long solidifications has been measured for different pulling rates at G = 28K/cm; results are given in Figure 3.4. For each pulling rate, 4 curves are given: the primary spacing evolution with solidification length, the

corresponding evolution of the selection factor SF = $\Delta\lambda/\lambda_{average}$, with $\Delta\lambda$ the standard deviation value of the average primary spacing, and the complete distributions of spacing for each point of the primary spacing curve.

Two kinds of evolution tendencies are observed: for pulling rates smaller than 2µm/s, the spacing keeps increasing with time while for larger ones, spacing first reaches a maximum value before decreasing and stabilizing.

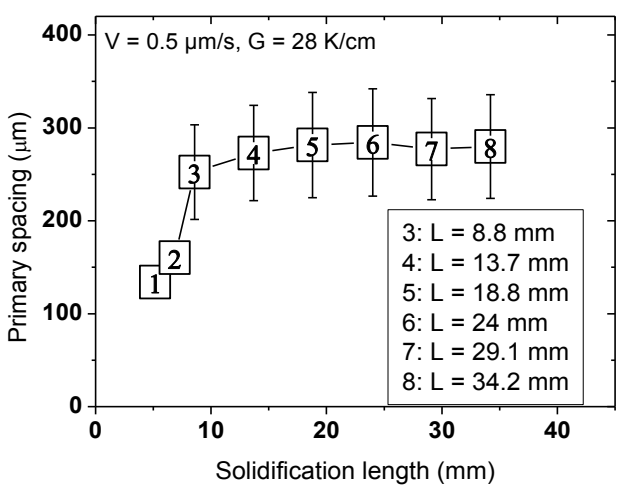

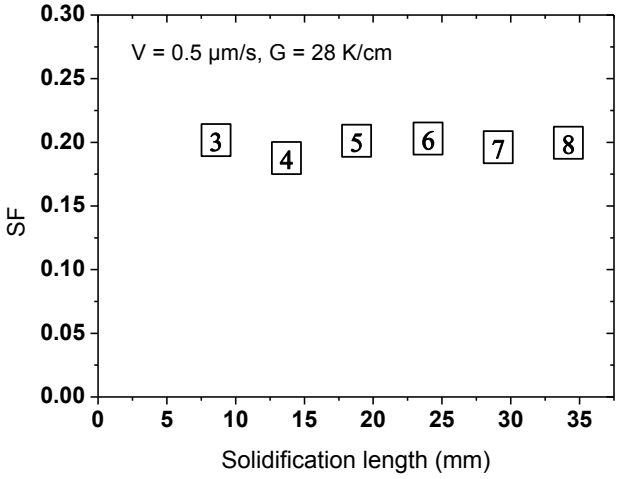

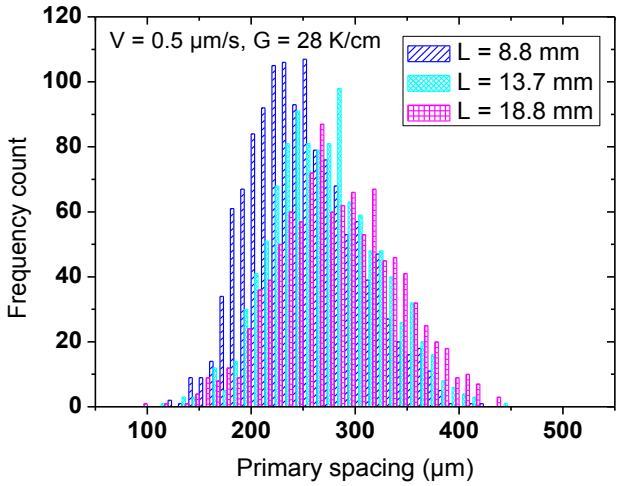

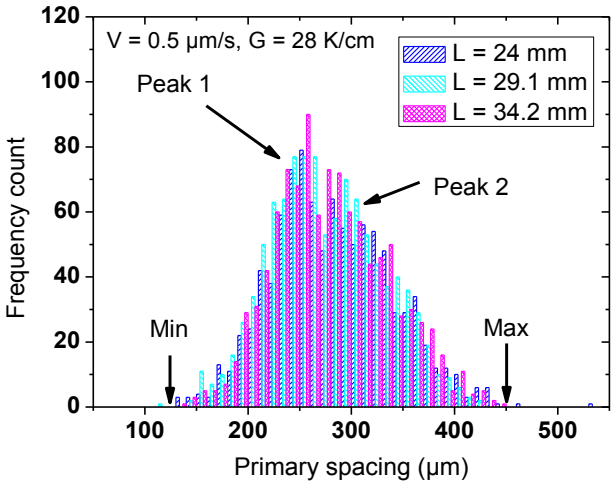

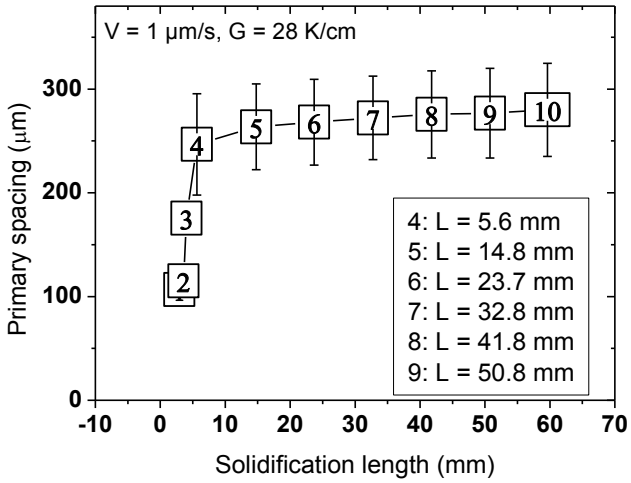
V = 1 µm/s, G = 28 K/cm
Primary spacing (µm)
Solidification length (mm)
4: L = 5.6 mm
5: L = 14.8 mm
6: L = 23.7 mm
7: L = 32.8 mm
8: L = 41.8 mm
9: L = 50.8 mm

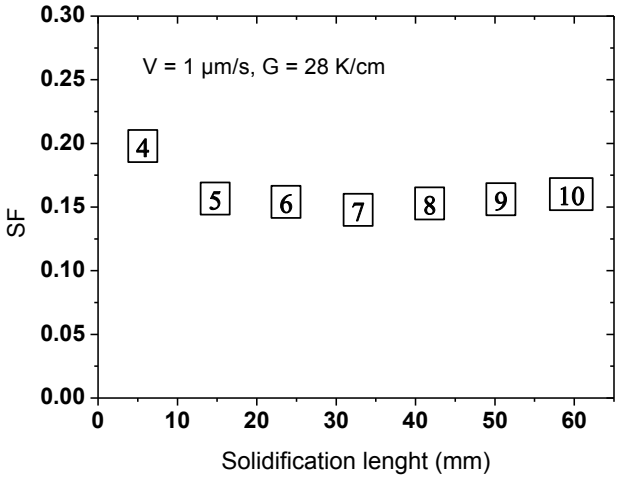
V = 1 µm/s, G = 28 K/cm
SF
Solidification lenght (mm)

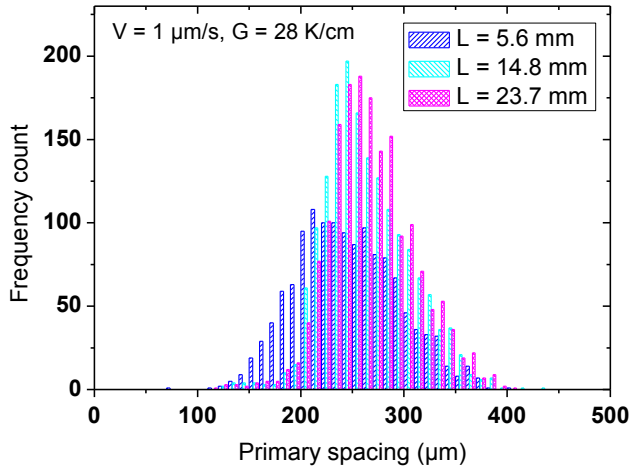
V = 1 µm/s, G = 28 K/cm
L = 5.6 mm
L = 14.8 mm
L = 23.7 mm
Frequency count
Primary spacing (µm)

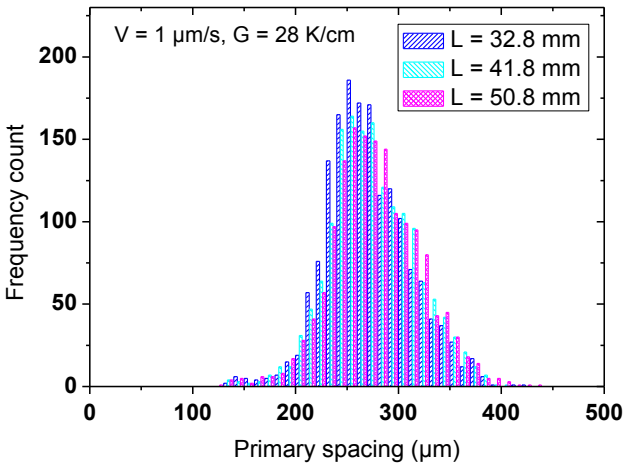
V = 1 µm/s, G = 28 K/cm
L = 32.8 mm
L = 41.8 mm
L = 50.8 mm
Frequency count
Primary spacing (µm)

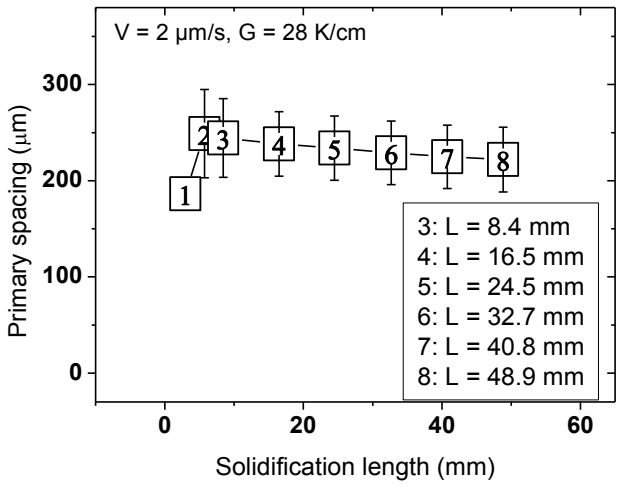
V = 2 µm/s, G = 28 K/cm
Primary spacing (µm)
Solidification length (mm)
3: L = 8.4 mm
4: L = 16.5 mm
5: L = 24.5 mm
6: L = 32.7 mm
7: L = 40.8 mm
8: L = 48.9 mm

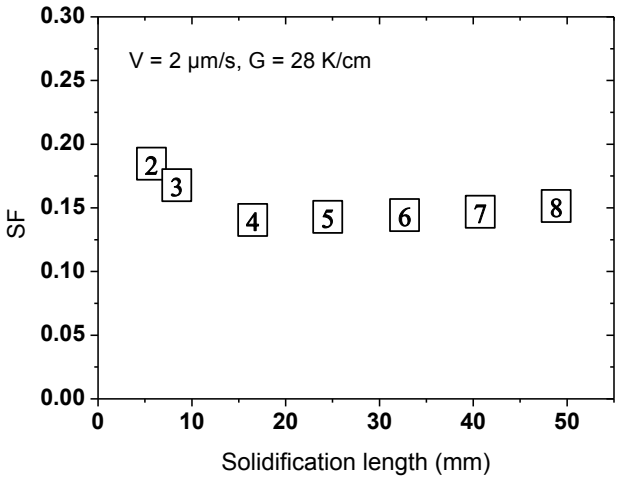
V = 2 µm/s, G = 28 K/cm
SF
Solidification length (mm)

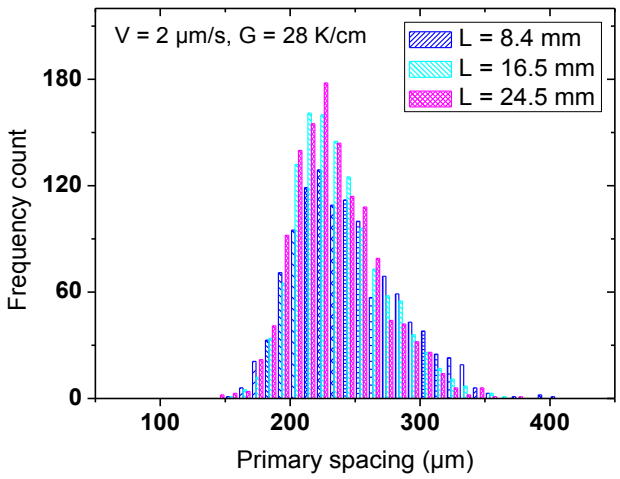
V = 2 μm/s, G = 28 K/cm
L = 8.4 mm
L = 16.5 mm
L = 24.5 mm
Frequency count
Primary spacing (μm)

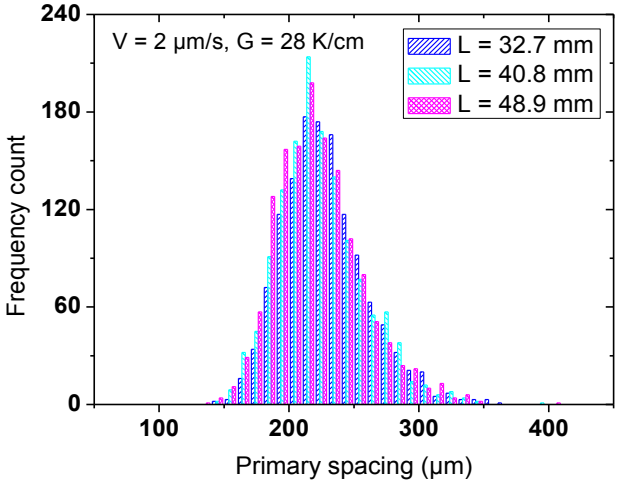
V = 2 μm/s, G = 28 K/cm
L = 32.7 mm
L = 40.8 mm
L = 48.9 mm
Frequency count
Primary spacing (μm)

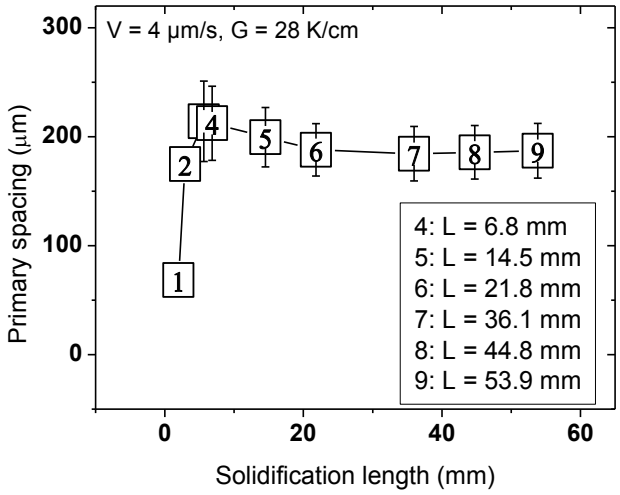
V = 4 μm/s, G = 28 K/cm
4: L = 6.8 mm
5: L = 14.5 mm
6: L = 21.8 mm
7: L = 36.1 mm
8: L = 44.8 mm
9: L = 53.9 mm
Primary spacing (μm)
Solidification length (mm)

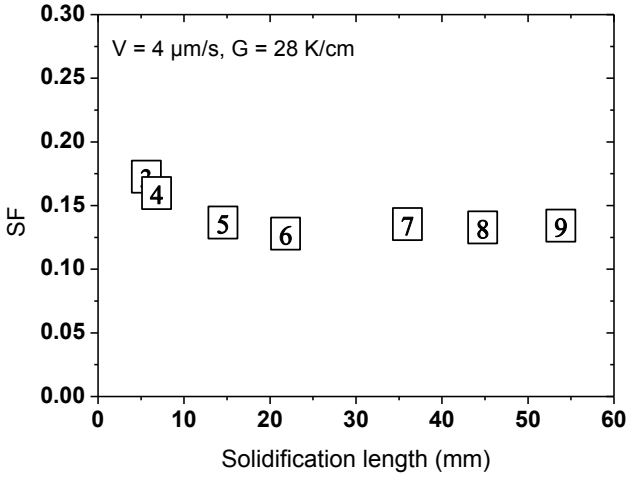
V = 4 μm/s, G = 28 K/cm
SF
Solidification length (mm)

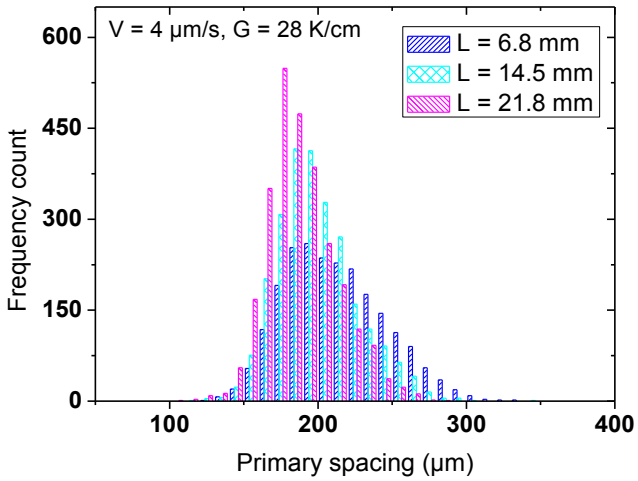
V = 4 μm/s, G = 28 K/cm
L = 6.8 mm
L = 14.5 mm
L = 21.8 mm
Frequency count
Primary spacing (μm)

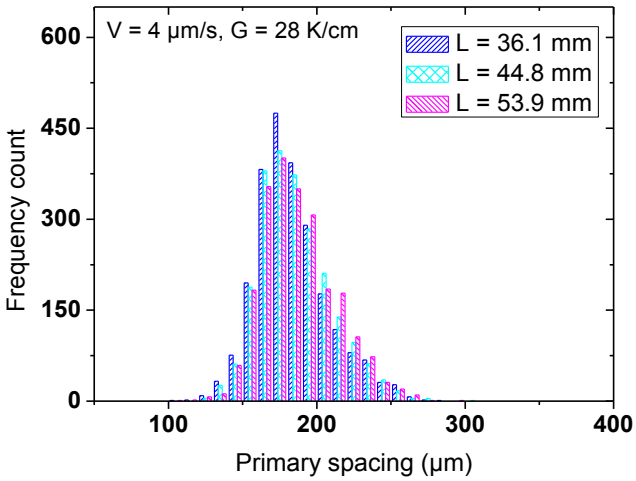
V = 4 μm/s, G = 28 K/cm
L = 36.1 mm
L = 44.8 mm
L = 53.9 mm
Frequency count
Primary spacing (μm)

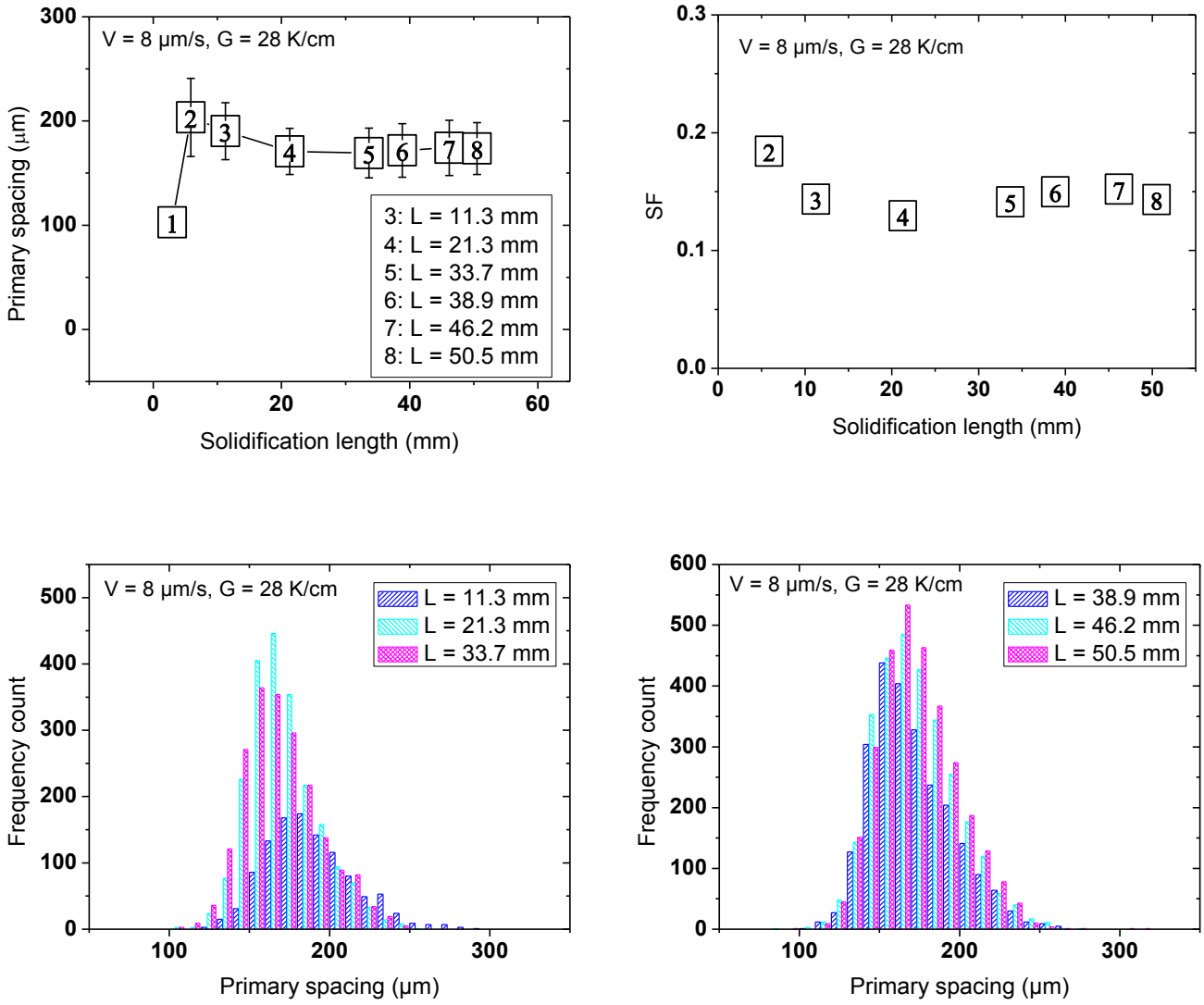

Figure 3.4. Primary spacing evolution during growth (as a function of solidification length) for different pulling rates (G=28 K/cm) and corresponding evolution of the primary spacing distribution and selection factor SF.

Table 3.1 is the summary of the structure type and of the adjustment mechanisms for all the constant pulling velocity experiments. The different items referred in the table are now described:

Table 3.1. Microstructure characteristics extracted from the observation of the movies corresponding to experiments at constant pulling rates.

Pulling rate(µm/s)	G (K/cm)	Microstructure	Interface shape	Tip splitting	Elimination by overgrowth	Sliding	
						radial	translation
0.5	28	Cell	Convex	x		x	
0.75	28	Cell	Convex	x	x	x	
1	28	Cell	Convex	x	x	x	
2	28	Cell	Flat	x(very few number)	x		x
4	28	Cell, Dendrite	Concave		x	x	x
6	28	Dendrite	Concave		x		x
8	28	Dendrite	Concave		x		x
12	28	Dendrite	Concave		x		x
16	28	Dendrite	Concave		x		x
0.25	12	Multiplet	Convex	x		x	
0.35	12	Multiplet +Cell	Convex	x		x	
0.5	12	Cell+Dendrite	Convex	x		x	
1	12	Cell+Dendrite	Convex	x			x
2	12	Dendrite	Convex		x		x
4	12	Dendrite	Flat		x		x
8	12	Dendrite	Concave				x
30	12	Dendrite	Concave				x

- Microstructure type: for G = 28µm/s, no secondary arm is developed during the growth and the tip shape is not possible to extract (classical criterions to discriminate dendrites from cells) so that, the difference between deep cells and dendrites from direct observation is hard to access. An indirect way to discriminate cells from dendrites is based on the difference of growth direction between those two structures. On a concave interface, Weiss et al. [145] have pointed out a radial sliding of cells towards the center whereas in the same macroscopic configuration, dendrites which are locked on a <*100*> direction of growth, do not present this radial sliding. The determination of microstructure type is easier for G = 12 K/cm as secondary branches are clearly observed.
- Interface shape : steady-state shape determined by side view observation
- Tip splitting and elimination by overgrowth : tip splitting is classically considered to occur at the upper limit of stable spacing for cell whereas this limit is associated to growth of tertiary arms for dendrites[50]. In our case, a very few experiments present tip splitting. They are characterized by low pulling rate and a growth with a convex interface shape. For those experiments, tip-splitting

really leads to 2 stable structures whereas in other experiments, when tip-splitting occurs, one of the two resulting tips quickly overgrowth the other one so that the initial cell size is recovered. Growth of tertiary arms has never been observed in the experiments considered here as secondary arms are not largely developed. The elimination by overgrowth of the surrounding members is common in our experiments and corresponds to the lower limit of stable spacings. Elimination of cellular/dendritic structures is also massive at sub-boundaries and, for convex interface, on the border. This will be detailed later.

- Gliding: gliding of structures is observed for all experiments. It may be radial, meaning that cells glide towards the center for a concave interface or towards the border for a convex interface. Translation means that groups of cells or dendrites are all sliding in the same direction. These points will be detailed in the following parts.

As previously mentioned, primary spacing increases continuously at low pulling rates whereas it presents an overshot for higher pulling rates. The transition between these 2 behaviors is roughly at V = 2µm/s, for which the interface is flat. So we will first detail the experiment at V_p = 2µm/s. From the observation of the video, no radial cell motion is found, is agreement with a flat interface. Instead, translation of groups of cells towards a sub-boundary is observed: Figure 3.5. New cells are then constantly generated at the crucible wall, and massively eliminated at the sub - boundary. Meanwhile, elimination of cells overgrown by neighbor cells is observed. Tip splitting is rare so that its effect on the spacing selection is negligible. The primary spacing presents a smooth decrease as a function of time after the initial growth. Classical mechanisms of spacing adjustment are based on elimination by overgrowth and tip-splitting but in that case, spacing adjusts through a balance between the generation of new cells at the border and elimination, especially at sub-boundary The slight decrease of the average primary spacing indicates that the number of cells created at the border is larger than those eliminated. The previously analyzed experiment (V = 2 µm/s) corresponds to a flat interface. Below this pulling rate, the interface is convex and the primary spacing grows monotonously before stabilizing. On the other side, for higher pulling rates, the interface is concave and presents an overshoot. We will start with the analyses of low pulling rate, with the support of the experiment at 0.5 µm/s. For V_p = 0.5µm/s, cells glide radially towards the border where they are eliminated. One detailed example is given in Figure 3.6. A zone marked with yellow dotted lines is enlarged for studying. Cells marked in yellow are followed with time to evidence their motion. Compared to the previous case at V=2 µm/s, cells are not formed on the border of the crucible as they glide from the central part. For this case, the generation of new cells proceeds by tip-splitting (noted TS on Figure 3.6); tip-splitting is for this experiment the unique source of generation of new cells. The convexity of the interface leads to the gliding of cells associated to their extension and once the cell reaches the limit of stable spacing, it splits as earlier

described by Bottin-Rousseau et al. [151]. The spacing distribution for V = 0.5 µm/s in Figure 3.4 presents a selection factor clearly higher than for other pulling velocities (SF (V = 0.5 µm/s) ~ 0.2 instead of below 0.15 for V ≥ 1 µm/s) pointing out its larger relative extension. A detailed analysis of the spacing distribution along the interface still has to be performed to analyses the two peaks, quite close in values, observed in the distribution.

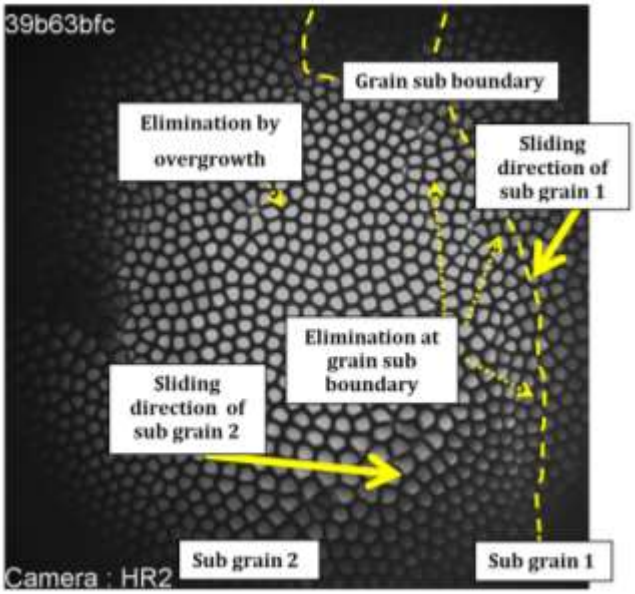

Figure 3.5. V = 2 µm/s, G = 28 K/cm t = 8h. The cell sliding direction of two major sub grains are indicated. The two kinds of cell elimination are also indicated.

For pulling rates larger than 2 µm/s, the interface turns to concave. The cell gliding becomes a mix of lateral motion towards the sub-boundaries and a radial motion towards the center due to concavity as shown in Figure 3.7. For these pulling rates, the mechanism of spacing adjustment is close to the one described at V = 2 µm/s. New cells are generated at the border; elimination is performed at sub-boundaries or also by classical overgrowth. No tip splitting is observed. Therefore, the selection proceeds by the competition between generation and elimination, similarly to the V = 2 µm/s one. A difference lies in the overgrowth of the average primary spacing observed in the earlier stage of spacing evolution. This peak means a larger elimination rate than generation rate while the two phenomena are compensating each other when primary spacing stabilizes.

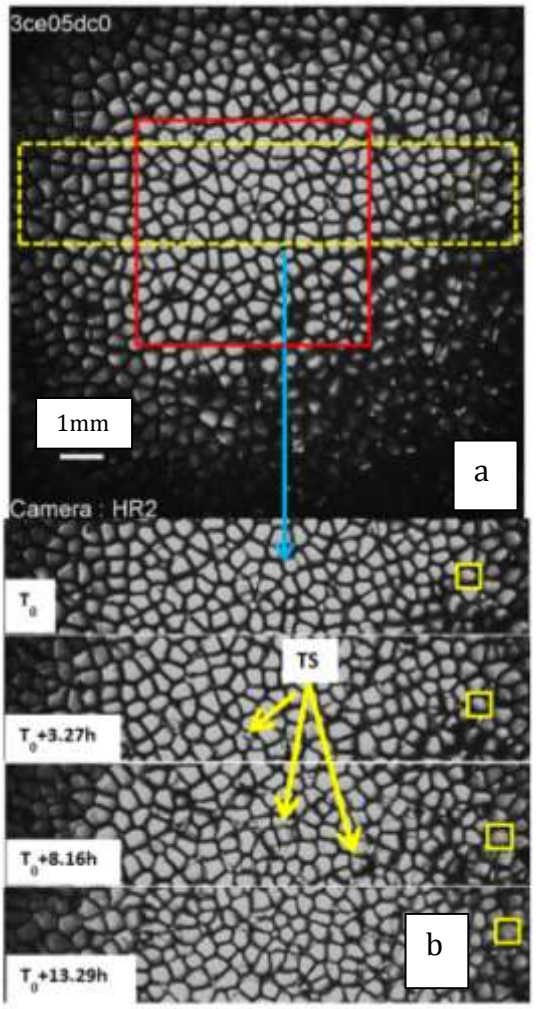

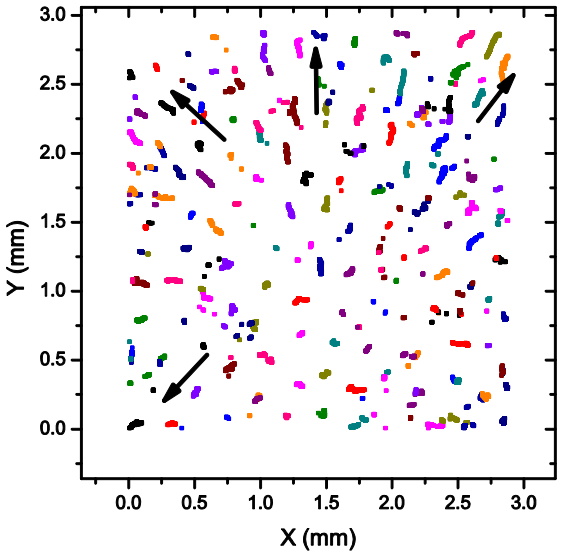

c

Figure 3.6. (V = 0.5 µm/s, G = 28 K/cm). a) Top view image of the whole interface at t = 8h. b) Snapshots at different times of the zone squared in yellow on a). "TS" refers to tip splitting events. c) Illustration of the radial cell gliding. Each color point corresponds to one cell followed during 3.9h. Area marked in red in a).

The evolution of the patterns ordering has been studied by the Minimal Spanning Tree method (see chapter 2). Results for G=28 K/cm are given in Figure 3.8. For each pulling rate the complete diagrams as well as a zoom on the evolution area are given. The distribution of the number of nearest neighbors and its evolution with time, for the same pulling rates, is given in Figure 3.9.

A similar evolution is noted for rates ranging from 1 to 4 µm/s. For these pulling rates, the disorder is initially decreasing (decrease of σ) before increasing again and stabilizing at an intermediate value; during evolution, the pattern turns to be closer to the hexagonal pattern line. The evolution of the distribution of the number of nearest neighbors confirms the evolution towards more hexagonal patterns as it clearly appears a decrease of numbers of 5 neighbors and 7 neighbors cells, quite numerous at the beginning of growth. For V = 8 µm/s, that corresponds to more dendritic pattern, order evolution is limited during growth due to an active dynamics of gliding, elimination and generation. For V = 0.5 µm/s, the disorder remains quite high during the whole experiment, with erratic variations of the MST points ; no particular evolution tendency

can be extracted from these measurements neither from the distributions of the number of nearest neighbors as 5-7 type defects remain numerous during the whole growth (Figure 3.9).

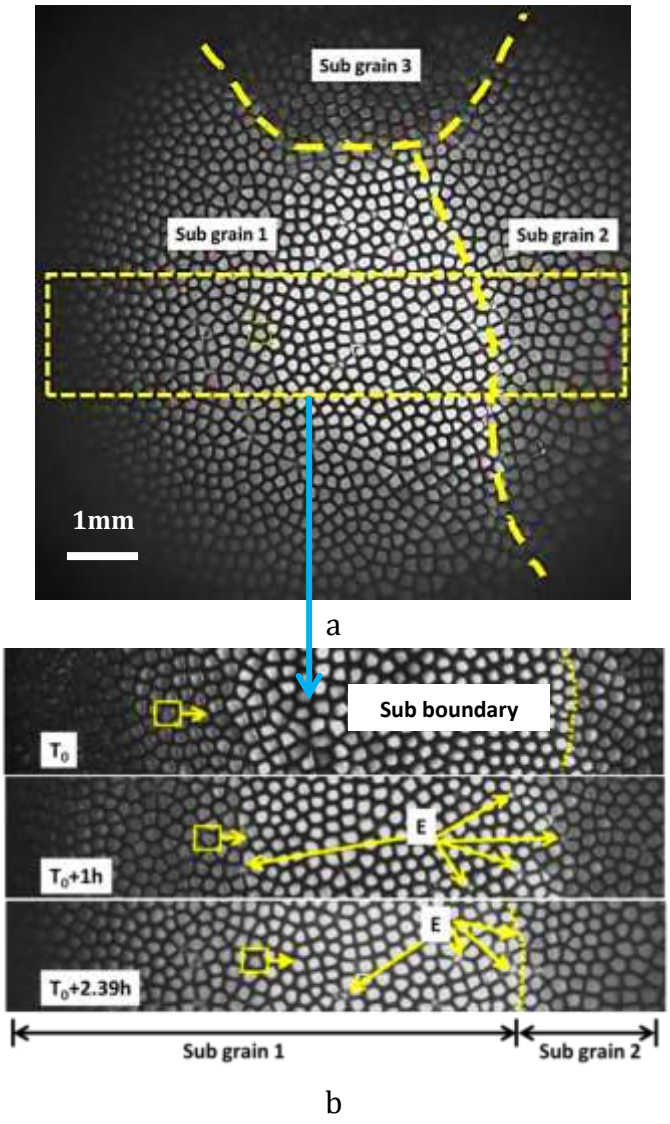

Figure 3.7. V = 4 µm/s, G = 28 K/cm. a) Top view image of the whole interface at t = 2.2h. b) Snapshots at different time of the area squared in yellow on a). "E" refers to elimination.

The very active dynamics associated to numerous, continuous and homogeneously distributed on the interface of tip-splittings may explain this lack of evolution; the pattern keeps being perturbed during the whole growth. For other pulling rates, generation and elimination, even if they are constantly active, are mainly located in specific areas (border of the crucible and sub-boundaries) so that a coherent dynamics of evolution may take place in areas that are collectively sliding.

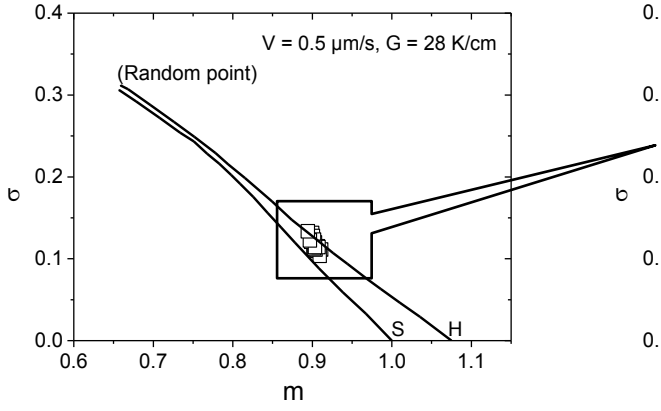
V = 0.5 μm/s, G = 28 K/cm
(Random point)
S
H
σ
m

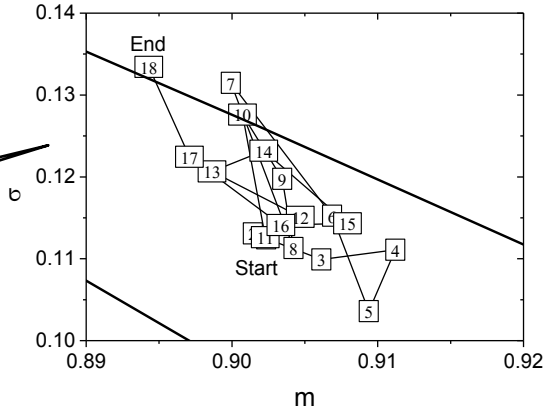
End
Start
σ
m

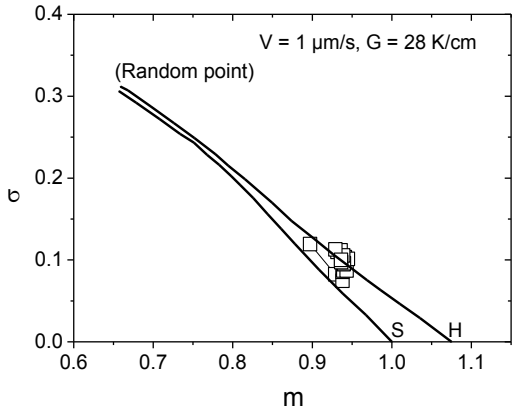
V = 1 μm/s, G = 28 K/cm
(Random point)
S
H
σ
m

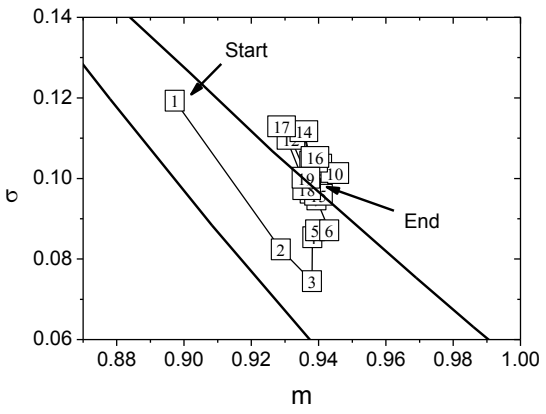
Start
End
σ
m

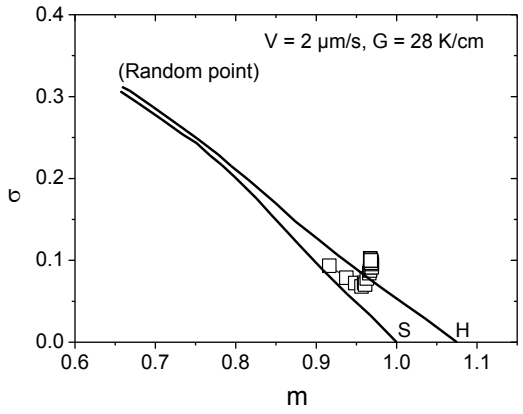
V = 2 μm/s, G = 28 K/cm
(Random point)
S
H
σ
m

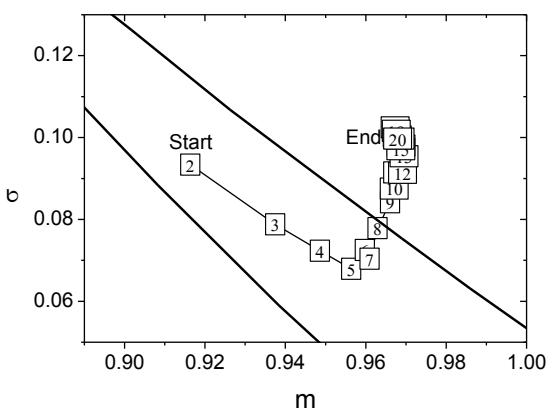
Start
End
σ
m

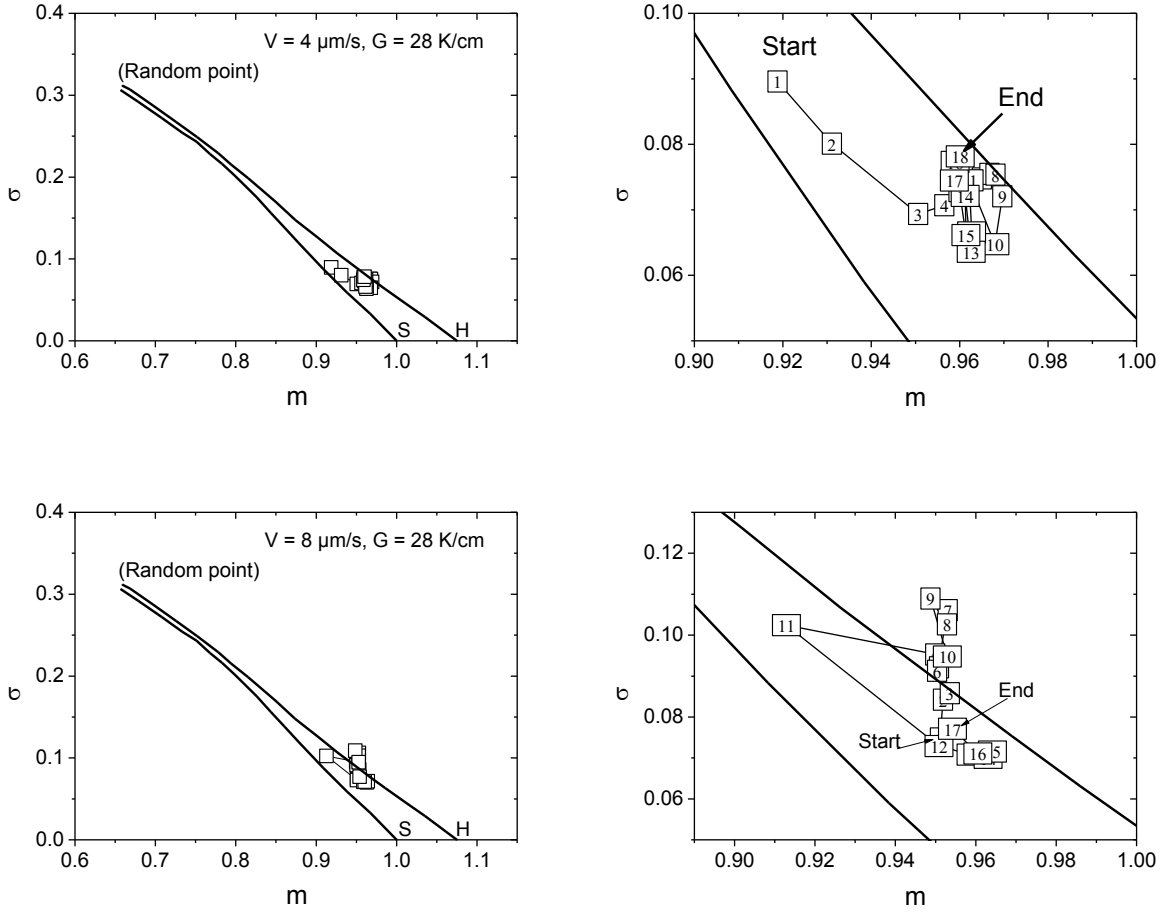

Figure 3.8. Study of the pattern order evolution during growth by the Minimal Spanning Tree analysis for different pulling rates at G=28 K/cm. Left side: global view; right side: zoom on the evolution area. The corresponding solidification lengths are listed in Table 3.2.

Table 3.2. Solidification lengths corresponding to the labels in the m-σ diagram in Figure 3.8.

Numbers	V=0.5 µm/s	V=1 µm/s	V=2 µm/s	V=4 µm/s	V=8 µm/s
1	5.1 mm	5.6 mm		5.6 mm	5.9 mm
2	6.9 mm	8.8 mm	5.7 mm	6.9 mm	11.3 mm
3	8.6 mm	11.8 mm	8.4 mm	9.4 mm	15.1 mm
4	10.1 mm	14.8 mm	11. mm	12.9 mm	17.9 mm
5	12.0 mm	17.8 mm	13.7 mm	14.5 mm	21.3 mm
6	13.7 mm	20.8 mm	16.5 mm	18.4 mm	27.2 mm
7	15.4 mm	23.7 mm	19.2 mm	19.1 mm	29.6 mm
8	17.1 mm	26.8 mm	21.8 mm	21.8 mm	33.6 mm
9	18.8 mm	29.8 mm	24.5 mm	22.8 mm	35.1 mm
10	20.5 mm	32.8 mm	27.2 mm	33.1 mm	37 mm
11	22.2 mm	35.8 mm	29.9 mm	36 mm	38.8 mm
12	24 mm	38.8 mm	32.7 mm	38.5 mm	40.8 mm
13	25.67893	41.8 mm	35.4 mm	41.1 mm	42.2 mm

14	27.4 mm	44.8 mm	38.0 mm	44.7 mm	45.7 mm
15	29.1 mm	47.8 mm	40.8 mm	47.9 mm	46.2 mm
16	30.8 mm	50.8 mm	43.5 mm	50.7 mm	48.6 mm
17	32.5 mm	53.8 mm	46.2 mm	53.8 mm	50.5 mm
18	34.2 mm	56.7 mm	48.9 mm	56.8 mm	
19	35.9 mm	59.6 mm	51.7 mm		
20	37.6 mm		54.2 mm		

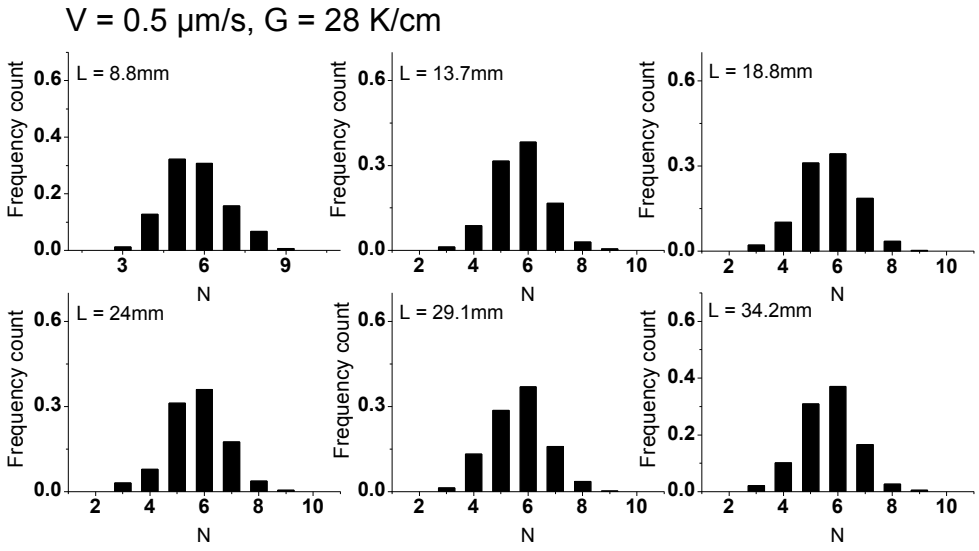

a

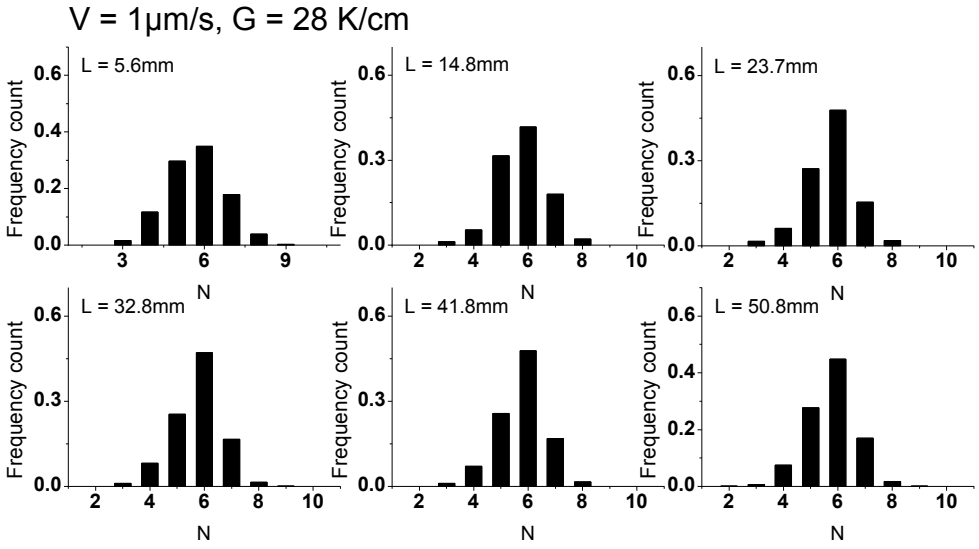

b

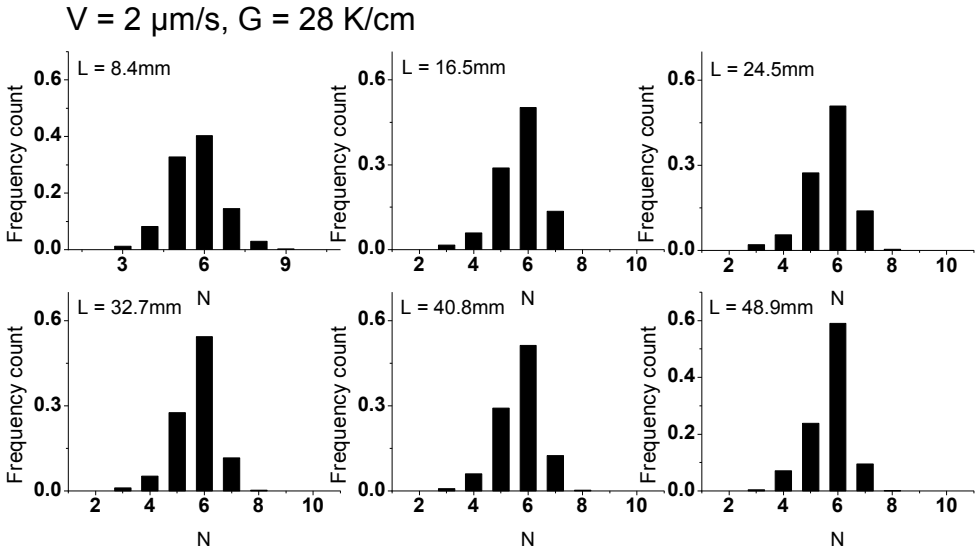
V = 2 μm/s, G = 28 K/cm
L = 8.4mm
L = 16.5mm
L = 24.5mm
L = 32.7mm
L = 40.8mm
L = 48.9mm
Frequency count
N

c

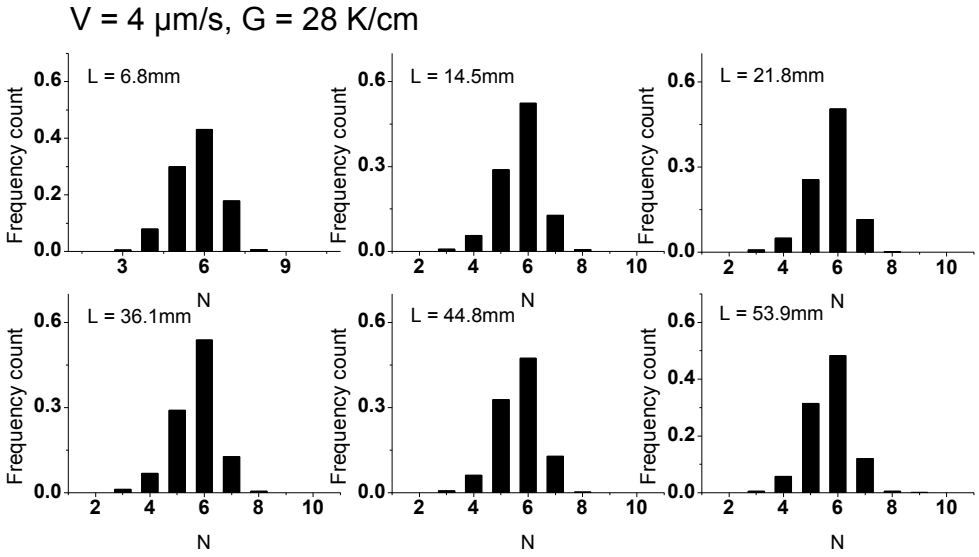
V = 4 μm/s, G = 28 K/cm
L = 6.8mm
L = 14.5mm
L = 21.8mm
L = 36.1mm
L = 44.8mm
L = 53.9mm
Frequency count
N

d

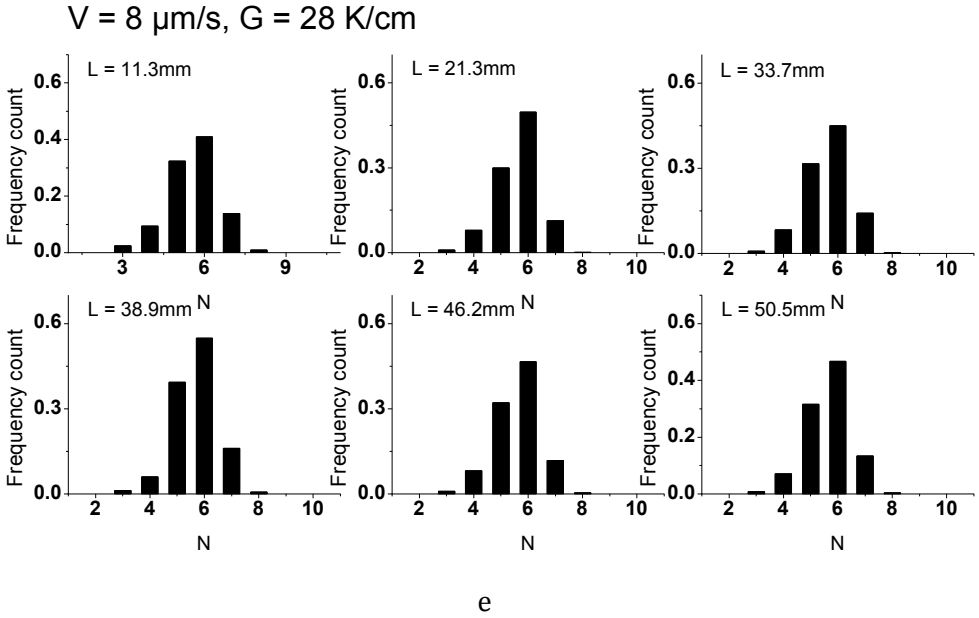

e

Figure 3.9. Evolution of the distribution of the number of nearest neighbors during growth, for each pulling velocity for G= 28K/cm.

3.5. Steady state growth

Theoretical models on cellular and dendritic spacings have been developed mainly for steady-state growth conditions. To compare with those models, the spacings for all pulling rates after long solidification times are studied. The interface morphology from top view during steady state growth is shown in Figure 3.10 and Figure 3.11 for temperature gradients of 28K/cm and 12 K/cm respectively.

Table 3.3 summarizes the characterization of the microstructure and the results of primary spacing measurements after ~50- 60 mm of growth. For this length, primary spacing is roughly stable for all pulling rates. For G=12 K/cm and V=30 µm/s, the experiment was very hard to perform : it was not possible to adjust the focus during experiment due to the high pulling rate and the time required for telescience monitoring so that quite quickly, structures were out of focus. That is why we used the value after only 15 mm of growth. However, considering the evolution curves of primary spacing that we described in the previous section, for this length, spacing should be not far from stable.

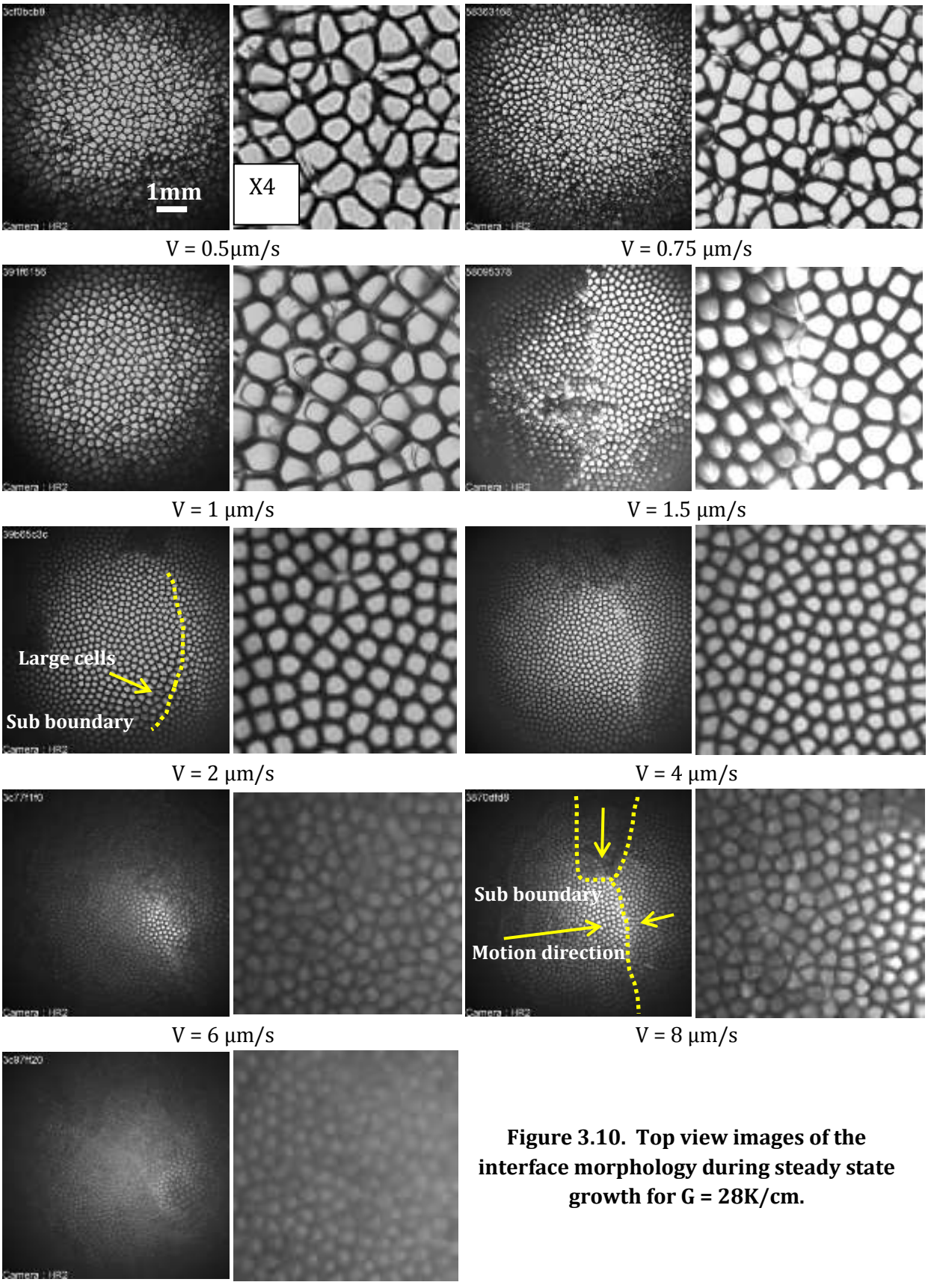

Figure 3.10. Top view images of the interface morphology during steady state growth for G = 28K/cm.

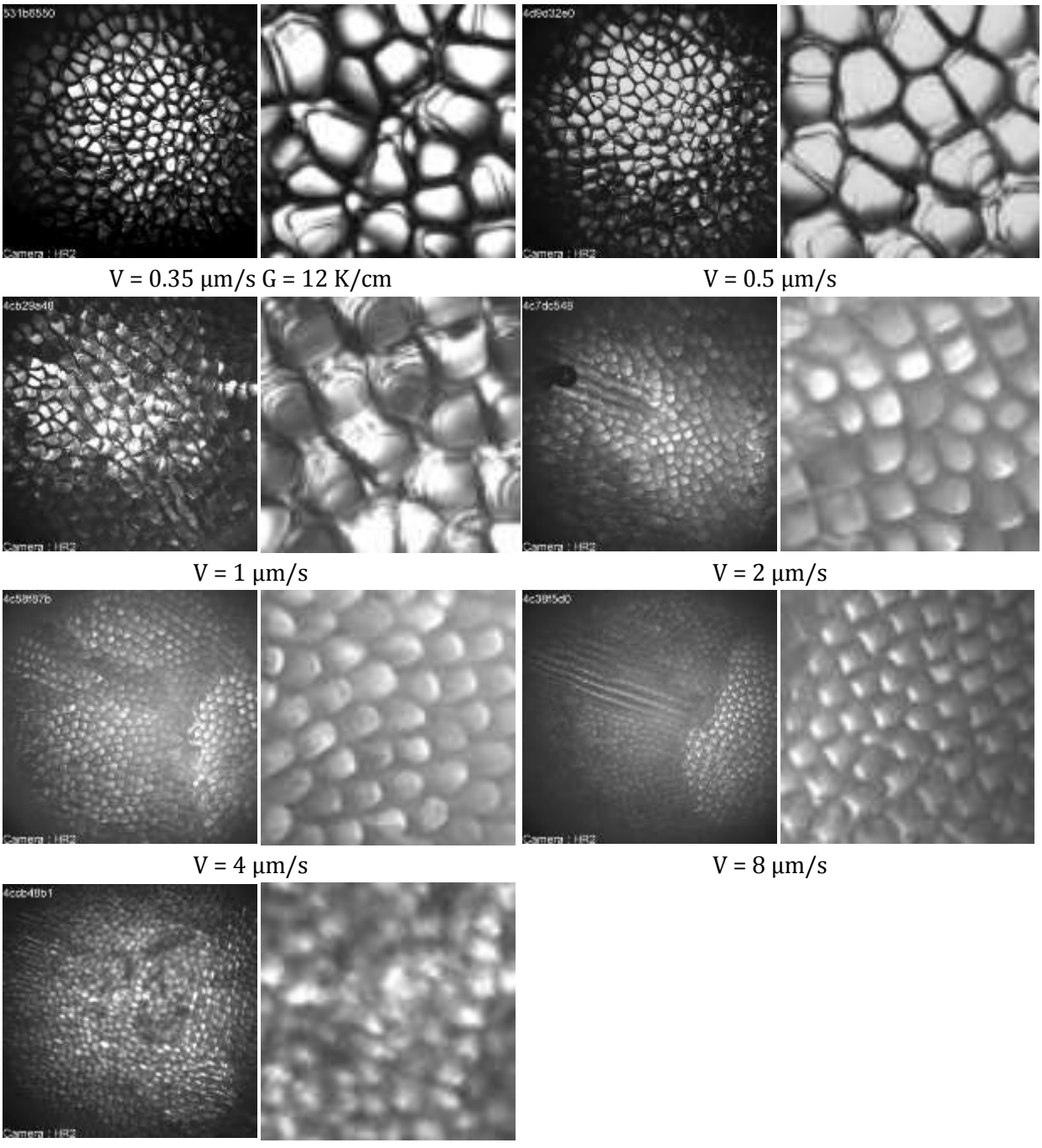

Figure 3.11. Top view images of the interface morphology during steady state growth for G = 12 K/cm.

Both cellular and dendritic structures are observed during steady state growth. The distinction between dendrites and cells is quite difficult from the direct observation of the top view images as side branches are not largely developed especially for G=28 K/cm. For G=12 K/cm, dendritic structures appear more clearly from V = 2 µm/s so that the transition velocity could be estimated between 1 and 2 µm/s.

Table 3.3. Summary of the primary spacing measurement results.

Solidification velocity µm/s	G K/cm	Interface morphologies	Primary spacing µm	Standard deviation µm	Solidification length mm
0.5	28	Cellular	267.5	59.7	39
0.75	28	Cellular	270.4	50.3	38.4
1	28	Cellular	279	43.8	59.6
1.5	28	Dendritic	252.5	31	59.4
2	28	Dendritic	219.6	33.7	59
4	28	Dendritic	184.7	24.1	56.8
6	28	Dendritic	170.5	23.9	48.4
8	28	Dendritic	173.1	24.9	50.5
12	28	Dendritic	160.1	22.8	43.7
0.25	12	Multiplet	499.2	97.5	59.6
0.35	12	Multiplet+Cellular	431.6	111.9	59.8
0.5	12	Cellular+Dendritic	442.5	99.2	59.2
1	12	Cellular+Dendritic	486.2	79.7	40.9
2	12	Dendritic	374.5	63	60.5
4	12	Dendritic	303.6	44	59.8
8	12	Dendritic	277.4	45	57.6
30	12	Dendritic	237.8	94	15.2

The variation of primary spacing with pulling rate for each temperature gradient is represented on Figure 3.12-a. Error bars correspond to the standard deviation extracted from the analysis of the spacing distribution. In most cases, these data come from the measurement method explained in chapter 2. But when the pattern is fully dendritic, separation of structures is too difficult and measurements are then performed using FFT method (see chapter 2). For the 2 gradients, a similar behavior is observed: the spacing increases for low pulling rates and then decreases with pulling rate.

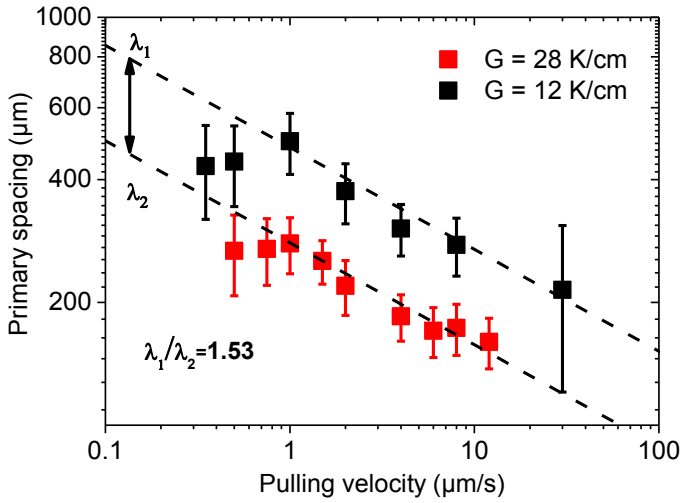

a

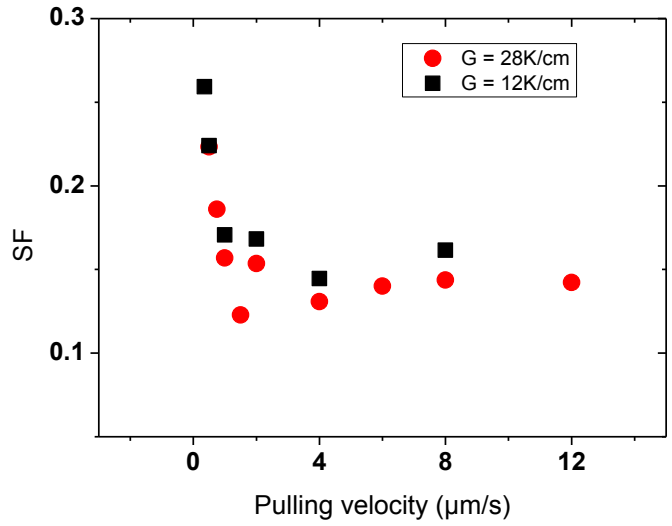

b

Figure 3.12. a) Evolution of primary spacing as a function of pulling rate and comparison with theoretical models. The dotted lines correspond to an exponent of -0.25 which correspond to the theoretical power law with an index of -0.25. b) The selection factor SF as a function of pulling velocity.

The histograms of the primary spacing and the selection factor as a function of pulling rate, measured at the end of solidification, are given respectively in Figure 3.13 and in Figure 3.12-b. The corresponding points of MST are given on Figure 3.14. The analyses are focused on G = 28 K/cm since the presence of multiple sub-grains associated to many different tilting of dendrites in case of G = 12 K/cm complicates the analysis: the areas where the dendrites are parallel to the growth axis are too small to support the MST measurement (more than 200 cells are needed to give a valid result for the MST measurement, see chapter 2).

The distribution measurement of Figure 3.13 confirms the fact that there is no unique selection of primary spacing. The width of the distribution is different and can be divided in two groups. The distributions for low pulling rates (Figure 3.13-a) are broad and present secondary peaks that could be analyzed as a superposition of distributions with different average values. The array disorder is larger in such cases as demonstrated on Figure 3.14. On the basis of the analyses previously conducted, these characteristics could result from the convexity of the interface that induces massive and continuous tip-splittings; actually, top-view images reveal that tip-splitting keeps occurring until the end of solidification. For larger pulling rates, the selection is sharper (Figure 3.13-b) and it becomes more and more sharp when the pulling rate increases, thus when the microstructure becomes more dendritic.

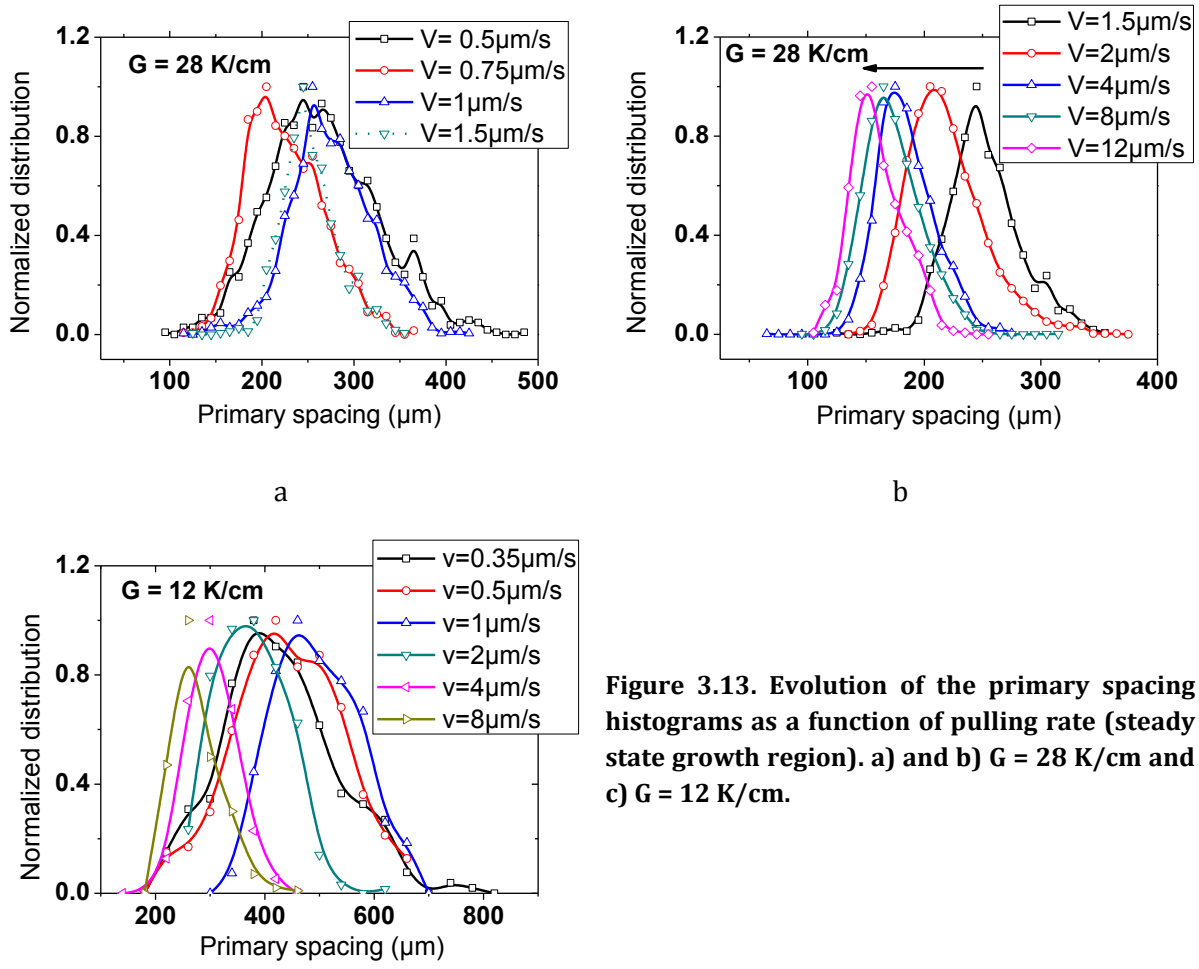

Figure 3.13. Evolution of the primary spacing histograms as a function of pulling rate (steady state growth region). a) and b) G = 28 K/cm and c) G = 12 K/cm.

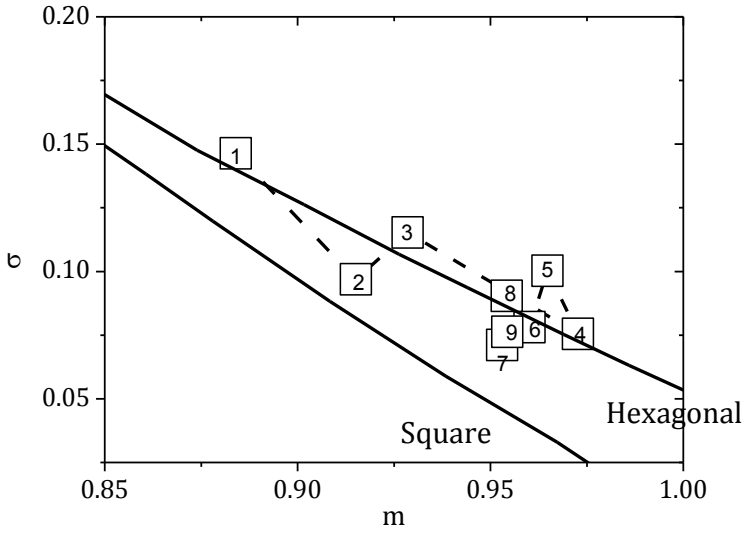

Figure 3.14. Evolution of MST as a function of pulling rate (steady-state growth region) for G = 28K/cm. Numbers 1 to 9 respectively correspond to pulling rates 0.5 µm/s, 0.75 µm/s, 1 µm/s, 1.5 µm/s, 2 µm/s, 4 µm/s, 6 µm/s, 8 µm/s and 12 µm/s.

Classical models [20][162][22] lead to a variation of the dendrite spacing with growth control parameters C, G and V as $\lambda = A \cdot C^{0.25} G^{-0.5} V^{-0.25}$,with A a constant depending on the alloy physical parameters. Our results are then compared with those theoretical models. The two dotted lines in Figure 3.12 correspond to a slope of -0.25 so that the dependence of primary spacing on the pulling rate for the decreasing part (V > 1µm/s) is well fitted by those models. Moreover, following those models, a variation of temperature gradient from 28K/cm to 12K/cm gives an increase of primary spacing of a factor $\frac{\lambda_{12\,K/cm}}{\lambda_{28\,K/cm}} = \sqrt{\frac{28}{12}} = 1.53$, that corresponds to the difference observed in our experiments. For the largest pulling rates, one may observe a small divergence of the experimental spacings that tend to be larger compared to the line of slope -0.25. For such pulling rates, latent heat generation is very important and may lead to a noticeable decrease of the thermal gradient at the interface, which could explain the deviation.

Measurements of primary spacing on ground in thin samples have been performed by Trivedi and co-workers using the same growth conditions that we applied in space so that the values can be compared to test the dimensionality effect. Two different thicknesses have been used: 100 µm and 200 µm. Their results of primary spacing measurements as a function of pulling velocity are superposed to ours on Figure 3.15 for G=28 K/cm. First of all, it appears that the measurements are largely different for the two thicknesses: spacings for the 100 µm thickness samples are far larger than for the 100 µm one. We may analyze this difference considering that 100 µm is smaller than the spacing observed in space so that the growth is laterally constrained in the transverse direction and a compensation leading to an overgrowth in the other direction occurs,

especially in the dendritic regime. For the 200 µm thickness, two different branches appear, respectively corresponding to cellular (small spacings) and dendritic structures (large spacings). A quite good superposition of space results with the dendritic branch of 200 µm sample is observed for large velocities. It clearly appears from these preliminary results that the spacing selection is strongly dependent on the dimensionality of pattern. A deep work remains to be conducted to analyze these differences, with the support of numerical simulation. The question of the modification of the steady-state branch structure by dimensionality has been already mentioned for example by S. Gurevitch et al. [1] and a dedicated study should be applied to analyze all our results.

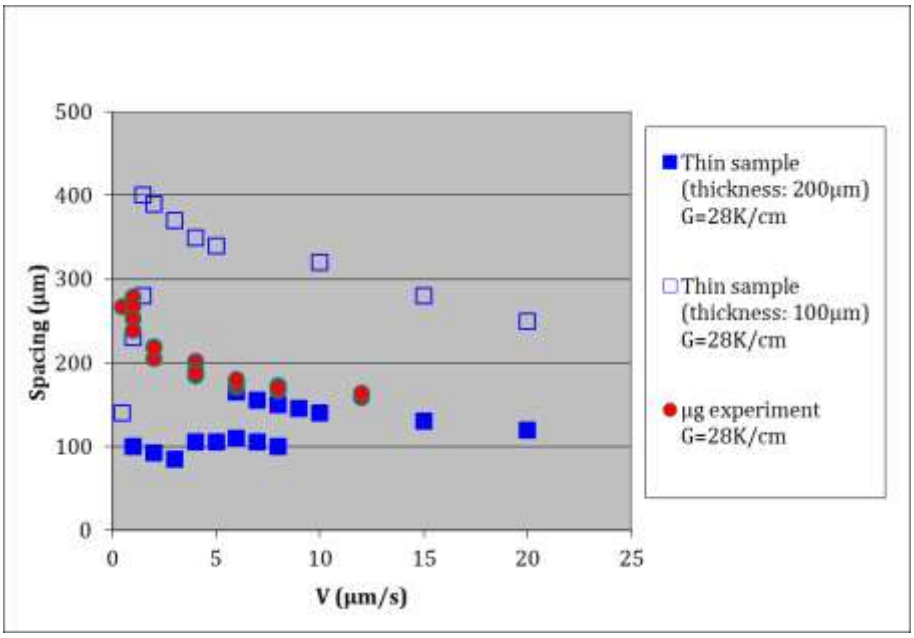

Figure 3.15. Comparison of primary spacing evolution with pulling rate for different crucible geometries (Thin samples measurements provided by R. Trivedi and co-works).

3.6. Conclusion

Experiments of long solidifications for a large range of pulling rates and two different thermal gradients have been analyzed to extract quantitative characteristics of the growth pattern. Primary spacing measurements as a function of time and growth parameters have been presented. The mechanisms of spacing adjustment have been described. It appears that in our bulk samples, collective motion of the pattern is always present, even in case of a macroscopically flat interface. This collective motion confirms to be a critical factor of spacing adjustment, giving the source of the new cells upstream the gliding direction (generally at the border of the interface for concave and flat interfaces) and elimination occurs downstream, on defects such as sub-boundaries or at the border (for convex interface). In our experiments, it appears that tip-splitting is not a

main mechanism for creation of new cells, except for convex interfaces where the radial motion of the cells leads to a stretching of their size and to their final splitting. For these convex interfaces, the distribution of spacing - even in steady state - is wider (weak selection) and the array disorder is larger than for concave or flat interface that do not present tip-splitting.

Steady-state measurements lead to benchmark data of spacing in extended patterns. Variation of spacing for flat and concave interfaces as a function of pulling rate and thermal gradient are consistent with classical growth models that predict power-law variations. Once more, the case of convex interface is slightly different and the average experimental spacings are smaller than the theoretical ones. The difference may come from the massive tip-splittings observed but we may also consider an effect of the microstructure nature (shallow cells) to explain the difference as those models have been designed for deep structures.

Finally the steady-state measurements have been compared to similar experiments (same growth parameters) performed on ground on thin samples. A striking effect of dimensionality is pointed out: the thickness of the bulk samples result in a large variation of primary spacing for the same growth condition. Moreover, two distinct branches of spacing values appear in thin sample for cellular and dendritic regimes whereas a continuous variation is observed in 3D samples.

The analysis of these data needs to be further deepened and the support of numerical simulation will be of great help. In particular, a study as a function of sample dimensionality of the stable branches of cells and dendrites would be interesting to clarify the comparison with ground results and to identify the role of selection mechanisms in the final primary spacing of the pattern.

Chapter 4. Secondary instabilities: cell array oscillation and multiplet

4.1. Introduction

Secondary instabilities can be considered as instabilities of the cellular steady solution [62]. Among the different kinds of secondary instabilities affecting the cellular pattern, the parity – broken and the oscillating – breathing modes have been already observed in thin samples [54,63]. These phenomena are here for the first time described in 3D – samples. The first part will be dedicated to the description of the oscillating patterns and the second one to patterns of multiplets formation and dynamics.

4.2. Oscillating patterns

In our studies, the oscillation of cell surface area A(t) is observed for the first time in extended 3D patterns. This kind of instability, often identified as a "vacillating-breathing" mode in theoretical and numerical studies [172], has been well characterized in solidification of eutectic systems in 2D on transparent analog [53][54][173][174]. The only experimental study on this oscillation mode in cellular patterns was done by Georgelin et al [54], in quasi 2D samples of transparent alloys. The features of this instability will be described and compared to the quasi – 2D situation so that dimensionality effects will be stressed.

4.2.1. Description of the oscillation mode

An example of the oscillation is illustrated in Figure 4.1. The Figure 4.1-a is a global view of the oscillating cellular array: the area in the center is enlarged and analyzed in Figure 4.1-b. The four images in Figure 4.1-b show the variation of the apparent cell surface as a function of time. It appears that these cell surfaces increase and decrease periodically. The apparent cell area results from the light guiding by cells body, position of groove is therefore define from the size of the bright area. In oscillating patterns, the spacing, which is defined as tip to tip distances, is not affected by the oscillation.

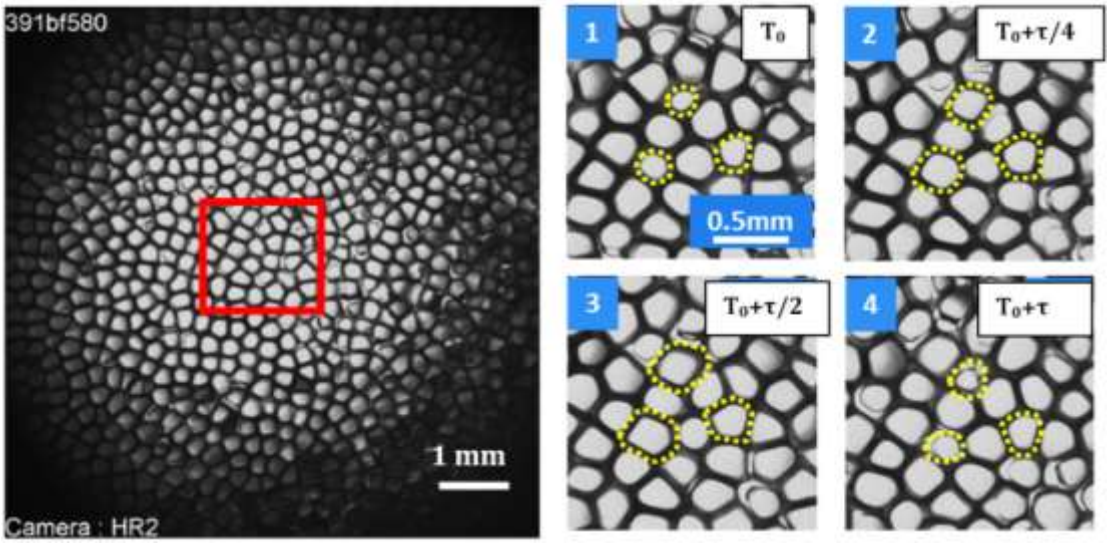

a b

Figure 4.1. Oscillating patterns (V = 1 µm/s, G = 28 K/cm). a), Global view at t = 13.9 h; b), enlarged area marked in a) at different times. b1), t=14.33 h. b2) t=14.56 h. b3), t=14.78 h. b4), t=15.13 h. The variation of cell surface is indicated with yellow dotted lines.

The oscillation mode was observed in a narrow range of pulling rates: from 0.5 to 1.5 µm/s for G = 28 K/cm and 0.5 µm/s for G = 12 K/cm. This range is close to the critical velocity. As summarized in Table 4.1, for some cases, the whole interface may be affected by oscillating but in other cases, oscillation affects only a part of the interface as illustrated in Figure 4.2, for two pulling rates, V = 0.75 and 1.5 µm/s (G = 28 K/cm). During the transient, (Figure 4.2-a and c), all cells oscillate. Some sub boundaries are indicated which separated the grain into two major parts with different crystalline orientations that may play an important role in the next step. Then with time, cells stop oscillating on the left (labeled “stable region”), while the oscillation carried on on the right (labeled “oscillating region”), the two regions being separated by a sub boundary.

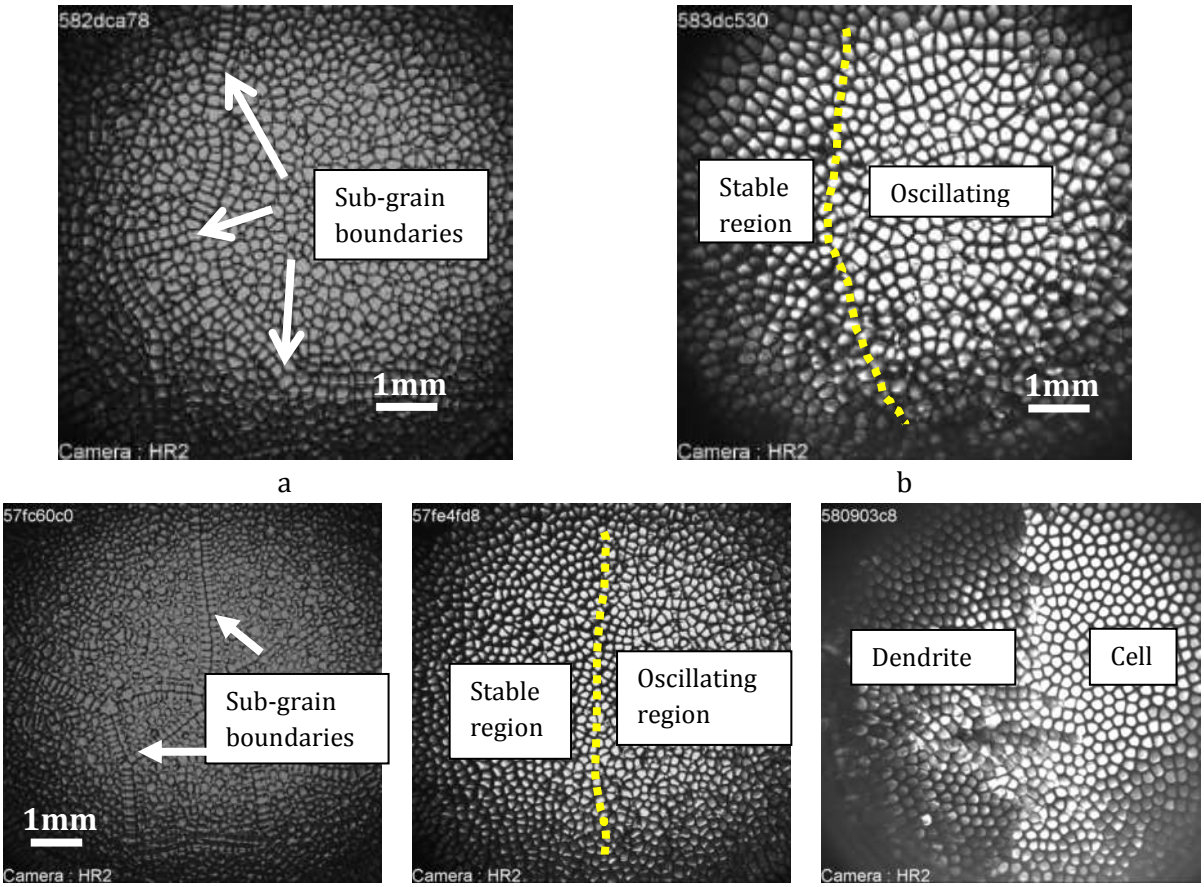

Figure 4.2. a) and b) are the initial (t = 2.3h) and final (t = 15h) stages of solidification with V = 0.75 µm/s and G = 28 K/cm. e), c), and d), correspond to the interface at t = 0.75h, 2.3h and 10.8h, with V = 1.5 µm/s and G = 28 K/cm.

Table 4.1. The zone of cellular array involved in oscillation.

Pulling rate (µm/s)	G (K/cm)	Involved range
0.5	28	Whole interface
0.75	28	Whole interface during the transient and half interface during steady-state
1	28	Whole interface
1.5	28	Half interface during the transient, and no oscillation during the steady-state
0.5	12	During transient, involved a few cells

4.2.2. Oscillation of the cell surface

In our experiments, oscillation is evidenced by the periodic variation of the apparent area of each cell. Therefore, a method was developed to measure the surface area variation of a large number of cells. All measurements of the apparent surface area A_i (t) of the cells seen from the top are done with Visilog® software, macro procedures have

been specifically developed for the systematic processing of the large number of images obtained during the microgravity experiments.

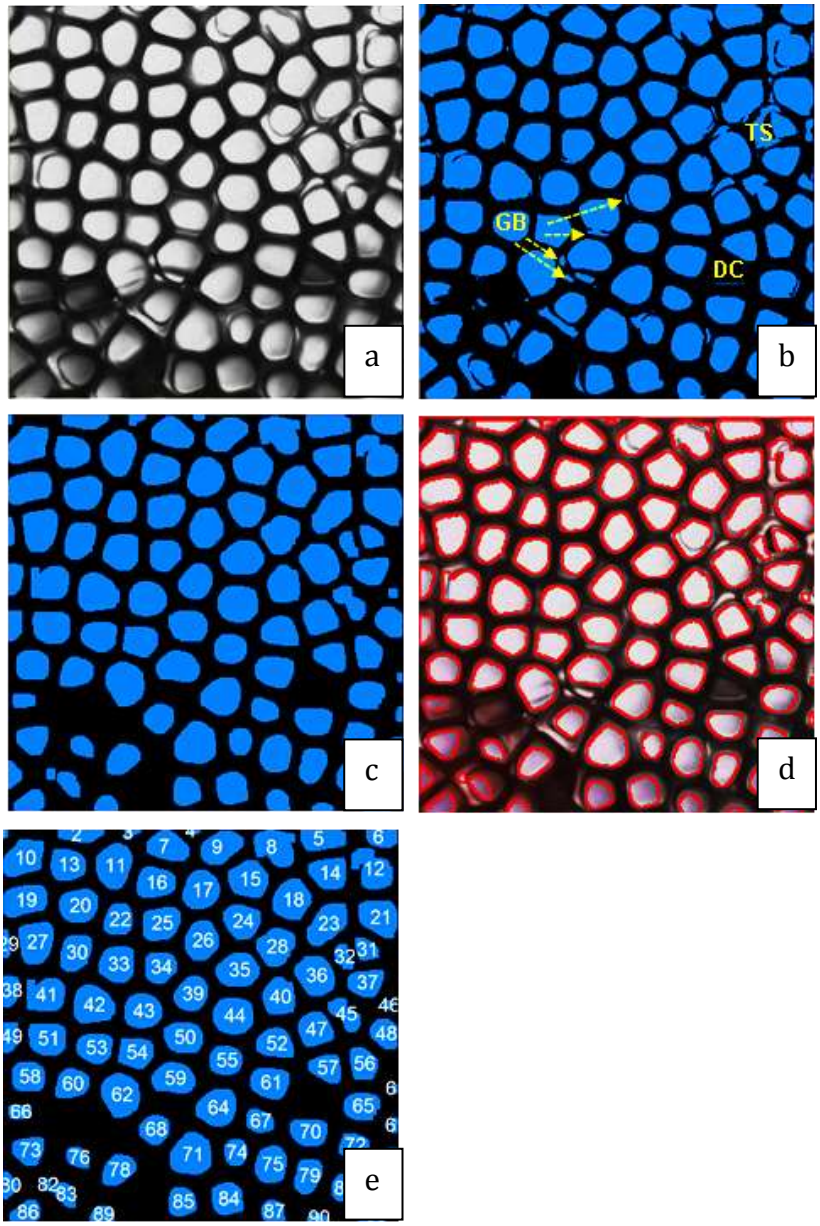

Figure 4.3. a) Initial raw image (3.2*3.2 mm^2): first image of the sequence of the oscillating array to be analyzed. b) Binary image. c) Binary image after processing with "opening function". d) Contours of apparent surface of cell caps on corrected binary image superposed to the initial raw image. e) Tagged binary image. (V = 1 µm/s, G = 28 K/cm)

Starting with the first raw image of a sequence (Figure 4.3-a), each initial grey-level image is transformed into a binary image by defining a threshold value which ensures that a large majority of cells are disconnected from their neighbors (Figure 4.3-b). At this step, a few cells having grey-level below threshold may disappear on the binary image (e.g. "DC"- Dark Cell- on Figure 4.3-b). Other defects also appear on this binary image,

mainly coming from: i) bright flat parts at groove bottoms (e.g. "GB" on Figure 4.3-b); ii) on-going tip-splitting (e.g. "TS" on Figure 4.3-b). To correct such defects, the "Opening function" of Visilog® is used to removes small objects or details attached to boundaries and also disconnect particles. The corrected binary image resulting from this procedure is shown in Figure 4.3-c. With this process, the number of defects becomes negligible: for instance, the previously observed "GB" defect on Figure 4.3-b has been cleaned on Figure 4.3-c and the "TS" defect has led to two different cells. The superposition of the contours of apparent cell surfaces after the processing to the initial image is given in Figure 4.3-d for comparison. Every single cell is then tagged (Figure 4.3-e): its position and its area A_i are measured. The same processing is then applied to the second image of the sequence, and so on. It is worth noticing that the key point is that we are able to keep the same tag number for each cell, all over the sequence of images, in spite of cell motion and tip splitting in array dynamics. The criterion to follow cells is to check each cell center position on image n+1, which has to be located in the cell area of image n. Otherwise, images with a smaller time delay should be considered. For the example presented above (pulling rate V = 1 µm/s), raw images are acquired at a frequency of 0.5 image/sec. Analyzing is sufficient for series of images sampling the dynamical phenomena at one image per minute to obtain meaningful unbiased measurements, and respect the tagging procedure. This process is implemented over the whole sequence, for each cell, to get surface area data as a function of time, $A_i(t)$ (extracted in pixel^2 and then converted into µm^2).

Using the automatic measurement method previously described, we measured and studied the $A_i(t)$ in a large zone (including about 60 cells, Figure 4.3). Several different behaviors are observed during oscillation and examples are shown in Figure 4.4

All data are normalized referring to the maximum and minimum sizes of appearing area of the considered cell.

$$A_{i\ normalize} = \frac{A_i(t) - A_{i,min}}{A_{i,max} - A_{i,min}}$$

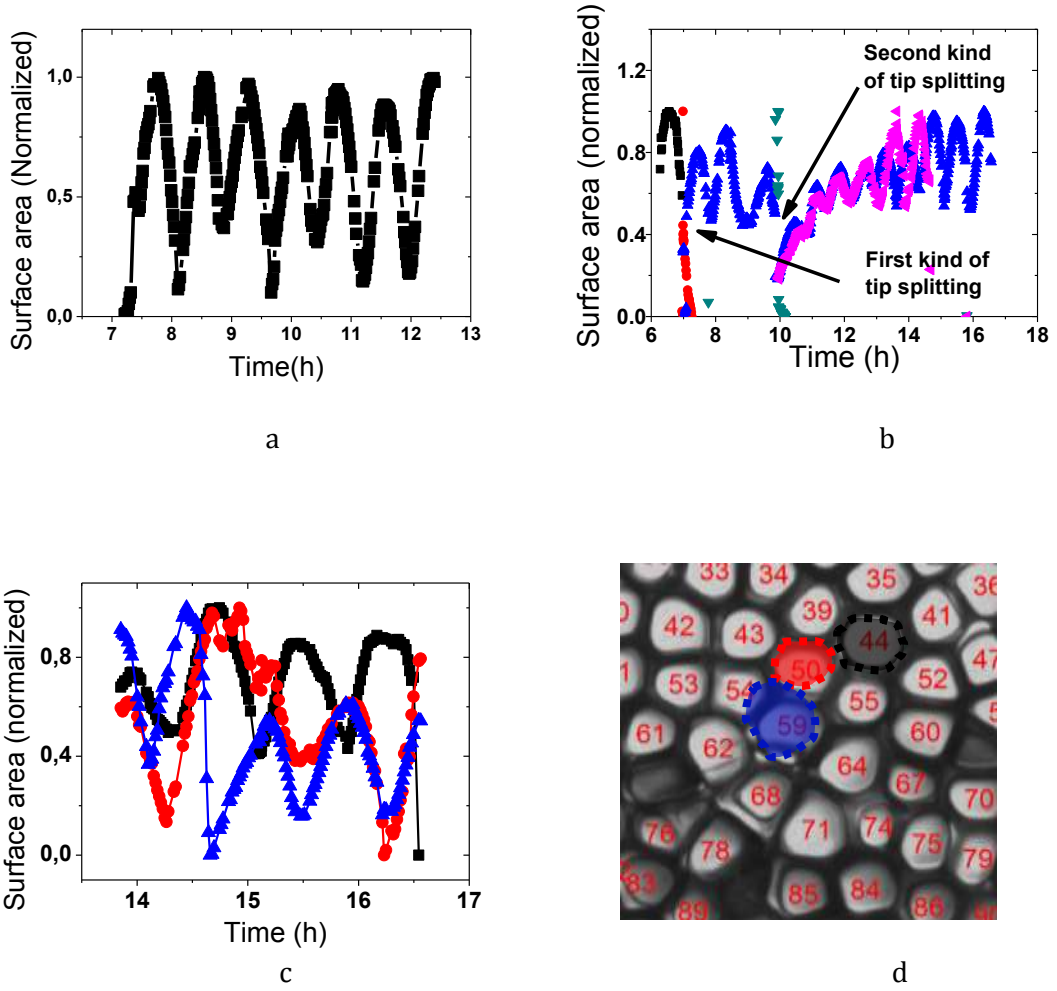

Figure 4.4. Different oscillation behaviors observed experimentally (V = 1 µm/s, G = 28 K/cm). a) Standard oscillation; b) Tip splitting during oscillation, the splitting time is indicated by arrows. The new born cells are in different colors. c) Phase shift during oscillation and d) relevant cells of the phase shift in c are labeled with similar colors.

a) Standard oscillation (Figure 4.4-a). We observe a periodic and regular oscillation of cell appearing area between its minimal and maximal values. The average area keeps constant, as well as the oscillation period and phase position. This is the standard oscillation mode, adopted by most of cells on long duration.

b) Oscillation with tip splitting. The two kinds of tip splittings observed in this work are shown in Figure 4.4-b. The first type occurred at about t = 7 h: the mother cell (black line) splitted in two (red and blue) tips; one of them dominates (the blue, in this case) and oversteps the other one, and the process of oscillation starts again. The second type of tip splitting happened at t = 10 h: after splitting, the two new cells survive and grow bigger, they oscillate with the same phase at the beginning of splitting until one of them shifts its phase (Figure 4.4-b).

c) Oscillation with phase shift. Phase shift may occur not associated to tip-splitting. On Figure 4.4-c, the blue and black cells oscillate with their own phases, while the red cell first oscillates in phase with the black cell and then shifts of phase to oscillate in phase with the blue one. During the process of phase shift, it is worth noticing that the cell structure has slightly changed because of the lateral movement of cells. Besides, no variation of first neighbor for red cell is observed.

4.2.3. Oscillation of the cell tip position

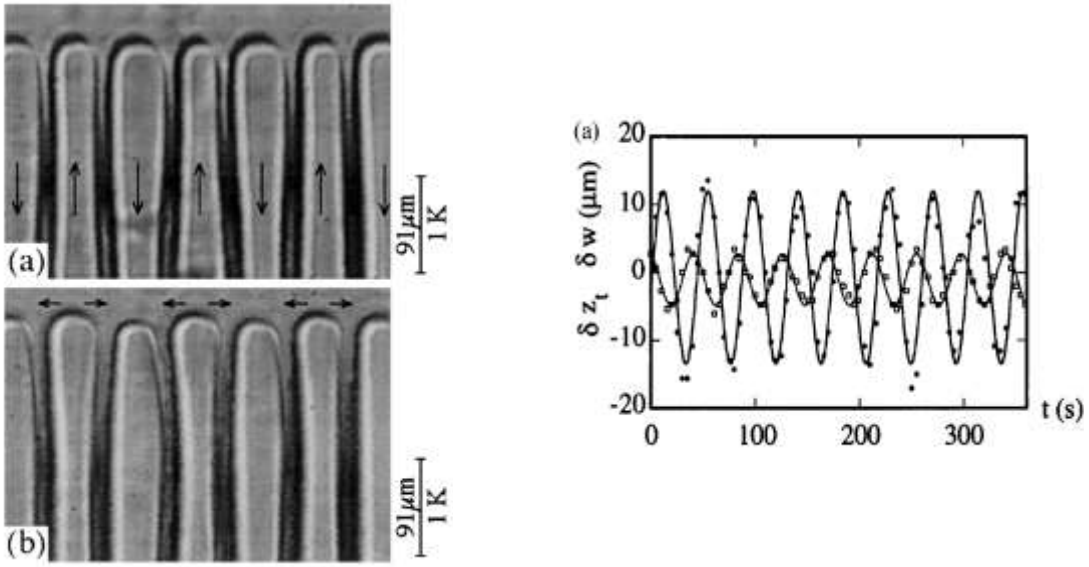

a b

Figure 4.5. Tip positions oscillate in a 2D sample with the same period of cell width oscillation [54]. **a), Cell cross the mean tip position: the thicker cells are moving down and the thinner ones are moving up. b), Cells reach external tip positions, the highest cells are thickening and the lowest cells are shrinking. Figure b, δZ_t and δw are the variation of tip position z and cell width w, respectively. Tip and width oscillation have the same period but a phase shift of 100°±10°.**

In 2D samples, the oscillation involves both the cell tip position and its width, as shown in Figure 4.5 [54]. This motivated us to evidence the variation of the tip position in our 3D samples. Since the resolution is not sufficiently high to determine the tip position from the side, the tip motion could only be measured from the interferometric images.

Tip position measurement from interferometry

The relative tip position between 2 cells could not be directly measured since all the cells in the interferometric images are isolated (Figure 4.6-a). So that the complete shape of the interface cannot be rebuilt.

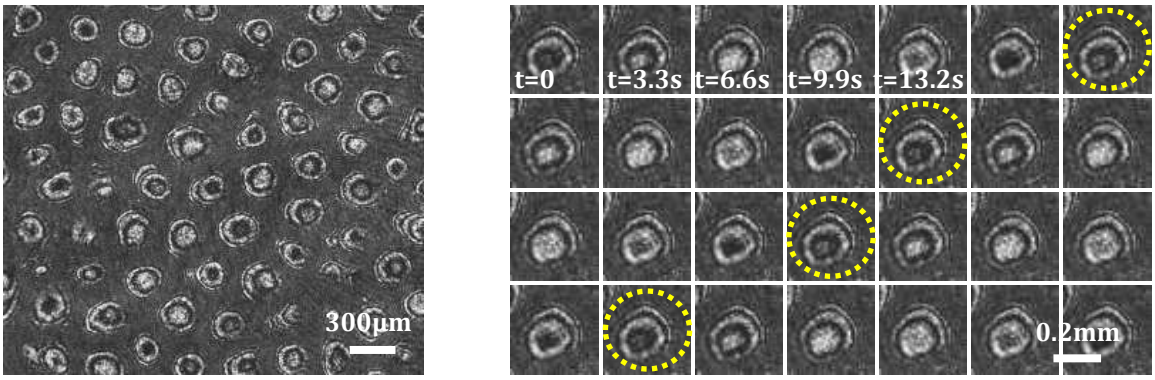

a b

Figure 4.6. a) Interferometric image obtained at v=1µm/s, G=28K/cm. The rings of white fringes represent each cell. b) Sequence of interferometric images for one cell. All images in the sequence are successive images with a time gap of 3.3s. Images start from left to right, from up to down. The images marked with yellow circles correspond to fringes in the same position.

Instead, we can measure the variation δv of the tip growth velocity v_{tip}, which is related to the tip position variation δz by:

$$\delta v = \delta z/dt \qquad 4.1$$

with $v_{tip} = v_p + \delta v$ and $z_{tip} = z_0 + \delta z$.

The tip growth velocity v_{tip} can be obtained as follows:

$$\lambda = \Delta t V_{tip} \Delta n_{sl} \qquad 4.2$$

where Δt is the time required to pass from one fringe to the following one, at the same location, Δn_{SL} (see equation 2.10).

Equation 4.2 relates the tip velocity to the fringe movement (Δt), in the interferometry sequence. In order to obtain more accurate measurements, Δt is deduced from the average time required for 5 fringes passing.

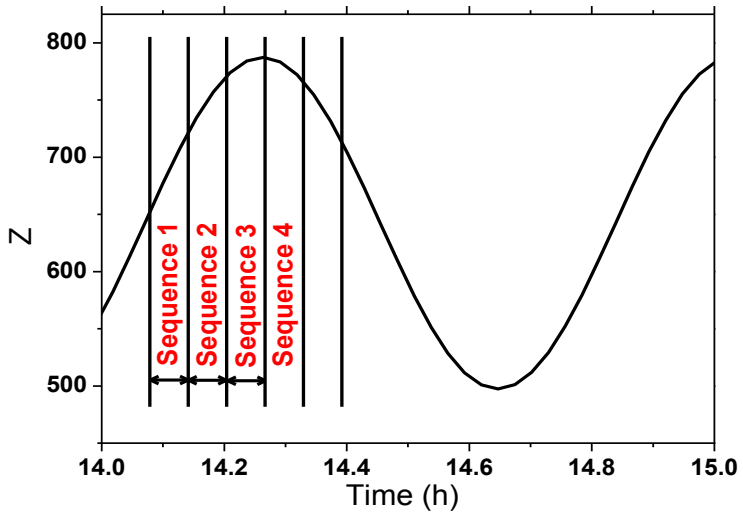

Figure 4.7. Selection of the image sequences from the measurement of the tip position oscillation.

The series of interferometric images roughly corresponding to one oscillation period are divided into several sequences (Figure 4.7) with no time slot between them. Each sequence contains 40 or 80 images so that the duration, which is about 260 s for a sequence with 80 images, is enough for 5 fringes to pass. The period is about 10 times longer than the duration of each sequence. So each image sequence is big enough to contain several fringes to pass and small enough to represent instantaneous values of V. To test this method, three cells are analyzed (Figure 4.8-a). Two of them oscillate in phase opposition and the third one has no oscillation. The tip velocity oscillation of the three cells should present the same behavior than the surface area one, in terms of phase shift and relative amplitude of oscillation. The variation of Δt as a function of t is given with the 3 cells. It clearly appears that the three curves are similar and do not present the expected behavior. This comparison illustrates that the variation of Δt obtained from the measurements does not correspond to the tip position oscillation. That may be due to that the tip position oscillation is very weak and this measurement is not sensitive enough. Based on Figure 4.8-b, the noise is evaluated ($\Delta t_{noise\ max}/\Delta t_{average}$) to ± 3%. That indicates that the Δz/z is smaller than 3%. Therefore, the tip position oscillation cannot be determined by this method.

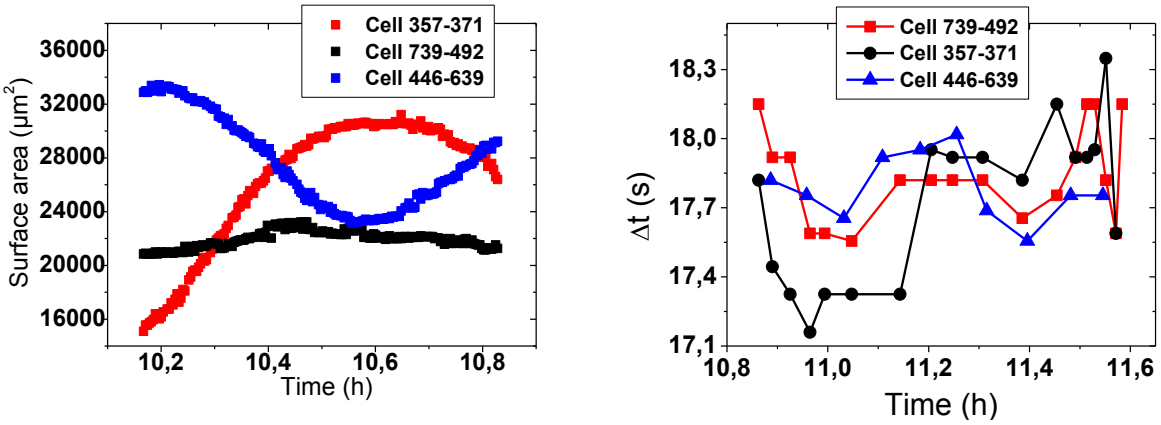

a b

Figure 4.8. Results obtained from the interferometry method. a) Three kinds of oscillation: 2 cells in opposite phase and the third one almost without oscillation. b) Corresponding results for the time needed to obtain the following same diameter fringe as a function of solidification time (which proportional to images/fringe).

Tip radius measurement

In theoretical models, the tip radius (R) of the dendrite structure is directly related to the tip growth velocity (V): $VR^2=C$ [20][175][22], where C is a constant. This formula can't be used here since our microstructure is cellular. Anyhow it is recognized that the tip growth velocity is related to the tip radius, smaller R corresponding to higher growth velocity, even for cellular microstructures. Therefore, tip velocity oscillation can be evidenced indirectly through the tip radius measurement.

The cross sections of cells are reconstructed from the interferometric images following the method introduced in Chapter 2. All the tip positions are settled to zero. The 0 point of z axis is chosen as the center of the fringes and keeps fixed during the whole reconstruction. Figure 4.9 shows the variation of the cell tip width from its minimal (the green starts) to its maximum (the black squares) during a half period of oscillation.

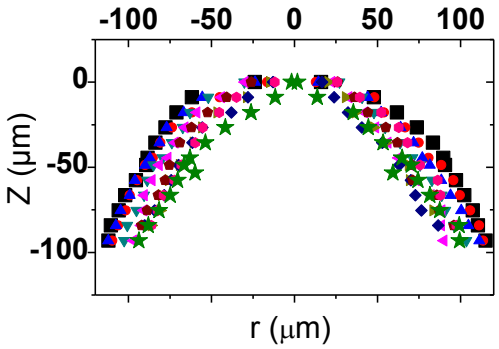

Figure 4.9. Reconstruction of the cross sections for one cell from its smallest width (the green stars) to its largest width (the black squares) (V = 1 µm/s and G = 28 K/cm).

According to reference [176], the tip radius of a cell could be extracted from a parabolic fit ($y = A + B(x - a)^2$) of the profile.

$$\frac{1}{R} = \left| \frac{y''}{(1 + y'^2)^{\frac{3}{2}}} \right| = |2B|$$

The tip radius of three cells are measured and plotted in Figure 4.10 (right part) together with the corresponding cell surface variation (left part) in the preceding period of time. These measurements cover the switch of the observation from top view mode to the interferometric mode. We can see the good continuity of the surface area oscillation and the tip radius oscillation. The period of tip radius oscillation is about 0.8 h, which is the same as the surface area oscillation one. We can conclude through this indirect measurement that the cell tip position oscillates with the same period as the cell width.

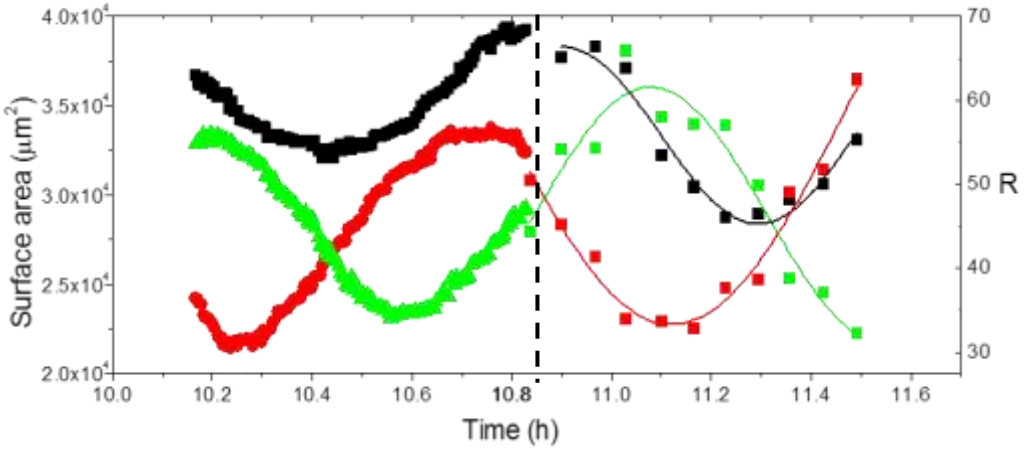

Figure 4.10. Tip radius (right) and surface (left) oscillations as a function of time (V = 1µm/s, G = 28K/cm).

4.2.4. Measurement of oscillation parameters

Table 4.2. Measurement of the period and the average primary spacing for all oscillating patterns observed in our experiments.

Gradient (K/cm)	Velocity (μm/s)	λ±Δλ (mm)	τ ±Δτ (s)
28	0.5	0.27±0.06	(7.46±0.43)x10^3
28	0.75	0.27±0.05	(4.57±0.7)x10^3
28	1	0.28±0.04	(2.86±0.12)x10^3
28	1.5	0.25±0.03	(1.58±0.16)x10^3
12	0.5	0.16±0.02	(9.58±1.3)x10^3

The periods of all oscillating patterns found in our experiments are measured and presented in Table 4.2, as well as the related primary spacings. The experimental data of period as a function of the pulling rate are fitted by a power law: $T = 2.8 \times 10^3 V^{-1.5}$ for G = 28 K/cm (Figure 4.11). Despite the different alloys and geometries, the exponent and prefactor obtained are both similar to those found in breathing modes in confined 3D experiments [54]. In thin samples, the confinement imposes cell arrangement in a row. Yet, for a sample thickness above ~25 μm, tip shapes are no longer ribbon-like (2D) but actually 3D [1]. The Péclet number Pe = λV/D is used to compared the cell size (λ) to the solutal length (D/V). In both 2D and 3D samples, interactions are limited to first-neighbors spacing since Pe~1 (0.5 < Pe < 1.5 in our experiments). This explains the similar power law exponent. Since the experimental data for other alloys is very limited, a possible interpretation for the agreement on the perfactor is related to the nature of the solvent (succinonitrile in both cases).

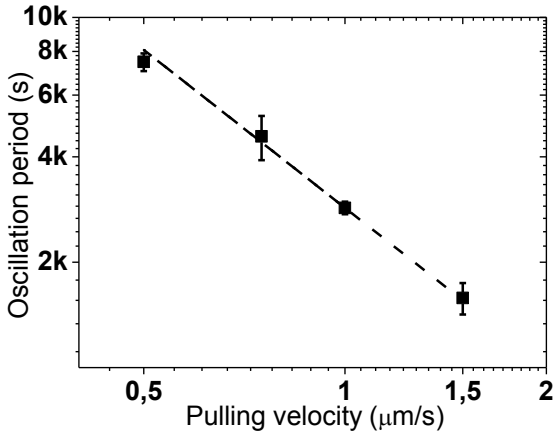

Figure 4.11, Oscillation period as a function of pulling rate (G=28K/cm). The dotted line corresponds to the power law T=2.8*10^3*V$^{(-1.5)}$.

4.2.5. *Coherence of the oscillating patterns*

The grown pattern, even in microgravity, is highly disordered and very far from the regular theoretical hexagonal tilling as illustrated in Figure 4.12-a. Typical topological defects mainly correspond to 5 or 7 nearest neighbors instead of 6. This is illustrated in Figure 4.12-d where the number of the first neighbors is given for each cell of the extended zone noted in Figure 4.12-a.

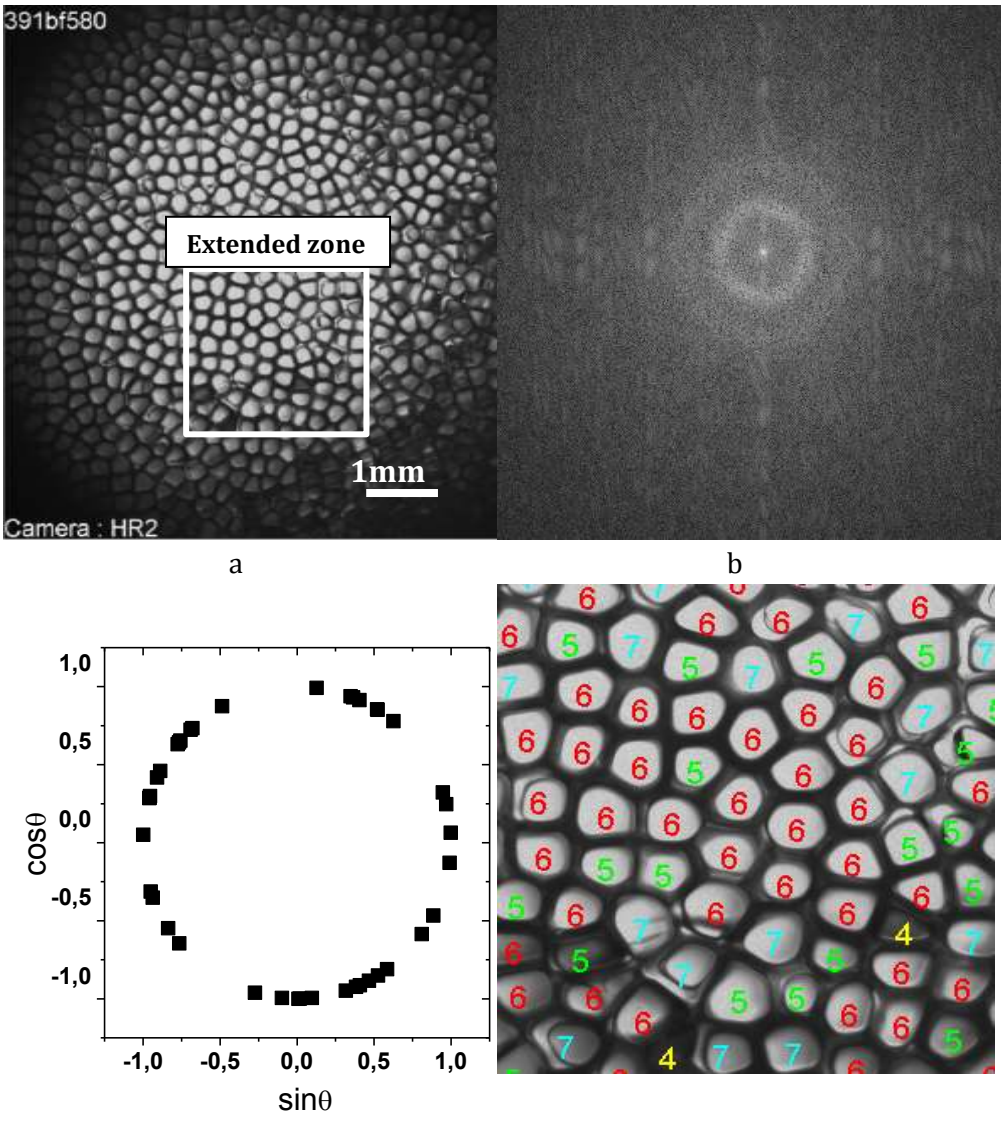

Figure 4.12. a) Oscillation zones considered in the analysis: extended zone which contains many defects. b) The central zone of the Fast Fourier Transform (FFT) of Figure a, the ring shape indicates the high disorder of the pattern structure. c) The phases θ are plotted on the unit circle at t=16h, the large scatter of phase indicates absence of global coherence of oscillation. d) Numbers of nearest neighbors labeled with different colored numbers.

One extended zone with an irregular cellular array is chosen, as showed in Figure 4.12-b. The oscillation periods of all cells of this are measured, and their instantaneous phases θ at t = 16 h are plotted on the unit circle (Figure 4.12-c). The homogeneous distribution of the phases on the unit circle indicates a globally incoherent oscillation attributed to the disorder of pattern. This is also the major difference compared with the 2D case where oscillation is coherent.

In the interface pattern, one may identify a particular pattern order that is associated to a particular ordering of oscillation characteristics. For example, the variation of the cell surfaces of cells labeled 1 to 7 in Figure 4.13 reveals three groups of cells (respectively 1-2-3, 4-5-6, 7) organized as three hexagonal sub-arrays that oscillate at the same period with a phase shift of ±2π/3 for long duration. Another example of oscillation coherency is illustrated in Figure 4.14: in a locally square pattern. The two cells on diagonal oscillate together (cell 54 and 42); but in phase opposition with the other group, for example, cell 43 and 48. A detailed analysis of the surrounding area shows that this coherency is limited to a zone of less than 10 cells as shown in Figure 4.13-a and Figure 4.14-a, with the labeling of cells oscillating together are labeled with the same color. For example, in Figure 4.13-a, cell 9 is also in the center of another hexagonal structure where it loses the coherence with cells 7 and 8. Other examples of square patterns are shown in Figure 4.13-a which are marked with white squares. A regular structure (like hexagonal or square) is a necessary but not sufficient condition to find group oscillation. For example in Figure 4.13-a, a hexagonal structure is indicated with dotted lines whose pattern oscillation is totally incoherent.

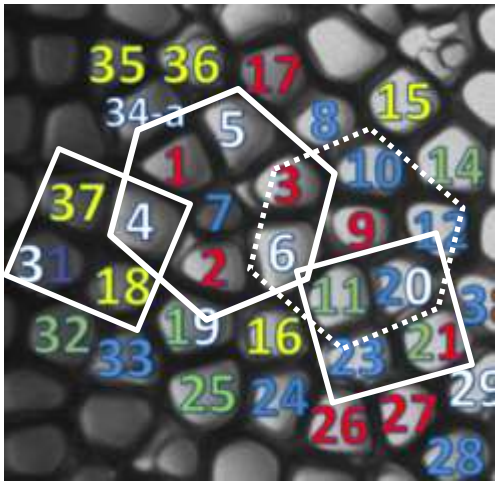

a

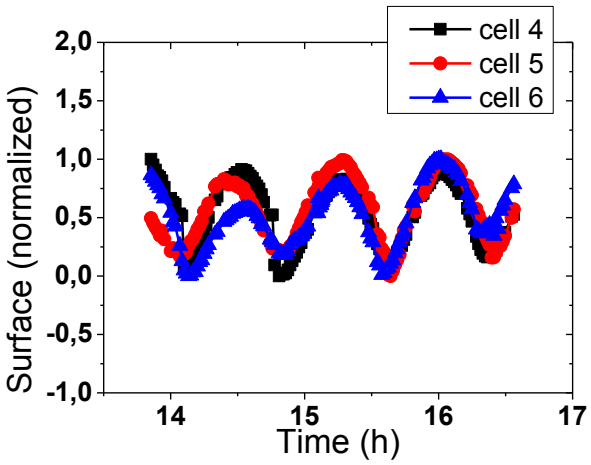

c

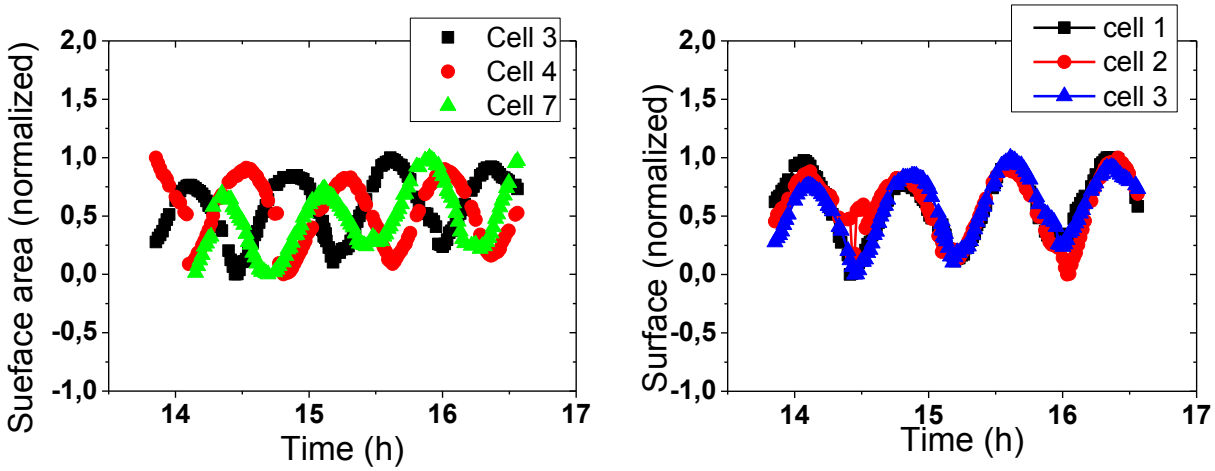

b d

Figure 4.13. Analysis of oscillation in a locally ordered area and its neighborhood. a) Locally order area: color label denote cells oscillating in phase. b-d) Appearing areas of cells of the three sub patterns distinguished in the hexagonal structure formed by cells 1 to 7. Cell 1,2,3 are phase shifted by 2π/3 with cells 4,5,6 and -2π/3 with cell 7.

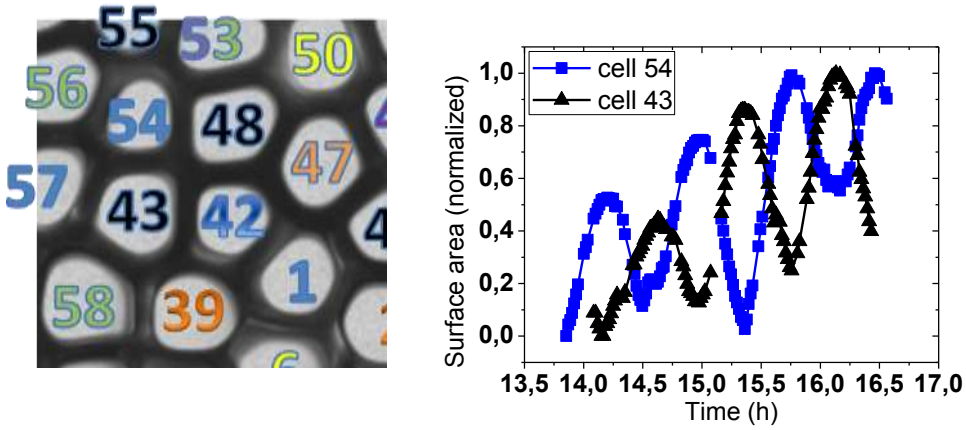

a b

Figure 4.14. Oscillation in a regular square structure (cells labeled with 42, 43, 48, 54). a, pattern structure at the beginning. b, a phase shift of π/2.

As mentioned earlier, phase shift is frequent during cell oscillation. It seems also related to the problem of disorder of the pattern. For example, cell 31, 19 and 20 see their phases shift from a phase opposition with their neighbors to another value, which may, as it's the case for cells 19 and 20, correspond to a coherence of hexagonal type.

Phase shift is obtained during the study of the oscillation patterns, illustrated in Figure 4.13-a. The cells labeled with two-color numbers (20, 21 and 31) are those whose oscillation phase shifts. This phase shift is often found at the intersection of two different ordered structures. For example, cell 19 and 20 are both in the hexagonal structure and there is a moment when they oscillate as a group with cell 6. But, they are influenced by

one of their nearest neighbors and change their oscillation phase to the neighbor phase (cell 25 and cell 23). This phase shift shows how cell interact with the nearest neighbors.

4.2.6. Comparison with simulation

To further understand the breathing mode, 3D phase-field simulations using an established quantitative approach for binary alloys have been carried out by A. Karma and D. Tourret (Northeastern University) and J-M Debierre and R. Guérin (IM2NP) and compared to our experimental results.

Several series of simulations were done. The first one used large rectangular domains, with periodic boundary conditions perpendicular to the growth direction, and tracked the entire transient recoil and destabilization of an initially planar interface. Those simulations produced a similar oscillation behavior as we obtained in the experiments; the average value of the oscillation period $\tau \sim 48.1$min is consistent with the experimental period $\tau \sim 45.6$min. In Figure 4.15-1, the phases of a large group of cells are scattered around the unit circle similarly to experimental data for example described in Figure 4.12. Additional simulations show that phase coherence is maintained spatiotemporally over the whole array when the initial condition corresponds to a perfect hexagonal order. Similar oscillation period and phase difference are obtained.

A series of simulations is also performed to investigate the range of existence of oscillation modes as a function of control parameters and cell spacing. The obtained results show that steady state solutions only exist over a limited range of cell spacings. Results show that cell spacings towards the end of the main branch display breathing oscillations when a gap is present and at high G (Figure 4.16-a).

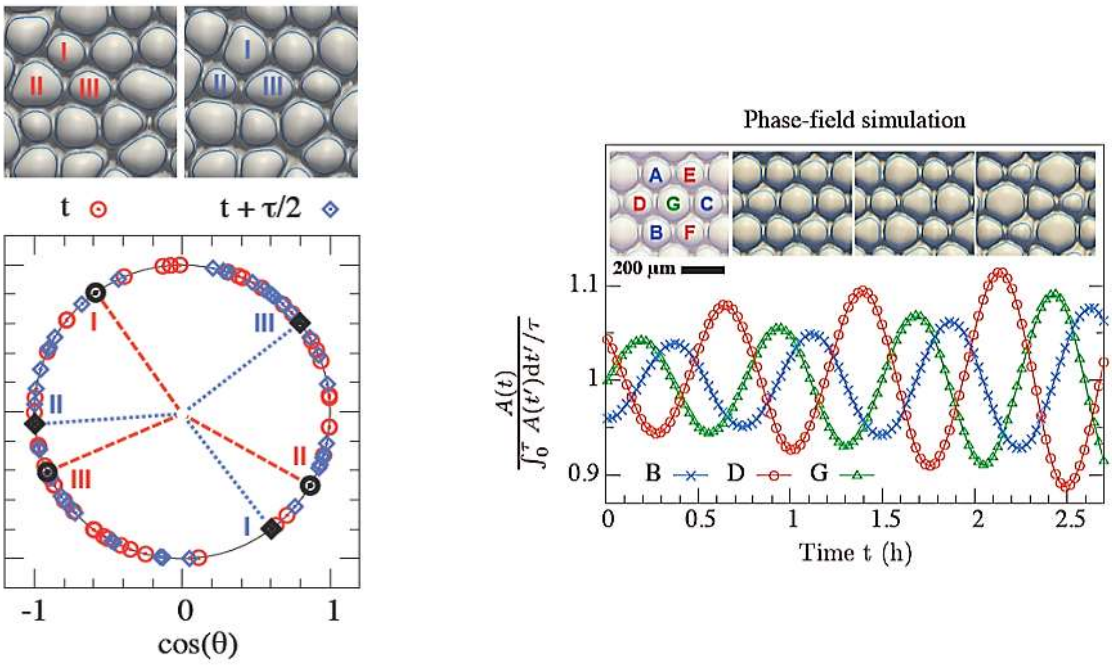

a b

Figure 4.15. Phase field simulation results. a) The large scatter of phases on the unit circle indicates absence of global coherence of oscillations. In disordered regions, temporary synchronization between first neighbor cells appears in simulation with ±2π/3 (tagged cells in figure 1). b) Short range correlation of hexagonal patterns at V=1 µm/s, G = 28K/cm. 3 groups of cells oscillate coherently with a mutual phase difference of ±2π/3.

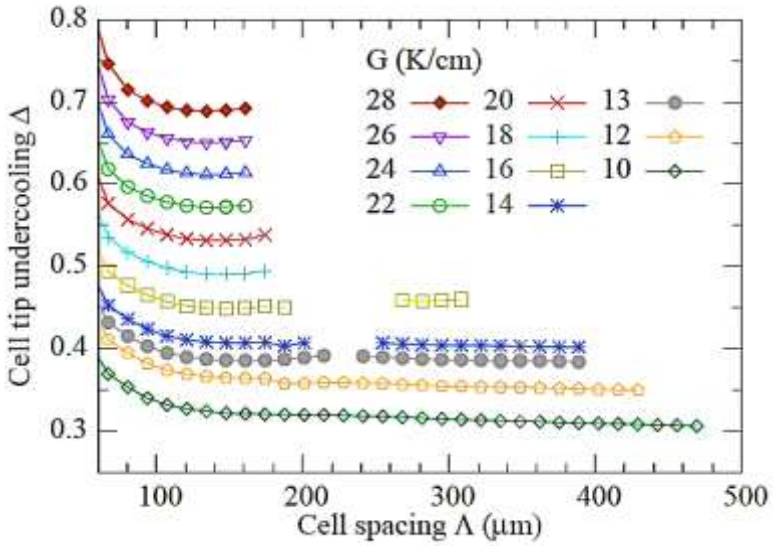

Figure 4.16. Phase field predictions of steady state branches of hexagonal cellular arrays for V = 1µm/s where Δ is the cell tip undercooling below the liquidus temperature normalized by the freezing range $mc_\infty(1-1/k)$. Breathing oscillations were found when a gap is present and at high G.

4.2.7. Conclusion: oscillating patterns

Oscillation of cellular pattern in 3D patterns is observed during the directional solidification of a transparent alloy for the very first time. This oscillation mode is found for a narrow range of pulling rates (between 0.5 and 1.5 μm/s). The oscillation periods are measured as a function of pulling rate and fitted with a power law. This law is very similar to the one obtained in thin samples. The tip position oscillation is measured through the tip radius and is found to have the same period of the appearing cell size oscillation. The coherence of oscillations is studied in large areas containing more than 40 cells. It reveals that oscillation is generally not coherent, in relation with the disorder of the pattern. In some locally ordered areas, presenting square on hexagonal tiling, oscillation may be coherent, displaying two sub – patterns shifted of $\pm 2\pi/3$ for the hexagonal case. This coherence is however spatially extremely limited, involving only the very first neighbors. In contradistinction, studies of oscillating patterns in thin samples, where cells are aligned, displayed global spatiotemporal coherence over large domains. Our analyses highlight the key influence of tiling order on oscillation dynamics. This incoherence is specific 3D phenomenon since the oscillation is totally coherent in 2D case. The experimental results are compared with phase field simulations and a good agreement is obtained.

4.3. Multiplet structure

Another interface morphology named multiplets is observed during the directional solidification experiment with 3D samples in μg. A similar structure was first observed in 2D samples by H. Jamgotchian et al [63] in directional solidification performed in a thin film with succinonitrile-acetone. Asymmetric cells in the doublets structures are shown in Figure 4.17 which presents 2 characteristic lengths: λ_{intra}, interspacing between 2 cells inside a doublet whose selection is sharp; and λ_{inter}, spacing between cells in adjoining doublets whose selection is weak. Their dynamical study confirmed the selection of the doublet interface as a new branch of cellular stable solution in nonlinear pattern formation. Brener et al [177] studied numerically the crystal growth in a channel, and they found that when the width of the channel exceeds a critical value, stable steady-state growth of nonsymmetrical fingers is observed. Further studies by Wang et al [178], with phase field simulations, indicate that the asymmetrical cells can only survive in a finite spacing, beyond the upper limit of symmetrical cell and smaller than the critical spacing for oscillatory instability. Doublet tips in a dendrite structures were studied by Ihle et al [179] with a 2D shape interface model. They found a stable solution which they called symmetry broken (SB) double finger, where the important parameters are the tip undercooling and the surface tension anisotropy. The dendrite tip doublet became unstable if the anisotropy exceeded a critical value. Ludwig [180] observed the

dendritic and cellular doublets in thin solid films growing along a borosilicate wall. Cellular doublets are stable at low concentrations while dendritic doublets are stable at high concentrations. Later studies [65][181], point out that the multiplets are solutions split of the main branches of singlet (Figure 4.18): one branch at low Peclet number Pe = $\lambda V/D$ (near the Eckhaus instability) and the other branch at high Pe. Those solutions with high Pe have the same shape as the experimentally observed multiplets. The low Pe branch has never been observed experimentally and they are generically unstable.

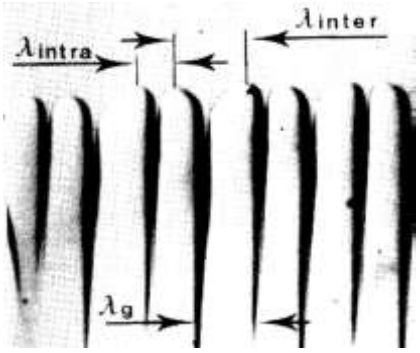

Figure 4.17. Cellular doublet, observed during directional solidification of thin films. The groove between the 2 cells in the doublet is shallower than the groove between the cells in adjoining doublets. The two characteristic lengths: λ_{intra} and λ_{inter} are illustrated. The classic primary spacing λ_g is the width of the cell [63]**. (Succinonitrile – 0.15 wt.% acetone. V = 4 µm/s, G = 65 K/cm).**

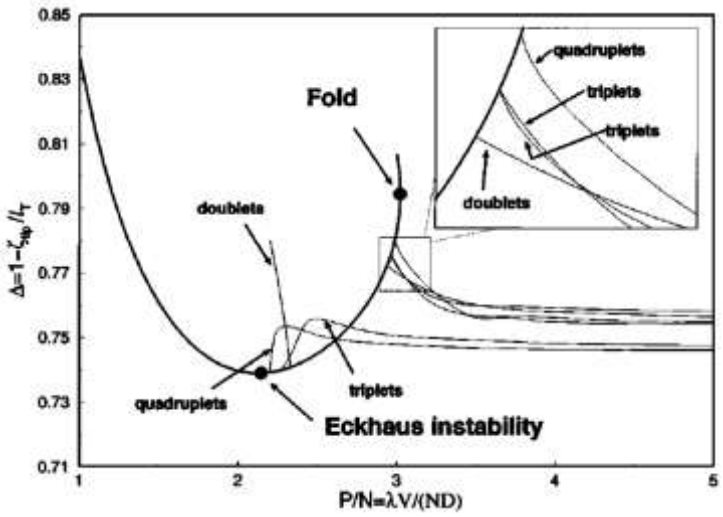

Figure 4.18. The main branches (single cellular) and the multiplets branches from the simulation results [65]**. The multiplets branches have 2 groups which correspond to high P and low P. The high P branch has the same shapes as experiments.**

4.3.1. General description in 3D

In our case, 3D multiplets structures are observed for 2 sets of experimental parameters: for V = 0.25 μm/s and G = 12 K/cm, multiplets structure invade the whole interface, while at V = 0.35 μm/s and G = 12 K/cm, they coexist with regular cells. The relevant range is between the smooth interface and oscillation instability. The following analysis are based on the results obtained at V = 0.25 μm/s and G = 12K/cm.

Typical bulk multiplet structures are schematically presented in Figure 4.19, Figure 4.20 and Figure 4.21. The direct observation image of Figure 4.19-a hardly reveals the presence of multiplets while the corresponding interferometric image of Figure 4.19-b enabled the detailed observation of the structure, with sub cells and the central pit. Several multiplet structures are reconstructed through the interferometric images with the software AutoCAD civil 3D. The principle of reconstruction was introduced in chapter 2. Through the reconstructed 3D images, morphologies of multiplets can be easily observed, especially the internal structure of multiplets. An example of the reconstructed 3D image is given in Figure 4.20. Two sub cells grow from the main structure, separated by a deep pit and two shallow grooves. Some other typical multiplets are shown in Figure 4.21, with 3, 4 and 5 sub cells. We did not observe multiplets with 6 or more sub - cells in our experiments.

In the following, the cells inside the multiplets will be called “sub cells”, “Top” will refer to the tip of sub - cells inside the multiplet, and “groove” to the groove between two adjacent sub cells (Figure 4.20). The complete structure is named multiplet. Depending on the number of the sub cells, the multiplet will be named doublet, triplet, …

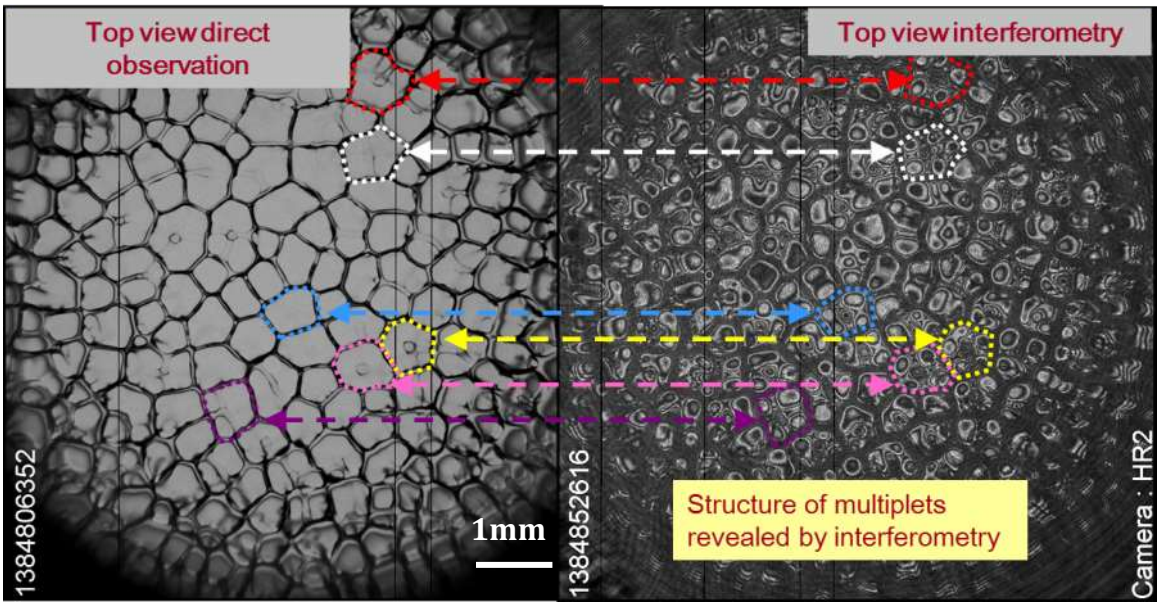

a **b**

Figure 4.19. a) Direct top view observation of multiplet pattern. b) Corresponding interferometric image, that reveals the details of the multiplet structures.

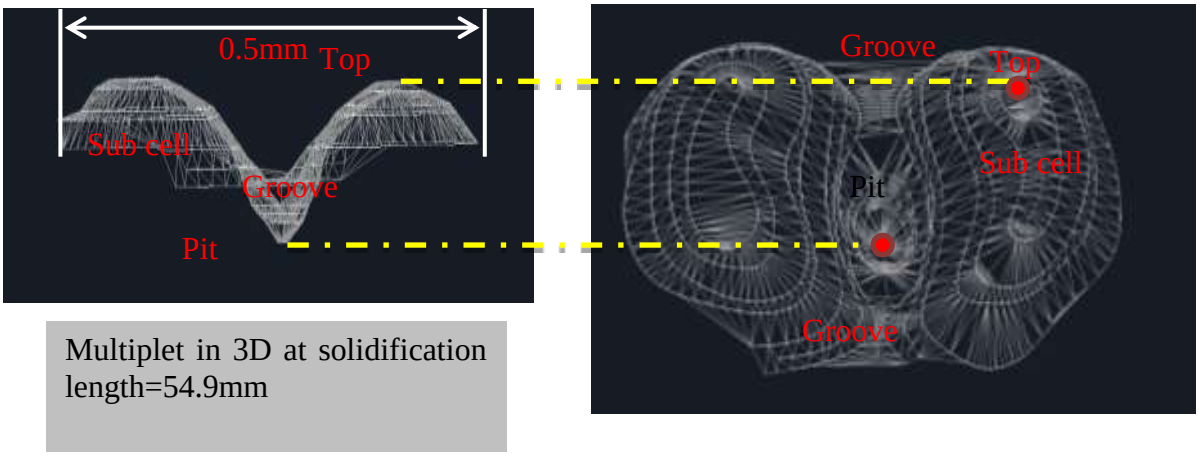

Multiplet in 3D at solidification length=54.9mm

Figure 4.20. Doublet reconstructed from the interferometric image. It shows the 2 sub cells and a pit in the center of the groove between the two sub cells.

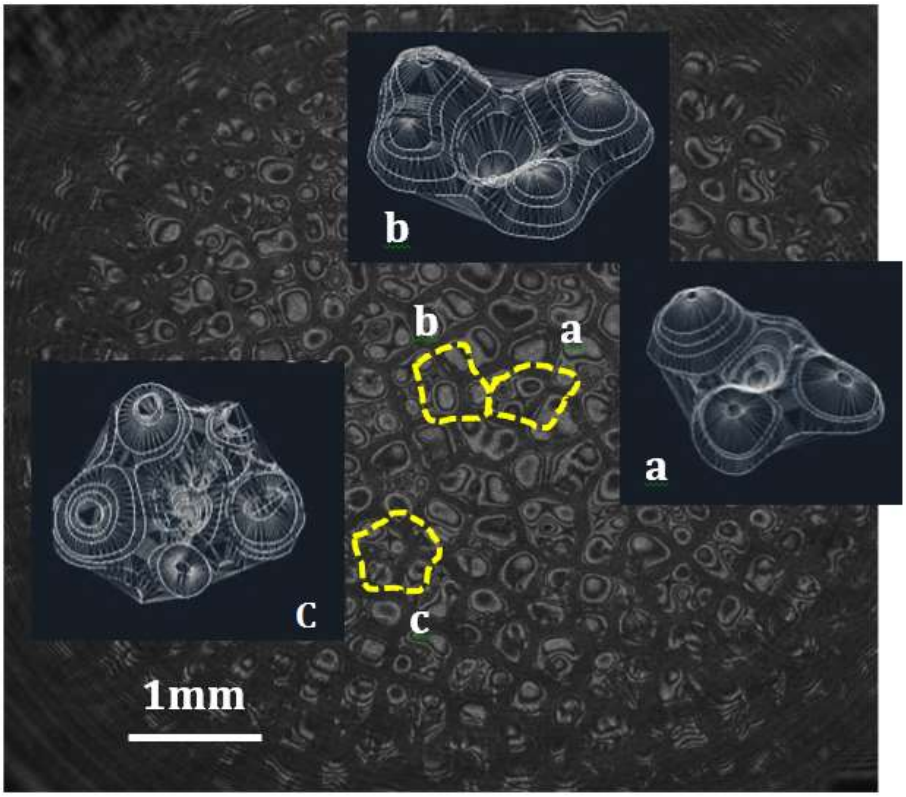

Figure 4.21, Typical multiplets (labeled a (triplet), b (quadruplet) and c (quintuplet)).

4.3.2. *Analysis of multiplet dynamics*

Formation and evolution

Before analyzing the formation of multiplets from top-view images, let us examine the interface from the side (Figure 4.22). The interface positions taken at the border and at the center are reported as a function of time on Figure 4.22-a. The absence of complete stabilization of the positions reveals that the steady-state is never really reached in this experiment (estimation of transient duration τ: $\tau \sim 4D/(kV^2)$ = 20.4 h). During this motion, an important observation is the increase of the convexity of the interface revealed by the difference between center and border positions. Example of the interface shape close to the end of solidification is given in Figure 4.22-b.

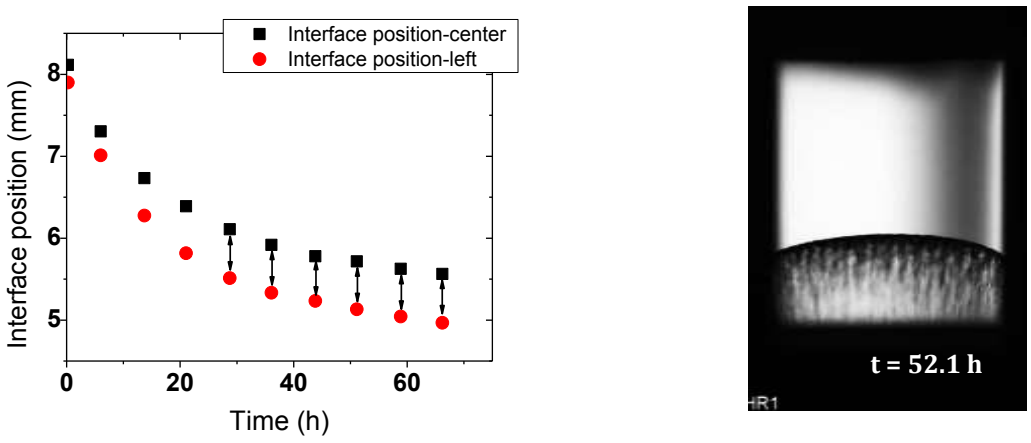

a b

Figure 4.22. a) Measurement of the interface recoil from side view observation. Difference between the motions of the center and the border of the interface gives the curvature evolution. b) Example of side-view image. (V = 0.25 µm/s, G = 12 K/cm).

Instability develops around t = 36h when local small poxes are observed (Figure 4.23-a). Instability develop and invades the whole interface at t = 41.9h (Figure 4.23-b). Images between Figure 4.23-b and c are unfortunately out of focus. Therefore, a second experiment with the same control parameters was done. For a unknown reason, the initial interface position (V = 0) had changed. In this case, instability triggering was delayed compared with the first experiment. But if we look at the image at the end of solidification of the second experiment, as illustrated in Figure 4.24-g and h, the interface morphologies are similar (comparison with Figure 4.23-c and d of the first experiments). Therefore, we believe that this variation of the temperature environment only delayed the evolution of instability and that the formation of the interface instability morphology in the second experiment is not significant different from the first one.

The interface morphology evolution from poxes to multiplets is illustrated in Figure 4.24. The Figure 4.24-b is the corresponding interferometric image of Figure 4.24-a: we evidenced some of the poxes by white circles. The poxes are found all around the interface although only those close to the border could be observed from Figure 4.24-a.

In Figure 4.24-c, some volcano like structures are formed beyond those poxes. Those volcanos - like structures are formed from growing poxes whose center begins to sink. They are first found at the interface border and then extended towards the center. The detailed evolution from a poxe to the multiplet structure is illustrated in Figure 4.25. In Figure 4.25-d, connections between “volcano-like” structures form to draw a pattern: Figure 4.24 e-f.

Figure 4.24-f to h illustrates the following steps of the morphology development. Figure 4.24-f shows the pit structures in the interface. In the central area, only pit structures are found. This is more clearly observed on the half interferometric image of the right side where cellular structures are already generated at the border. The evolution of pattern progresses from border towards the center as illustrated in Figure 4.23-c and Figure 4.24-g: sub-cells start to appear on the border while the cellular pattern is not completely drawn in the center. Grooves continue to form towards the center eventually leading to a complete pattern of large cells: Figure 4.23d-e and Figure 4.24-h.

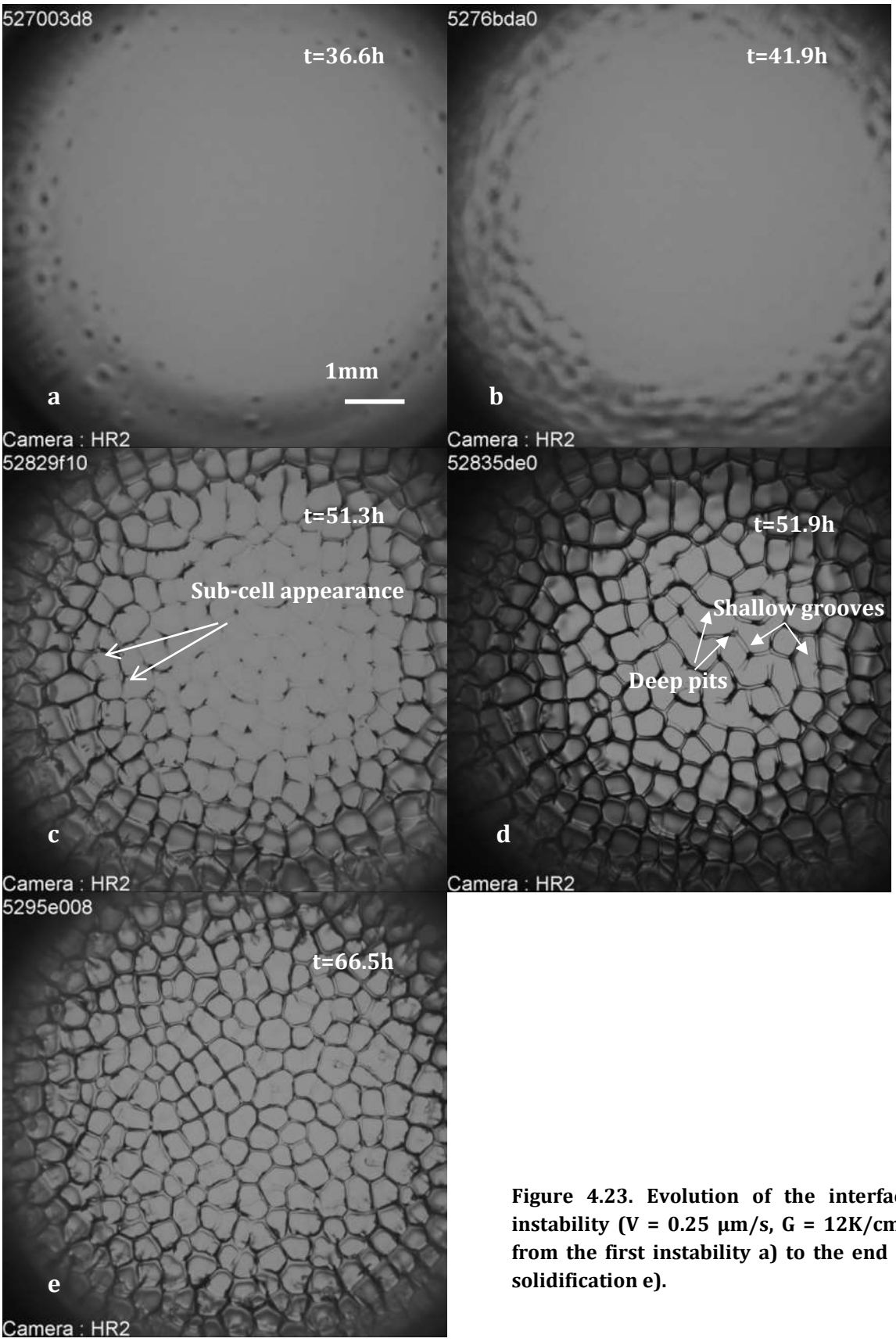

Figure 4.23. Evolution of the interface instability (V = 0.25 µm/s, G = 12K/cm), from the first instability a) to the end of solidification e).

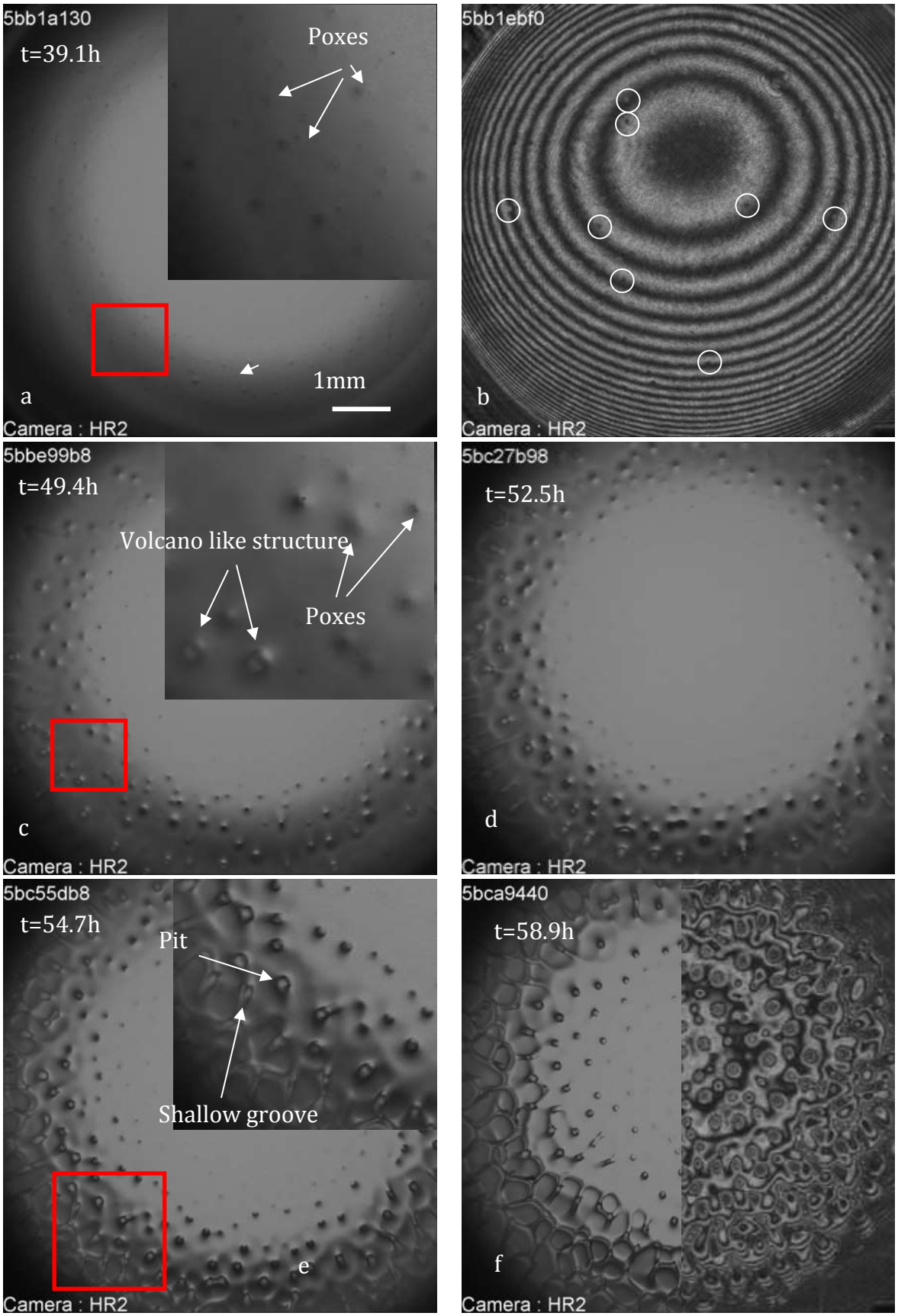
5bb1a130
t=39.1h
Poxes
1mm
a
Camera : HR2
5bb1ebf0
b
Camera : HR2
5bbe99b8
t=49.4h
Volcano like structure
Poxes
c
Camera : HR2
5bc27b98
t=52.5h
d
Camera : HR2
5bc55db8
t=54.7h
Pit
Shallow groove
e
Camera : HR2
5bca9440
t=58.9h
f
Camera : HR2

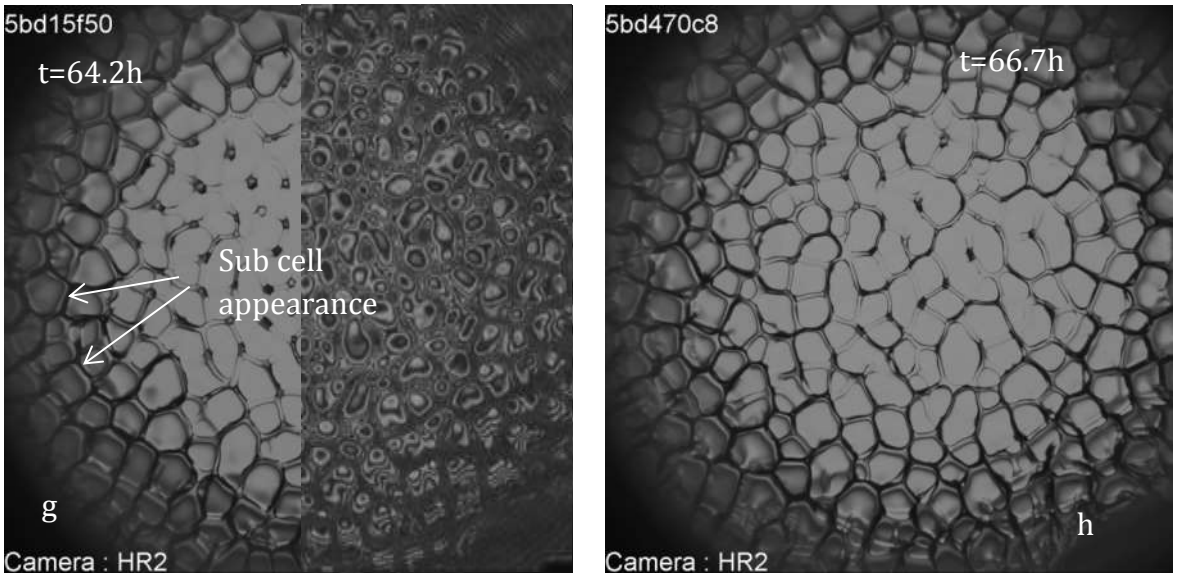

Figure 4.24. Initial transient from a smooth interface to a multiplet structure. Experimental results from another run with the same control parameters and (V = 0.25µm/s, G = 12K/cm).

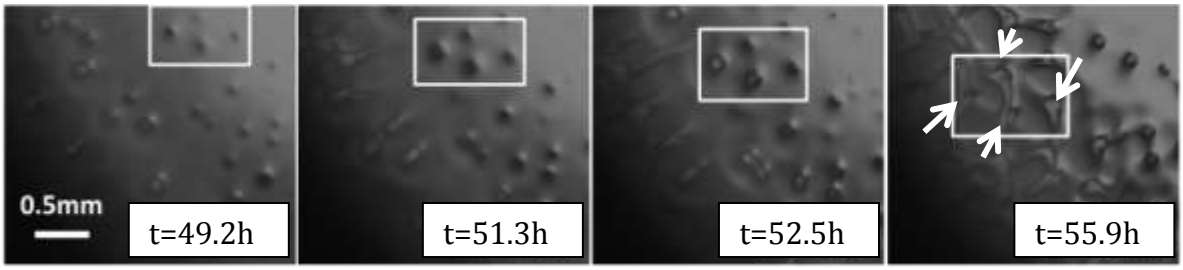

a b c d

Figure 4.25. Detailed evolution of the interface instability evolution from a) poxes, b) amplification of poxes, c) formation in the center of poxes: "volcano-like" structures, d) formation of ridges between poxes.

A multiplet structure is reconstructed as a function of time to study the evolution of its components, and the 3D images are illustrated in Figure 4.26. The evolution starts from shallow cells (Figure 4.26-a): the tip of the shallow cell is almost flat so the tip can be considered as a new flat interface. Then, the tip begins to sink and 4 tips of sub cells are generated (Figure 4.26-b). The 4 sub cells grow up and the pit becomes deeper. At the end of solidification, one of the largest sub cells start to split into 2 sub cells (Figure 4.26-e).

This evolution will continue by separating the multiplets with 5 tops into two independent structures, (one doublet and one triplet). The old pit disappeared and a new one forms inside the triplet.

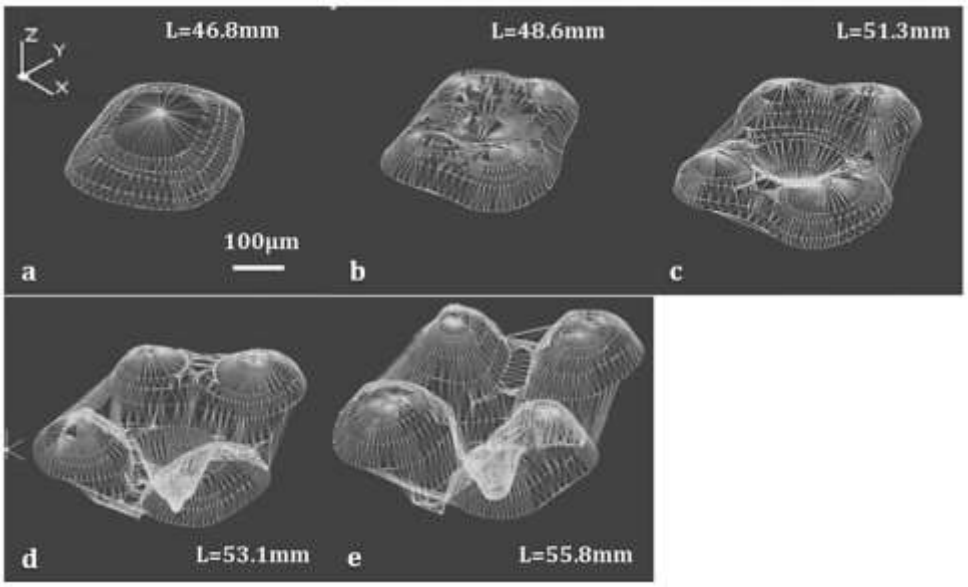

Figure 4.26. Evolution of a multiplet structure from one single shallow cell to 5 sub-cells (V = 0.25µm/s, G = 12K/cm). Reconstruction from the interferometry images (L: the solidification length).

Analysis of size evolution

One of the dynamic characteristic of the spacing selection for both sub cells and multiplet is the tip splitting (for multiplets structure, the tip splitting means one or more sub cells emerging from the mother structure.). Elimination of multiplets or sub cells by the over growth by the surrounding microstructures is not observed during the solidification. Another important dynamical adjustment comes from the lateral movement caused by the convex interface. Multiplets at the border will eliminate due to this lateral movement. A detailed study is necessary to understand the influence of the movement on the dynamics of the multiplets spacing selection and their structure. The interface is convex during the whole growth. In such a convex interface, multiplets move laterally towards the border (Figure 4.27), as it was reported for cellular growth on a convex interface [151][146]. The lateral drift velocities of two multiplets at different positions are measured and the results are shown in Figure 4.27. The slip velocity for the multiplet c which is far from the center is 3 times higher than the central one (multiplet B). In fact, the velocity imposed to the multiplet depends on the interface slope at its location.

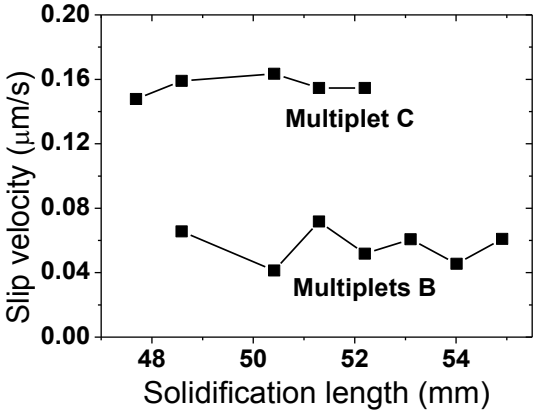

Figure 4.27. Slip velocity for 2 multiplets at different radial positions. Multiplet B is in the center and multiplet C is far from the border.

We estimated the position of the center (the highest point in the interface), which is not always the same as the geometric center, by supposing that all microstructures should slide away from the curvature center. The traces of three multiplets that slide to different directions are measured and plotted in Figure 4.28. Their traces are prolongated and intersect at one point considered as the curvature center.

The evolution of the cellular size on a concave interface was calculated by Weiss et al [146] without influence of convection, in the case of no generation and elimination of new cells. In that case the cell size variation is a simple geometric phenomenon described by

$$A(r) = \frac{A_0}{{r_{A0}}^2} r^2$$

where A(r) is the cell size, r is the distance between the multiplet geometric center and the curvature center. A_0 and r_{A0} are the initial size and initial distance, respectively.

This model indicates that if the total number of cells is constant, they should grow to fill the space as long as they slide away from the center (for a concave interface: the inversed situation).

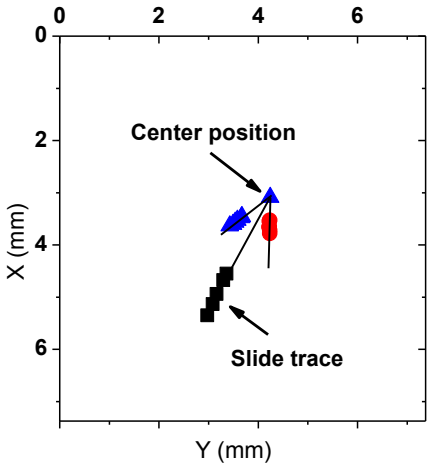

Figure 4.28. Determination of the curvature center. Three different multiplets are followed and their slip traces are plotted. The start point of the three traces is the center of the solid liquid interface curvature.

The evolution of the surface area as a function of time for the three multiplets indicated in Figure 4.21 is measured. The results are plotted in Figure 4.29 and compared with those obtained applying the model developed by Weiss et al [146]. The evolution of the multiplets surface areas is in good agreement with the model predictions. This indicates that the growth of the multiplet surface area is simply a consequence of the macroscopic convexity of the interface.

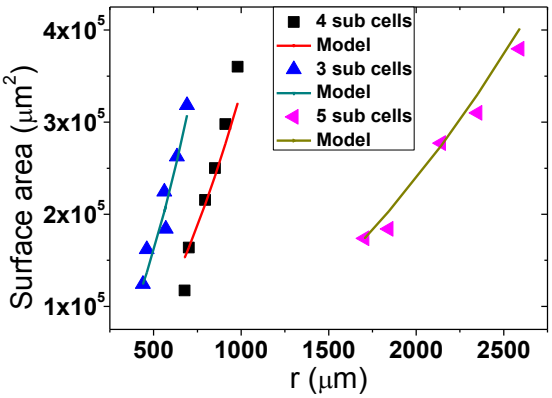

Figure 4.29. Evolution of the multiplet size with radial position. The solid lines correspond to the results obtained using the model developed by Weiss et al [146].

Since the multiplet surface area is determined by its radial position, its variation is measured as a function of radius. The interface is divided into several rings of same width (80 pixels, 576 μm) as illustrated in Figure 4.30. The average surface of all the multiplets located in the same ring is then calculated at different times. Results are presented in Figure 4.31, not directly as the function of time, but of the solidification length which is proportional to time. Measurement started from a solidification length of

48.6 mm. With this solidification length, the microstructures in central areas are still connected together, so that the measured multiplets surface in the central area (0 < r < 1 mm) are extremely large and exceed the display zone. But for r > 1 mm, multiplet structures already can be identified. From L = 50.4mm, all multiplet structures are distinguished. The 3 graphs of Figure 4.31 are the same but they highlight different stages of evolution.

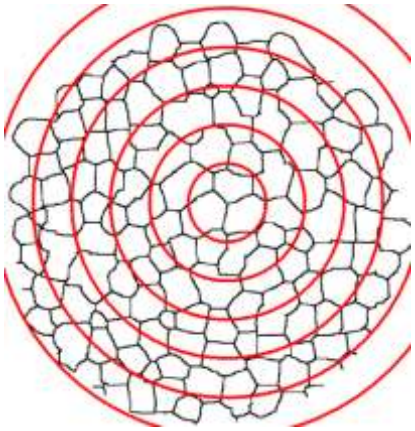

Figure 4.30. Measurement of the multiplet size distribution as a function of radius. The red circles divide the sample in different parts; the average surfaces of each circle are measured and plotted.

Figure 4.31-a: during the first stage of growth, the radius distribution indicates an increase of size between the central and the border area. (Variation with R) as well as in increase of average size of multiplets with time (relative position of the 3 curves)

Figure 4.31-b: effect of tip splitting. When the multiplet size reaches a critical value, it starts to split and the average surface area drops quickly. This process first dominates on the border but it extends progressively towards the center.

Figure 4.31-c: Except in the very central part, a homogeneous radial distribution is obtained in this stage. Most multiplets structures have finished their splitting process. The global decrease of size of multiplets with times pointed by Figure 4.31 is associated to a decrease of their multiplicity (number of sub-cells) as it will be described in the following part.

In fact, the dynamic of cell growth on a curved interface for a 2D sample has been carefully studied by Bottin-Rousseau and Pocheau [151]: similarly to this work, they observed the cell drift along the interface and widening till they reached a critical width for which they divided into 2 cells. Then each new cell resumed the same evolution.

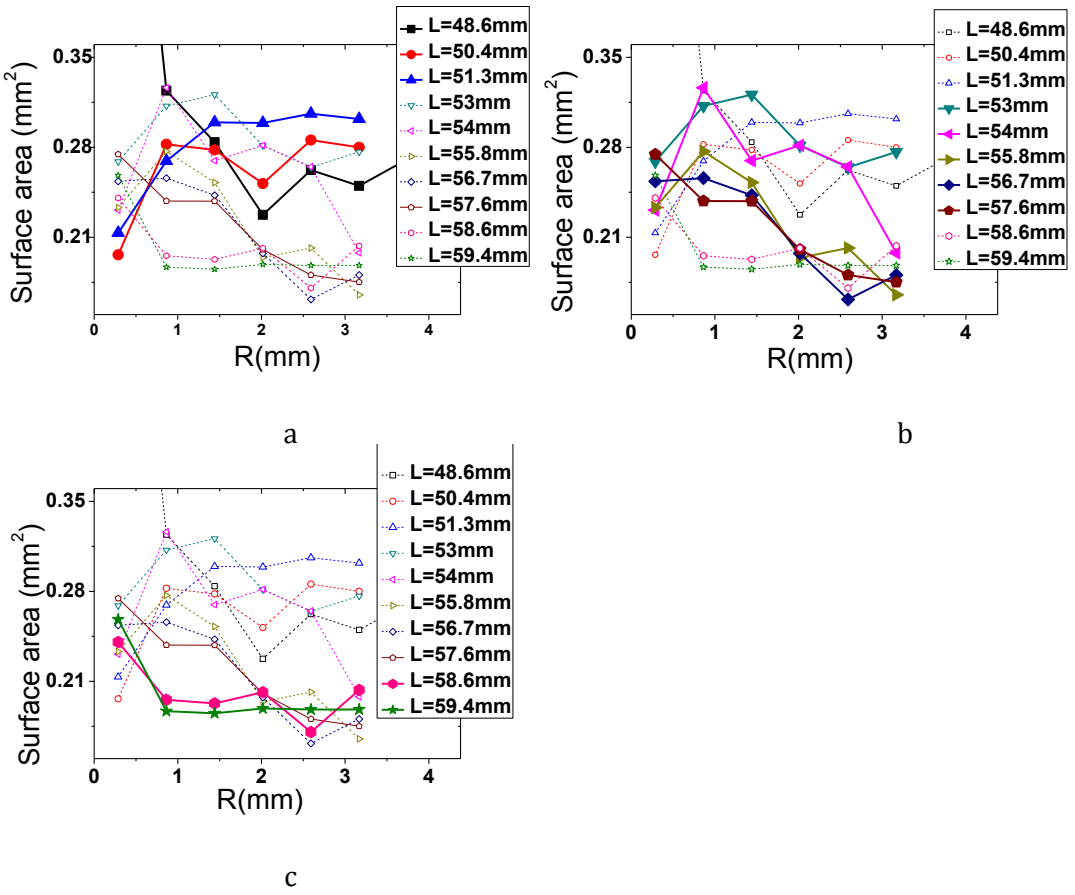

Figure 4.31. Average surface distribution as a function of radius for different solidification lengths L. Figure a), b) and c) correspond to different stages of evolution. V = 0.25 µm/S, G = 12 K/cm.

Analyses are then performed to determine the upper limit size of stable multiplets that correspond to the critical size for splitting. Some multiplets with different number of sub cells are selected for this analysis. Their shape reconstruction and surface area measurements as a function of time are performed using the process developed with Visilog software and already described in the first part of chapter 4 for the oscillation period measurement. Results are given in Figure 4.32. The tip splitting process in a multiplet structure involves several steps. As shown in Figure 4.32-c, the first splitting happens at about L = 54 mm when a multiplet with 5 sub cells arrives at its maximum size, then the multiplet splitted into a triplet, a doublet and a single cell (new sub cells may be generated during growth so that the total number of sub cells before and after dividing may not be conserved). The doublet and triplet continue to grow until L = 58 mm, when the triplet splits into a doublet and a single cell and the doublet into two single cells. The single cell formed during the splitting at L = 54 mm finally develops into a doublet.

It appears that the critical size is proportional to the number of sub cells as evidenced in Figure 4.32-d. This indicates that the splitting is not really related to the multiplets size but to the sub cell behavior during multiplet growth.

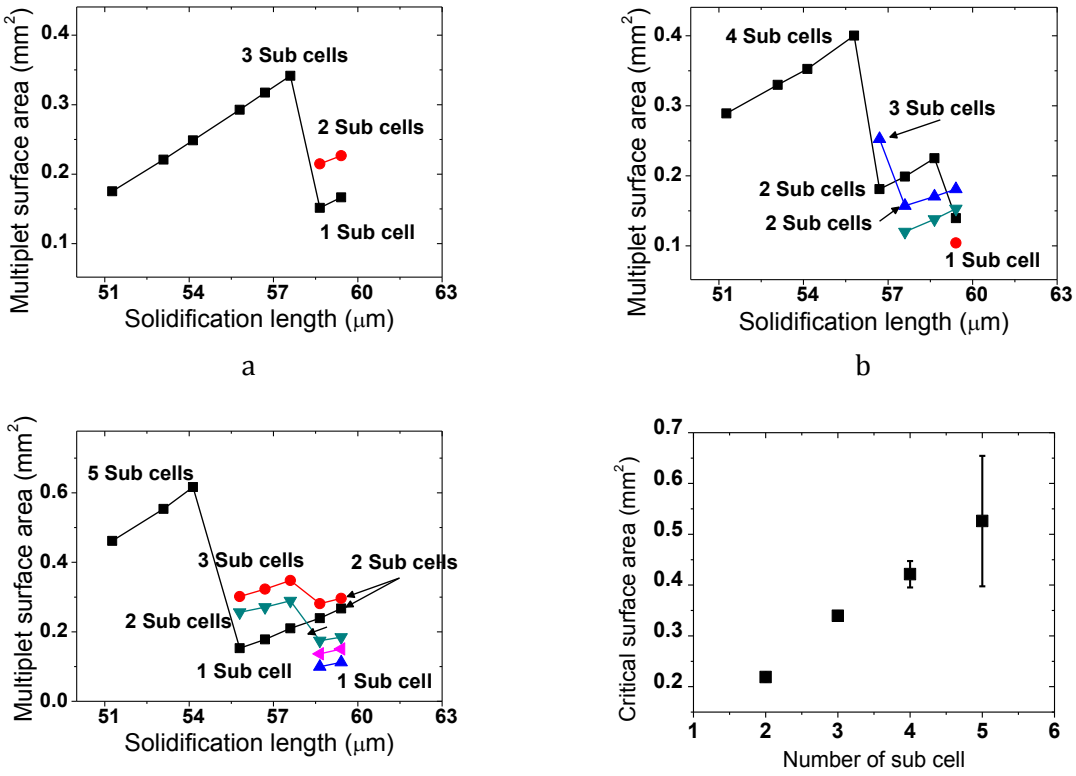

Figure 4.32. a) b) c) Size evolution and splittings of multiplets of respectively 3, 4 and 5 sub cells. d) Critical size as a function of the number of sub cells. (V = 0.25 µm/s, G = 12 K/cm)

Measurement of the characteristic parameters

Several parameters are required to characterize the complex structure of multiplets. As in 2D samples [63]: λ_{intra}, defines the spacing between 2 sub cells inside the same multiplet (excluding the spacing crossing the pit), and λ_{inter}, define the spacing between sub cells of adjacent multiplets. The spacing between the geometric centers of two adjacent multiplets is defined as λ_M. It is related to the multiplet size (see Figure 4.33, the two kinds of primary spacing are indicated).

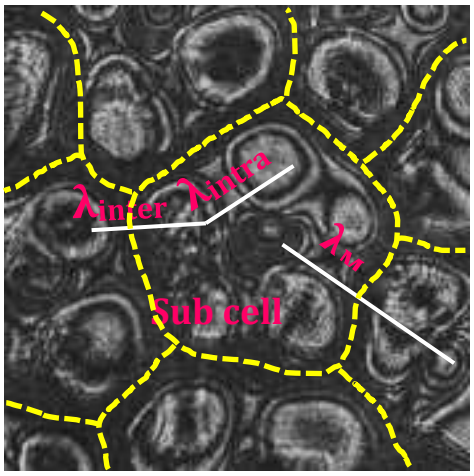

Figure 4.33. Characteristic parameters of a multiplet. Multiplest are separated by the yellow dotted lines.

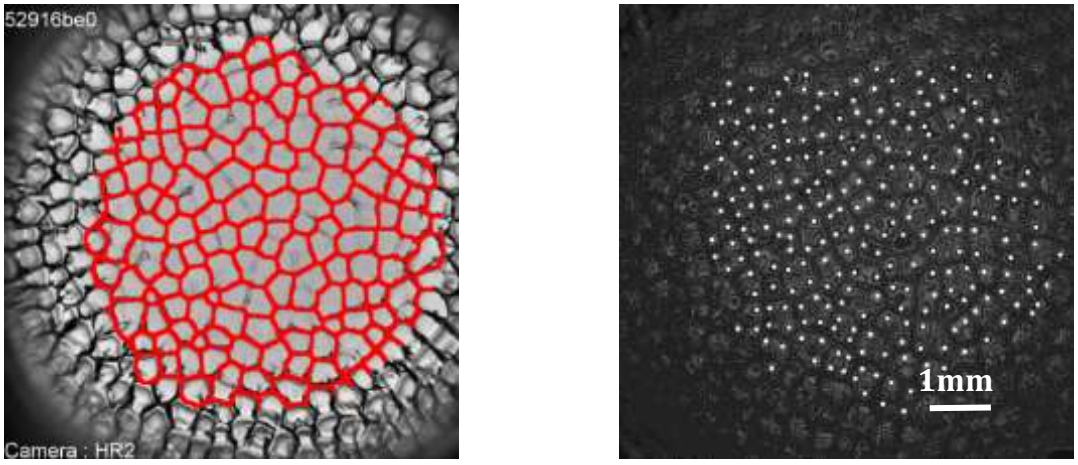

a b

Figure 4.34. Example of images processed for primary spacing measurements. a) Extracted multiplet structures superposed on the top view image. b) Location of the sub cell tips labeled with white dots from the interferometric image.

The primary spacing for multiplets and sub cells are measured and the relevant methods are illustrated in Figure 4.34. For multiplets measurements, just like the ordinary cellular pattern, the shape of each multiplet is extracted and sketched through the white line as show in Figure 4.34-a. The primary spacing is measured as the distance between the geometric centers of 2 adjacent multiplets. For the sub cells, they are identified manually from the interferometry image (Figure 4.34-b). The tips of the sub cells are labeled by white dots. This sub cell spacing measurement is mixing the inter and intra spacing since there is no way to separate the two kinds of spacing systematically trough computer program.

Results of spacing measurements are given in Figure 4.35 and Figure 4.36 as a function of the solidification length. The evolution of the multiplet primary spacing contains three stages as indicated in Figure 4.35-a. The three stages can be related to the three stages of

multiplet surface evolution illustrated in Figure 4.31. In fact, this measurement is just the average of the multiplet area measurement with radial length. The first stage starts when all multiplets can be distinguished and it points out the growth of multiplets. The second stage shows that a great amount of multiplets have reached their critical size so that the average primary spacing drops quickly. The last stage corresponds to the end of splitting process.

The sub cell average spacing evolution (Figure 4.35-b) shows a drop of λ during the first stage, which can be explained by the generation of new sub cells during the growth of multiplets. After this stage, the size of sub-cells is almost constant as also evidenced in Figure 4.36-a where the distribution of primary spacing does not present any remarkable evolution between 51.4 mm and 58.6 mm of growth. This indicates that the majority of sub cells are generated during the first stage. And the multiplet structures are not fully developed until the end of first stage. The variation of sub cell primary spacing in second stage indicates a decrease of the total number of sub cells before a return to the average spacing that is kept until the end of experiment. The origin of this evolution is not identified yet.

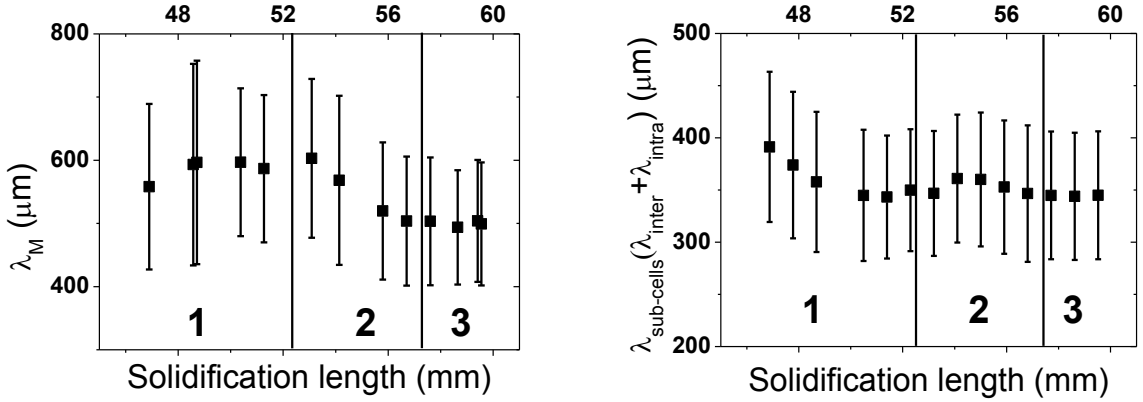

a b

Figure 4.35. Time evolution of the primary spacing of a) multiplet and b) sub cells.

In Figure 4.36 the histograms of primary spacing as a function of solidification length are presented. The sub cells present a behavior similar to cellular structures with a pick of spacing selection. This distribution is quite different to those found in 2D samples [63] where 2 peaks corresponding to the different selections between λ_{inter} and λ_{intra} were observed.

The spacing of both multiplets and sub cells are presented in Figure 4.37-a with a log scale where the primary spacing for all different pulling rates are plotted together. It is interesting to note that the spacing of multiplet structure is located close to the same

line of the evolution of the primary spacing for dendritic structures. Meanwhile, the spacing for sub cells is found in the tendency of cellular spacing evolution.

Results of Minimal spanning tree (MST) measurements are shown in Figure 4.37-b. The two solid lines correspond to an array of hexagonal and square structure respectively. The sub cells always have a higher order level compared with multiplet structure. It is noticed that both sub cells and multiplets have a similar behavior: disorder increases at the beginning and goes back to the first point. The multiplet patterns tends to be more "hexagonal" when compared to sub cell patterns even if the difference is not so obvious.

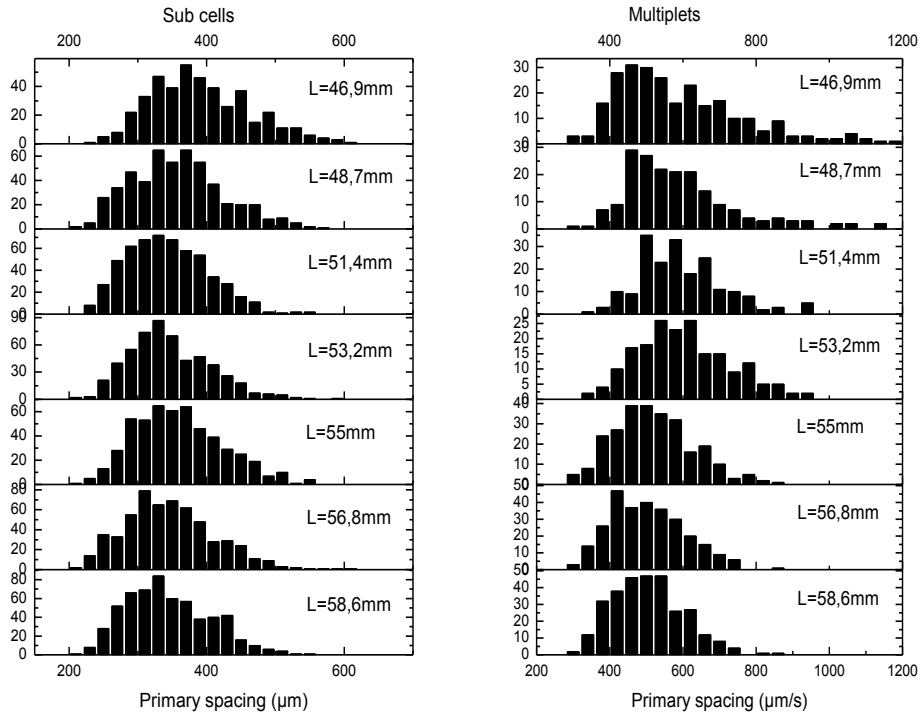

Figure 4.36. Distribution of the sub cell primary and multiplets spacings, L is the solidification length.

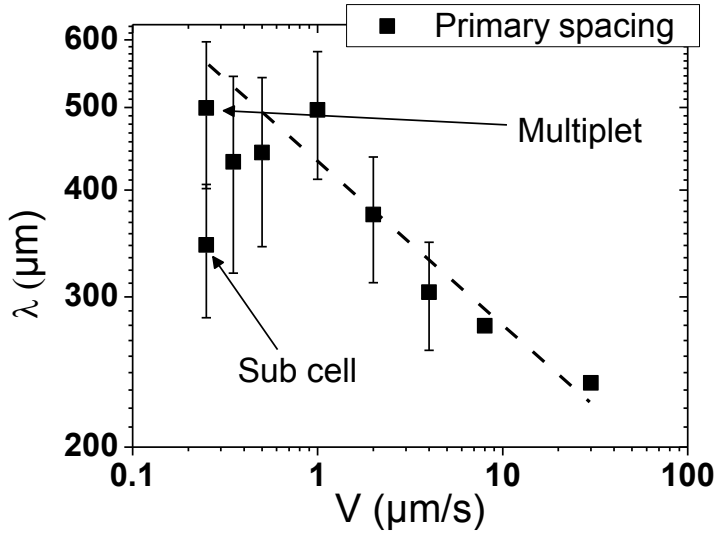

a

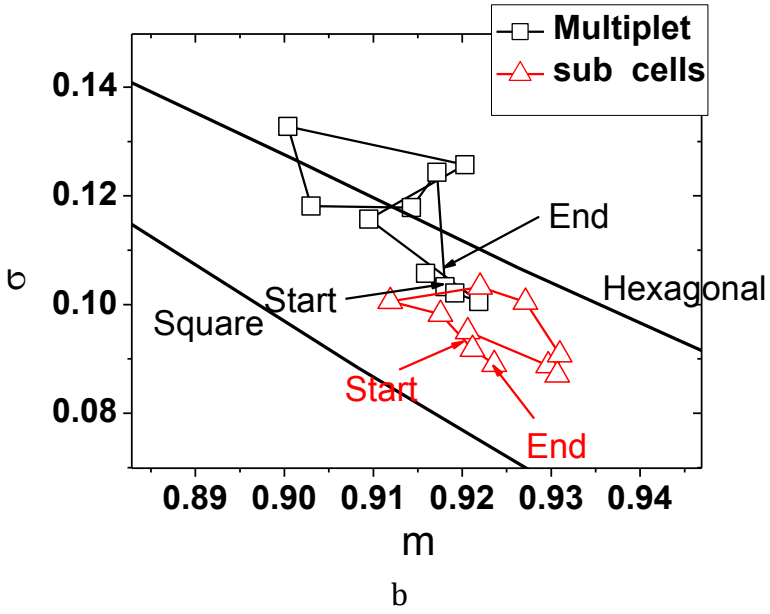

b

Figure 4.37. a) Primary spacing as a function of pulling rate. b) The minimal spanning tree for both multiplet and sub cells. (V = 0.25 µm/s, G = 28 K/cm).

Some parameters, like the λ_{inter}, λ_{intra}, $\lambda_{sub\ cell\text{-}pit}$ and the depth of the pit, should be measured individually. Those parameters characterize the properties inside the multiplets. The systematic measurement with software is not yet available. Therefore, we chose the 3 typical structures in Figure 4.21 to obtain manually those characteristic parameters. Multiplets A and B are in the center of the interface and C is closer to the border. Results are shown in Figure 4.38 and Figure 4.39.

Figure 4.38-a shows the amplitude between each tip of the sub cells and the bottom of the pit, for multiplets B and C. The depth evolution has the same behavior for the two

multiplets. It can be divided into three parts: 1) slow evolution, the amplitude increase from 0 to 160 µm; 2) fast evolution, where amplitude increases faster from 160 µm to 400 µm; 3) saturation at about 400 µm. This evolution includes the growth of the sub cells and the deeping of the pit. The superposition of the depth measurement for all sub cells of a multiplet is consistent with a unique growth velocity for all of them. The delay of growth observed between the two multiplets is due to their different radial positions; as already mentioned, a propagation of morphological instability is observed from the border towards the center due to convexity. However the amplitude of saturation is the same; this fact may indicate a steady – state growth.

Measurements of different spacings inside the multiplet begin when the sub cells and pit are developed and stop when the multiplet splits. Both $\lambda_{sub\ cell\text{-}pit}$ and λ_{intra} increase during the solidification (Figure 4.38-b and Figure 4.39-a, respectively). The origin of this increase is attributes to the multiplet surface growth. Instead, λ_{inter} keeps constant at about 300 µm during the solidification (Figure 4.39-b). This measurement of λ_{inter} and λ_{intra} gives us some information that cannot be obtained from the previous measurement of the mixed sub cells spacing. The λ_{inter} and λ_{intra} follow different selection rules during the growth. The constant value of λ_{inter} indicates that there is no variation of the width of the groove between two adjacent multiplets and that this selection is sharp. On the contrary, internal grooves are transitional and evolve continuously during growth.

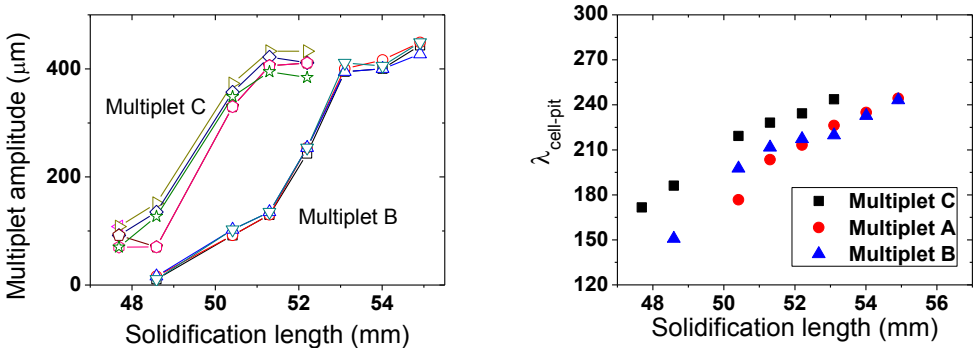

a b

Figure 4.38. a). Amplitude between the sub cell tip and the bottom of the pit. b). Average value of the spacing between the sub cells and the pit. (V = 0.25 µm/S, G = 12 K/cm)

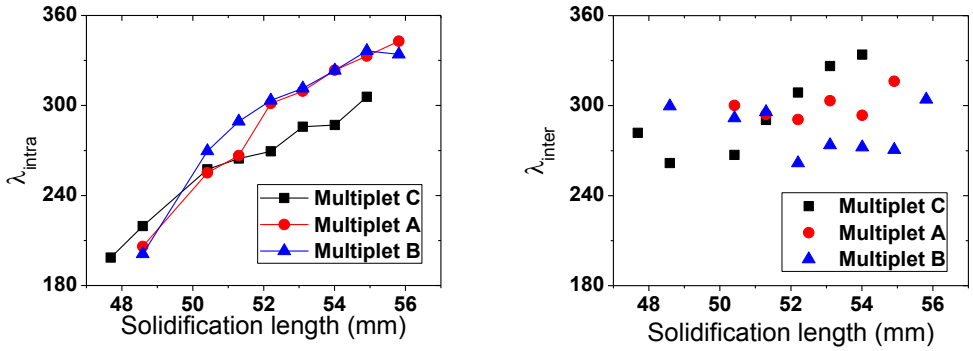

a b

Figure 4.39. λ_{intra} and λ_{inter} for 3 multiplets as a function of the solidification length. (V = 0.25 µm/S, G = 12 K/cm)

4.3.3. Conclusion and discussion

Multiplets structures in directional solidification are observed for the first time in a 3D sample, in a narrow range of pulling rates close to the critical velocity. A much complex pattern is observed when compared to 2D doublets. Several measurements are done to characterize multiplets properties and dynamics. The basic origin of spacing evolution is found to be associated to their radial movement to the convex interface, which includes the splitting of the multiplet structure and cell elimination at the border. Measurement of the evolution of multiplet surfaces confirmed that the increase of multiplet surface (or spacing) is simply the consequence of this lateral movement. This also explains the increase of the intra spacing and the splitting due to the stretching of multiplet structure. The evolution of multiplet structure shows that they start growing as cells, and once a critical spacing value is reached, sub cells appear by tip splitting. A sharp selection of the spacing between adjacent multiplets is revealed by its insensitivity to the multiplet growth that in contrary induces a growth of the internal spacing. The question of multiplet formation for the same growth parameters for a macroscopically flat interface is still open considering the crucial influence of convexity on the multiplet dynamics in our experiment. Numerical simulation in 3D phase field has started in the TMS team of IM2NP and DSIP group in Boston on this multiplet topic that should help to clarify this issue.

Chapter 5. Comparison 1g versus μg

5.1. Introduction

Convection in the melt is always present in bulk samples during solidification on ground. Since the theoretical models are based on the diffusive transport mode, the effects of convection in both metallic and transparent organic systems have been widely investigated. These studies show that the existence of convection may greatly affect the interface morphology: first, fluid flow induces a shift of the critical transition velocity from smooth/cellular to cellular/dendritic interface, tending to delay those transitions of alloy with $k < 1$ [182],[26],[22]. The primary spacing when convection is present is smaller than for μg experiments and secondary arm spacing is found to increase due to the convection in the liquid grooves between dendrites [182],[183],[75]. The distribution of cells and dendrites spacing was found to be broader and irregular under the influence of convection [83]. In directional solidification, the concentration redistribution in front of the interface results in a lateral gradient of microstructures [184], and also localized microstructures [71]. The growth direction and tip velocity of cellular and dendritic structures are also affected by the flow. The dendrite tips were found to grow in the opposite direction of the flow [85], while cells grow following the fluid flow direction [185]. The dendrite tips or secondary arms which grow against the flow have a smaller tip radius and grow faster than those following the flow direction [85–87].

To analyze the effect of convection, series of comparative experiments on ground were realized after the DSI insert return on earth. Those ground experiments were carried out with the same control parameters, the only difference being the presence of convection.

5.2. Nature of convection

In absence of forced convection, generated on purpose to enhance heat and solute transports, convection on earth is driven by buoyancy. Natural convection in directional solidification can come from density differences between two phases, non-uniform surface tension (Marangoni convection) at the interface, or the density difference in a temperature or concentration gradient (thermal convection or solutal convection). The first two kinds of convection are usually negligible when the third one is present [66,67].

Thermosolutal convection (also called double diffusive convection) appears during upward directional solidification for partition coefficient $k<1$ when the solute is lighter than the solvent. In our experiments, $k=0.2$ but $\rho_{camphor} > \rho_{SCN}$, thermosolutal convection is negligible.

The thermal field in the crucible has been calculated using the CrysVUn® software for different growth conditions are given in Figure 5.1. The macroscopic shape of the interface at rest reflects the liquids shape; depending on its location in the adiabatic area, it may be concave or convex. The final steady-state interface position depends on its initial position at V = 0 and the pulling velocity during solidification. In our experiments, a curved interface is generally observed: most of the time, the interface is concave. But for low gradient and low pulling rates, a convex interface is observed.

Concave interface:

The origin of the concavity of the interface is the low conductivity of the alloy compared to the crucible one. Therefore, the latent heat generated during pulling is mainly evacuated radially through the crucible wall. A radial thermal gradient is then generated at the solid-liquid interface. As the heat at the border diffuses faster than in the center, the center is hotter than the border, isotherms are curved and the interface turns to concave: Figure 5.1.-b.

Convex interface:

For lower pulling rates, generation of latent heat is weak and, depending on the thermal field, the interface may remain in an area where isotherms shapes are convex: for example, Figure 5.1.-d. This means that the dominant heat flux in that case is the entering one generated by the hot zone heater.

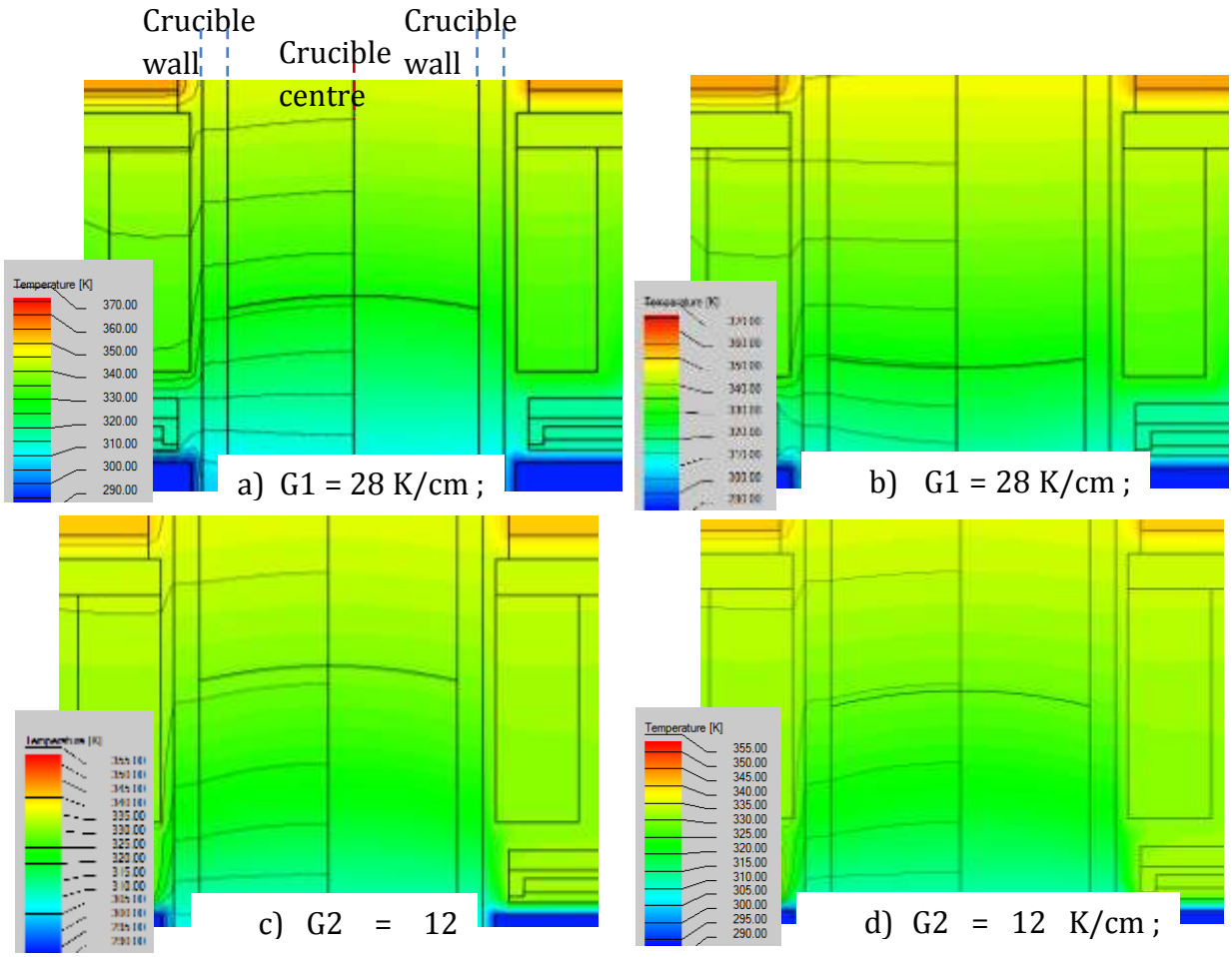

Figure 5.1. CrysVUn simulation of the thermal field in the "adiabatic" area of DECLIC-DSI (axisymmetric geometry) With SCN-0.24 %pds camphor. The dark line corresponds to the interface, thus revealing its shape for different thermal and growth conditions. a) and c) Interface shape at rest (V=0) for the 2 different sets of temperatures that we applied during our experiments, respectively named G1 (= 28 K/cm) and G2 (= 12 K/cm); b) Interface shape during growth (V=8 µm/s) for G1; d) Interface shape during growth (V = 0.5 µm/s) for G2.

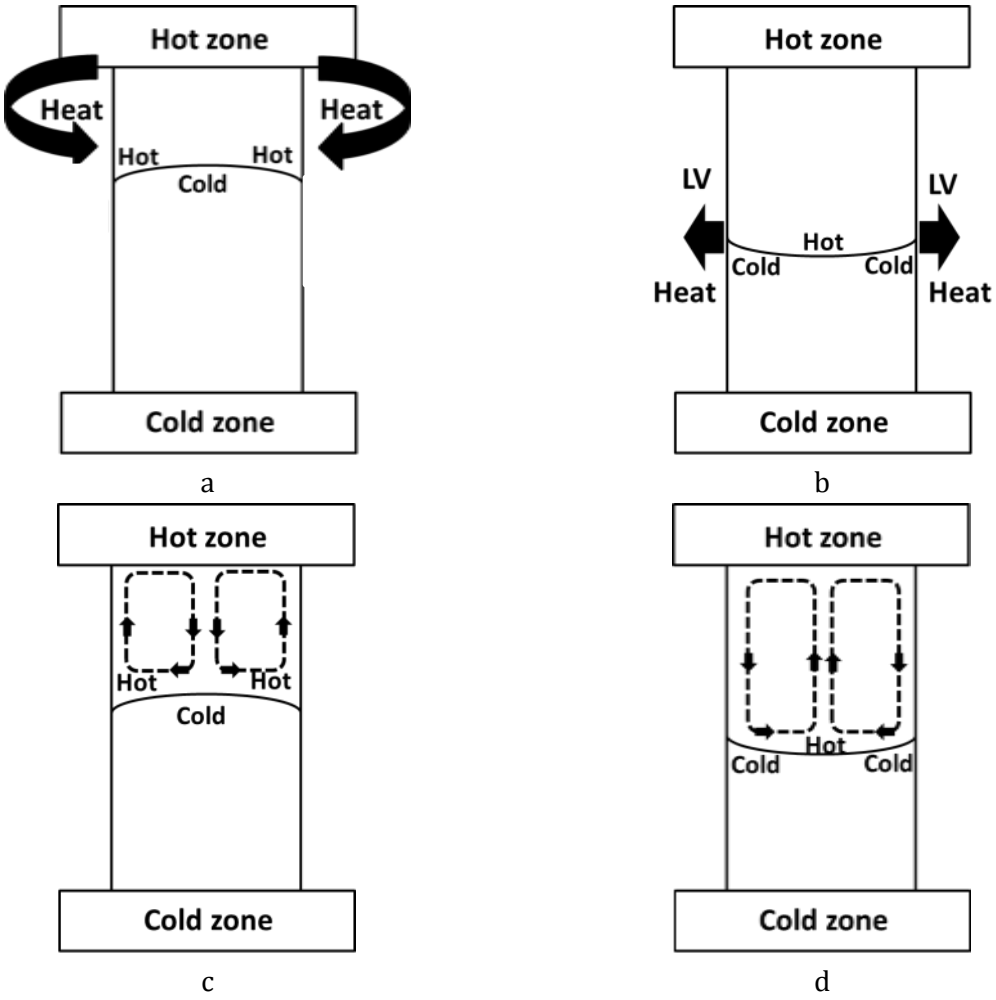

Figure 5.2. The concave a) and convex b) interfaces observed in our experiments, and the respective convection fluid flows (c and d).

On ground, the radial thermal gradient induces thermal convection. In case of a concave interface, the liquid in the center is hotter than on the border: the hot liquid with lower density is driven upwards by the buoyancy so that a convection loop ascending in the center and descending on the border forms. For a convex interface, the hot liquid is at the border and the cold liquid is in the center, so the direction of the fluid flow is inversed (Figure 5.2). A simulation done with CrysVUn (Figure 5.3) illustrates the different fluid flow directions depending on the interface shape [150]. In that case, the interface shape is controlled by adjusting the temperature of the Booster Heater (BH): If the BH is switched off, the interface is concave. For a temperature of BH of 55°C, the interface becomes flat while at 65 °C it turns to convex. Figure 5.3-d gives the variation of the radial component of fluid flow along the interface for these 3 situations. It illustrates the inversion of the fluid flow between concave and convex interfaces, and that a quasi-zero flow is obtained for a flat interface.

As a conclusion, thermal convection is dominated either by the evacuation of latent heat or by the heat injection from the furnace. The radial thermal gradient at the interface

and the resulting interface shape indicates the dominant phenomenon and the fluid flow direction.

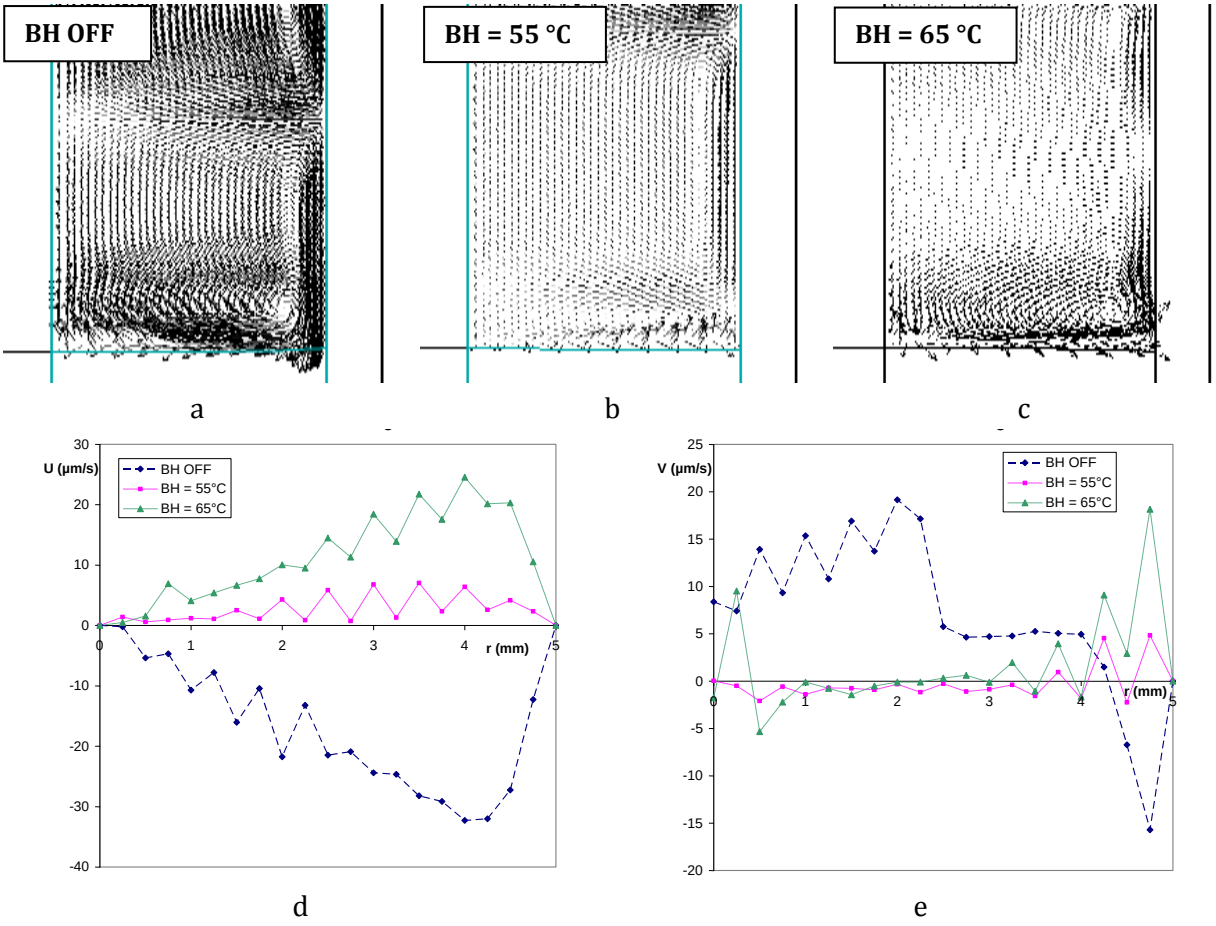

Figure 5.3. Simulation with CrysVUn. The interface curvature changes with the Booster heater (BH) temperature. a-c, the velocity field with BH off (concave interface), BH temperature of 55 °C (quasi-planar interface) and 65 °C (convex interface), respectively; d and e, the radial and axial fluid flow velocity at 0.22mm above the interface, respectively. (SCN-0.1% pds camphor, V = 5 µm/s, G = 18K/cm)

5.3. Experimental procedure

Experiments in the DSI have been realized on ground in the DECLIC engineering model. The two different sets of temperatures used in µg, respectively corresponding to G_1 = 28 K/cm and G_2 = 12 K/cm have been used. Values of thermal gradients on ground have been checked by the same in situ measurement method used in space (see chapter 2) and it appeared that the gradients are slightly reduced by convection, giving $G_{1,1g}$ = 24 K/cm and $G_{2,1g}$ = 11 K/cm. For each run, the gradient is kept constant, and the pulling rate is changed from 0.5 µm/s to 30 µm/s. The observation and image treatment methods are the same as for the µg experiments in chapter 3. The primary spacing has been measured and the results are compared with the µg experiments.

5.4. Comparison between µg and ground experiments

5.4.1. Effect of convection on the critical velocity of morphological instability of the planar front

The critical velocity from planar to cellular interface is shifted towards higher velocity on ground as illustrated in Figure 5.4. For G = 12 K/cm, cells are fully developed at V = 0.5 µm/s (Figure 5.4-a) whereas for the same velocity, the interface is still smooth on ground (Figure 5.4-b). A similar behavior is observed for G = 28 K/cm comparing Figure 5.4 c and d.

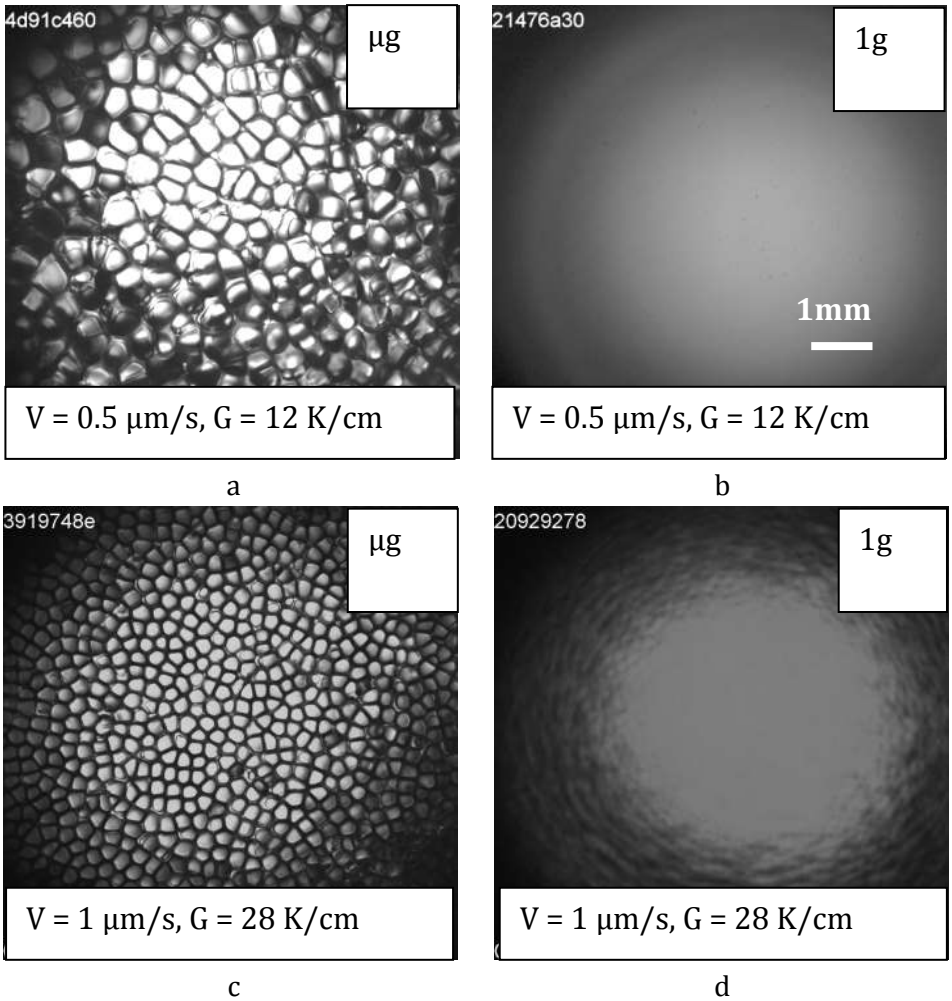

Figure 5.4. Top view of the interface: a) and b), at V=0.5 µm/s, G = 12 K/cm. c), d) and,e) at V=1 µm/s, G = 12 K/cm. All images are taken at the solidification length of 43 mm.

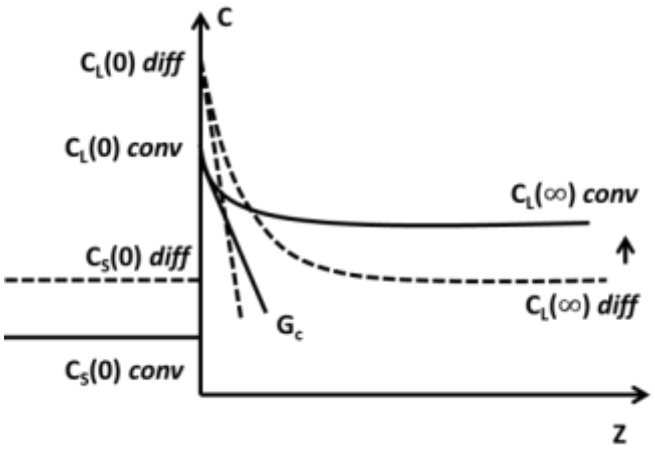

Figure 5.5. Concentration profile in front of the solid liquid interface with (solid lines) and without convection (dotted lines).

The critical velocity V_c, in diffusive transport condition, is calculated taking into account the constitutional super-cooling criterion:

$$V_c = \frac{DGk}{mC_\infty(k-1)} \qquad 5.1$$

where the D is the diffusion coefficient, G the temperature gradient, k the solute redistribution coefficient, m is the liquidus slope, C_∞ the liquid concentration far from the interface.

The velocity is equal to 0.25 µm/s for G = 12 K/cm and 0.49 µm/s for G = 28 K/cm, in µg experiments. Both of them are lower than the critical velocity in 1g experiments. The cause of that difference is related to natural convection. The toric convection transports the solute from the interface neighborhood to the liquid far from the interface, and this tends to increase the concentration far away from the interface C_∞ and reduce the thickness of the solute boundary layer δ. As a consequence of the mass conservation principle, the solute concentration in the liquid at the interface $C_L(0)$ decreases compared to diffusive conditions, as well as the solute concentration in the solid $C_s(0)$ which is related to $C_L(0)$ by the partition coefficient k. Therefore, the concentration gradient at the interface decreases ($G_{c\,conv} < G_{c\,diff}$) as illustrated in Figure 5.5, the driving force for the interface instability m G_c is reduced, inducing a stabilization of the interface and the shift of critical velocity.

The interface instability driving force m $G_{c\,conv}$ can be written as k_{eff} m $G_{c\,diff}$ with:

$k_{eff} = \frac{C_s(0)}{C(\infty)}$ the effective segregation coefficient.

k_{eff} = 1 in case of a purely diffusive situation, it tends towards k when the solute boundary layer decreases (convective mode). Therefore the M.S. criterion for morphological stability $G/(mG_{c\ conv}) \geq S$ (S~1) turns to:

$$G/(mG_{c\ diff}) \geq k_{eff} \qquad 5.2$$

The effective segregation coefficient can then be estimated in our experiments comparing the critical velocities on ground and in μg:

$$\frac{V_{c\ conv}}{V_{c\ diff}} = \frac{1}{k_{eff}} \qquad 5.3$$

From Equation 5.3, k_{eff} is about 0.5 for both temperature gradients.

5.4.2. *Radial gradient of microstructure.*

The comparison of 1g and µg top and side view images, for pulling rates varying from 2 to 16 µm/s (G = 28 K/cm) is given in Figure 5.6. For high pulling rates (V = 12 and 16 µm/s), the solid liquid interface dropped out of the observation zone of the longitudinal section, so that the interface shape is unknown.

The bright and grey parts of side-view images correspond to the liquid and solid respectively, as indicated in Figure 5.6. The black line in the grey part is the solid-liquid interface. The solute accumulation effect is obvious: the interface shape of ground experiments are more curved compared to µg ones, except for V = 8 µm/s. This effect is present even for a quasi-flat interface (V = 2 µm/s).

The origin of this difference in interface curvature is well known: the solute rejected upon solidification is swept by the convection and accumulated at the center, for a concave interface, or at the border, for a convex interface (see Figure 5.7). The liquid solute concentration then varies along the interface, thus modifying locally the equilibrium temperature of the interface. Accumulation induces a decrease of the interface temperature and a resulting increase of the curvature. These accumulation effects can be noticed from the modification of the interface shape: the interface front recoils where the solute accumulates.

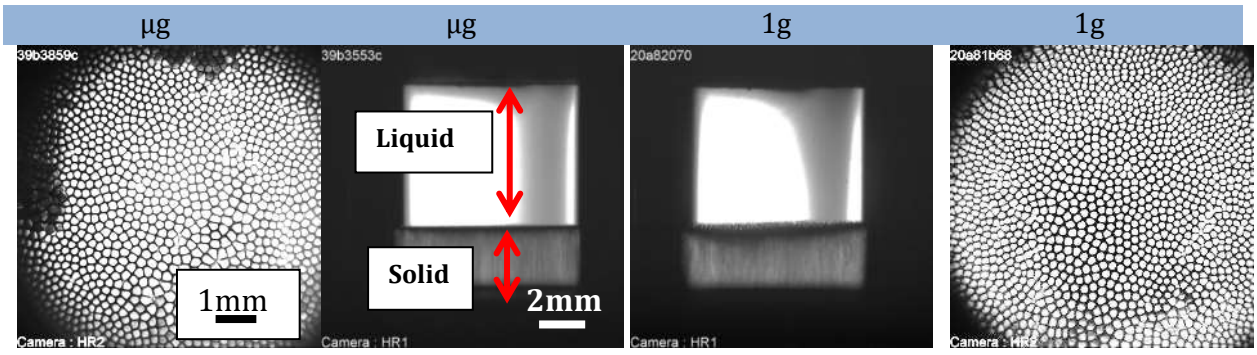

V = 2 µm/s, G = 28 K/cm

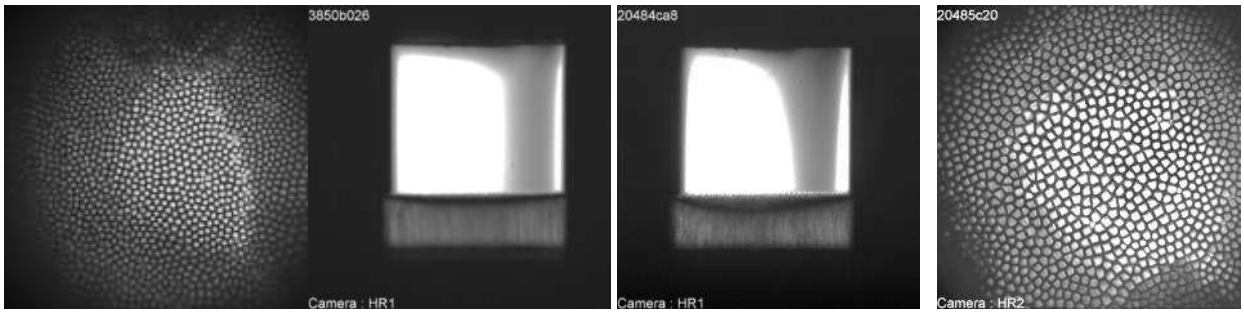

V = 4 µm/s, G = 28 K/cm

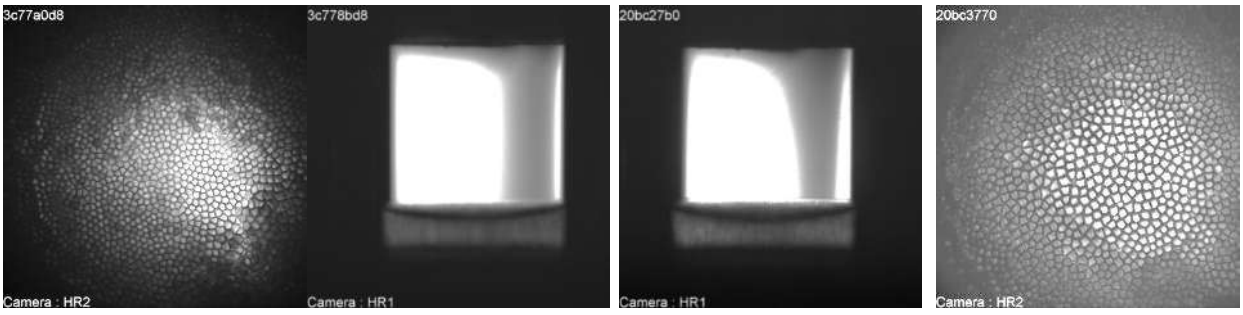

V = 6 μm/s, G = 28 K/cm

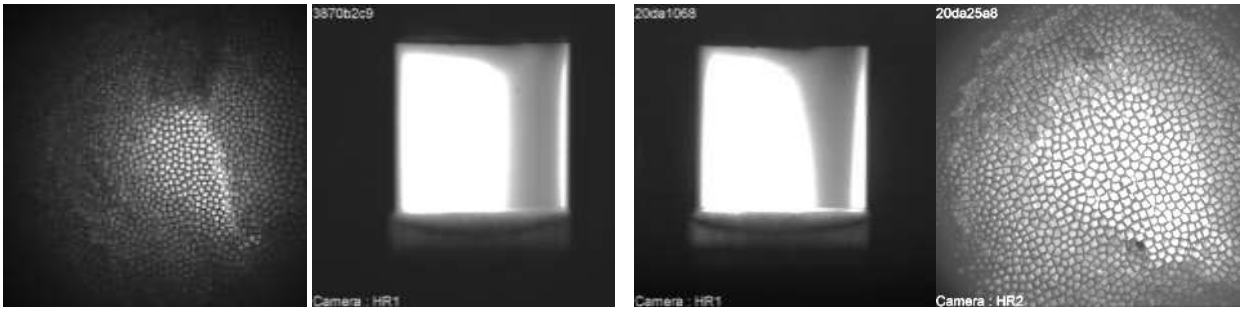

V = 8 μm/s, G = 28 K/cm

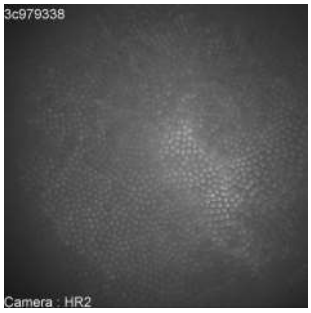

No image

No image

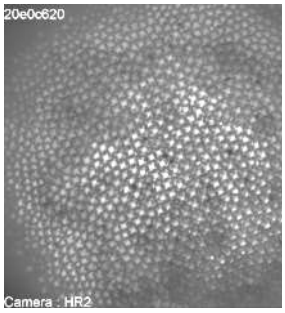

V = 12 μm/s, G = 28 K/cm

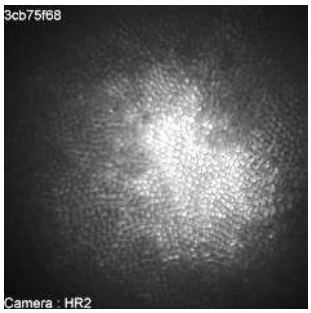

No image

No image

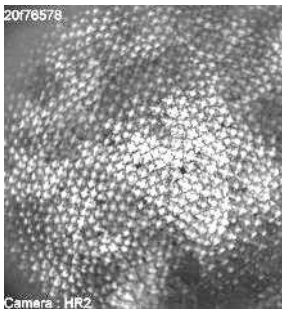

V = 16 μm/s, G = 28 K/cm

Figure 5.6. Comparison of microstructures and interface shapes in μg and on ground for different pulling rates (G = 28 K/cm, solidification length ~34 mm).

The maximum effect of convection at the interface curvature is found at V = 4 μm/s. For a higher pulling rate, V = 6μm/s, the difference became smaller until no difference (for V = 8 μm/s). It may be surprising as latent heat increases with pulling rate, as well as convective flow. The curvature difference between μg and 1g interface shapes should keep increasing. We may analyze this "saturation" effect on the interface shape on the basis of the microstructure evolution. For 6 and 8 μm/s, deeper structures develop

(deep cells and dendrites) so that the latent heat generation is more distributed along the mushy zone and the curvature difference is reduced.

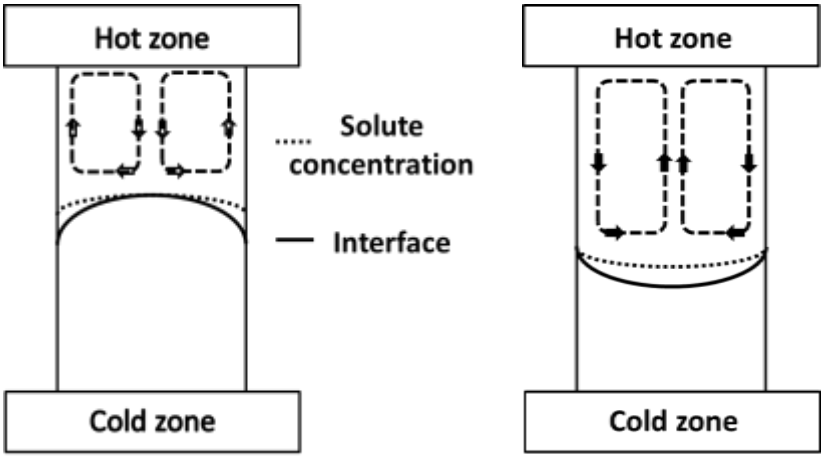

a b

Figure 5.7. Schematic presentation of the effect of solute accumulation under the effect of convection. a) Convex interface. b) Concave interface.

The variation of solute concentration along the interface directly affects microstructure formation and selection. Morphological instability develops during the transient stage while the solute boundary layer builds up. The gradient of concentration induces an inhomogeneous triggering of instability as instability first develops in higher concentration areas. This is for example illustrated on Figure 5.8 that corresponds to a growth with a convex interface. In that case, solute accumulates near the crucible wall where, as the consequence, starts the formation of cells. During transient, the boundary layer increases everywhere so that morphological instability progressively propagates towards the center (see Figure 5.8-b).

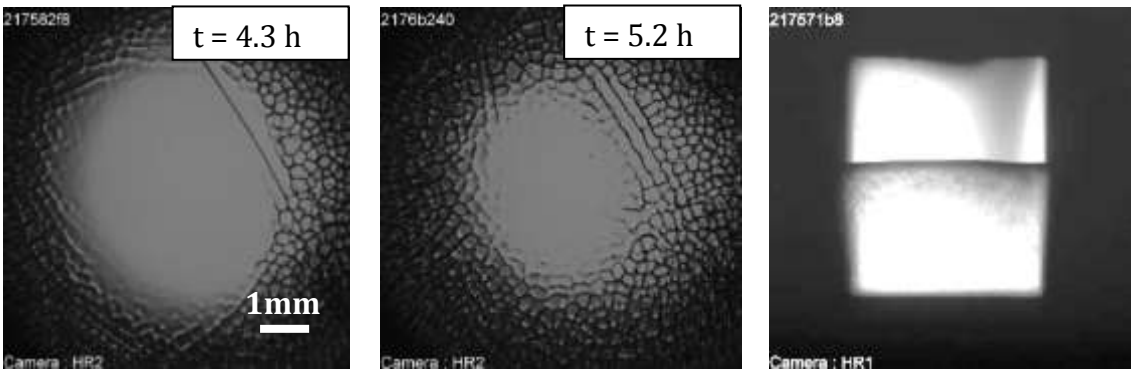

a b c

Figure 5.8. Progression of the morphological instability during transient (V = 1 µm/s, G = 12 K/cm) a) t = 4.3 h. b) t = 5.2 h. c) Side view at t = 4.3h.

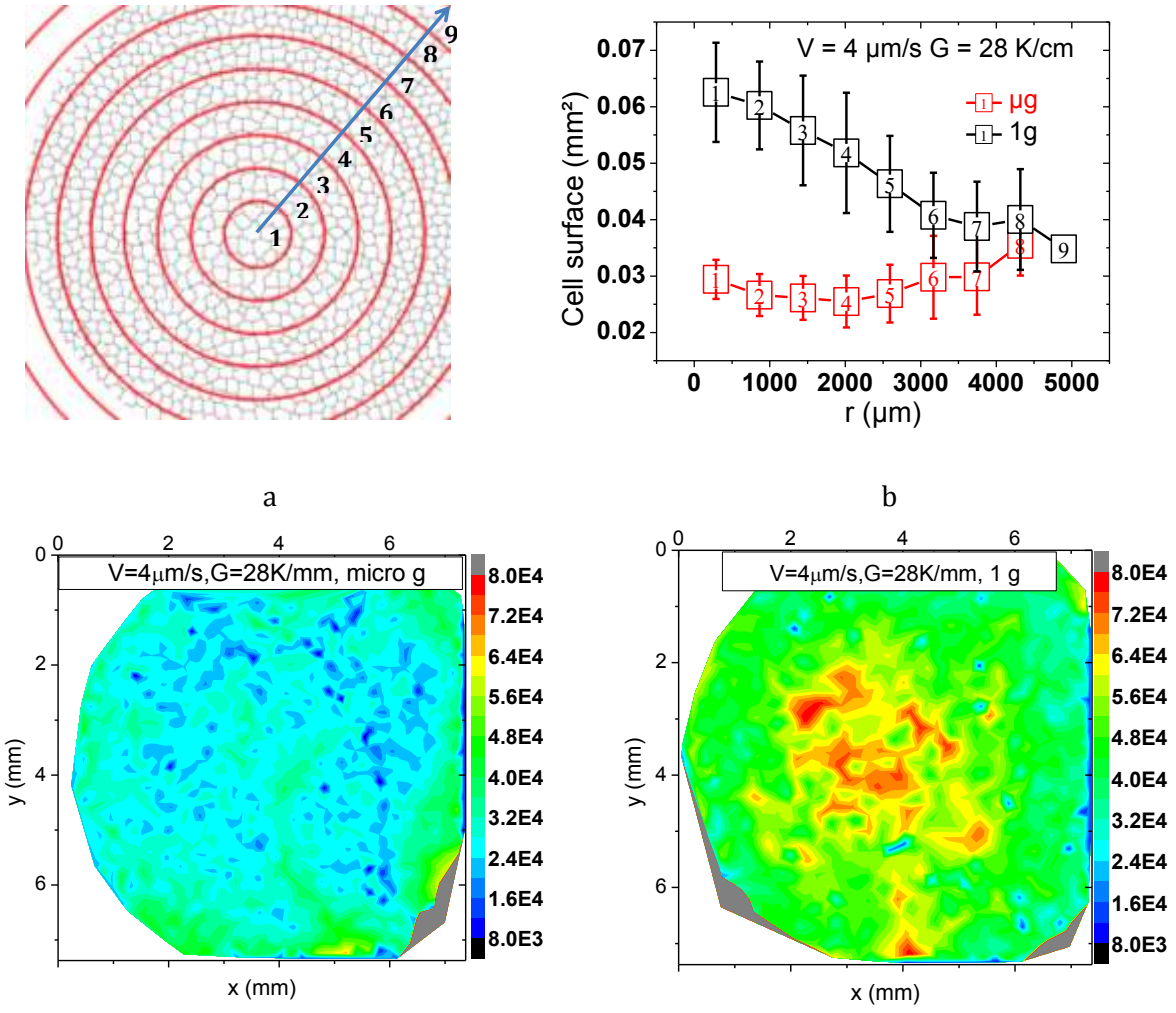

Figure 5.9. Measurement of the radial distribution of the cell size, with v = 4 µm/s, G = 28 K/cm. Figure a) is an example where the image is cut from the center. The numbers of the circles are indicated. Figure c) and d) are the maps of the cell size for µg and 1g, respectively.

The observation of top-view images reveals a difference between µg and ground experiments in term of microstructure homogeneity. For example, for V_p = 4 µm/s on ground, larger cells are observed in the center compared to the border, whereas cell size is more homogeneous in µg (Figure 5.9 c and d: the map of cell size gives a direct observation of the cell size variation, with red and blue color corresponding to the largest and smallest cells, respectively). This pulling rate is chosen for detailed analyzes as the differences of interface shape are maximum. For this, the interface is splitted in 9 circular areas in which the average cell areas are measured (Figure 5.9-a). The results of these measurements for 1g and µg are given in Figure 5.9-b. A roughly linear decrease of the cell surface from the center to the border of the interface is observed on ground whereas the cell surface in µg is radially homogeneous. This results is typical of a toric

convection ascending in the center and descending at the border, as already reported elsewhere for the same geometries and succinonitrile based alloys [71][145].

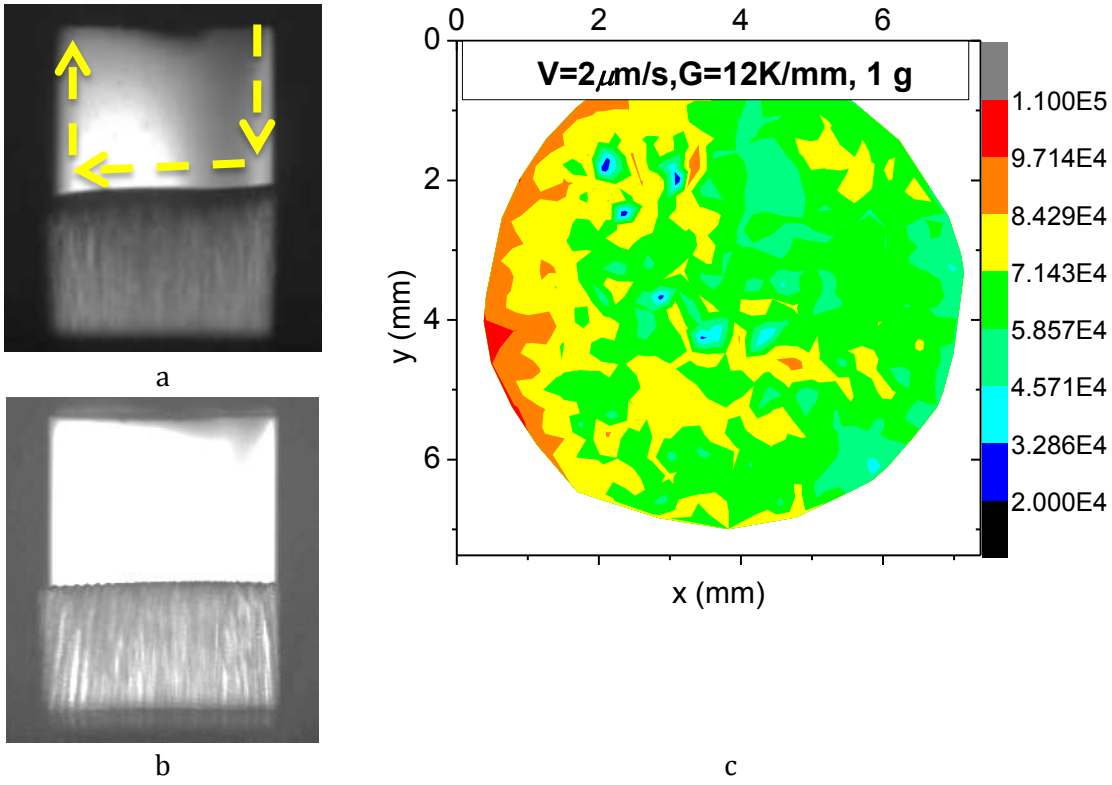

Figure 5.10. a) Asymmetric convection descending at right and ascending at the left. b) Side view from the μg experiments. c) The primary spacing map showing cell size gradient from right to left. (V = 2 μm/s and G = 12 K/cm)

Another interesting situation is the one obtained at G = 12 K/cm for V_p = 2 μm/s. In μg, the interface is almost perfectly flat (Figure 5.10-a) but on ground, the interface presents a non-axisymmetric shape with the left border lower than the right side (Figure 5.10-c), associated to a thermal gradient from left to right. In that case, a unique loop of convection takes place, ascending on the left and descending on the right, as illustrated on Figure 5.10-c. The gradient of solute concentration along the interface due to fluid flow is then from the right side to the left side. The map of primary spacing reflects this variation as λ tends to be larger on the left side of the sample. It is worth noting that spacing variation are not very large and are probably reflecting the very low fluid flow velocities associated to this very low interface tilt. Close to the border, the interface presents some curvature associated to solute accumulation (left) and depletion (right).

For this pulling rate, the interface shape in μg indicates that latent heat evacuation, which is an axisymmetric phenomenon, is compensated at the interface by other thermal fluxes. In that case, any thermal asymmetry of the system will become dominant and amplified by convection on ground, thus explaining the non – axisymmetric interface shape.

5.4.3. *Evolution of primary spacing with pulling rate*

The primary spacing was measured as a function of pulling rate and compared to the results obtained in µg condition as presented in Figure 5.11. For the two studied gradients, the primary spacing increases with pulling rate on ground.

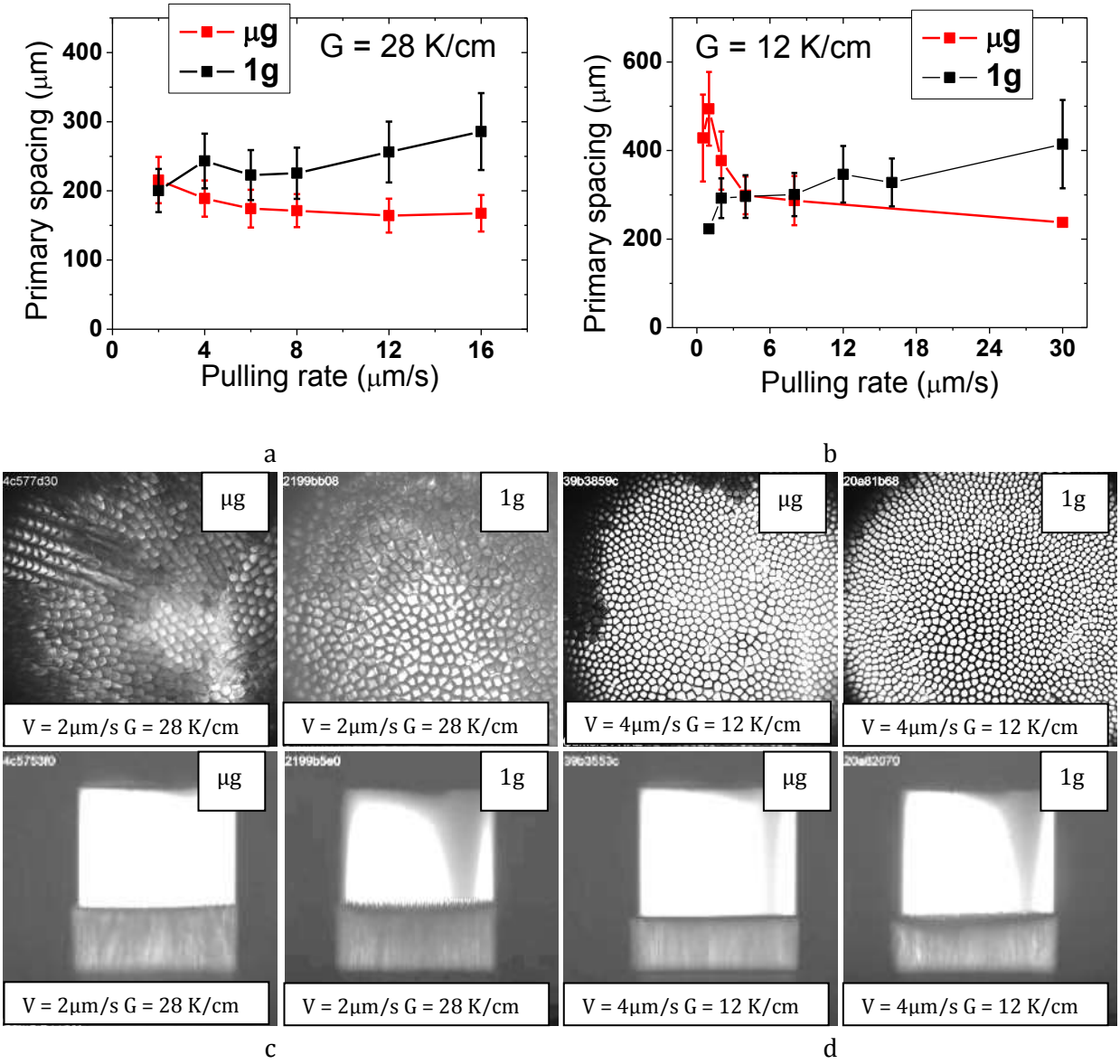

Figure 5.11. Primary spacing as a function of pulling rate, for 1g and µg conditions: a, G=28K/cm; b, G=12K/cm. c and d are the comparative top view and side view images for the 2 pulling rates.

For G = 28 K/cm, at V = 2 µm/s (first point of Figure 5.11-a), the primary spacing is similar in µg and on ground. In that case, both interfaces are always flat, which is associated to a very weak convection (Figure 5.3-b). When the pulling rate increases, spacings on ground turn to higher values than in µg, and the difference keeps increasing

with pulling rate. For those velocities, interfaces are concave, which is associated to a toric convection ascending in the center and descending on the border.

For G=12K/cm (Figure 5.11-b), the primary spacing evolution should be studied in two parts. If the pulling rate is smaller than 4µm/s, the convection tends to decrease the primary spacing. This difference becomes smaller when the pulling rate increases. If the pulling rate is higher than 4µm/s, the convection tends to increase the primary spacing, as in the case of G = 28K/cm.

The different convection effect on the primary spacing, for G = 12K/cm, is related to the change of flow direction (associated to the change of interface shape). For V < 4µm/s, with a convex interface, the flow descends in the center and ascends in the border. A relationship to link the primary spacing under convection to the fluid velocity is proposed by [183]:

$$\lambda = \lambda_0 \left(1 + \frac{U_{\parallel}}{V}\right)^{-\frac{1}{2}} \qquad 5.4$$

$U_{\parallel}$ is the downward component of fluid velocity, λ and λ_0 are the primary spacings respectively with and without influence of convection. It is worth noting that this equation was developed for a downward component of fluid flow, taking into account the modification of transport in grooves due to an additional component of velocity $U_{\parallel}$ to the growth velocity V. Extending its use to upward velocities, negative value of $U_{\parallel}$ can be obtained. This extension is for sure limited to weak values of fluid velocity compared to growth rate using this relation, a smaller spacing is obtained on ground for a downward flow in the center (case of convex interface) whereas it becomes larger for a upward flow (case of concave interface). The fluid flow velocities are the estimated using Equation 5.4 and results are given in Table 5.1. The variation of fluid velocity as a function of pulling rate is given in Figure 5.12

Table 5.1, Fluid velocities estimated from Equation 5.4.

Pulling rate(µm/s)	G(K/cm)	Downward flow velocity (µm/s)
1	12	3.9
2	12	1.3
4	12	0.076
8	12	-0.72
30	12	-20.1

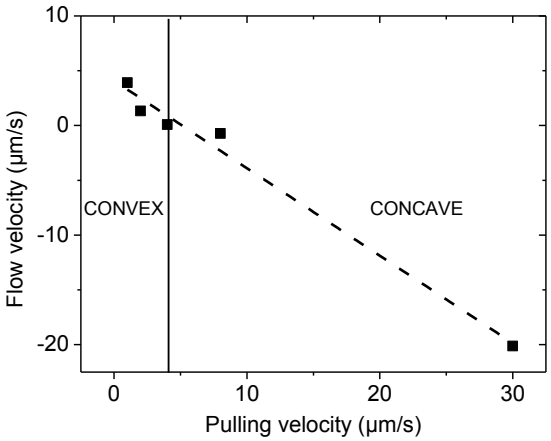

Figure 5.12. The downward component of fluid flow velocity as a function of pulling velocity, and its linear fitting.

Anyway, the increasing of concentration in the liquid due to the convection could also affect the steady state primary spacing since the concentration is one of the control parameters; and this effect increases with the fluid velocity.

If we compare the results obtained in this work with transparent organic alloys to those obtained for metallic alloys, the evolution of primary spacing exhibits major differences. For metallic systems, the convection tends to reduce the primary spacing and its effect vanishes when the pulling rate increases [166]. This discrepancy is related to the different origins of convection. The latent heat always diffuses efficiently through the solid in the metallic solidification experiments so that its effect is negligible compared to the effect of heat injection of the furnace in the liquid area, as discussed in chapter 2. Therefore, in metallic systems as in the case of a convex interface for our organic system, the primary spacing on ground is lower than in µg. The heat injection from the furnace does not strongly depend on pulling velocity, compared to latent heat generation, so that fluid flow velocity can roughly be considered as constant. When the growth rate becomes large enough, the effect of fluid flow is then negligible. Consequently, the interface shape is convex and the convection flow is similar to the studied case with pulling rates smaller than 4 µm/s for G = 12 K/cm.

The primary spacing histograms for G = 28 K/cm and 12 K/cm were obtained as a function of the pulling rate for 1g and µg conditions, and are shown in Figure 5.13. A similar distribution is observed at V = 2 µm/s G = 28 K/cm and V = 4 µm/s, G = 12 K/cm, when the convection is weak. For higher pulling rates, the results from 1g experiments show larger distributions compared to the µg one and a shift of the histograms peaks was observed. The convection not only increases the average primary spacing, but it also enlarges the distribution. This effect is consistent with the radial variation of primary spacing associated to the radial gradient of concentration, which we evidenced in section 4.2.

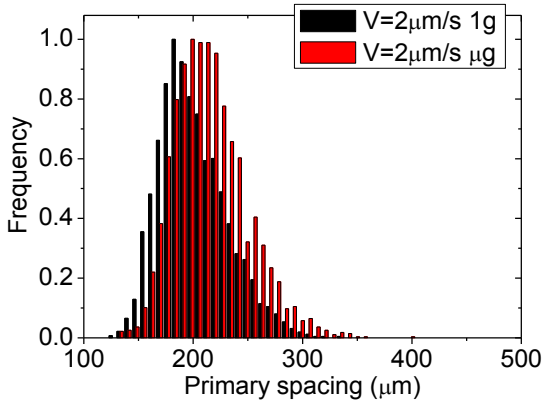
V=2μm/s 1g
V=2μm/s μg
Frequency
Primary spacing (μm)

a

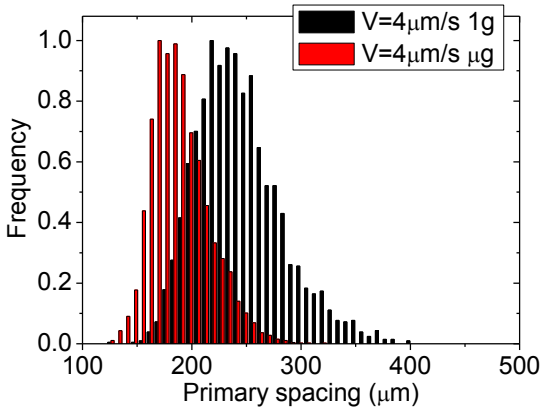
V=4μm/s 1g
V=4μm/s μg
Frequency
Primary spacing (μm)

b

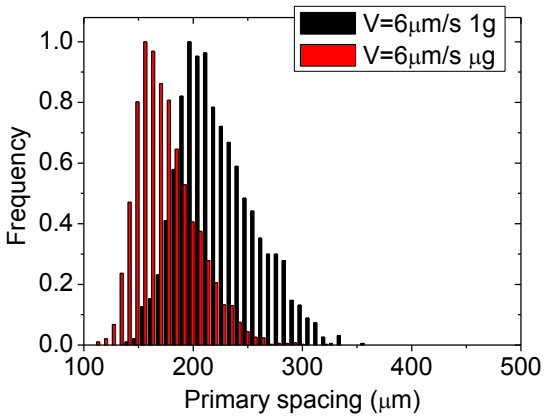
V=6μm/s 1g
V=6μm/s μg
Frequency
Primary spacing (μm)

c

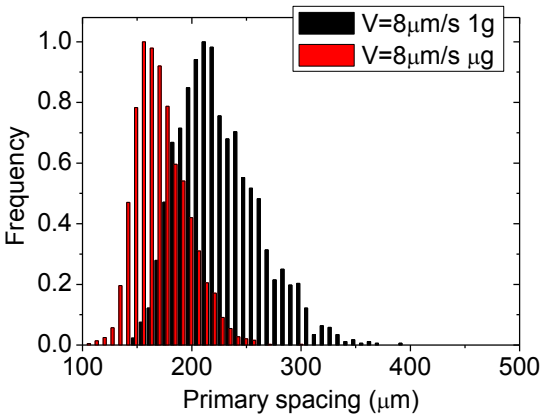
V=8μm/s 1g
V=8μm/s μg
Frequency
Primary spacing (μm)

d

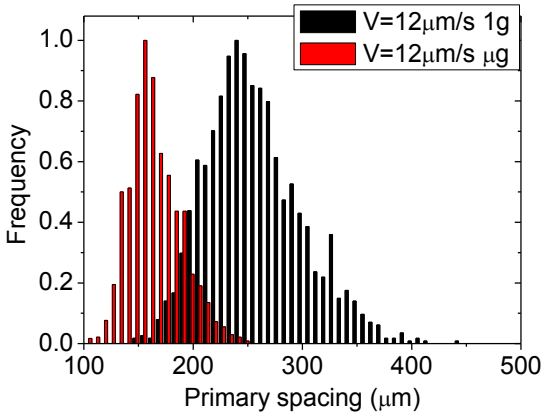
V=12μm/s 1g
V=12μm/s μg
Frequency
Primary spacing (μm)

e

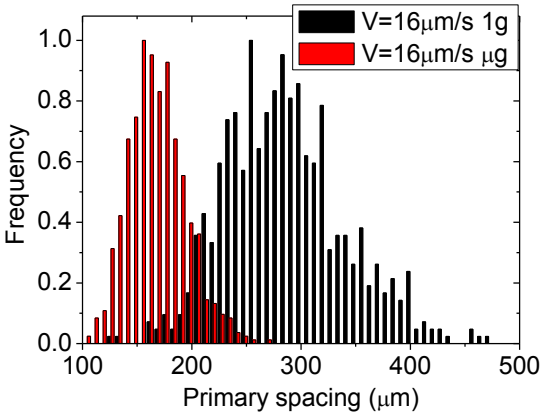
V=16μm/s 1g
V=16μm/s μg
Frequency
Primary spacing (μm)

f

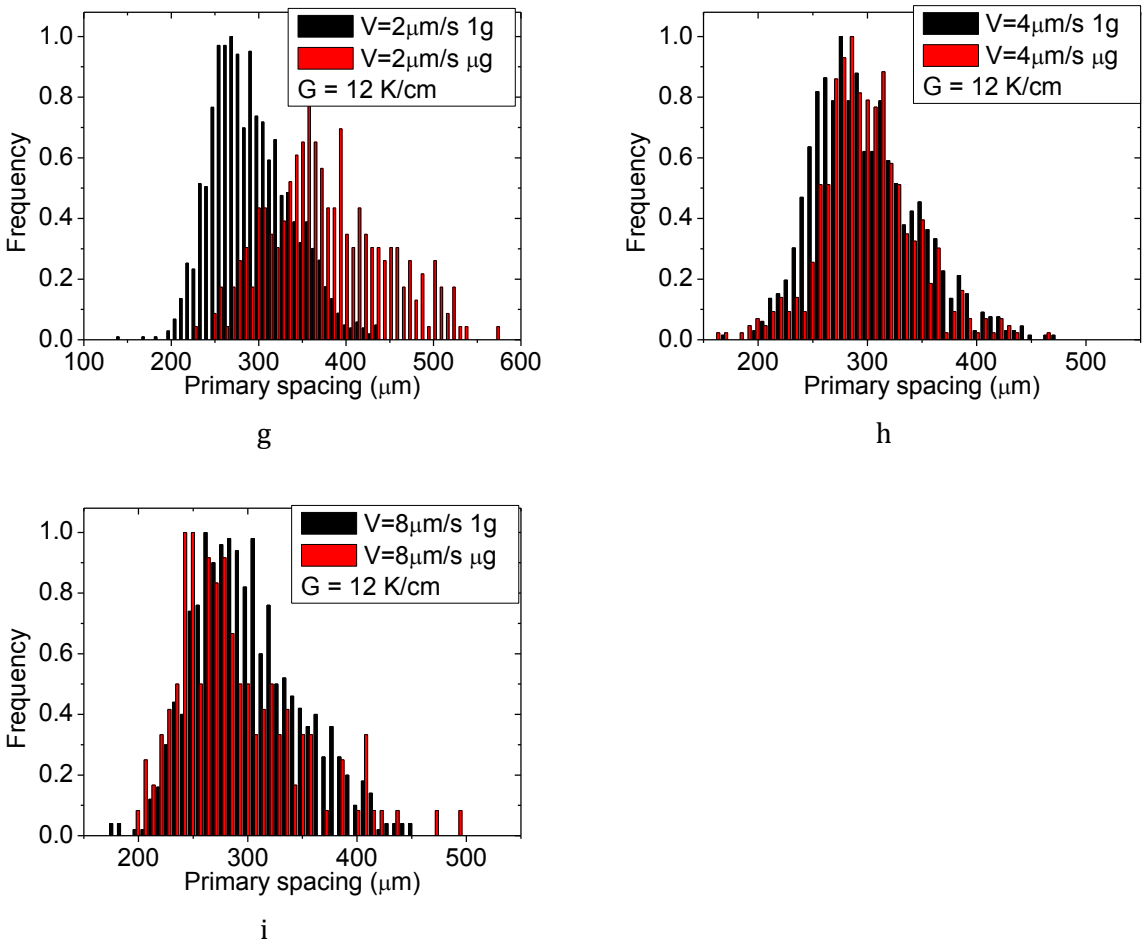

Figure 5.13. Histograms of primary spacing in 1g and μg.

5.5. Conclusion

We studied the influence of convection through the comparison of similar experiments achieved in micro gravity and on ground. The presence of convection increases the critical velocity of transition from planar interface to cellular structure and induces radial gradient of solute concentration which results in a radial gradient of the primary spacing. The average primary spacing is drastically modified by the presence of convection. In contrary with observation on metallic systems, the difference between spacing on ground and in microgravity does not vanished when the pulling rate increases. It appears that this behavior is related to different convection origins. For transparent systems, the main origin of radial thermal gradient, which is the driving force of convection, is the latent heat generation. This phenomenon keeps increasing with pulling rate so that the difference of spacing between μg and ground experiments increases with pulling rate. This latent heat generation induces a concave interface and

the spacing on ground is larger than in μg. For some particular thermal cases, and low pulling rate, one may recover the situation observed in metallic system: radial thermal gradient is due to heat fluxes of the heating device, the interface is convex and the primary spacing on ground is lower than in μg. The convection velocities have been estimated from the difference of primary spacing on ground and in μg using a model developed for metallic systems. However, all those comparative studies evidence once again that convection greatly modifies the interface microstructure morphology therefore stressing the importance of benchmark experiments in absence of convection (μg experiments) to validate numerical models of solidification.

Conclusions and perspectives

The study of solidification microstructure formation is of uppermost importance in the design and processing of new materials. Directional solidification is a powerful technique to study pattern formation since the growth parameters can be accurately controlled. One of the key problems in pattern evolution is the prediction of the specific pattern developed under given growth conditions. Pattern selection occurs under dynamic conditions of growth in which the unstable initial state with a smooth solid liquid interface goes through the process of reorganization into a rather periodic array. In situ observation of the solid-liquid interface is a precious tool to get a detailed knowledge of the entire time-evolution of the interface pattern. This explains the very extensive use of transparent organic analogs that behave like metallic alloys regarding solidification but are transparent to visible light so that classical optical techniques are efficient for their observation.

Extensive ground-based studies carried out in metallic and organic bulk samples have clearly established the presence of significant convection under the growth conditions which give rise to cellular and dendritic structures; this fluid flow interacts with morphological instability thus modifying the characteristics of microstructure. Fluid flow elimination on earth can be obtained by reducing the size of samples but even if such configurations have led to very large progress in understanding the dynamics of solidification, they do not perfectly represent 3D samples and quantitative data extracted from 2D systems cannot be extrapolated to 3D. Fluid flow elimination in 3D samples demands the reduced-gravity environment of space.

The studies presented in this thesis were conducted using the Directional Solidification Insert (DSI) dedicated to in situ and real time characterization of the dynamical selection of the solid-liquid interface morphology on BULK samples of transparent materials. It was developed by the French Space Agency (CNES) in the frame of the DECLIC project (DEvice for the study of Critical LIquids and Crystallization) and it is installed on the International Space Station (ISS) to benefit from a microgravity environment. Directional solidification experiments have been conducted on a succinonitrile-0.24wt% camphor alloy during more than 1 year in space so that a large range of experimental conditions could be explored. Thanks to the in situ diagnostics of the DECLIC-DSI, the whole formation and evolution of the microstructure could be registered. Once the instrument was brought back on earth, similar experiments have been performed to analyze the influence of convection.

The combination of in situ observation on transparent systems and microgravity environment during a so long period offered a very unique possibility to study directional solidification and dynamics of patterns, so that benchmark data required to validate and develop theoretical or numerical modeling could be obtained. During my

thesis, I had to analyze the data resulting from these experiments. It is worth noting that the amount of images generated by each solidification is huge so that an important part of my work dealt with the development of efficient and accurate analysis methods to extract quantitative data from the images. I will first briefly summarize this activity before presenting the most striking scientific results. I will end with a presentation of perspectives.

- **Development of analysis methods**

An important point to notice is that the quality of images in terms of contrast, brightness homogeneity and visibility of interface microstructure strongly depends on growth parameters and on the microstructure developed. Furthermore, visibility changes a lot during one solidification between the initial planar front and the fully developed cellular and dendritic pattern. One of my first goals was then to elaborate a procedure of successive image treatments that fits to the largest number of images to obtain a binary image where each cell/dendrite can be identified. This image is used as an input to several complex macro-procedures that I have developed using a software dedicated to image analysis (Visilog) to extract quantitative measurements that characterize the pattern in terms of primary spacing distribution, number of nearest neighbors, level of disorder (Minimal Spanning Tree).

Specific procedures had also to be developed to treat interferometric images and be able to reconstruct the shape of individual structures (cell, dendrite or multiplet). Those reconstructions are used to extract geometric characteristics of the structures.

- **Scientific conclusions**

- **Formation and evolution of the pattern: primary spacing selection**

Long solidifications at constant pulling rates, for two different values of thermal gradient, have been analyzed. The pattern and its evolution have been described and its quantitative characteristics as a function of time have been measured. The evolution of experimental steady-state primary spacings with pulling velocity and temperature gradient is in good agreement with classical models.

Dynamics of primary spacing selection has been carefully described. It reveals that the classical mechanisms (tip-splitting, overgrowth) that mark the limits of stable spacing and lead to the adjustment of spacing are generally not dominant. Indeed, spacing adjustment was found mainly proceeding through a mechanism of source (where cells are created) and sink (where cells disappear), with collective motion of structures between them. This phenomenon had already been observed in the laboratory in case of concave interfaces with a collective motion of cell towards the center of the interface. In space, it appeared that even for cases of macroscopically roughly flat interfaces,

collective gliding is observed towards defects such as sub-boundaries that act as sink. A perfectly flat interface is unreachable in 3D systems due to the geometry and thermal characteristics of the different materials used, but moreover, defects may create local curvature that affects the whole pattern. Curvature affects the dynamics and potentially the whole selection process so that relevant comparison requires that this curvature is included in modeling.

- **Secondary instabilities : Oscillating patterns and multiplets**

The extended homogeneous patterns obtained in microgravity enabled us to observe secondary instabilities of the cellular pattern for the very first time in 3D solidification. For a restricted range of growth control parameters, the cellular pattern presents breathing oscillations. Oscillating cells are characterized by a periodic variation of both their apparent size (in the (x, y) plane) and of their tip position (in the vertical z direction). Up to know, such oscillating cellular pattern had been studied only in thin samples [54] and a global spatiotemporal coherence over large domains was exhibited by experiments. In contradistinction, present microgravity experiments reveal a richness of 3D breathing modes with limited spatiotemporal coherence only. Our analyses highlight the absence of global coherence of cell oscillations, excepting in locally ordered areas where synchronization of neighbor cells may happen.

In another range of control parameters, another type of secondary instability has been identified that corresponds to multiplet formation; the structure and dynamics of those multiplets have been described. A much complex structure is observed when compared to 2D doublets [63]. Once more, it appeared that the macroscopic curvature of the interface, convex in the growth conditions corresponding to multiplet observation, is critical on the dynamics of these multiplets, affecting the spacing selection, their splitting process and then their multiplicity and stability.

- **Influence of convection**

We studied the influence of convection through the comparison of similar experiments in microgravity and on ground. In such 3D cylindrical transparent systems, convection usually comes from the difficulty to evacuate latent heat that results in a radial thermal gradient revealed by the concavity of the interface. Such configuration is inversed compared to experiments in metallic systems, that usually present a convex interface, and it leads to major behavior differences: the primary spacing on ground is larger than in space and the difference between μg/1g spacings increases with pulling rate due to the constant increase of latent heat generation whereas it tends to vanish in metallic systems when pulling rate is comparable to or higher than fluid velocity.

However, the large differences between microgravity and ground experiments strike the importance of microgravity experiments to validate theoretical and numerical modeling

as it is the only possibility to get homogeneous patterns with controlled and homogeneous growth parameters.

➢ Perspectives

At the end of this thesis, I am conscious that many analyses and results here presented raise questions that still deserve deepen in. The huge amount of data obtained led us to make some choices of topics and maybe to limit the other ones to the first analysis level:

- The critical point of interface curvature influence on pattern dynamics and spacing selection needs to be further documented. This implies to carefully correlate curvature to pattern motion in terms of pattern velocity, sliding direction and influence of defects. Solidifications with pulling rate jump have been performed but have not yet been analyzed whereas they should provide crucial information on spacing selection processes. Our analyses have clearly demonstrated that pattern sliding, associated to a mechanism of source and sink for the generation and elimination of cells maybe dominant in our samples. We may wonder how it affects the values of average spacing as well as the maximum and minimal spacings. Such questions would greatly benefit of a support of numerical simulations (3D phase-field) to study the existence branches of structures, with and without lateral motion induced by curvature, and to compare the selected spacings in both conditions.

- Initial transients analyses performed in chapter 3 evidenced large discrepancies between theories and experiments. The contributions to the front recoil of latent heat generation and modification of thermal field by pulling (thermal recoil) need to be evaluated with the help of global thermal simulations (for example using CrysVUn software) but however, as they both should vanish when the pulling rate is decreased, they could not be sufficient to explain the differences between the experimental recoil and the theoretical solutal one. Several hypotheses are currently investigated in the team, mainly related to the knowledge of physical parameters of the alloy.

- The analyses of convection influence led us to link the primary spacing on ground to the fluid velocity. The use of the model of Lehman et al. [183], developed for fluid flow towards the tips, was extended to flow away from the tips assuming low fluid velocities. Detailed analyses of fluid velocity through numerical simulation, for example using CrysVUn model, should be performed to sustain those analyses.

In addition to those different points, that deal with the analyses of the experiments performed in space on the SCN-0.24wt% Camphor alloy, a new set of experiments will be performed in close collaboration between IM2NP (UMR CNRS 7334 & Aix Marseille

Université; teams MCA & TMS), and the teams of Pr. R. Trivedi (Iowa State University, Iowa) and of Pr. A. Karma (Northeastern University, Boston, Massachusetts). The preparation of the sample is currently underway in the team for a first DSI reflight (DSI-R).

DSI-R:

The alloy chosen during the first flight campaign already performed was very adequate to explore the largest range of possible microstructure from the planar front to fully dendritic structures. The new set of experiments will focus on investigating the formation of well-developed dendritic array structures that are of direct technological relevance for the solidification and casting industry. The experiments will focus on elucidating (i) the fundamental mechanism of sidebranch formation, (ii) the interaction of primary array and the secondary sidebranch structures, (iii) the mechanism of the cell to dendrite transition, and (iv) the dependence of cell and dendrite tip shapes on growth conditions. Experiments already performed have yielded interesting observations of dendritic array structures (Figure 1), which suggest the existence of possible coherent modes of dendritic sidebranching. However, for the SCN-0.24wt% camphor alloy, dendrites were only observed in a high velocity regime where the solidification front developed significant curvature due to the combination of the rejection of latent heat and the much lower thermal conductivity of the alloy than its quartz container wall. In addition, dendrite tip radii are too small to be accurately resolved at those high velocities. The new set of experiments will be conducted for a higher composition (SCN-0.5wt% camphor alloy) where dendritic arrays form at a lower pulling velocity where the front curvature is minimized. Figure 1(b-e) shows the results of preliminary ground based experiments and phase-field simulations, which demonstrate that well-developed dendritic array structures form for a lower pulling speed V_P = 10 μm/s for a thermal gradient G = 23 K/cm. The ground based experiments and phase-field simulations are in excellent agreement for these growth conditions. In addition, those simulations predict a dendrite tip radius of 14 μm, which should be sufficiently large to be accurately resolved by interferometry. Additional simulations and ground based experiments are in progress to develop the flight matrix of growth conditions.

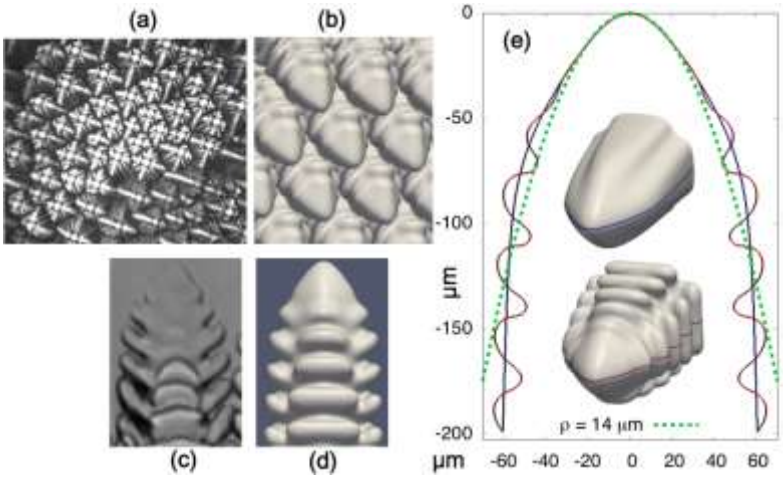

Figure.1. Experimental and simulated dendritic array structures. (a) experiment in µg for a SCN-0.24wt% camphor alloy with V_P = 30 µm/s and G = 12 K/cm. (b-e) Preliminary results for SCN-0.5wt% camphor alloy with V_P = 10 µm/s and G = 23 K/cm: (b) phase-field simulations of dendritic array, (c-d) comparison of dendrite observed in thin-sample ground-based experiments (c) and simulated (d), and (e) longitudinal sections of the simulated dendrites without (blue curve) and with (red curve) thermal fluctuations; parabolic fit of tip region (green dashed line) yields a tip radius of 14 µm (Numerical simulations : A. Karma and co-workers, Northeastern Univ, USA ; experiments in thin samples : R. Trivedi and co-workers, Iowa State Univ., USA).

DSI-2R:

Beyond DSI-R, a second reflight is foreseen. Indeed very striking observations of secondary instabilities (multiplets, oscillating patterns) have also been performed for the very first time in extended 3D patterns close to the critical pulling rate that corresponds to the transition between planar and cellular growth. Both thin-sample experimental and modeling studies point that the stability domain of multiplets or oscillatory structures is usually limited to 1 to 4 times the critical rate and in the SCN-0.24wt% camphor, these critical velocities were very low (below 0.5 µm/s for the applied thermal gradients), so that those structures appeared only in very narrow range of pulling rates. A third set of experiments is foreseen in the DECLIC-DSI that will focus on investigating those secondary instabilities of the cellular regime, using a lower composition such as for example SCN- 0.1wt% camphor. The increase of onset velocity of the primary morphological instability resulting from a reduced composition will lead to an extension of the stability domain in terms of pulling rate.

Nomenclature

G	the axial temperature gradient
G_w	weighted temperature gradient
G_c	the concentration gradient
V	pulling velocity
V_G	growth velocity
V_ϕ	growth velocity at the phase boundary
V_C	critical velocity of the transition from planner interface to unstable interface
V_{MS}	critical velocity calculated from MS theory
V_{cd}	critical velocity of the transition from cell to dendrite
n	normal at the phase boundary
C_0	initial solute concentration of a binary alloy
C	solute concentration in the melt
C_S	solute concentration at the solid
C_t	the tip concentration
C_L^*	dimensionless tip concentration
T	temperature
T_M	melting temperature
t	solidification time
D_L	solute diffusion coefficient in the melt
D_{th}	thermal diffusivity
L	latent heat of fusion per unit volume
k	solute partition coefficient
k_{eff}	effective solute partition coefficient
$K_{i\ (i=S\ or\ L)}$	the thermal conductivities of solid and liquid
m	liquidus slope
$\Gamma = T_M\gamma/L$	Gibbs-Thomson coefficient
γ	surface tension
κ	the local interface curvature
l_s	solute diffusion length
l_T	thermal diffusion length
l_c	capillary length
ΔT_0	the equilibrium freezing range
ΔT^*	non dimensional undercooling = $\Delta T/\ \Delta T_0$
Pe	Peclet number
Pe_R	radius Peclet number
z	coordinate of solidification direction
$\phi(x,t)$	sinusoidal perturbation of MS
$\delta(t)$	the initial amplitude of MS theory

λ_{cd}	local critical spacing of transition from cell to dendrite
Ω	the dimensionless supersaturation
σ^*	stability constant
$\vec{u}$	fluid velocity vector
p	the dynamic pressure
ν	the kinematic viscosity
ρ	the density
β_T	the thermal expansion coefficient
β_C	the opposite of the solutal expansion coefficient
δ	boundary layer thickness
Δ	nondimentional boundary layer thickness = δ/l_s
δ_{str}	the strength of crystal anisotropy
φ	crucible diameter
$U_{\parallel}$	the downward component of fluid velocity

Reference

[1] S. Gurevich, A. Karma, M. Plapp, R. Trivedi, Phase-field study of three-dimensional steady-state growth shapes in directional solidification, Phys. Rev. E. 81 (2010) 011603.

[2] R.Marcout, Raymond G, B Martin, G.Cambon, DECLIC: a facility to investigate fluids and transparent materials in microgravity conditions in ISS, 57th Int. Astronaut. Congr. (2006).

[3] E. Teghtsoonian, B. Chalmers, Furture observations on the macromosaic structure of tin single crystals, Can. J. Phys. 30 (1952) 388–401.

[4] M.J. Buerger, The Non-existence of a Regular Secondary Structure in Crystals, Zeitschrift Fiir Krist. 89 (1934) 242.

[5] J. Rutter, B. Chalmers, A prismatic substructure formed during solidification of metals, Can. J. Phys. 31 (1953) 15–39.

[6] R. Trivedi, Y. Shen, S. Liu, Cellular-to-dendritic transition during the directional solidification of binary alloys, Metall. Mater. Trans. A. 34 (2003) 395–401.

[7] J.S. Langer, Instabilities and pattern formation in crystal growth, Rev. Mod. Phys. 52 (1980) 1–28.

[8] R. Trivedi, Theory of dendritic growth during the directional solidification of binary alloys, J. Cryst. Growth. 49 (1980) 219–232.

[9] W. Kurz, D.J. Fisher, Fundamentals of Solidification, Trans Tech Publications, 1986.

[10] W. Tiller, K. Jackson, J. Rutter, B. Chalmers, The redistribution of solute atoms during the solidification of metals, Acta Metall. 1 (1953) 428–437.

[11] W.W. Mullins, R.F. Sekerka, Stability of a Planar Interface During Solidification of a Dilute Binary Alloy, J. Appl. Phys. 35 (1964) 444.

[12] M.A. Eshelman, R. Trivedi, The planar to cellular transition during the directional solidification of alloys, Acta Metall. 35 (1987) 2443–2452.

[13] R.F. Sekerka, A Stability Function for Explicit Evaluation of the Mullins-Sekerka Interface Stability Criterion, J. Appl. Phys. 36 (1965) 264.

[14] J.A. Warren, J.S.Langer, Prediction of dendritic spacing in a directional-solidification experiment, Phys. Rev. E. 47 (1993) 2702.

[15] W. Losert, B.Q. Shi, H.Z. Cummins, Evolution of dendritic patterns during alloy solidification: onset of the initial instability., Proc. Natl. Acad. Sci. U. S. A. 95 (1998) 431–8.

[16] J.P. Garandet, G. Boutet, P. Lehmann, B. Drevet, D. Camel, A. Rouzaud, et al., Morphological stability of a solid–liquid interface and cellular growth: Insights from thermoelectric measurements in microgravity experiments, J. Cryst. Growth. 279 (2005) 195–205.

[17] M. Hennenberg, B. Billia, Further analysis of the analogy between cellular solidification and viscous fingering, J. Phys. I. 1 (1991) 79–95.

[18] A. Pocheau, M. Georgelin, Cellular arrays in binary alloys: from geometry to stability, J. Cryst. Growth. 250 (2003) 100–106.

[19] C. ZENER, Kinetics of the decomposition of austenite, Trans. Aime. 167 (1946) 550.

[20] J.D. Hunt, Solidification and casting of metals, London, 1979.

[21] W. Kurz, D.J. Fisher, Dendrite growth at the limit of stability: tip radius and spacing, Acta Metall. 29 (1981) 11–20.

[22] R. Trivedi, Interdendritic Spacing: Part II. A Comparison of Theory and Experiment, Metall. Trans. A. 15 (1984) 977–982.

[23] R. Trivedi, K. Somboonsuk, Pattern formation during the directional solidification of binary systems, Acta Metall. 33 (1985) 1061–1068.

[24] M.A. Eshelman, R. Trivedi, Wavelength selection of cellular patterns, Scr. Metall. 22 (1988) 893–898.

[25] V. Seetharaman, M.A. Eshelman, R. Trivedi, Cellular spacings—II. Dynamical studies, Acta Metall. 36 (1988) 1175–1185.

[26] B.Billia, R. Trivedi, Pattern formation in crystal growth, in: D.T.J. Hurle (Ed.), Handb. Cryst. Growth, Elsevier, North Holland, 1993: pp. 899–1073.

[27] M. Georgelin, A. Pocheau, Onset of sidebranching in directional solidification, Phys. Rev. E. 57 (1998) 3189–3203.

[28] K. Somboonsuk, J.T. Mason, R. Trivedi, Interdendritic Spacing: Part I. Experimental Studies, Metall. Trans. A. 15 (1984) 967–975.

[29] M.A. Eshelman, V. Seetharaman, R. Trivedi, Cellular spacings—I. Steady-state growth, Acta Metall. 36 (1988) 1165–1174.

[30] G. Horvay, J.. Cahn, Dendritic and spheroidal growth, Acta Metall. 9 (1961) 695–705.

[31] D.. Temkin, Growth rate of the needle-crystal formed in a supercooled melt, Sov. Phys. Dokl. 5 (1960) 609.

[32] R. Trivedi, Growth of dendritic needles from a supercooled melt, Acta Metall. 18 (1970) 287–296.

[33] J.. Langer, H. Müller-Krumbhaar, Theory of dendritic growth—I. Elements of a stability analysis, Acta Metall. 26 (1978) 1681–1687.

[34] S.-C. Huang, M.E. Glicksman, Overview 12: Fundamentals of dendritic solidification—I. Steady-state tip growth, Acta Metall. 29 (1981) 701–715.

[35] R. TRIVEDI, J.T. MASON, The effects of interface attachment kinetics on solidification interface morphologies, Metall. Trans. A, Phys. Metall. Mater. Sci. 22 (1991) 235–249.

[36] S.-C. Huang, M.E. Glicksman, Overview 12: Fundamentals of dendritic solidification—II development of sidebranch structure, Acta Metall. 29 (1981) 717–734.

[37] T. Fujioka, R.F. Sekerka, Morphological stability of disc crystals, J. Cryst. Growth. 24-25 (1974) 84–93.

[38] P. Pelcé, Dynamics of Curved Fronts, Academic press, San Diego, 1988.

[39] W.J. Boettinger, J.A. Warren, C. Beckermann, A. Karma, Phase field simulation of solidification 1, Annu. Rev. Mater. Res. 32 (2002) 163–194.

[40] A. Karma, Phase-field Modeling, in: M.I. of T. Sidney Yip (Ed.), Handb. Mater. Model., 2005: pp. 2087–2130.

[41] A. Karma, W.-J. Rappel, Phase-field method for computationally efficient modeling of solidification with arbitrary interface kinetics, Phys. Rev. E. 53 (1996) R3017–R3020.

[42] A. Karma, W.-J. Rappel, Quantitative phase-field modeling of dendritic growth in two and three dimensions, Phys. Rev. E. 57 (1998) 4323–4349.

[43] A. Karma, Y. Lee, M. Plapp, Three-dimensional dendrite-tip morphology at low undercooling, Phys. Rev. E. 61 (2000) 3996–4006.

[44] B. Echebarria, A. Karma, M. Plapp, Quantitative phase-field model of alloy solidification, Phys. Rev. E. 70 (2004) 061604.

[45] R. Folch, M. Plapp, Quantitative phase-field modeling of two-phase growth, Phys. Rev. E. 72 (2005) 011602.

[46] C. Beckermann, H.-J. Diepers, I. Steinbach, A. Karma, X. Tong, Modeling Melt Convection in Phase-Field Simulations of Solidification, J. Comput. Phys. 154 (1999) 468–496.

[47] X. Tong, C. Beckermann, A. Karma, Velocity and shape selection of dendritic crystals in a forced flow, Phys. Rev. E. 61 (2000) R49–R52.

[48] J.C. Ramirez, C. Beckermann, A. Karma, H.-J. Diepers, Phase field modeling of binary alloy solidification with coupled heat and solute diffusion, Phys. Rev. E. 69 (2004) 051607.

[49] S.-Z. Lu, J.D. Hunt, A numerical analysis of dendritic and cellular array growth: the spacing adjustment mechanisms, J. Cryst. Growth. 123 (1992) 17–34.

[50] J.D. Hunt, S.Z. Lu, Numerical modeling of cellular/dendritic array growth: spacing and structure predictions, Metall. Mater. Trans. A. 27 (1996) 611–623.

[51] R. Trivedi, W. Kurz, Solidification microstructures: A conceptual approach, Acta Metall. Mater. 42 (1994) 15–23.

[52] C. Misbah, A. Valance, Secondary instabilities in the stabilized Kuramoto-Sivashinsky equation, Phys. Rev. E. 49 (1994) 166–183.

[53] P. Cladis, J. Gleeson, P. Finn, H. Brand, Breathing mode in a pattern-forming system with two competing lengths, Phys. Rev. Lett. 67 (1991) 3239–3242.

[54] M. Georgelin, A. Pocheau, Oscillatory Instability, Limit Cycle, and Transition to Doublets in Directional Solidification, Phys. Rev. Lett. 79 (1997) 2698–2701.

[55] P. Kopczynski, W. Rappel, A. Karma, Critical Role of Crystalline Anisotropy in the Stability of Cellular Array Structures in Directional Solidification., Phys. Rev. Lett. 77 (1996) 3387–3390.

[56] A. Karma, A. Sarkissian, Morphological instabilities of lamellar eutectics, Metall. Mater. Trans. A. 27 (1996) 635–656.

[57] K. Kassner, C. Misbah, Coupling between crystalline anistropy and spontaneous parity breaking in lamellar eutectic growth, Phys. Rev. A. 45 (1992) 7372–7384.

[58] A. Valance, C. Misbah, D. Temkin, K. Kassner, Analytic theory for parity breaking in lamellar eutectic growth, Phys. Rev. E. 48 (1993) 1924–1941.

[59] K. Kassner, J. Debierre, B. Billia, N. Noël, H. Jamgotchian, Cellular structures in three-dimensional directional solidification: Simulation and analysis, Phys. Rev. E. 57 (1998) 2849–2861.

[60] M. Plapp, M. Dejmek, Stability of hexagonal solidification patterns, Europhys. Lett. 65 (2004) 276–282.

[61] C. Misbah, Dynamiques complexes et morphogenèse, Springer Paris, Paris, 2011.

[62] K. Kassner, C. Misbah, H. Müller-Krumbhaar, A. Valance, Directional solidification at high speed. I. Secondary instabilities., Phys. Rev. E. Stat. Phys. Plasmas. Fluids. Relat. Interdiscip. Topics. 49 (1994) 5477–5494.

[63] H. Jamgotchian, R. Trivedi, B. Billia, Array of doublets: A branch of cellular solutions in directional solidification, Phys. Rev. E. 47 (1993) 4313–4322.

[64] P. Coullet, R. Goldstein, G. Gunaratne, Parity-breaking transitions of modulated patterns in hydrodynamic systems, Phys. Rev. Lett. 63 (1989) 1954–1957.

[65] P. Kopczyn-acuteski, W. Rappel, A. Karma, Cellular multiplets in directional solidification, Phys. Rev. E. 55 (1997) R1282–R1285.

[66] B. Caroli, C. Caroli, C. Misbah, B. Roulet, Solutal convection and morphological instability in directional solidification of binary alloys. - II. Effect of the density difference between the two phases, J. Phys. 46 (1985) 1657–1665.

[67] D. Schwabe, Marangoni effects in crystal growth melts, Physico-Chem. Hydrodyn. (1981) 263.

[68] Y. Marietti, J.-M. Debierre, T. Bock, K. Kassner, Pattern formation in directional solidification under shear flow. II. Morphologies and their characterization, Phys. Rev. E. 63 (2001) 066302.

[69] Y. Marietti, J.-M. Debierre, T. Bock, K. Kassner, Pattern formation in directional solidification under shear flow. I. Linear stability analysis and basic patterns, Phys. Rev. E. 63 (2001) 066301.

[70] D. Medvedev, T. Fischaleck, K. Kassner, Influence of external flows on crystal growth: Numerical investigation, Phys. Rev. E. 74 (2006) 031606.

[71] H. Jamgotchian, N. Bergeon, D. Benielli, P. Voge, B. Billia, R. Guérin, Localized Microstructures Induced by Fluid Flow in Directional Solidification, Phys. Rev. Lett. 87 (2001) 166105.

[72] S.R. Coriell, D.T.J. Hurle, R.F. Sekerka, Interface stability during crystal growth: The effect of stirring, J. Cryst. Growth. 32 (1976) 1–7.

[73] J.J. Favier, A. Rouzaud, Morphological stability of the solidification interface under convective conditions, J. Cryst. Growth. 64 (1983) 367–379.

[74] J.A. Burton, R.C. Prim, W.P. Slichter, The Distribution of Solute in Crystals Grown from the Melt. Part I. Theoretical, J. Chem. Phys. 21 (1953) 1987.

[75] B. Drevet, H. Nguyen Thi, D. Camel, B. Billia, M.. Dupouy, Solidification of aluminium–lithium alloys near the cell/dendrite transition-influence of solutal convection, J. Cryst. Growth. 218 (2000) 419–433.

[76] M.D. Dupouy, D. Camel, J.J. Favier, Natural convection in directional dendritic solidification of metallic alloys—I. Macroscopic effects, Acta Metall. 37 (1989) 1143–1157.

[77] H. Jamgotchian, N. Bergeon, D. Benielli, P. Voge, B. Billia, In situ observation and interferometric characterization of solid-liquid interface morphology in directionally growing transparent model systems., J. Microsc. 203 (2001) 119–27.

[78] Y.-J. CHEN, S.H. DAVIS, Flow-induced patterns in directional solidification: localized morphologies in three-dimensional flows, J. Fluid Mech. 421 (2000) 369–380.

[79] S.R. Coriell, M.R. Cordes, W.J. Boettinger, R.F. Sekerka, Convective and interfacial instabilities during unidirectional solidification of a binary alloy, J. Cryst. Growth. 49 (1980) 13–28.

[80] D.T.J. Hurle, E. Jakeman, A.A. Wheeler, Effect of solutal convection on the morphological stability of a binary alloy, J. Cryst. Growth. 58 (1982) 163–179.

[81] G. Young, S. Davis, Directional solidification with buoyancy in systems with small segregation coefficient, Phys. Rev. B. 34 (1986) 3388–3396.

[82] M. Hennenberg, A. Rouzaud, D. Camel, J.J. Favier, Morphological and thermosolutal instabilities inside a deformable solute boundary layer during unidirectional solidification, J. Cryst. Growth. 85 (1987) 49–58.

[83] H. Nguyen Thi, B. Billia, L. Capella, Cellular arrays during upward solidification of Pb-30 wt% T1 alloys, J. Phys. 51 (1990) 625–637.

[84] B. Billia, S.R. Coriell, Solidification Cellulaire d'Alliages Pb-Tl Lors de l'Expérience D1-WLGHF- 02, in: Sixth Eur. Symp. Mater. Sci. Under Microgravity Cond., The Agency, Bordeaux, France, 1986: p. 597.

[85] T. Okamoto, K. Kishitake, I. Bessho, Dendritic structure in unidirectionally solidified cyclohexanol, J. Cryst. Growth. 29 (1975) 131–136.

[86] B. Appolaire, V. Albert, H. Combeau, G. Lesoult, Experimental Study of Free Growth of Equiaxed NH4Cl Crystals Settling in Undercooled NH4Cl-H2O Melts, ISIJ Int. 39 (1999) 263.

[87] M.E. Glicksman, E. Winsa, R.C. Hahn, T.A. Lograsso, S.H. Tirmizi, M.E. Selleck, Isothermal dendritic growth— a proposed microgravity experiment, Metall. Trans. A. 19 (1988) 1945–1953.

[88] H.N. Thi, B. Billia, H. Jamgotchian, Influence of thermosolutal convection on the solidification front during upwards solidification, J. Fluid Mech. 204 (2006) 581.

[89] M.G. Worster, CONVECTION IN MUSHY LAYERS, Annu. Rev. Fluid Mech. 29 (1997) 91–122.

[90] J.R. Sarazin, A. Hellawell, Channel formation in Pb-Sn, Pb-Sb, and Pb-Sn-Sb alloy ingots and comparison with the system NH4CI-H2O, Metall. Trans. A. 19 (1988) 1861–1871.

[91] S. LIU, A. HELLAWELL, Experiments with constrained chimney-plume flows in the system ammonium chloride–water: comparison with the unconstrained case, J. Fluid Mech. 388 (1999) 21–48.

[92] S. Boden, S. Eckert, B. Willers, G. Gerbeth, X-Ray Radioscopic Visualization of the Solutal Convection during Solidification of a Ga-30 Wt Pct In Alloy, Metall. Mater. Trans. A. 39 (2008) 613–623.

[93] J.C. Ramirez, C. Beckermann, Evaluation of a rayleigh-number-based freckle criterion for Pb-Sn alloys and Ni-base superalloys, Metall. Mater. Trans. A. 34 (2003) 1525–1536.

[94] Q. Li, H.N. Thi, H. Jamgotchian, B. Billia, Preferred-pattern formation during the initial transient in cellular solidification, Acta Metall. Mater. 43 (1995) 1271–1278.

[95] S.R. Coriell, G.B. McFadden, R.F. Sekerka, Effect of anisotropic thermal conductivity on the morphological stability of a binary alloy, J. Cryst. Growth. 100 (1990) 459–466.

[96] J. Langer, Lectures in the theory of pattern formation, Chance Matter, J. Souletie, J. Vannimenus R. Stora, Eds. (1987) 629.

[97] M.E. Glicksman, S.P. Marsh, The dendrite, in: J.D. Hunt (Ed.), Hand B. Cryst. Growth, Elsevier, Amsterdam, 1993: pp. 1075–1122.

[98] J.S. Langer, Lectures in the theory of pattern formation in chance and matter, Ec. D'ete Les Houches, Holl. (1986).

[99] E. Ben-Jacob, P. Garik, The formation of patterns in non-equilibrium growth, Nature. 343 (1990) 523–530.

[100] J. Deschamps, M. Georgelin, A. Pocheau, Crystal anisotropy and growth directions in directional solidification, Europhys. Lett. 76 (2006) 291–297.

[101] C.A. Gandin, M. Eshelman, R. Trivedi, Orientation dependence of primary dendrite spacing, Metall. Mater. Trans. A. 27 (1996) 2727–2739.

[102] S. Akamatsu, G. Faivre, T. Ihle, Symmetry-broken double fingers and seaweed patterns in thin-film directional solidification of a nonfaceted cubic crystal, Phys. Rev. E. 51 (1995) 4751–4773.

[103] S. Akamatsu, T. Ihle, Similarity law for the tilt angle of dendrites in directional solidification of non-axially-oriented crystals, Phys. Rev. E. 56 (1997) 4479–4485.

[104] S. Akamatsu, G. Faivre, Anisotropy-driven dynamics of cellular fronts in directional solidification in thin samples, Phys. Rev. E. 58 (1998) 3302–3315.

[105] T. Okada, Y. Saito, Simulation of unidirectional solidification with a tilted crystalline axis, Phys. Rev. E. 54 (1996) 650–655.

[106] S.R. Coriell, R.F. Sekerka, The effect of the anisotropy of surface tension and interface kinetics on morphological stability, J. Cryst. Growth. 34 (1976) 157–163.

[107] K.. Jackson, Growth and Perfection of Crystals, Wiley, New York, NY, 1958.

[108] K.. Jackson, Mechanism of growth, Liq. Met. Solidif. (1958) 174–186.

[109] K.A. Jackson, J.D. Hunt, Transparent compounds that freeze like metals, Acta Metall. 13 (1965) 1212–1215.

[110] J. Timmermans, Plastic crystals: A historical review, J. Phys. Chem. Solids. 18 (1961) 1–8.

[111] A. Michils, Recherches stoechiométriques V.VIII. LA PLASTICITÉ D'UN GROUPE PARTICULIER DE CRISTAUX ORGANIQUES, Bull. Des Sociétés Chim. Belges. 57 (2010) 575–617.

[112] P.E. Cladis, A prepared pattern with wavelength selection in directional solidification, J. Stat. Phys. 64 (1991) 1103–1119.

[113] J. Deschamps, M. Georgelin, A. Pocheau, Growth directions of microstructures in directional solidification of crystalline materials, Phys. Rev. E. 78 (2008) 011605.

[114] B. Kauerauf, G. Zimmermann, S. Rex, M. Mathes, F. Grote, Directional cellular growth of succinonitrile–0.075wt% acetone bulk samples, J. Cryst. Growth. 223 (2001) 265–276.

[115] L. Sturz, G. Zimmermann, S. Rex, M. Mathes, B. Kauerauf, Analysis of diffusive cellular patterns in directional solidification of bulk samples, Metall. Mater. Trans. A. 35 (2004) 239–246.

[116] B. Kauerauf, G. Zimmermann, S. Rex, B. Billia, H. Jamgotchian, J.D. Hunt, Directional cellular growth of succinonitrile–0.075wt% acetone bulk samples Part 2: Analysis of cellular pattern, J. Cryst. Growth. 223 (2001) 277–284.

[117] G.E. Rindone, Materials processing in the reduced gravity environment of space, in: Mater. Res. Soc. Symp. Proc., 1982.

[118] H. Walter, Fluid sciences and materials science in space, Springer Berlin et al., 1987.

[119] D.J. Jarvis, O. Minster, Metallurgy in Space, Mater. Sci. Forum. 508 (2006) 1–18.

[120] J. Garca-Ruiz, J. Drenth, M. Ries-Kautt, A. Tardieu, A world without gravity-Research in space for health and industrial processes., ESA SP. 1251 (2001).

[121] M. Glicksman, Solidification research in microgravity, in: ASM Handb., 2008: pp. 398–401.

[122] L.L. Regel, Materials processing in space: theory, experiments, and technology, Consultants Bureau, 1990.

[123] M.D. Dupouy, D. Camel, J.J. Favier, Natural convective effects in directional dendritic solidification of binary metallic alloys: Dendritic array primary spacing, Acta Metall. Mater. 40 (1992) 1791–1801.

[124] M.E. Glicksman, A.O. Lupulescu, Dendritic crystal growth in pure materials, J. Cryst. Growth. 264 (2004) 541–549.

[125] M.B. Koss, J.C. LaCombe, L.A. Tennenhouse, M.E. Glicksman, E.A. Winsa, Dendritic Growth tip velocities and radii of curvature in microgravity, Metall. Mater. Trans. A. 30 (1999) 3177–3190.

[126] J.C. LACOMBE, M.B. KOSS, M.E. GLICKSMAN, Tip Velocities and Radii of Curvature of Pivalic Acid Dendrites under Convection-Free Conditions, Metall. Mater. Trans. A. 38 (2007) 116–126.

[127] L. Sturz, G. Zimmermann, In-situ and real-time investigation of the columnar-equiaxed transition in the transparent alloy system neopentylglycol-camphor onboard the sounding rocket TEXUS-47, J. Phys. Conf. Ser. 327 (2011) 012002.

[128] A. Kharicha, M. Stefan-Kharicha, A. Ludwig, M. Wu, Simultaneous Observation of Melt Flow and Motion of Equiaxed Crystals During Solidification Using a Dual Phase Particle Image Velocimetry

Technique. Part I: Stage Characterization of Melt Flow and Equiaxed Crystal Motion, Metall. Mater. Trans. A. 44 (2012) 650–660.

[129] A. Kharicha, M. Stefan-Kharicha, A. Ludwig, M. Wu, Simultaneous Observation of Melt Flow and Motion of Equiaxed Crystals During Solidification Using a Dual Phase Particle Image Velocimetry Technique. Part II: Relative Velocities, Metall. Mater. Trans. A. 44 (2012) 661–668.

[130] A. Ludwig, W. Kurz, Direct observation of solidification microstructures around absolute stability, Acta Mater. 44 (1996) 3643–3654.

[131] A. Ludwig, W. Kurz, Cellular growth of a dilute binary alloy at high solidification velocities, Scr. Mater. 35 (1996) 1217–1222.

[132] M. Ginibre, S. Akamatsu, G. Faivre, Experimental determination of the stability diagram of a lamellar eutectic growth front, Phys. Rev. E. 56 (1997) 780–796.

[133] S. Akamatsu, S. Bottin-Rousseau, M. Perrut, G. Faivre, V.T. Witusiewicz, L. Sturz, Real-time study of thin and bulk eutectic growth in succinonitrile–(d)camphor alloys, J. Cryst. Growth. 299 (2007) 418–428.

[134] S. Bottin-Rousseau, M. Perrut, C. Picard, S. Akamatsu, G. Faivre, An experimental method for the in situ observation of eutectic growth patterns in bulk samples of transparent alloys, J. Cryst. Growth. 306 (2007) 465–472.

[135] J.P. Mogeritsch, A. Ludwig, In-situ observation of coupled growth morphologies in organic peritectics, IOP Conf. Ser. Mater. Sci. Eng. 27 (2012) 012028.

[136] R.N. Grugel, Composite growth in hypermonotectic alloys, Metall. Trans. B. 22 (1991) 339–348.

[137] A. Ludwig, J. Mogeritsch, M. Kolbe, G. Zimmermann, L. Sturz, N. Bergeon, et al., Advanced Solidification Studies on Transparent Alloy Systems: A New European Solidification Insert for Material Science Glovebox on Board the International Space Station, JOM. 64 (2012) 1097–1101.

[138] H. Nguyen-Thi, G. Reinhart, N. Mangelinck-Noël, H. Jung, B. Billia, T. Schenk, et al., In-Situ and Real-Time Investigation of Columnar-to-Equiaxed Transition in Metallic Alloy, Metall. Mater. Trans. A. 38 (2007) 1458–1464.

[139] R.H. Mathiesen, L. Arnberg, K. Ramsøskar, T. Weitkamp, C. Rau, A. Snigirev, Time-resolved x-ray imaging of aluminum alloy solidification processes, Metall. Mater. Trans. B. 33 (2002) 613–623.

[140] B. Billia, N. Bergeon, H. Nguyen Thi, H. Jamgotchian, J. Gastaldi, G. Grange, Cumulative Mechanical Moments and Microstructure Deformation Induced by Growth Shape in Columnar Solidification, Phys. Rev. Lett. 93 (2004) 126105.

[141] R.H. Mathiesen, L. Arnberg, X-ray radiography observations of columnar dendritic growth and constitutional undercooling in an Al–30wt%Cu alloy, Acta Mater. 53 (2005) 947–956.

[142] H. Yasuda, I. Ohnaka, K. Kawasaki, A. Sugiyama, T. Ohmichi, J. Iwane, et al., Direct observation of stray crystal formation in unidirectional solidification of Sn–Bi alloy by X-ray imaging, J. Cryst. Growth. 262 (2004) 645–652.

[143] B. Li, H.D. Brody, A. Kazimirov, Synchrotron microradiography of temperature gradient zone melting in directional solidification, Metall. Mater. Trans. A. 37 (2006) 1039–1044.

[144] G. Reinhart, A. Buffet, H. Nguyen-Thi, B. Billia, H. Jung, N. Mangelinck-Noël, et al., In-Situ and Real-Time Analysis of the Formation of Strains and Microstructure Defects during Solidification of Al-3.5 Wt Pct Ni Alloys, Metall. Mater. Trans. A. 39 (2008) 865–874.

[145] C. Weiss, N. Bergeon, N. Mangelinck-Noël, B. Billia, Effects of the interface curvature on cellular and dendritic microstructures, Mater. Sci. Eng. A. 413-414 (2005) 296–301.

[146] C. Weiss, N. Bergeon, N. Mangelinck-Noël, B. Billia, Cellular pattern dynamics on a concave interface in three-dimensional alloy solidification, Phys. Rev. E. 79 (2009) 011605.

[147] S. Akamatsu, S. Bottin-Rousseau, G. Faivre, Experimental Evidence for a Zigzag Bifurcation in Bulk Lamellar Eutectic Growth, Phys. Rev. Lett. 93 (2004) 175701.

[148] G. PONT, S. Barde, B. Zappoli, F. Duclos, Y. Garrabos, C. Lecoutre, et al., DECLIC A FACILITY FOR THE STUDY OF CRYSTAL GROWTH AND CRITICAL FLUIDS, 60th Int. Astronaut. Congr. (2009).

[149] G.Cambon, B.Zappoli, R.Marcout, Y.Garrabos, F.Cansell, D.Beysens, et al., No Title, in: Proceddings 48th Int. Astronaut. Congr., Turin, 1997.

[150] C. Weiss, Solidification dirigée d'alliages transparents 3D : dynamique de formation de la microstructure interfaciale en présence de convection naturelle, l'Université d'Aix-Marseille, 2006.

[151] S. Bottin-Rousseau, A. Pocheau, Self-Organized Dynamics on a Curved Growth Interface, Phys. Rev. Lett. 87 (2001) 3–6.

[152] S. Liu, P. Mazumder, R. Trivedi, A new thermal assembly design for the directional solidification of transparent alloys, J. Cryst. Growth. 240 (2002) 560–568.

[153] J.N.Sherwood, The plastically crystalline state, Wiley, 1979.

[154] J. Teng, S. Liu, Re-determination of succinonitrile (SCN)–camphor phase diagram, J. Cryst. Growth. 290 (2006) 248–257.

[155] V.T. Witusiewicz, L. Sturz, U. Hecht, S. Rex, Thermodynamic description and unidirectional solidification of eutectic organic alloys: I. Succinonitrile-(d)camphor system, Acta Mater. 52 (2004) 4561–4571.

[156] V.T. Witusiewicz, U. Hecht, S. Rex, On the question of phase equilibria in the succinonitrile–(D)camphor system, J. Cryst. Growth. 375 (2013) 84–89.

[157] A. Pocheau, J. Deschamps, M. Georgelin, Dendrite growth directions and morphology in the directional solidification of anisotropic materials, JOM. 59 (2007) 71–76.

[158] B. Billia, H. Jamgotchian, H. Nguyen Thi, Statistical analysis of the disorder of two-dimensional cellular arrays in directional solidification, Metall. Trans. A. 22 (1991) 3041–3050.

[159] D.G. McCartney, J.D. Hunt, Measurements of cell and primary dendrite arm spacings in directionally solidified aluminium alloys, Acta Metall. 29 (1981) 1851–1863.

[160] C. Dussert, G. Rasigni, M. Rasigni, J. Palmari, A. Llebaria, Minimal spanning tree: A new approach for studying order and disorder, Phys. Rev. B. 34 (1986) 3528–3531.

[161] R.M. Macfarlane, E. Courtens, T. Bischofberger, Detailed Refractive Index Measurement near Melting in a Plastic Crystal: Succinonitrile, Mol. Cryst. Liq. Cryst. 35 (1976) 27–32.

[162] W. Kurz, D.J. Fisher, Dendrite growth at the limit of stability: tip radius and spacing, Acta Metall. 29 (1981) 11–20.

[163] E. Çadirli, İ. Karaca, H. Kaya, N. Maraşli, Effect of growth rate and composition on the primary spacing, the dendrite tip radius and mushy zone depth in the directionally solidified succinonitrile–Salol alloys, J. Cryst. Growth. 255 (2003) 190–203.

[164] H. Kaya, E. Çadırlı, K. Keşlioğlu, N. Maraşlı, Dependency of the dendritic arm spacings and tip radius on the growth rate and composition in the directionally solidified succinonitrile–carbon tetrabromide alloys, J. Cryst. Growth. 276 (2005) 583–593.

[165] J.J. Favier, P. Lehmann, B. Drevet, J.P. Garandet, D. Camel, S.R. Coriell, A study of morphological stability during directional solidification of a Sn−Bi alloy in microgravity, in: Mater. Fluids Under Low Gravity, Berlin, Germany, 1996: pp. 77–94.

[166] H. Nguyen Thi, Y. Dabo, B. Drevet, M.D. Dupouy, D. Camel, B. Billia, et al., Directional solidification of Al–1.5wt% Ni alloys under diffusion transport in space and fluid-flow localisation on earth, J. Cryst. Growth. 281 (2005) 654–668.

[167] R. Trivedi, N. Bergeon, B. Billia, B. Echebarria, A. Karma, S. Liu, et al., In situ characterization of interface-microstructure dynamics in 3D-Directional Solidification of model transparent alloys, Microgravity - Sci. Technol. 16 (2005) 133–137.

[168] N. Bergeon, A. Ramirez, L. Chen, B. Billia, J. Gu, R. Trivedi, Dynamics of interface pattern formation in 3D alloy solidification: first results from experiments in the DECLIC directional solidification insert on the International Space Station, J. Mater. Sci. 46 (2011) 6191–6202.

[169] T.F. Bower, H.D. Brody, M.C. Flemings, Measurements of solute redistribution in dendritic solidification, in: Trans. Metall. Soc. AIME, 1966: p. 11.

[170] C.E. Chang, W.R. Wilcox, Control of interface shape in the vertical bridgman-stockbarger technique, J. Cryst. Growth. 21 (1974) 135–140.

[171] P. Haldenwang, R. Guerin, Transverse thermal effects in directional solidification, J. Cryst. Growth. 244 (2002) 108–122.

[172] K. Kassner, C. Misbah, H. Müller-Krumbhaar, Transition to chaos in directional solidification, Phys. Rev. Lett. 67 (1991) 1551–1554.

[173] B. Grossmann, K. Elder, M. Grant, J. Kosterlitz, Directional solidification in two and three dimensions, Phys. Rev. Lett. 71 (1993) 3323–3326.

[174] P. Kopczyński, W.-J. Rappel, A. Karma, Critical Role of Crystalline Anisotropy in the Stability of Cellular Array Structures in Directional Solidification, Phys. Rev. Lett. 77 (1996) 3387–3390.

[175] W. Kurz, D.J. Fisher, No Title, Acta Metall. 29 (1981).

[176] M. Georgelin, A. Pocheau, Characterization of cell tip curvature in directional solidification, J. Cryst. Growth. 268 (2004) 272–283.

[177] E. Brener, H. Müller-Krumbhaar, Y. Saito, D. Temkin, Crystal growth in a channel: Numerical study of the one-sided model, Phys. Rev. E. 47 (1993) 1151–1155.

[178] Z. Wang, J. Wang, J. Li, G. Yang, Y. Zhou, Quantitative investigation of cellular growth in directional solidification by phase-field simulation, Phys. Rev. E. 84 (2011) 041604.

[179] T. Ihle, H. Müller-Krumbhaar, Fractal and compact growth morphologies in phase transitions with diffusion transport, Phys. Rev. E. 49 (1994) 2972–2991.

[180] a. Ludwig, Dendritic and cellular doublets: Morphologies of thin solid films growing along a substrate during the initial state of solidification of bulk melts, Phys. Rev. E. 59 (1999) 1893–1898.

[181] W. Losert, D. Stillman, H. Cummins, P. Kopczyński, W.-J. Rappel, A. Karma, Selection of doublet cellular patterns in directional solidification through spatially periodic perturbations, Phys. Rev. E. 58 (1998) 7492–7506.

[182] R. Trivedi, S. Liu, P. Mazumder, E. Simsek, Microstructure development in the directionally solidified Al–4.0 wt% Cu alloy system, Sci. Technol. Adv. Mater. 2 (2001) 309–320.

[183] P. Lehmann, R. Moreau, D. Camel, R. Bolcato, A simple analysis of the effect of convection on the structure of the mushy zone in the case of horizontal Bridgman solidification. Comparison with experimental results, J. Cryst. Growth. 183 (1998) 690–704.

[184] N. Noël, H. Jamgotchian, B. Billia, Influence of grain boundaries and natural convection on microstructure formation in cellular directional solidification of dilute succinonitrile alloys in a cylinder, J. Cryst. Growth. 187 (1998) 516–526.

[185] T. Huang, S. Liu, Y. Yang, D. Lu, Y. Zhou, Coupling of couette flow and crystal morphologies in directional freezing, J. Cryst. Growth. 128 (1993) 167–172.

Résumé

Introduction générale

La solidification est une transition de phase de l'état liquide à l'état solide qui, pour une substance pure, se produit lorsque la température est réduite en dessous d'une valeur critique à une pression constante. Les propriétés physiques et l'arrangement atomique des phases avant et après la transition sont considérablement modifiées. Pour les systèmes à plusieurs composants, les phases liquide et solide sont généralement de compositions chimiques différentes données par l'équilibre thermodynamique, tant que la transformation n'est pas trop rapide.

La solidification est l'une des étapes les plus importantes de la chaîne de production industrielle. En effet, les propriétés finales, en particulier mécaniques, du matériau dépendent de la microstructure formée lors de la solidification. Par exemple, une microstructure colonnaire dendritique est recherchée lors de la fabrication des aubes de turbines de moteurs d'avions soumises à des températures de fonctionnement très élevées car cette microstructure améliore les propriétés en fluage du matériau et augmente ainsi la durée de vie des pièces. Par contre, une structure de grains équiaxes est recherchée dans les pièces soumises à des sollicitations mécaniques homogènes et isotropes, comme par exemple dans les blocs moteurs de voitures. Outre la structure de grains, les propriétés mécaniques dépendent également des caractéristiques fines de la microstructure. L'espacement des branches secondaires dendritiques, associée à une micro ségrégation des espèces chimiques, est un paramètre clé à contrôler pour ajuster la limite d'élasticité et la dureté. Afin de pouvoir obtenir un matériau aux propriétés recherchées, il est donc impératif de maitriser l'étape de solidification. Des modèles numériques permettant de prédire les caractéristiques microstructurales en fonction des paramètres de contrôle du procédé de solidification et de la géométrie des pièces constitueraient un outil industriel majeur mais leur élaboration est conditionnée à la connaissance des mécanismes fondamentaux de la solidification et leur validité repose sur la comparaison à des expériences de références.

La solidification dirigée est une technique puissante pour étudier la formation de microstructure puisque les paramètres de croissance peuvent être contrôlés indépendamment. La formation de la microstructure est un processus dynamique dans

lequel le réseau cellulaire ou dendritique se développe, s'organise et s'ordonne progressivement. C'est pourquoi l'utilisation d'alliages transparents, analogues aux alliages métalliques, qui permettent l'observation continue *in situ* et en temps réel par des méthodes optiques[1] est intéressante.

Les nombreuses études menées au sol sur des échantillons massifs, métalliques ou organiques, ont clairement établi la présence et l'influence d'une convection importante dans les conditions de croissance qui donnent naissance à des structures cellulaires et dendritiques. L'écoulement modifie la structure de la couche limite solutale et perturbe ainsi l'uniformité de la microstructure[2]. L'élimination de la convection sur terre peut être obtenue par réduction de la taille des échantillons. De nombreuses expériences sur les systèmes transparents ont été menées en échantillons minces (quasi-2D de forme)[3] ou en tubes capillaires. Même si de telles configurations ont conduit à des progrès très importants dans la compréhension de la dynamique de la solidification, de tels systèmes ne correspondent pas à des réseaux étendus 3D et les résultats ne peuvent pas en être extrapolés4. Des expériences en réseau étendus 3D sont nécessaires mais requièrent la microgravité pour permettre d'éliminer la convection et ses effets.

Dans le cadre du projet scientifique MISOL3D (MIcrostructures de SOLidification 3D) sélectionné par le CNES, l'équipe Microstructures de Croissance Auto-organisées de l'IM2NP a participé au développement de l'Instrument DECLIC et de son insert DSI (Directional Solidification Insert) dédié à l'étude in situ de la formation des microstructures colonnaires cellulaires et dendritiques 3D sur des analogues transparents en régime de transport diffusif. Les expériences spatiales ont débuté en décembre 2009 avec le commissioning de l'instrument DECLIC-DSI à bord de la Station Spatiale Internationale (ISS). Jusqu'en mars 2011, les expériences spatiales se sont enchaînées avant le retour sur terre du DSI. L'instrument a ensuite été utilisé jusqu'en janvier 2012 au sol pour mettre en évidence sur le même échantillon les effets convectifs. Mon travail de thèse a porté sur l'analyse des expériences réalisées dans ce cadre, au sol et en microgravité.

---

[1] H. Jamgotchian et al., (2001) *J. of Microscopy* 203 : 1

[2] H. Jamgotchian et al. (2001) *Phys. Rev. Lett*. 87 : 166105 ; T. Schenk et al. (2005) *J. Crystal Growth* 275 : 201

[3] K. Somboonsuk et al. (1984) *Met. Trans*. 15A : 967 ; R. Trivedi et al. (1985) *Acta Metall* 33 : 1061 ; S. Akamatsu et al. (1995) *Phys. Rev. E* 51 : 4751 ; J. Deschamps et al. (2008) *Phys. Rev. E* 78 : 011605

[4] N. Bergeon et al. (2005) *Adv. Space Res*. 36 : 80 ; S. Gurevich S,et al. (2010) *Phys. Rev. E* 81: 011603

Dispositif expérimental et méthodes d'analyse

L'instrument DECLIC (Dispositif d'Etude de la Croissance et des LIquides Critiques) est un instrument compact, multiutilisateurs, dédié à l'étude en microgravité, dans la Station Spatiale Internationale, des milieux transparents dans le domaine de la physique des fluides et de la science des matériaux. La partie commune de l'instrument rassemble l'essentiel des ressources électroniques et optiques. Trois inserts dédiés à chacune des expériences scientifiques et contenant les éléments spécifiques de celles-ci, complètent l'instrument. Le DSI (Directional Solidification Insert) est l'un de ces 3 inserts. Le contrôle de l'instrument se fait par l'intermédiaire du CADMOS (Centre d'Aide au Développement des activités en Micropesanteur et des Opérations Spatiales). Capable de fonctionner en automatique, l'instrument peut également être piloté en temps réel par téléscience. Concrètement, nous disposons d'une visualisation permanente de l'expérience via l'interface Web Visuweb (CADMOS-CNES) ainsi que d'un lien permanent audio avec l'équipe de contrôle du CNES via le logiciel Ivods (NASA) ; sur notre demande, les modifications de paramètres d'expériences ou d'observation sont envoyées à l'instrument par le CADMOS.

Le four est de type Bridgman, avec 3 zones chaudes séparées d'une zone froide par la zone adiabatique dans laquelle est généralement localisée l'interface.

En solidification dirigée, les 3 paramètres de contrôle de la formation de la microstructure sont : la concentration en soluté, fixée au sol au cours de l'élaboration du creuset, le gradient thermique G et la vitesse de tirage V_P (qui correspond à la vitesse de solidification en régime stationnaire). Pour une concentration et un gradient thermique fixés, l'augmentation de la vitesse de tirage permet de passer d'un front plan à basse vitesse, vers une interface cellulaire puis dendritique à grande vitesse. Nous avons travaillé à deux valeurs de gradient thermique différentes pour lesquelles nous avons effectué de nombreuses solidifications à V_P différentes, entre 0,1 et 30 µm/s.

La cartouche contenant l'alliage préparé au laboratoire (succinonitrile – 0.24 %pds camphre) est composée d'un creuset, en quartz, de diamètre interne 1 cm, permettant une longueur de solidification de 10 cm et d'un système de compensation de volume permettant d'absorber les variations du volume de l'alliage au cours de ses changements d'états.

Trois modes d'observation différents sont disponibles. Ils sont schématiquement représentés en Figure 14.

- l'observation directe le long de l'axe de croissance est le mode le plus fréquemment utilisé. Il fournit une vue de dessus de l'interface qui permet de suivre au cours du temps la formation et l'évolution de la microstructure : Figure 14-a et b.

- l'observation transverse fournit une vue de côté de l'interface qui permet essentiellement de suivre le mouvement de l'interface et sa courbure : Figure 14-c et d.

- un interféromètre est installé le long de l'axe de croissance. L'analyse des images interférométriques permet de reconstruire la forme de l'interface ou des structures (cellules, pointes de dendrites) ainsi que de mesurer des vitesses locales de croissance : Figure 14-e.

Une quantité considérable de données, essentiellement sous forme d'images a été obtenue durant ces campagnes d'expériences si bien que l'un des premiers objectifs de mon travail a été de développer des procédures d'analyse d'image (logiciel Visilog), systématiques et fiables, permettant d'extraire des caractéristiques quantitatives du réseau. La première étape consiste, par une série de traitement d'images, à obtenir une image binaire où chaque structure (cellule ou dendrite) peut être identifiée, numérotée et caractérisée individuellement. L'image est ensuite utilisée en entrée de macroprocédures que j'ai développées pour extraire les distributions d'espacement primaire (taille caractéristique des structures), le nombre de premiers voisins de chaque structure, le niveau d'ordre du réseau (caractérisation par l'Arbre de Longueur Minimale).

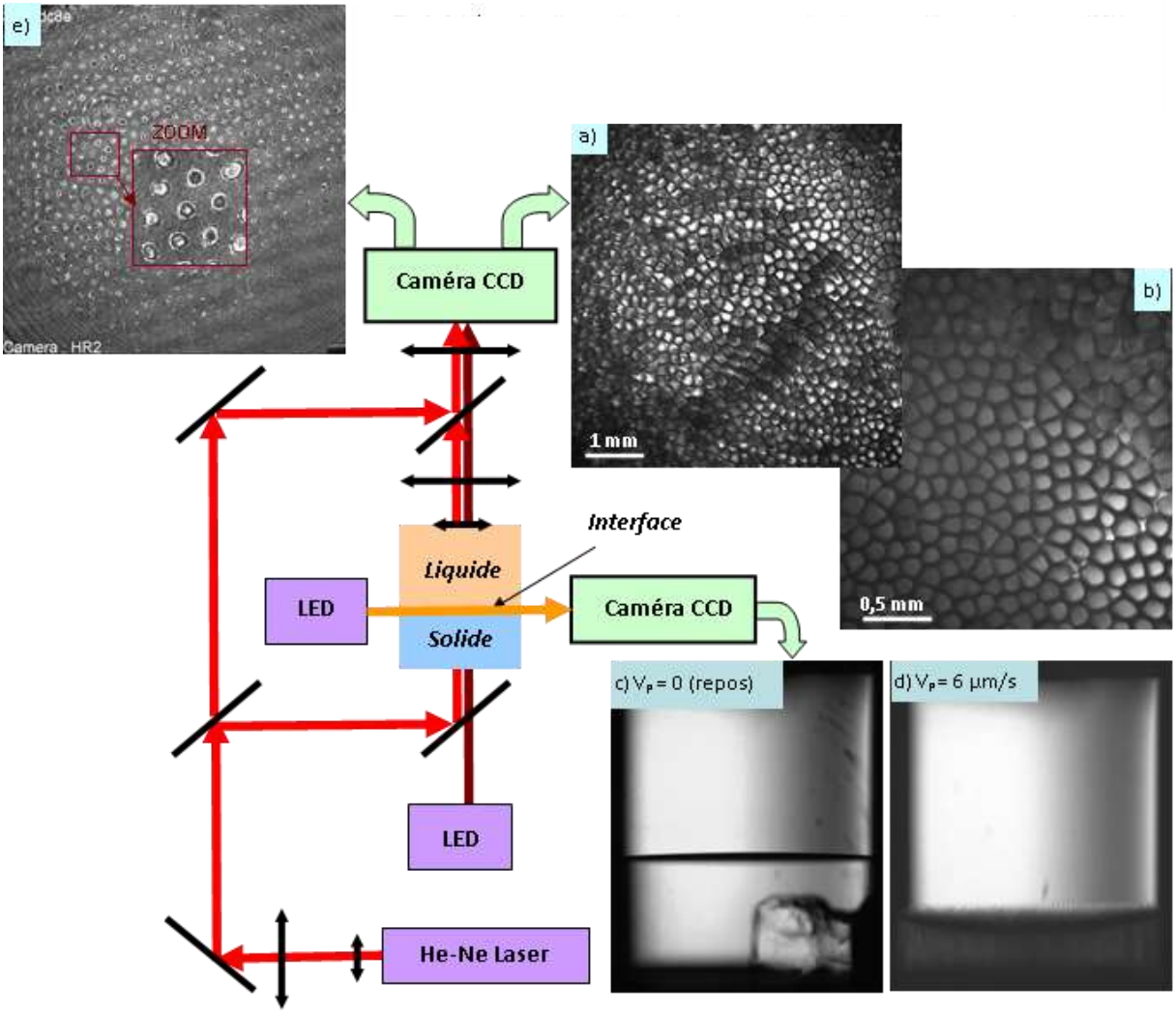

Figure 14. Schéma des diagnostics optiques et exemples des types d'images obtenues (SCN-0.24%pds camphre – G = 28 K/cm): a) and b) observation directes (V = 6 µm/s) ; c) and d) observation transverses ; e) observation interférométries.

Caractérisation des réseaux : formation, évolution et état stationnaire

Les expériences de solidifications longues, à vitesse constante, en partant d'une interface au repos, ont été analysées pour étudier la formation du réseau et identifier les mécanismes d'ajustement de l'espacement primaire.

Les premiers stades de la formation de la microstructure ne dépendent que très peu de la vitesse de tirage. Ils sont par exemple décrits dans la **Figure 15** pour V = 4 µm/s (G =2 8 K/cm). L'interface au repos (V = 0) est lisse (**Figure 15**-a) et l'instabilité morphologique après démarrage du tirage débute par la formation de vallées le long des sous-joints de grains : **Figure 15**-b. Entre ce réseau de sous-joints, l'interface est toujours lisse mais des poxes, ondulations circulaires de la surface, peuvent apparaître. Le réseau de vallées s'étend progressivement et se coupe dans la direction transverse pour former des prémices de cellules. Simultanément, une ondulation uniforme de la surface apparaît et envahit l'interface (**Figure 15**-c) ; cette ondulation est associée à la première longueur d'onde visible de l'instabilité morphologique. L'amplitude de la modulation d'interface augmente, des canaux se forment mais les cellules sont difficilement identifiables : **Figure 15**-d. A ce stade, la dynamique est très rapide et le réseau très désordonné. Le désordre diminue ensuite progressivement et un réseau de cellules apparaît finalement : **Figure 15**-e. La dynamique de réseau ralentit alors pour se limiter à l'ajustement progressif de l'espacement primaire et à la mise en ordre du réseau : **Figure 15**-f.

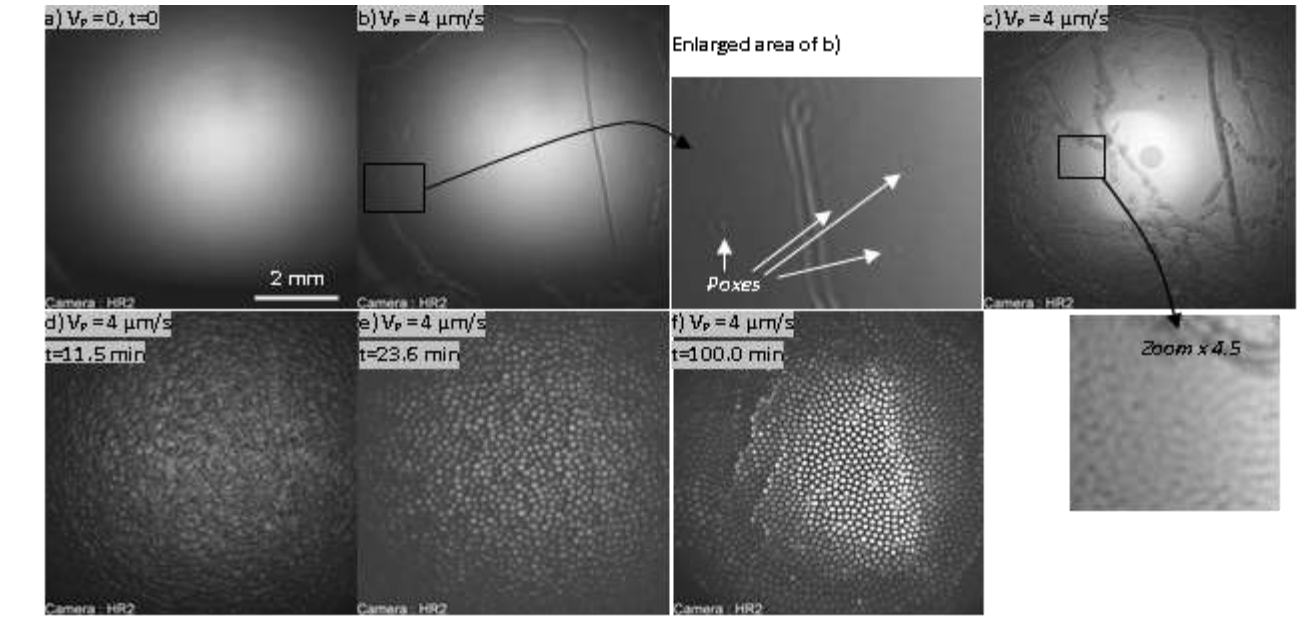

Figure 15 . Formation et évolution de la microstructure pour V = 4 µm/s (SCN – 0.24 %pds Camphre, G = 28 K/cm)

A titre d'exemple, la Figure 112 montre l'évolution de l'espacement primaire en fonction du temps pour 2 vitesses de tirages différentes (G = 28 K/cm). En deçà de 2 µm/s, l'interface est macroscopiquement faiblement convexe. Cela engendre un glissement lent des cellules du centre du creuset vers le bord, accompagné d'un étirement des structures conduisant à de nombreux tip-splittings (division du sommet) ; les cellules s'éliminent au niveau du bord du creuset. C'est le cas à 1 µm/s même si l'interface n'est que très faiblement convexe et que cette dynamique de glissement et de tip-splitting reste extrêmement limitée. Par contre, au-delà de V = 2 µm/s, une croissance excessive de l'espacement est suivie par une diminution qui nécessite la création de cellules. Il est apparu à l'analyse que le mécanisme prédominant de création de ces cellules n'était pas le tip-splitting mais un mécanisme de type puits (où les cellules sont éliminées) – source (où les cellules sont créées). La source est souvent en bordure du creuset et le réseau glisse vers le puits sous l'effet de la courbure macroscopique de l'interface. Les défauts de type sous-joints jouent souvent le rôle de puits. Ces analyses correspondent à des interfaces macroscopiquement concaves.

Ces résultats mettent en lumière l'influence de la courbure macroscopique de l'interface, inévitable en 3D. L'effet de cette courbure, et des mécanismes spécifiques d'ajustement de l'espacement associés, sur les valeurs d'espacements primaires moyens et leur distribution devra être analysée de façon plus approfondie, par exemple en simulation numérique par champ de phase.

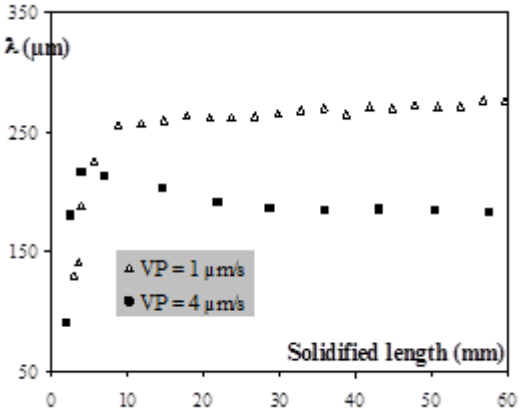

Figure 112. Evolution de l'espacement primaire au cours de la solidification pour V = 1 µm/S et 4 µm/s (SCN – 0.24 %pds camphre, G = 28 K/cm

La caractérisation des réseaux en régime stationnaire permet d'obtenir les données de références (« Benchmark data ») nécessaires à la validation et calibration des modèles théoriques et/ou numériques. Plusieurs modèles théoriques[5] ont été proposés dans la littérature pour décrire la variation de l'espacement primaire en fonction des trois paramètres de contrôle (vitesse de tirage V, gradient thermique G et concentration solutale C_0). Ces modèles donnent une variation en loi de puissance de $\lambda = A \cdot C^{0.25} G^{-0.5} V^{-0.25}$, avec A

[5] W. Kurz et al. (1981) *Acta Metallurgica*. 29: 11 ; R. Trivedi, (1984) M*etallurgical Transactions A* 15:. 977

une constante fonction des caractéristiques de l'alliage. Un bon accord avec ces modèles a été obtenu. (**Figure 17**).

Enfin, les mesures à l'état stationnaire (ou quasi-stationnaire) ont été comparées à des expériences similaires (mêmes paramètres de croissance) réalisées en échantillons minces par l'équipe de R. Trivedi (Iowa State University, USA) dans le cadre d'une collaboration. Un effet saisissant de la dimensionnalité est souligné: varier l'épaisseur des échantillons conduit à une grande variation de l'espacement primaire pour les mêmes conditions de croissance. Par ailleurs, deux branches distinctes de valeurs d'espacements apparaissent dans l'échantillon mince pour les régimes cellulaires et dendritiques alors qu'une variation continue est observée dans les échantillons 3D.

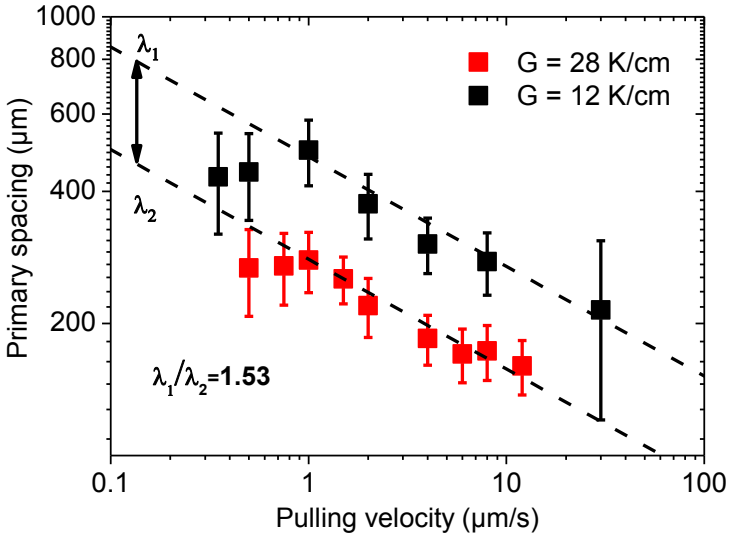

Figure 17. Evolution de l'espacement en fonction de vitesse de tirage dans échelle log-log et comparé avec des modèles classique.

Instabilités secondaires du réseau cellulaire

La possibilité inédite d'étudier in situ des réseaux étendus homogènes (absence de convection) nous a permis d'observer des instabilités secondaires du réseau cellulaire, qui jusqu'à maintenant n'avaient pu être étudiées qu'en 2D[6], révélant de ce fait une complexité supplémentaire. A très basse vitesse et gradient faible, nous avons observé des multiplets, particulièrement bien révélés par l'interférométrie. Leur structure 3D ainsi que leur dynamique ont été étudiées. A basse vitesse également mais gradient thermique plus important, nous avons pu observer des réseaux oscillants qui se manifestent par une oscillation périodique de la taille apparente des cellules (dans le plan x,y) ainsi que de la position de leurs pointes (position suivant z) . Les analyses ont été complétées par des simulations numériques par la méthode du champ de phase réalisées par l'équipe du Pr. Karma (Northeastern Univ, Boston, USA) et l'équipe TMS de l'IM2NP (R. Guérin & J.M. Debierre), sur ces structures oscillantes. Ces deux types d'instabilités secondaires, instabilités de la solution stable cellulaire, correspondent respectivement aux modes de 'vacillation breathing' et 'broken parity '.

Réseaux oscillants

La manifestation évidente de l'oscillation de réseau est la variation périodique de la surface apparente des cellules. Il est à noter que l'espacement primaire, défini comme la distance centre à centre de cellules voisines, n'est pas affectée par l'oscillation, celle-ci se faisant par un mouvement des sillons. Des analyses interférométriques nous ont permis de mettre en évidence l'oscillation de la vitesse des pointes – et donc de leur position verticale- par l'intermédiaire de la mesure de l'évolution temporelle du rayon de courbure des pointes de cellules. Ce mode d'oscillation apparait dans une gamme étroite de paramètres. La période d'oscillation a été mesurée en fonction de la vitesse de tirage ; elle varie suivant une loi de puissance similaire aux observations qui avaient été faites en échantillons minces.

Des différences fondamentales ont été observées entre le cas tridimensionnel et le cas des réseaux en lames minces concernant la cohérence spatio-temporelle des oscillations. En lames minces, les cellules voisines oscillent en opposition de phase et cette cohérence se maintient à longue distance. Par contre, dans le cas tridimensionnel, les oscillations

[6] M. Georgelin et al., (1997) *Physical Review Letters*. 79:. 2698 ; H. Jamgotchian et al., (1993) *Physical Review E* 47: 2698

sont généralement incohérentes du fait du désordre intrinsèque du réseau ; dans des zones localement ordonnées peut apparaitre une cohérence des oscillations à courte distance. Par exemple, un ordre local hexagonal est associé à 3 sous-réseaux qui oscillent chacun avec un déphasage de ± 120° par rapport aux autres sous-réseaux. Un ordre local carré est associé à 2 sous-réseaux oscillant en opposition de phase. Ces résultats mettent en lumière les relations complexes entre le pavage du réseau et sa dynamique. (**Figure 18**)

Les simulations en champ de phase 3D recoupent les résultats expérimentaux tant au niveau de la période de l'oscillation que des caractéristiques de cohérence spatio - temporelle.

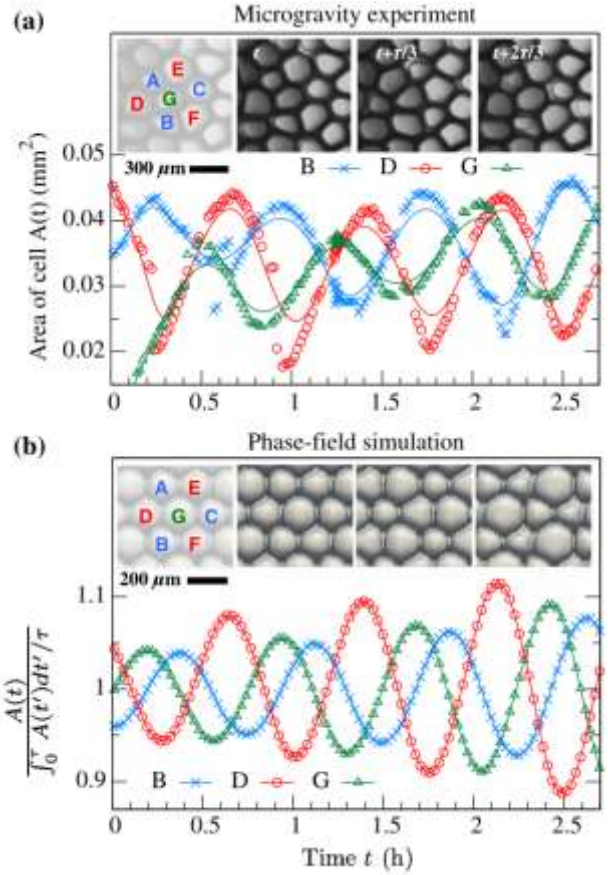

Figure 18. Corrélation de courte portée des réseaux hexagonaux à V = 1 µm / s, G = 28 K / cm. a) trois groupes de cellules oscillent cohérente avec un décalage de phase de 2π/3. b) la simulation de champ de phase recoupent la même oscillation cohérente.

Multiplets

Des structures de multiplets ont été observées dans une gamme très étroite de vitesses de tirage proche de la vitesse critique, à bas gradient thermique. La 3ème dimension confère à ces structures une complexité supérieure par rapport aux structures bidimensionnelles observées en lames minces. La formation, l'évolution et la caractérisation géométrique des multiplets sont étudiées par la reconstruction 3D des

images interférométriques. Le multiplet se présente comme une structure présentant plusieurs « sous-cellules » (« sub-cell ») séparées par des sillons peu profonds se rejoignant dans un puits plus profond (« pit ») : (**Figure 19**). L'évolution des paramètres caractéristiques (espacements, amplitude, dérive…) des multiplets au cours du temps a été mesurée. Les conditions expérimentales pour lesquelles sont observés des multiplets sont associées à une interface fortement convexe, ce qui implique un glissement des structures vers le bord du creuset, ainsi qu'un étirement de ces structures. Les mesures ont mis en évidence une fois de plus la forte influence de la courbure sur la dynamique d'évolution de ces structures. L'étirement entraine une croissance de la surface des multiplets qui conduit à sa coupure en multiplets de multiplicités moindres. La question de la formation des multiplets pour les mêmes paramètres de croissance pour une interface plane reste de ce fait ouverte compte-tenu l'influence cruciale de la courbure sur la dynamique des multiplets. Des simulations numériques en champ de phase 3D sont en cours, ce qui devrait permettre de clarifier ce problème.

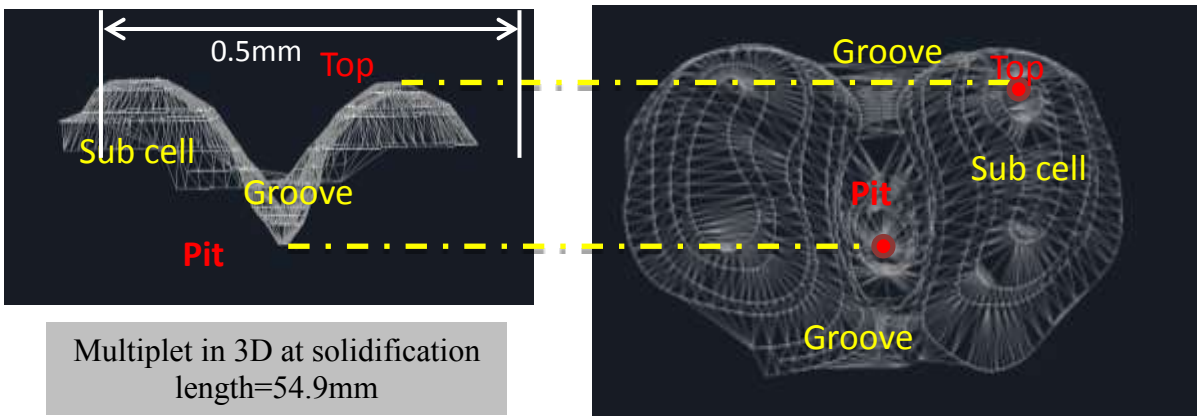

Figure 19. Doublet forme reconstruite à partir de l'image interférométrique. Il montre les 2 « sous-cellules » et un puits au centre du sillon entre les deux « sous-cellules ».

Influence de la convection : étude comparative des expériences au sol et en microgravité

La convection est toujours présente lors de la solidification au sol d'échantillons massifs. Afin d'étudier l'influence de la convection, des expériences similaires à celles réalisées dans l'espace (même paramètres de contrôle) ont été conduites dans l'insert DSI après son retour sur terre. Dans nos échantillons, la convection est d'origine thermique : les gradients thermiques radiaux au niveau de l'interface induisent un mouvement du fluide chaud vers le haut, et une convection torique s'établit. Suivant le sens du gradient thermique radial (et donc la forme – convexe ou concave – de l'interface), la convection est ascendante au centre du creuset et descendante au bord (interface concave), ou descendante au centre et ascendante sur le bord (interface convexe). Les flux thermiques vont déterminer le signe de ce gradient thermique, et les effets associés. Dans la plupart des cas, le phénomène dominant est le problème de l'évacuation, par les parois du creuset, de la chaleur latente libérée pendant la solidification ; l'interface est dans ce cas concave. A faible vitesse, ce phénomène peut devenir négligeable et la courbure va être déterminée par la position de l'interface dans le champ thermique de la zone adiabatique ; elle pourra être alors soit concave (dominance de flux sortants : près de la zone froide) ou convexe (dominance de flux entrant : près de la zone chaude).

Un des premiers effets mis en évidence est l'augmentation de la vitesse critique de transition front plan-cellulaire en présence de convection, conformément à des observations et modèles antérieurs[7]. Conformément à des études antérieures réalisées au laboratoire[8], nous avons également pu mettre en évidence l'effet de la convection sur l'homogénéité de la microstructure. La convection perturbe la couche solutale en avant de l'interface, créant ainsi un gradient radial de concentration solutale et donc une rampe des paramètres de contrôle le long de l'interface. Un gradient d'espacement primaire est ainsi observé.

Nous avons également comparé les espacements primaires moyens en régime stationnaire (**Figure 20**) : au sol, l'espacement primaire augmente de façon continue tandis qu'en régime diffusif, il décroit. Les courbes se croisent pour une vitesse de croissance correspondant à l'interface plane : l'égalité des espacements s'explique alors par une convection extrêmement faible (gradient thermique radial ~ nul). Les vitesses

[7] Trivedi, R et al.(2001) *Science and Technology of Advanced Materials* 2.1: 309–320..

[8] B.Billia, and R Trivedi. (1993) *Handbook of Crystal Growth*. Elsevier. Print.

inférieures correspondent à des interfaces convexes, et des espacements en présence de convection inférieurs aux espacements en microgravité. Cette situation est en accord avec les résultats d'études sur échantillons métalliques[9] (interface toujours convexe). Par contre, quand les interfaces sont concaves, l'espacement au sol devient supérieur à l'espacement en microgravité et cette différence s'accentue avec la vitesse de tirage, ce qui diffère fortement des comportements observés dans les alliages métalliques pour lesquels les effets convectifs s'atténuent quand la vitesse de tirage augmente et que la vitesse du fluide devient négligeable par rapport à la vitesse de tirage. Ces différences fondamentales de comportement sont liées à l'origine fondamentalement différente de la convection dans les deux types d'alliages. Dans les alliages transparents, la chaleur latente générée étant proportionnelle à la vitesse de tirage, la convection augmente avec celle-ci ; la courbure des isothermes dans les alliages métalliques n'est pas liée à l'évacuation de la chaleur latente mais à la différence de conductivité entre le solide et le liquide. Les vitesses de convection ont été estimées à partir des différences d'espacement primaire en utilisant un modèle[10] développé dans le cas des interfaces convexes et que nous avons extrapolé au cas concave. Ces estimations demandent encore à être validées par des analyses plus approfondies et éventuellement des simulations numériques de la convection.

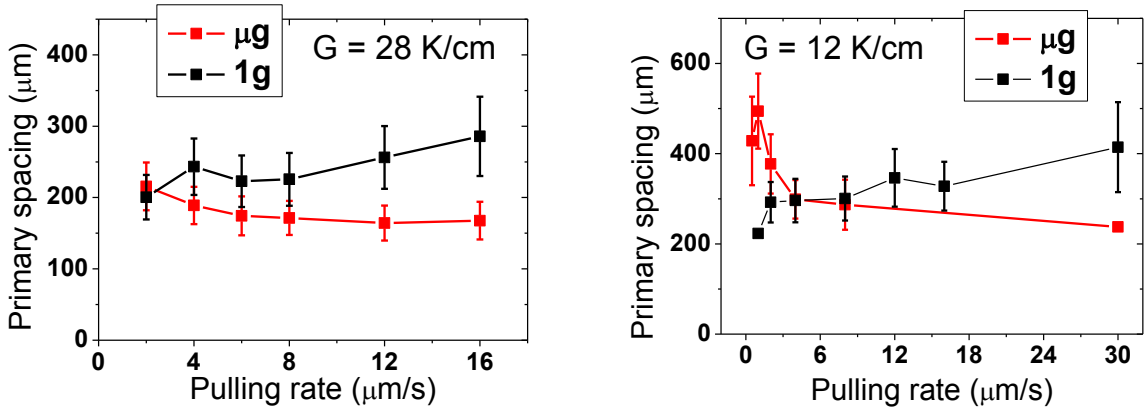

Figure 20. Espacement primaire en fonction de la vitesse de tirage, pour des conditions de μg et 1g.

[9] Nguyen Thi, H. et al. (2005) *Journal of Crystal Growth* 281.2-4 : 654–668.

[10] Lehmann, P. et al. (1998) *Journal of Crystal Growth* 183.4 : 690–704.

Conclusion – Perspectives

La formation et l'évolution de réseaux cellulaires et dendritiques étendus a été étudiée en solidification sur un alliage organique transparent (succinonitrile-0.24%pds camphre), analogue aux alliages métalliques, par observation in situ et en temps réel de l'interface en régime de croissance diffusif. L'évolution des paramètres caractéristiques des réseaux ainsi que les mécanismes de cette évolution ont été présentés. Ils révèlent un rôle critique de la courbure macroscopique de l'interface, inévitable en échantillons massifs. L'obtention, grâce à la microgravité, de réseaux homogènes étendus a permis l'étude d'instabilités secondaires (réseaux oscillants et multiplets) jamais jusqu'à maintenant étudiés en réseaux étendus, conférant une complexité supplémentaire aux dynamiques de ces phénomènes. En particulier, il est apparu dans le cas des réseaux oscillants, que –contrairement au cas 2D – la cohérence spatiotemporelle des oscillations était extrêmement limitée du fait du désordre intrinsèque du réseau 3D. L'influence de la convection sur les caractéristiques des réseaux a pu une fois de plus être pointée, confirmant l'utilité des études en microgravité pour l'obtention de données de références.

Ces travaux se prolongeront par la poursuite de l'analyse des données obtenues au cours des expériences discutées précédemment mais également par la réalisation de deux nouvelles séries d'expériences spatiales sur des échantillons de compositions différentes. Le choix des compositions permettra de focaliser les études dans un cas, sur le régime dendritique, dans l'autre cas, sur le domaine d'apparition des instabilités secondaires.

RESUME DE LA THESE

Afin de clarifier et caractériser les mécanismes fondamentaux de formation des réseaux étendus cellulaires et dendritiques en régime diffusif, des expériences de solidification dirigée permettant l'observation in situ en temps réel de l'interface solide-liquide d'un alliage transparent (succinonitrile – 0,24%pds camphre), modèle des alliages métalliques, ont été réalisées dans l'instrument « DECLIC Directional Solidification Insert » à bord de la Station Spatiale Internationale. Des procédures spécifiques d'analyse d'images ont été développées pour caractériser quantitativement les réseaux et extraire des données de référence à comparer aux modèles théoriques ou numériques. Les mécanismes d'évolution et de sélection de l'espacement primaire sont décrits et reliés à la courbure macroscopique de l'interface qui apparait comme un paramètre important de la dynamique de réseau. L'obtention de réseaux homogènes étendus nous a permis d'observer des instabilités secondaires du régime cellulaire pour la première fois dans des systèmes tridimensionnels. Dans une fenêtre étroite des paramètres de contrôle, le réseau cellulaire présente des oscillations caractérisées par une variation périodique de la taille des cellules et de la hauteur de leurs pointes. Nos analyses mettent en évidence l'absence de cohérence globale de l'oscillation, exceptée dans des zones localement ordonnées dans lesquelles les oscillations de cellules voisines peuvent être synchronisées. Dans une autre gamme de paramètres de contrôle, la formation de multiplets -autre type d'instabilité secondaire- a été observée. La structure et la dynamique de ces multiplets est décrite. Enfin, des essais comparatifs ont été réalisés au sol, pour les mêmes paramètres de croissance, afin de clarifier l'influence de la convection. Les différences entre les expériences au sol et en microgravité, en particulier concernant l'espacement primaire, sont reliées à l'amplitude de la convection.

Mots-clés: Solidification dirigée, alliage transparent, microgravité, observation in situ, microstructure, convection, instabilité secondaire, réseau oscillant, multiplet.

SUMMARY

To clarify and characterize the fundamental physical mechanisms active in the formation of three-dimensional (3D) arrays of cells and dendrites, in situ monitoring of series of experiments on a transparent alloy (succinonitrile – 0.24 wt% camphor), model of metallic systems, was carried out under low gravity in the DECLIC Directional Solidification Insert on-board the International Space Station. Image analysis procedures have been developed to quantitatively characterize the patterns and get benchmark data to compare with theoretical or numerical modelling. The mechanisms of primary spacing evolution and selection are described and related to the macroscopic interface curvature that appeared to be a critical parameter. The extended homogeneous patterns obtained in microgravity enabled us to observe secondary instabilities of the cellular pattern for the very first time in 3D patterns. For a restricted range of growth control parameters, the cellular pattern presents breathing oscillations characterized by a periodic variation of both appeared cell size and tip position. Our analyses highlight the absence of global coherence of cell oscillations, except in locally ordered areas where synchronization of neighbor cells may happen. In another range of control parameters, another type of secondary instability has been identified that corresponds to multiplet formation; the structure and dynamics of those multiplets are also described. Finally, comparative experiments have been performed on ground with similar growth parameters to point out the influence of convection. The differences between ground and microgravity results, especially regarding the primary spacing, are related to fluid flow magnitude.

Keywords: Directional solidification, transparent alloy, microgravity, in situ observation, microstructure, convection, secondary instability, oscillating pattern, multiplet.